Quantum Optomechanics for Hybrid Spin–Membrane Entanglement

Ph.D. thesis

Christoffer Østfeldt

Submitted to
University of Copenhagen
Niels Bohr Institute
Ph.D. School of Science

They say that a person's personality is the sum of their experiences. But that isn't true, at least not entirely, because if our past was all that defined us, we'd never be able to put up with ourselves. We need to be allowed to convince ourselves that we're more than the mistakes we made yesterday. That we are all of our next choices, too, all of our tomorrows.

- Fredrik Backman, 1981– , *Anxious People*

Colophon

This thesis was set with LaTeX 2_ε using the *memoir* class.
The font is Libertine 10/12.6, on normal A4 paper.
Graphics created using Matplotlib under Python 3.8, Ti*k*Z/pgf, as well as Inkscape with `ComponentLibrary` (CC BY-NC 3.0) by Alexander Franzen.

Quantum Optomechanics for Hybrid Spin–Membrane Entanglement

Author Christoffer Østfeldt
Advisor Prof. Dr. Eugene S. Polzik

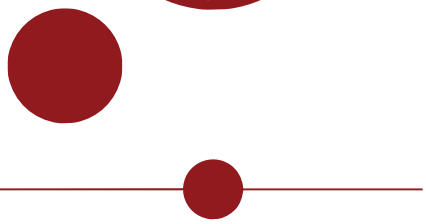

UNIVERSITY OF COPENHAGEN

QUANTOP

The Danish Center for Quantum Optics
The Niels Bohr Institute

This thesis has been submitted to the
PhD School
of
The Faculty of Science
University of Copenhagen
October 4TH 2022

Abstract

The second quantum revolution, signaled by the emergence of practical quantum technologies such as secure quantum communication, quantum computing and quantum limited and enhanced sensing, is pushing the need for ever better experimental control and design of quantum systems. However, with this development has come the realization that one single quantum system may not efficiently implement all the different tasks needed for, e. g., a "Quantum Internet", or generalized quantum computers. To this end, hybrid quantum systems, incorporating fundamentally disparate material systems have been proposed, efficiently harnessing the advantages and capabilities of the different sub-systems.

In this thesis, we report on the continued development of a hybrid spin–mechanics quantum system, ultimately showcased by the successful demonstration of steady-state conditional entanglement between the spin and mechanics, as witnessed by the conditional variance $V_c = 0.83 \pm 0.02 < 1$, below the separability limit.

The optomechanical system consists of a out-of-plane vibrational mode of a soft-clamped, highly stressed silicon nitride membrane, which is embedded in a high-finesse free-space optical cavity, realizing a Membrane-in-the-Middle optomechanical system, and mounted in a 4 K cryostat. Significant improvements to the optomechanical assembly over previous work allow for a much easier implementation of optomechanical systems into hybrid setups, and allows for full electronic control of cavity resonance as well as membrane position in the cavity standing wave.

The spin system is prepared in a warm (330 K) ensemble of optically pumped cesium atoms confined in a spin-preserving microcell. The collective atomic spin is co-aligned with an external magnetic field around which the spin performs Larmor precession. This effectively prepares the spin in the highest energy state, thus implementing an effective negative mass reference frame for the optomechanical system.

The itinerant light field probing the two systems reads out their collective degrees of freedom, and, together with the effective negative mass of the spin, allows for a Quantum Back-Action Evading measurement, reducing the probe-induced measurement noise by 2.6 dB compared to the mechanics-only case, or 4.6 dB compared to the case with two detuned systems, both significant improvements over previously reported results. Furthermore, a non-local cooling of the Einstein–Podolsky–Rosen (EPR) variables reduces the combined thermal noise of the systems by 2.5 dB.

Implementation of optimized Wiener filtering of the measured photo current, together with the noise suppressing mechanisms, allows state estimation at an uncertainty level of the (entangled) continuous variable EPR-like state, with *deterministic* conditional variance below the separability limit, demonstrating entanglement.

The implemented hybrid quantum system paves the way towards teleportation based quantum protocols in spin-mechanics hybrid interfaces, as well as measurements of motion beyond the standard quantum limits of sensitivity.

Sammenfatning

Den anden kvanterevolution, der markeres ved fremkomsten af praktisk anvendelige kvante-teknologier såsom sikker kvantekommunikation, kvanteberegninger, samt kvantebegrænsede og –forbedrede målinger, øger behovet for forbedring af den eksperimentelle kontrol over og design af kvantesystemer. Med denne udvikling er kommet en erkendelse af at et enkelt kvantesystem med sandsynlighed ikke er i stand til at implementere alle de forskellige opgaver der er nødvendige for f.eks. et "kvante-internet", eller en generaliseret kvantecomputer. Derfor er hybride kvantesystemer, der inkorporerer forskelligartede systemer, blevet foreslået som en mulig løsning til effektivt at udnytte fordele og kapaciteter af de forskellige delsystemer.

I denne afhandling rapporterer vi den fortsatte udvikling af et hybridt spin–mekanik-kvantesystem, i sidste ende ved at demonstrere succesfuld stationær betinget sammenfiltring (*eng: entanglement*) mellem spin og mekanik, som bevidnes af den betingede varians $V_c = 0.83 \pm 0.02 < 1$, som er under separabilitetsgrænsen.

Det optomekaniske system består af en "blødt-fæstnet" (*eng: soft-clamped*), stærkt udspændt siliciumnitrid-membran der har en vibrationel mode ud af planet. Membranen er indlejret i en højfinesse åben (*eng: free-space*) optisk kavitet, som dermed udgør et "Membran-i-Midten" optomekanisk system, der monteres i en 4 K-kryostat. En betydelig forbedring af den optomekaniske samling i forhold til tidligere, gør det langt nemmere at implementere optomekaniske systemer i hybride opstillinger og muliggør fuld elektrisk kontrol over kavitetsresonans så vel som membranpositionen i kavitetens stående bølge.

Spinsystemet forberedes i et varmt (330 K) ensemble af optisk pumpede cæsiumatomer, indeholdt i en spinbevarende mikrocelle. Det kollektive atomspin er orienteret langs et eksternt magnetisk felt, hvorom spinnet foretager Larmorpræcession, hvilket effektivt forbereder spinnet i det højeste energiniveau, og dermed implementerer en referenceramme for det optomekaniske system med effektiv negativ masse.

Det rejsende optiske felt der prober de to systemer udlæser deres kollektive frihedsgrader, og sammen med den effektive negative masse af spinnet tillader dette en kvantetilbagekoblingsundvigende måling, der reducerer den probeforårsagede målestøj med 2.6 dB sammenlignet med mekanikken alene, eller 4.6 dB sammenlignet med tilfældet hvor de to systemer er ude af resonans, begge betydelige forbedringer i forhold til tidligere resultater. Ydermere reducerer en ikke-lokal køling af Einstein–Podolsky–Rosen (EPR)-variablerne den samlede termiske støj af systemerne med 2.5 dB.

Implementering af optimeret Wiener-filtrering af den målte fotostrøm, sammen med de støjreducerence mekanismer, tillader tilstandsestimation med en præcision på (den sammenfiltrede) kontinuert-variabel EPR-lignende tilstand, med *deterministisk* betinget varians under separabilitetgrænsen, hvilket demonstrerer sammenfiltring.

Det implementerede hybride kvantesystem baner vejen mod teleportationsbaserede kvanteprotokoller med spin–mekanik-hybridsystemer, såvel som målinger af bevægelse under standardkvantegrænserne for følsomhed.

Acknowledgments

There are many, many people, where without their help and support, I would not have been able to finish my Ph.D.

First and foremost my thanks must go to Eugene. First of all, for giving me the opportunity to do a Ph.D. with you, on an immensely interesting and challenging project like the hybrid experiment. Secondly, for always being a supportive supervisor, who knows when to push and when to leave us alone – but always with the knowledge that you are there if we need you. But most importantly, I must thank you for your unwavering support when I fell ill in the early summer of 2021. Overcoming a depression, while working as a Ph.D. student, with all the external pressure of time-limited contracts and pressure to perform in a competitive world, would not have been possible without the true compassion and steadfast support you showed me, when I needed it the most. I am truly grateful for your exemplary help.

My wonderful colleagues in the hybrid experiment all deserve my highest praise. Michał Parniak, Rodrigo Thomas and Christoffer "Chris" Møller was the core experimental group behind the entanglement efforts, with Emil Zeuthen forming the theorist division. From each one of you I have gained tremendous insights into both science and Life™ in general. Chris, your enthusiasm and always positive attitude is impossible to not envy you. You were always curious in the best way, although your lack of ability to estimate the duration of a task is unrivaled. Michał, I have learned so much from you; I admire your grasp of both theory and experiment. Emil, you are a force to be reckoned with; a theoretical one man army, and the—to my mind—best kind of theoretician: one who understands and appreciates experimental necessities and possibilities. Rodrigo, I loved working with you; your enthusiasm, belief in your colleagues and willingness to help made every day a joy. I miss our bike rides.

Christian Bærentsen, Sergey Fedorov and Peyman Malekzadeh, the three newest additions to the team also deserve my highest praise. Christian, for taking on the atomic part of the setup with vigor – filling the void after Rodrigo is by no means a small task. Sergey, your eagerness to push for a deeper understanding is admirable; where I would almost always advocate the "measure it, and see if you can make sense of it"-approach, you insist that we *think*, and I try to learn from you. Peyman, I know joining an experiment as a new Ph.D. is never easy, and I know that my illness left you in a vacuum at times. You're making great strides in mastering the beast that the hybrid experiment is.

Jörg Helge Müller and Jürgen Appel, the latter of whom left us for greener pastures at DFM, the German powerhouse duo of Quantop, together and individually deserve my thanks. First, for taking me on as Master's student on the nanofiber experiment, and teaching me the intricacies of cold atom experiments. Later, for being the all round technical and scientific geniuses that makes the inner workings of an experimental research group tick. Jörg, you do not get enough praise for being an overall wonderful person, a brilliant guitarist[1] and a patient teacher. Jürgen, you are missed.

(1) Now turn up that amp!

To the inhabitants of the Fock dungeon, Ivan Galinsky and Georg Enzian. Thanks for the banter, the good-spirited teasing and the scientific collaborations.

Former members, Andi Barg and Yeghishe Tsaturyan, and newcomer Chao Meng, also deserve thanks.

To the wider Quantop group, current and former colleagues: Jonas B. Mathiassen, Jean-Baptiste Sylvain Béguin, Jacob Thornfeldt Hansen, Signe Markussen, Jens Arnbak, Karsten Dideriksen, Michael Zugenmaier, Rebecca Schmieg, Tulio Brasil, Jun Jia, Ryan Yde, Valerii Novikov (and probably a lot of people I forgot): thank you all. You've all contributed to making Quantop a wonderful place to work. To the people in SLAB, photonics and the theory group: thanks for always being willing to share your knowledge and equipment with those in need of help. The cooperation makes the whole section a better place.

The NBI mechanical workshop, led by the formidable Dennis Westphal Wistisen, and the electronic counterpart, is a vital part of experimental physics at this institute. Without the swift, competent help of skilled technicians[2] who make our custom experimental equipment[3], and repair broken equipment, what we do would be impossible. A big thanks to everybody at the workshop!

Life is not all physics, and family and friends deserve my warmest gratitude as well. Mom & dad, and my two darling siblings Benedicte and Benjamin: you may not understand what I am doing, but your love and support in life is tremendously important nonetheless. To my wonderful friends, Sofie, Viktor, Arvad, Anine[4]: thank you for the company, the laughs, the helping hands in time of need. Sofie & Viktor: Thanks for the trust you put in Freja and me. Arvad: Thanks for making me hang in, when undergraduate studies were less than joyous.

Finally: Freja, my wonderful wife. I couldn't have done it without you. The journey from young university students, figuring out a path in the world, to where we are today—with a beautiful, healthy baby girl, a house and high hopes for the future—has been an absolute joy. I look forwards to many more years with you (but no more Ph.D.s!). Thank you for your patience and support. I love you.

(2) magicians?

(3) For us, most prominently the optomechanical cavities.

(4) And many more, that I have forgotten.

Preface

Wellcome to my thesis. Before the show starts in earnest in Chapter 1, allow me these few pages to provide a very brief overview of what can be expected and the organization of the content, as well a number of small musings about what thesis writing is all about, and how we may all improve written science communication.

This Thesis at a Glance

In Part I I will try to give a suitable exposition of both the field of quantum optics in general, and quantum optomechanics in particular, as well as a suitably detailed walkthrough of the formalism we will use to describe what is going on. We start out in Chapter 1, where we introduce the thesis by noting the historical perspectives of coupling motional degrees of freedom to light, and quantum mechanics of meso- and macroscopic objects. In Chapter 2 we outline the previous work, in the field and in Quantop. In Chapter 3 I introduce a theoretical description of optomechanical systems, before following up with practical implementation details in Chapter 4. Following that, in Chapter 5, an introduction to alkali spin systems—the other main actor in our play—is given.

Part II changes gear, and is of a much more technical nature. Here, I discuss the process of designing and implementing a new optomechanical cavity assembly. In Chapter 6 the design of the cavity itself is introduced. In Chapter 7 a simple numerical model guiding this process is introduced, and compared to experimental experience. Finally, I detail our endeavours towards minimizing the detrimental effect of mechanical modes of the cavity mirrors in Chapter 8.

Part III is about the physics of hybrid systems. After a technical intermezzo in Chapter 9, we get to the main course: the entanglement of our spin oscillator to a mode of our mechanical device. Chapter 10 details the results published in Rodrigo A. Thomas et al. (2020)[1]. After this, we round off the thesis with a brief set of concluding remarks in Chapter 11, which also includes a short summary of progress since the publication of the entanglement work.

Finally, there are a number of appendices in Part IV, containing supplementary information.

(1) Rodrigo A. Thomas et al. (2020). "Entanglement between distant macroscopic mechanical and spin systems". In: *Nature Physics* 17, pp. 228–233.

What is the Purpose of a Thesis?

One way to answer why you, as a reader, should care to read this thesis, is for me to state why I believe we write theses in the first place. To me, there are three main reasons to undertaking the task of writing a document like this, and each reason comes with its own distinct audience:

1. To disseminate scientific knowledge and assess the quality of the work performed in relation to the Ph.D.; this is the conventional target audience and goal of a thesis: the scientific community at large and Assessment Commitee in particular, and the awarding of the degree. While the first is also partially covered by publications in journals and at scientific, many things are not

well suited for publication in four page letters, and can thus only be found in larger works like a thesis.

2. To preserve institutional knowledge within a research group; once a research group has been going for a while, the accumulated back-catalog of theses can, if written with this in mind, become an invaluable treasure trove of scientific insights, experimental know-how and all the things that are deemed too mundane to be published in papers, but without which the science would fall apart.

3. To introduce newcomers to the field, group and experiment; working on the edge of the known, as fundamental research is by definition supposed to do, we often fall short when looking for suitable literature for new students in the field. The books have simply not been written, or are not updated near often enough to keep up with the evolution of the field, and journal articles often necessitate extensive prior knowledge of the field. Theses written by recent students on an experiment (be they M.Sc. or Ph.D.) can serve as a much easier introduction to the field and literature.

Striking the balance between these, sometimes opposing, interests or goals is an art. While an experienced researcher may prefer brevity, new students and later generations seeking to understand finer details of the work may value verboseness. I hope that the resulting balance is useful to as many as possible, and not too offensively dredging for anybody.

With this in mind, it is hopefully also apparent that the three parts outlined above will be of different relevance to the three different audiences I have proposed. For example, Part II may well be of larger interest to following generations of students than to absolute newcomers, and Part I will probably be of less significance to the seasoned researcher.

A Couple of Notes on Stylistic Choices and Science Communication

Abbreviations[2] are, for better or worse, a significant part of written communication in physics, especially in the terse prose of papers and letters – a not wholly unproblematic tendency; see, e. g., Hales, Williams, and Rector (2017)[3]. Here, in the thesis format, we can most often afford spending the extra few characters to spell things out; the exception being things that are almost exclusively referred to by their abbreviation, and in figures, where the space is limited. I will do my best to ensure clarity is not lost, but should I fail, the reader can consult the Nomenclature on page 227.

Most figures in this thesis has been plotted with color blind-friendly colors. These come with the added benefit of being perceptually uniform, i. e., having a smoothly, monotonic change in brightness throughout a color scale, and thus also vastly better for those of us with normal color vision. For a discussion see, e. g., the excellent paper by Crameri, Shephard, and Heron (2020)[4]. For my fellow scientists: please stop using `jet` and all it's siblings. For the color blind people that may come across this thesis: if you find anything that can be improved, please do let me know.

(2) Especially, for some reason, Three Letter Abbreviations (aka. TLA).

(3) Andrew H. Hales, Kipling D. Williams, and Joel Rector (2017). "Alienating the Audience: How Abbreviations Hamper Scientific Communication". In: *APS observer* 30.

(4) Fabio Crameri, Grace E. Shephard, and Philip J. Heron (2020). "The misuse of colour in science communication". In: *Nature Communications* 11 (1), pp. 1–10.

The thesis makes ample use of the margins. In there I will put supporting figures—the ones meant, for example, to remind the reader exactly *what* does a generalized Laguerre polynomial look like—as well as "foot"notes and other ancillary text. Citations appear in the text in a fashion similar to most other theses I have come across, but for most references there will also be a full reference in the margin (marked as a "foot"note), at least the first time a reference appears, or when it is central to the point being discussed. As a general rule (to which there will probably be exceptions), marginal content is *marginal*. Ignoring it should not lead to any major loss of information.

Science communication with a single author invariably raises the question of what pronouns to use—personal pronouns, that is. Does one write "I" or "we"? Or does one perhaps mix? Although I do not know of any rules, experience tells me that tradition favors the plural form, "we", although what is often meant is indeed the singular (royal) "we". I will try to make a slightly different choice. When I believe that something is truly my own doing or opinion, the text will reflect that; whenever the work presented is the result of a collaboration with colleagues, which it is more often than not, "we" will be the pronoun of choice. As always, there are bound to times where this rule does not hold.

Finally, I cannot recommend the paper "What's Wrong with these Equations?" by Mermin (1989) enough. It is, to me, mandatory reading for anyone writing prose with math.

Brief Table of Contents

Abstract v

Preface ix

Detailed Table of Contents xv

List of Publications xxi

Part I Introduction 1

1 **Introduction** 3
Background, motivation and a rough overview of the work presented.

2 **Previous Work** 9
The work in the field and in Quantop, prior to and during this project. I briefly summarize the main milestones and results.

3 **Basic Optomechanics** 21
Basic optomechanics is introduced. Canonical system, equations of motions, dissipation & noise. Also, some needed math is introduced.

4 **Optomechanics in Practice** 69
Practical implementation details of a membrane-in-the-middle optomechanical system. Cryostats, Q-measurements, membrane fabrication & other dirty details.

5 **Alkali Spin Systems** 87
The physics of alkali atomic spin systems.

Part II A New Hybrid Cavity 121

6 **A New Cavity** 123
A new optomechanical cavity design for hybrid optomechanics is presented. We introduce several important degrees of freedoms to the cavity, compared to earlier, semi-monolithic designs. We present a set of associated problems, and how we overcame these.

7 **Higher Order Optical Modes in an Optomechanical Cavity 133**
A numerical model for evaluating hybridization and splitting of higher order optical modes in optomechanical cavities. The model gives valuable insight into the detrimental effects of membrane tilt, wavefront curvature and clipping losses. The model is compared to experimental data.

8 **New Mirrors 149**
New mirrors for the optomechanical cavity. What we want to achieve, design parameters, FEM-simulations, mirror mode characterization.

Part III Measuring Motion in a Negative-Mass Reference Frame 161

9 **The Hybrid Setup 163**
A brief overview of the technical aspects of the hybrid setup. Lasers, detection and acquisition, basic data analysis.

10 **Entanglement Between Distant Oscillators 175**
We report the creation and experimental verification of entanglement between the spin and mechanical subsystems of the hybrid setup. This section contains the main scientific result of the thesis.

11 **Conclusion & What's Next 201**
A brief summary of the thesis and the results. We put this work and our progress into a wider context, and try to give some idea about where the hybrid experiment in particular is moving.

Part IV Appendices etc. 207

A Experimental Parameters 209

B Si_3N_4 Material Constants 211

C Laguerre-Gaussian Modes 213

D BAC Detectors 217

E The Schur Complement 219

List of Figures 221

List of Tables 225

Nomenclature 227

Bibliography 231

Detailed Table of Contents

Abstract v

Preface ix

Brief Table of Contents xiii

List of Publications xxi

Part I Introduction 1

1 Introduction 3
Background, motivation and a rough overview of the work presented.
1.1 The Historical Perspective 3
1.2 Quantum Mechanics of Macroscopic Objects 5

2 Previous Work 9
The work in the field and in Quantop, prior to and during this project. I briefly summarize the main milestones and results.
2.1 The Field in General 9
2.1.1 Spin Systems 11
2.1.2 High-Q Mechanical Oscillators 12
2.1.3 Quantum Optomechanics 14
2.1.4 Hybrid Systems 14
2.2 Quantop 15
2.2.1 The Room Temperature Alkali Spin System 16
2.2.2 An Optomechanical System in the Quantum Regime 16
2.2.2.1 The Monolithic Cavity Design 16
2.2.3 The Hybrid System 17
2.2.3.1 Quantum Backaction-Evasion, QBAE 17
2.3 Quantum Mechanics-Free Subspaces 18

3 Basic Optomechanics 21
Basic optomechanics is introduced. Canonical system, equations of motions, dissipation & noise. Also, some needed math is introduced.
3.0 Transforming to the Frequency Domain 22
3.0.1 The Fourier Transform 22
3.0.2 Power Spectral Density (PSD) 23
3.1 The Harmonic Oscillator 24

3.2 Membranes as Oscillators 26
3.3 Dissipation & Noise 29
3.3.1 Brownian Noise & the Fluctuation-Dissipation Theorem 29
3.4 Quantum Mechanics 31
3.5 Radiation Pressure Coupling 35
3.6 Optical Cavities 36
3.7 Canonical Cavity Optomechanics 41
3.7.1 The Optomechanical Hamiltonian 42
3.7.2 Heisenberg–Langevin Formalism 44
3.7.3 Input–output Formalism 46
3.8 Membrane-in-the-Middle (MIM) Optomechanics 52
3.8.1 The Transfer Matrix Model (TMM) 52
3.9 Cavity Optomechanical Effects 58
3.9.1 OMIT 58
3.9.2 Ponderomotive Squeezing 61
3.9.3 Static Bistability 64

4 Optomechanics in Practice 69
Practical implementation details of a membrane-in-the-middle optomechanical system. Cryostats, Q-measurements, membrane fabrication & other dirty details.
4.1 Membrane Fabrication 69
4.1.1 Membrane Generations 69
4.1.2 Modes of the Phononic Bandgap Membranes 71
4.1.3 Membrane Thickness 72
4.1.3.1 Membrane Reflection 72
4.1.3.2 Effect on Q 72
4.2 Optical Cavities in Practice 75
4.2.1 Gaussian Modes 75
4.2.2 Mode Matching to a Cavity 77
4.3 The Cryostat 79
4.3.1 Janis ST-100 LHe Crystat 79
4.3.2 Why Not Closed Cycle? 80
4.4 Q-measurements 81
4.4.1 Ringdown Measurements 82
4.5 Membrane Temperature Calibrations 84

5 Alkali Spin Systems 87
The physics of alkali atomic spin systems.
5.1 Spin Ensembles 87
5.1.1 Cesium 87
5.1.2 The Holstein–Primakoff Approximation 91
5.2 Negative Effective Mass 92
5.3 Stokes Parameters 94
5.3.1 Measuring the Stokes Parameters 95
5.4 The Faraday Interaction 96
5.5 Input-output Relations 98
5.6 Magneto-Optical Resonance Spectroscopy (MORS) 100

5.7 Spin Coated Microcells 101
5.8 Motional Averaging 103
5.9 Practical Implementation Details 104
5.9.1 Experimental Setup 104
5.9.2 The Magnetic Shield 105
5.9.3 Optical (re-)Pumping 106
5.9.3.1 Spin Temperature 107
5.9.4 Optical Readout 108
5.10 Coherently Induced Faraday Rotation (CIFAR) 111

Part II A New Hybrid Cavity 121

6 A New Cavity 123
A new optomechanical cavity design for hybrid optomechanics is presented. We introduce several important degrees of freedoms to the cavity, compared to earlier, semi-monolithic designs. We present a set of associated problems, and how we overcame these.
6.1 Motivation & Context 123
6.2 Requirements and Design Constraints 125
6.3 The Solution 126
6.3.1 Aligning the Cavity 129
6.3.1.1 Practical Alignment Procedure 131

7 Higher Order Optical Modes in an Optomechanical Cavity 133
A numerical model for evaluating hybridization and splitting of higher order optical modes in optomechanical cavities. The model gives valuable insight into the detrimental effects of membrane tilt, wavefront curvature and clipping losses. The model is compared to experimental data.
7.1 Context & Motivation 134
7.2 A Numerical Model 135
7.3 Model Results 141
7.4 Experimental Data 146
7.5 Design Guidelines Learned 148

8 New Mirrors 149
New mirrors for the optomechanical cavity. What we want to achieve, design parameters, FEM-simulations, mirror mode characterization.
8.1 Why new Mirrors? 149
8.2 FEM-simulations 150
8.2.1 Comparing to Old Mirrors 150
8.2.2 Simulating New Mirrors 151
8.3 Choosing the Mirror Coatings 155
8.4 Delivered Mirrors – Mechanical Mode Characterization 158
8.5 Delivered Mirrors – Optical Properties Characterization 158

Part III Measuring Motion in a Negative-Mass Reference Frame 161

9 The Hybrid Setup 163
A brief overview of the technical aspects of the hybrid setup. Lasers, detection and acquisition, basic data analysis.
9.1 Experimental Equipment and Details 163
9.1.1 Lasers 163
9.1.1.1 M Squared Ti:Sapph 163
9.1.1.2 Lasers for Atomic Pumping and Repumping 165
9.1.2 Acquisition System and Detectors 166
9.1.2.1 DAQ card 166
9.1.2.2 High Quantum Efficiency Balanced Detectors 166
9.1.3 Cavity Locking 167
9.2 Experiment Layout 168
9.3 The Periodogram Estimator - Finite Time PSD 171
9.3.1 Discrete Time 171
9.3.2 Variance of the Periodogram Estimator 172

10 Entanglement Between Distant Oscillators 175
We report the creation and experimental verification of entanglement between the spin and mechanical subsystems of the hybrid setup. This section contains the main scientific result of the thesis.
10.1 EPR States 175
10.2 Hybrid Input-Output Relations 178
10.2.1 Simplified Input-Output Relations 181
10.2.2 Matrix Formulation 183
10.3 Quantum Backaction Evasion 185
10.4 Wiener Filtering 186
10.4.1 Wiener Filtering 101 186
10.4.2 Finding the Wiener Filter 189
10.4.3 Stochastic Trajectories with Deterministic Variance 190
10.4.4 Optimum EPR Variables 191
10.5 Putting the Theory to Work 192
10.5.1 Variying the Larmor Frequency 196
10.5.2 Uncertainties 197

11 Conclusion & What's Next 201
A brief summary of the thesis and the results. We put this work and our progress into a wider context, and try to give some idea about where the hybrid experiment in particular is moving.
11.1 Conclusion 201
11.2 The Next Step: Teleportation 202
11.2.1 Experimental Shortcomings in the Hybrid Setup 203

Part IV Appendices etc. 207

A Experimental Parameters 209

B Si_3N_4 Material Constants 211

C Laguerre-Gaussian Modes 213

D BAC Detectors 217

E The Schur Complement 219

List of Figures 221

List of Tables 225

Nomenclature 227

Bibliography 231

List of Publications

Rodrigo A. Thomas*, Michał Parniak*, **Christoffer Østfeldt***, Christoffer B. Møller*, Christian Bærentsen, Yeghishe Tsaturyan, Albert Schließer, Jürgen Appel, Emil Zeuthen, and Eugene S. Polzik, *"Entanglement between distant mechanical and spin systems"*, Nature Physics 17, pp. 228–233 (2020).

* *These authors contributed equally.*

Rodrigo A. Thomas, **Christoffer Østfeldt**, Christian Bærentsen, Michał Parniak, and Eugene S. Polzik, *"Atomic Spin System Calibrations by Coherently Induced Faraday Rotation"*, Optics Express 29.15, pp. 23637-23653 (2021)

Publications not Related to this Work

Publications not directly related to the work contained in this thesis, but published during my Ph.D. enrollment.

Christoffer Østfeldt, Jean-Baptiste S. Béguin, Freja T. Pedersen, Eugene S. Polzik, Jörg H. Müller, and Jürgen Appel, *"Dipole force free optical control and cooling of nanofiber trapped atoms,"* Opt. Lett. 42, pp. 4315-4318 (2017)

Signe B. Markussen, Jürgen Appel, **Christoffer Østfeldt**, Jean-Baptiste S. Béguin, Eugene S. Polzik and Jörg H. Müller, *"Measurement and simulation of atomic motion in nanoscale optical trapping potentials,"* Appl. Phys. B 126, 73 (2020).

Part I

INTRODUCTION

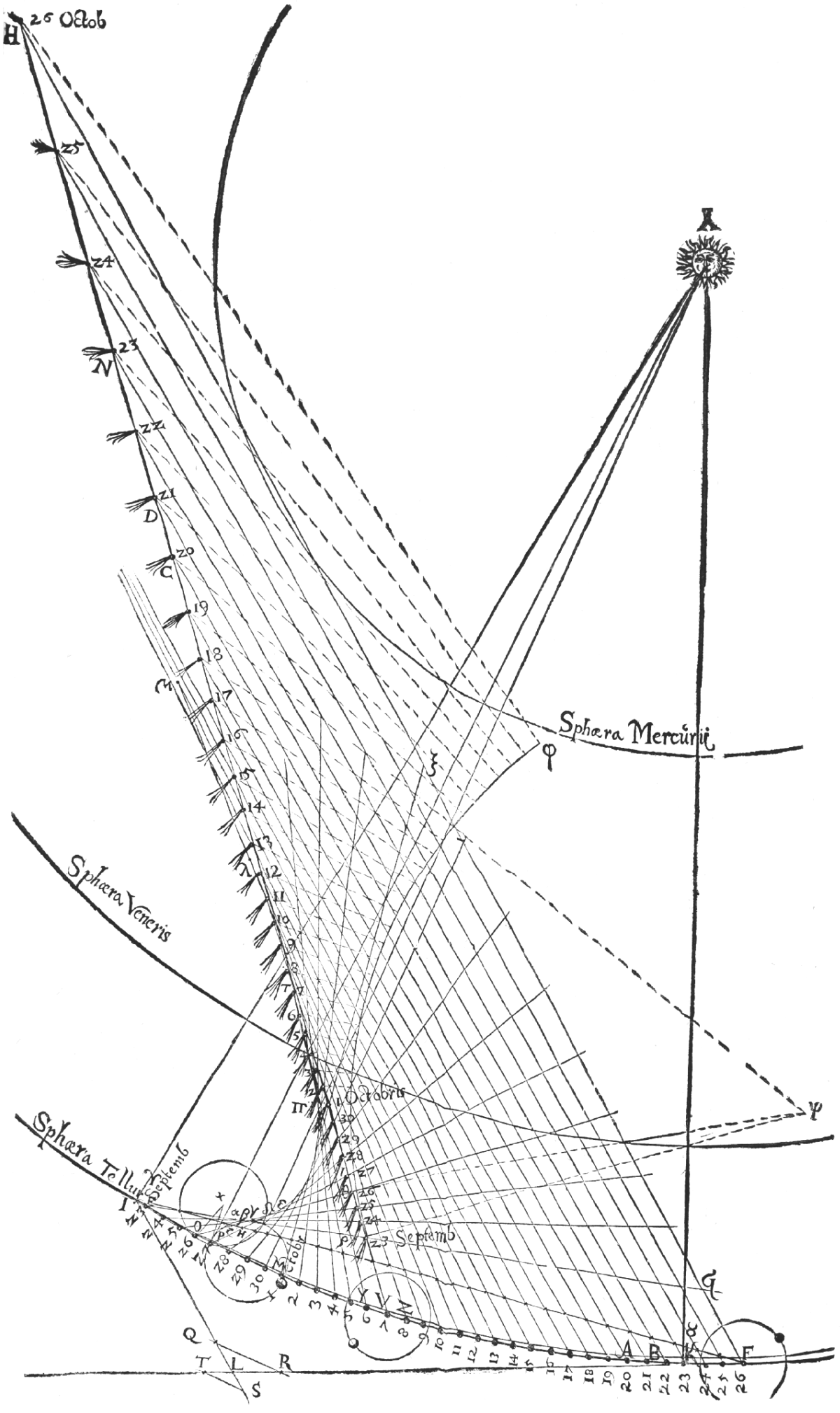
H
26 Octob
25
24
23
N
22
21
D
20
C
19
18
17
16
15
14
13
12
11
10
9
8
7
6
5
4
3
2
1
Sphæra Mercurii
Sphæra Veneris
Sphæra Telluris
Octobris
Septemb
Octobr
Septemb
A
B
K
F
Q
T
L
R
S

Chapter 1

Introduction

> "The story so far:
> In the beginning the Universe was created.
> This has made a lot of people very angry and been widely regarded as a bad move.
>
> Douglas Adams, *The Restaurant at the End of The Universe*

Background, motivation and a rough overview of the work presented.

Figure 1.1: The comets tail pointing away from the sun, led Kepler to suggest the concept of radiation pressure in Keplero (1619). Also see opposing page.

(1) Iohanne Keplero (1619). *De Cometis libelli tres.* Typis Andreae Apergeri, p. 168.

(2) W. Bowen and Milburn (2015) note that this Kepler probably thought about things differently; in that case, his work remains, to my knowledge, the first reported data reliably supporting radiation pressure.

(3) James Clerk Maxwell (1873). *A treatise on electricity and magnetism.* Vol. 1. Clarendon press.

(4) Peter Lebedew (1901). "Untersuchungen über die Druckkräfte des Lichtes". In: *Annalen der Physik* 311.11, pp. 433–458.

(5) Although for our Sun, the radiation pressure is responsible for less than a permille of the total pressure at the center (Carroll and Ostlie 2007, p. 296).

Photo on opposite page: Keplero (1619). Illustration in the public domain.

1.1 The Historical Perspective

In this thesis we will be dealing with two overarching topics: The coupling of matter and light—specifically the effect of and on light from the *motional degrees of freedom* of a solid membrane as well as the "movement" of a collective spin of an atomic ensemble—and secondly, the problem of tracking said movement.

That light and motion couples, is in no way obvious – light is massless, after all. That it *does* indeed couple was proposed in 1619 by Johannes Kepler (Keplero 1619)[1], when he observed that the tails of comets always point away from the sun[2].

James Clerk Maxwell, setting forth the combined theoretical description of light as electromagnetic waves, suggested that light could carry momentum (Maxwell 1873)[3], which, in 1901 Lebedew[4] showed experimentally to be true: light carries momentum, and therefore exerts pressure on objects.

Though this force seems evasive and insignificant, it also lends itself to maintaining the balance on some of the largest scales in the universe; it provides, for example, part of the pressure, which prevents stars from collapsing on themselves[5]. For larger and hotter stars, the effect actually dominates that of gas pressure (Carroll and Ostlie 2007, p. 341) in the core.

While the scales at which stars operate are rather large, we will be dealing with the other extreme: the smallest amounts of light, *photons*. Single quanta of light, each carrying energy $\hbar\omega$ and linear momentum $\hbar k$, as well as spin $\pm\hbar$, where $\hbar$ is the *reduced Planck constant* $\hbar = h/2\pi = 1.055 \times 10^{-34}\,\mathrm{J\,s}$, ω is the angular optical frequency and $k = 2\pi/\lambda$ is the wavenumber, while λ is the optical wavelength.

For the wavelength of choice for this thesis, 852 nm, which is equivalent to an optical frequency of $\omega/2\pi = 3.12 \times 10^{14}\,\mathrm{Hz}$, this amounts to an energy of $2.3 \times 10^{-19}\,\mathrm{J}$ and momentum of $7.8 \times 10^{-28}\,\mathrm{kg\,m/s}$ – both minuscule amounts. It is therefore clear, that if we are to expect any tangible effect, whatever we go around trying to push with our light needs to be rather light.

That we are able to even consider studying such minute quantities is a testament to the technological advancement over the last century or so, especially the advent of the laser[6], the optical descendant of the microwave-range *maser* (see Gordon, Zeiger, and Townes (1955)[7]). These extremely monochromatic and highly coherent sources of light have revolutionized the art of measurement in immeasurable ways. This important experimental tool, together with the advent of computers and digital data acquisition, as well as the incredible advances in material science and (nano)fabrication technology, has allowed the field of quantum optomechanics to bloom within the last decade or so.

One related field worthy of special mention in this context, is that of gravitational wave detection, culminating in the first direct detection of a gravitational wave in September 2015 and reported in Abbott et al. (2016)[8]. In LIGO, distortion of spacetime is measured by detecting directly the change of optical phase induced by the moving mirrors. This is optomechanics in a very pure fashion, with kg-size massive objects.

The field of optomechanics grew out of the early works related to gravitational sensing. In the late 60's V. Braginsky and his colleagues, interested in interferometric measurements, theoretically (V. B. Braginsky and Manukin 1967)[9] and a few years later experimentally (V. B. Braginsky, Manukin, and Tikhonov 1970)[10] showed the *ponderomotive*[11] effect of (microwave) radiation on mechanical objects.

Caves (1980)[12] demonstrated that *quantum* fluctuations of the light, and the ponderomotive effects of these, set a limit to the achievable precision in interferometric measurements[13]. The year after, in Caves (1981)[14], he suggested circumventing this limitation by injecting squeezed light into the interferometer. Around the same time, Braginsky and colleagues formalized the concept of *quantum nondemolition* (QND) measurements (Vladimir B. Braginsky, Vorontsov, and Thorne 1980)[15], that allows noise-less detection of *single* variables, following prior work by Braginsky, Unruh, Khalili, Caves, Drever and others[16].

But, as will be discussed in further detail below, the probe light of LIGO also perturbs the mirrors, and thus sets a lower boundary on the achievable sensitivity. The stream of photons, each carrying minute momenta, added together gives rise to a time-fluctuating force, which kicks the suspended mirrors in the detector arms.

This *quantum back-action*, the quantum noise effects driving the system being probed by light, is a real contributor to the limits of achievable precision in LIGO. But, as we shall see later in this thesis, such quantum back-action can be *evaded*,

(6) Indeed, the fact LASER has in practice lost its status as an abbreviation and become just a regular noun, speaks volumes in terms of its importance to modern science. It has even been verbed into "lase" and adjectivized into "lasing".

(7) J. P. Gordon, H. J. Zeiger, and C. H. Townes (1955). "The Maser—New Type of Microwave Amplifier, Frequency Standard, and Spectrometer". In: *Phys. Rev.* 99 (4), pp. 1264–1274.

(8) B. P. Abbott et al. (2016). "Observation of Gravitational Waves from a Binary Black Hole Merger". In: *Phys. Rev. Lett.* 116 (6), p. 061102.

(9) V. B. Braginsky and A. B. Manukin (1967). "Ponderomotive Effects of Electromagnetic Radiation". In: *Soviet Physics JETP*.

(10) V. B. Braginsky, A. B. Manukin, and M. Yu Tikhonov (1970). "Investigation of dissipative ponderomotive effects of electromagnetic radiation". In: *Soviet Physics JETP*.

(11) From latin *pondus*, weight, and *motive*, inciting motion.

(12) Carlton M. Caves (1980). "Quantum-Mechanical Radiation-Pressure Fluctuations in an Interferometer". In: *Phys. Rev. Lett.* 45 (2), pp. 75–79.

(13) The paper has one of the best abstracts I've ever read: "The interferometers now being developed to detect gravitational waves work by measuring small changes in the positions of free masses. There has been a controversy whether quantum-mechanical radiation-pressure fluctuations disturb this measurement. This Letter resolves the controversy: They do."

(14) Carlton M. Caves (1981). "Quantum-mechanical noise in an interferometer". In: *Phys. Rev. D* 23 (8), pp. 1693–1708.

(15) Vladimir B. Braginsky, Yuri I. Vorontsov, and Kip S. Thorne (1980). "Quantum Nondemolition Measurements". In: *Science* 209.4456, pp. 547–557.

(16) See Vladimir B. Braginsky, Vorontsov, and Thorne (1980) for more details.

by the introduction of another quantum system, with effective negative mass – and we have exactly such a system. This quantum back-action evading measurement is being proposed as one way of boosting the sensitivities of LIGO and similar detectors (Khalili and Polzik 2018; Zeuthen, Polzik, and Khalili 2019)[17],[18].

It is in a sense poetic that quantum optomechanics forked off from gravitational wave detection to become a field of its own, only for it now to come back to gravitational wave physics with possible solutions to current limitations.

(17) F. Ya. Khalili and E. S. Polzik (2018). "Overcoming the Standard Quantum Limit in Gravitational Wave Detectors Using Spin Systems with a Negative Effective Mass". In: *Phys. Rev. Lett.* 121 (3), p. 031101.

(18) E. Zeuthen, E. S. Polzik, and F. Ya. Khalili (2019). "Gravitational wave detection beyond the standard quantum limit using a negative-mass spin system and virtual rigidity". In: *Phys. Rev. D* 100 (6), p. 062004.

1.2 Quantum Mechanics of Macroscopic Objects

When quantum mechanics emerged in the early 20th century, it was a theory of very small things. A theory of electrons and atoms. But technological advances has been steadily moving the domain of applicability of quantum mechanics to larger and larger objects. In the words of W. Bowen and Milburn (2015, preface)[19]

> The quantum theory originated in the study of natural systems: atoms, molecules, solids and light. Despite the difficulty in reconciling quantum theory with our classical intuitions, it is a remarkably successful theory. It is often claimed that one should not be alarmed by this, as it is unreasonable to expect our classical intuitions to apply in such an unfamiliar domain as atomic physics. However, quantum theory does not contain within it any law that forbids us from applying it to bigger and bigger things, even the entire universe in the case of quantum cosmology. The quantum-classical border is not co-located with the microscopic–macroscopic border.

(19) W.P. Bowen and G.J. Milburn (2015). *Quantum Optomechanics*. Taylor & Francis.

Instead, this border turns out to be located between systems that are *isolated* and *strongly coupled to their environment*. In essence, modern engineering has allowed us to construct ever more macroscopic devices, that are suitably isolated from their environment[20], and therefore suitably described by the laws of quantum mechanics.

(20) Engineering the environments themselves is also of large importance – a discipline called *reservoir engineering*.

One central feature of quantum mechanics is that properties of non-commuting operators, like position and momentum, cease to be definite values, but must be replaced with (complex valued) wavefunctions, $\psi(x)$, where the probability of finding the particle in any given position interval δx is proportional to $|\psi(x)|^2 \delta x$. For many quantum states, these functions are nice, smooth functions, centered around a single, well defined maximum – in particular *Gaussian* states are very "classical"; they resemble the classical notions of, e. g., position, but with some added "fuzziness" or *indeterminancy*[21]. This is, by far the type of quantum states that we will encounter most of in this thesis – and to make matters worse, we will often only care about the variance of the state, not the mean values.

(21) The usual English word used for this concept is "uncertainty", as in "Heiseinbergs Uncertainty Principle". I personally prefer the German "Unbestimmtheitsrelation" (or Danish "ubestemthedsrelation"), because it conveys the probabilistic nature of quantum mechanics more clearly. It is not about our lack of knowledge – it is about the fundamental lack of a well defined value.

But these "nice" states are not the only ones worth discussing. In particular, the opposite end of the spectrum of quantum states involves functions that are manifestly *not* related to the nice probability densities mentioned above; e. g., a particle may be in a state with two local maxima. This is sometimes loosely referred to as the particle "being in two places at once". This class of *non-Guassian* states is inherently "more quantum" than the Gaussian ones, and putting a truly macroscopic object into such a state is a long term experimental goal.

Putting large objects into such a state would directly lead to experimentally interesting situations, where one can start wondering what kind of gravitational field such a superposition state produces – see, e. g., W. Bowen and Milburn (2015, chapter 10) for a discussion.

Whether the physical systems under investigation here is truly macroscopic is a question worthy of consideration. The membranes, in particular the oscillating defect pads, discussed in Chapter 4, are large enough that they can be seen by the naked eye, having a transverse size of hundreds of μm – comparable to the transverse size of human hair. However, they are extremely thin, with thicknesses of only tens of nm. Compared to, e. g., the kilogram-scale mirrors in LIGO, our membranes are tiny; compared to atoms our membranes are absolutely gargantuan. In that sense, they fall nicely above the "microscopic-macroscopic" border alluded to by Bowen & Milburn, and are not objects that have been historically considered quantum in nature.

⁂

Another important feature of quantum mechanics is that measurements fundamentally disturb the systems under investigation. This is related to, but not identical, to the indeterminacy discussed above; for detailed discussions see Erhart et al. (2012)[22] and Ozawa (2003)[23].

This *quantum back-action*, i. e., the read-out by the probe of perturbations of the system it has itself imprinted on the system, is of both fundamental and practical interest. In LIGO, quantum noise induced by the probing laser sets real, tangible limitations to the achievable sensitivity, and overcoming this would allow for significant improvement in detection of gravitational waves, since the volume of observable universe grows to the third power with the distance of the furthest observable phenomena. On a more fundamental limit, the question is whether we can feasibly side-step or *evade* this detrimental effect, by playing tricks[24].

The trick that we will employ in this thesis is the *negative mass reference frame* or *quantum mechanics-free subspaces*; the negative effective mass will be introduced in Chapter 5.

The short and handwavy explanation of the idea, suitable for a teaser like this, is that we can probe *two* systems with the same (optical) probe, where the probe induced perturbations are of opposite and equal size. In this way, we can probe specific combinations of the degrees of freedom of the two systems, which are (in principle) free from the probe induced perturbations, or "quantum mechanics free".

Subjecting the two systems to these correlated perturbations is also what ultimately allows us to prepare them in a joint quantum state, with variances below that of either individual systems lower allowed (ground state) variance. It can be shown that when such a state is created, the two are *entangled*, i. e., their individual states cannot be fully described without explicitly including the other system. They are *non-separable*. How this comes about in practice is the topic of Chapter 10.

⁂

An introduction would not be complete without at least a cursory introduction to our main actors, and the stage on which they are to perform. For us, the two systems are a soft-clamped phononically shielded membrane made from silicon nitride, embedded in an opt(omechan)ical cavity; and the collective spin of a large number of room temperature cesium atoms, contained in a spin-preserving coated

(22) Jacqueline Erhart et al. (2012). "Experimental demonstration of a universally valid error–disturbance uncertainty relation in spin measurements". In: *Nature Physics*, p. 15.

(23) Masanao Ozawa (2003). "Universally valid reformulation of the Heisenberg uncertainty principle on noise and disturbance in measurement". In: *Phys. Rev. A* 67 (4), p. 042105.

(24) Of course, simply breaking the established limits, and booking a plane ticket for Stockholm is also a good option, but we sometimes have to settle for less.

cell. To interrogate these systems, and correlate them, we probe first the spin system and then the optomechanics in a cascaded fashion with a beam of light tuned close to an atomic resonance, before finally detecting the fluctuations of the light. A cartoon depiction of the system can be seen in Fig. 1.2.

Both the membrane and the spin are, to very good approximation, *harmonic oscillators*. The membrane perhaps most obviously, by virtue of being essentially a drum skin; the spin oscillator by considering only fluctuations transverse to the big collective spin – fluctuations which precess around an external magnetic field, B, aligned to the collective spin direction. The spin oscillator realizes the negative mass oscillator described above, as by flipping the direction of the magnetic field, the direction of precession can be changed[25]. This is shown in the phase space diagrams in Fig. 1.2, where the spin and membrane systems oscillate in different directions.

(25) If this feels a little hand-wavy, more details shall be provided in Chapter 5.

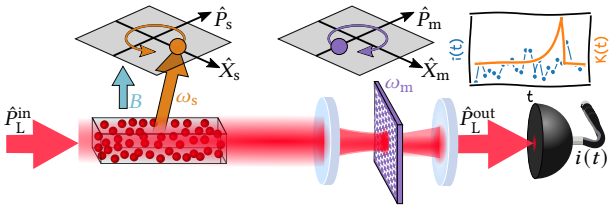

Figure 1.2: Cartoon model of the hybrid experiment. A single beam of light, $\hat{P}_L^{in}$ probes the two systems in a cascaded fashion. The first system is the collective spin (subscript s) of a cesium ensemble precessing in a magnetic field, and the second is the motion of a membrane (subscript m) embedded in an optical cavity. After interaction, the output light $\hat{P}_L^{out}$ is detected, and the photocurrent $i(t)$ digitized. The photocurrent is analyzed with a filter $K(t)$ to estimate the EPR variables, Eq. (1.1). By aligning the magnetic field along the direction of the collective spin, the spin oscillator realizes an effective negative mass, and precesses the opposite way of the positive mass membrane. Figure also appears in Rodrigo A. Thomas et al. (2020).

After detection, the digitized photocurrent $i(t)$ contains information about the two systems, and their collective properties. By fitting a suitable filter $K(t)$ to the data, we may infer the desired properties of the oscillators. In essence, our main objective is to find a suitable physical model, which allows us to find the filter $K(t)$ that correctly estimates what we want to know.

The two systems are each described by their (dimensionless) position and momentum, $(\hat{X}_i, \hat{P}_i)$. The EPR variables are then constructed as

$$\begin{bmatrix} \hat{X}_{\text{EPR}} \\ \hat{P}_{\text{EPR}} \end{bmatrix} = \frac{1}{\sqrt{2}} \begin{bmatrix} \hat{X}_m + \hat{X}_s \\ \hat{P}_m - \hat{P}_s \end{bmatrix}, \tag{1.1}$$

i. e., the sum of the positions, and the difference of momenta. Demonstrating entanglement will, in the end, amount to showing that we can measure these two EPR variables with a variance below one:

$$\text{Var}\left[\hat{X}_{\text{EPR}}\right] + \text{Var}\left[\hat{P}_{\text{EPR}}\right] < 1, \tag{1.2}$$

which can be compared to the single system limits, which strictly enforces

$$\text{Var}\left[\hat{X}_i\right] + \text{Var}\left[\hat{P}_i\right] \geq 1, \tag{1.3}$$

for $i \in \{\mathrm{s}, \mathrm{m}\}$. In other words, the main goal is tracking the combined degrees of freedom, the EPR variables, so precisely that the variance of our estimate is below that permitted for a single system—an endeavour necessitating high precision and low noise in our detection, as well as an efficient extraction of information from the collected data.

In short, this thesis is about the experimental realization of an entangled quantum state of a spin oscillator and a carefully engineered macroscopic membrane, using quantum back-action evasion and a negative mass reference frame. This endeavour, while extremely specific in its scope, ties into a larger scientific context, with both fundamental and technological relevance.

Chapter 2

Previous Work

> “Our imagination is stretched to the utmost, not, as in fiction, to imagine things which are not really there, but just to comprehend those things which *are* there.
>
> Richard Phillips Feynman

The work in the field and in Quantop, prior to and during this project. I briefly summarize the main milestones and results.

In the previous chapter, I set the stage for this thesis by painting with a somewhat broad brush; what are the concepts and large scale goals of this work? In this chapter, I will try to give a more detailed walkthrough of the scientific background and contemporary scientific environment.

Literally thousands of publications could be listed here, but doing such a thing would do absolutely nobody a favor. As such, this must be almost by definition a superficial walkthrough, highlighting only a small subset of relevant literature.

The chapter is in two main parts: the field at large, followed by a discussion of my reasearch group, Quantop. Where does our group and our work fit into the larger picture of quantum optics and related subjects?

2.1 The Field in General

What do I mean by “the field”? Quantum optics, in the broadest sense, i. e., the interface between material quantum mechanical systems and electromagnetic radiation, will encompass most of the relevant parts. The electromagnetic radiation may be either light or microwave radiation, and the material systems can encompass an extremely wide array of different systems. A subset of possible systems is depicted in Fig. 2.1; this “zoo” of quantum system ranges from mechanical res-

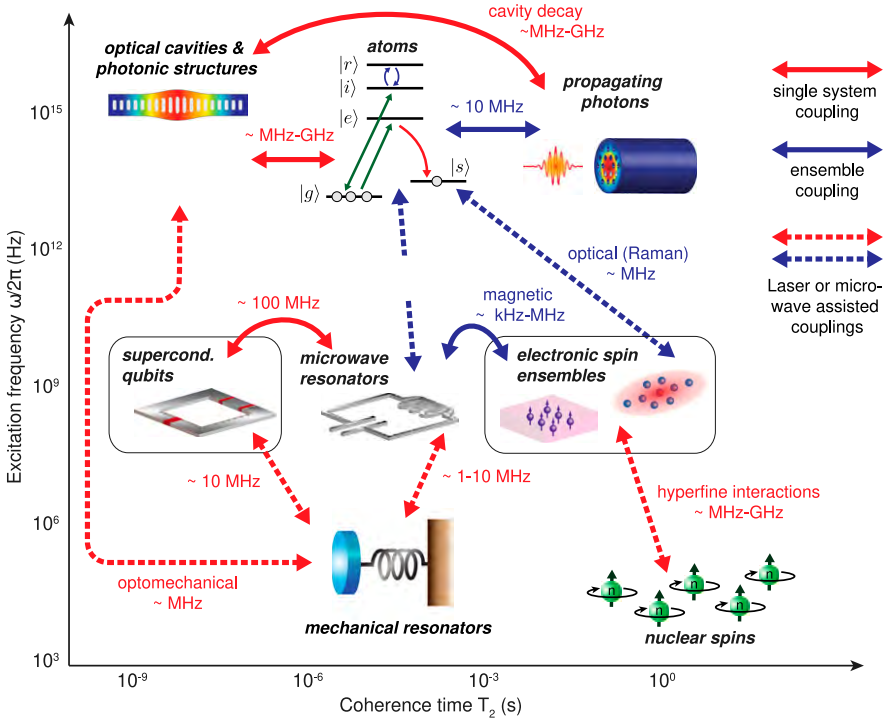

Figure 2.1: The zoo of quantum platforms. A wide array of quantum system, ranging from mechanical oscillators to propagating photons, together offer a wide array of advantages and disadvantages. Their combination into hybrid systems, coupled either directly (solid lines) or through radiation (dashed lines), provides synergistic effects: deficiencies in one system can be alleviated by others. Reproduced from Kurizki et al. (2015), Copyright 2015 National Academy of Sciences.

onators, to nuclear spins, superconducting qubits or electronic spin ensembles and travelling photonic qubits.

Kurizki et al. (2015)[1] sets out a vision of implementing effective quantum technologies in Hybrid Quantum Systems, HQSs, harnessing the best properties of each constituent system to perform different roles for quantum tasks such as quantum information processing, (quantum) secure communication, and high-precision quantum-limited sensing (Degen, Reinhard, and Cappellaro 2017)[2]. For example, one material system may show exceptional coherence times, making it a good candidate for quantum memory applications, while other systems may exhibit more flexible experimental control, rendering them a good option for computational qubits.

A similar sentiment was proposed in the seminal paper by Kimble (2008)[3], who introduced the concept of a "quantum internet", which necessitates "quantum interconnects, which convert quantum states from one physical system to those of another in a reversible manner".

In that sense, it is interesting to follow the development of individual quantum systems as well as the different transduction and coupling schemes and techniques developed, *and* demonstrating quantum mechanical effects such as entanglement

(1) Gershon Kurizki et al. (2015). "Quantum technologies with hybrid systems". In: *Proceedings of the National Academy of Sciences* 112.13, pp. 3866–3873.

(2) C. L. Degen, F. Reinhard, and P. Cappellaro (2017). "Quantum sensing". In: *Rev. Mod. Phys.* 89 (3), p. 035002.

(3) H. J. Kimble (2008). "The quantum internet". In: *Nature* 453.7198, pp. 1023–1030.

and teleportation between different systems, thereby paving the way for novel hybrid quantum systems.

Notable quantum platforms not covered in this thesis include systems such as quantum dots (Lodahl, Mahmoodian, and Stobbe 2015)[4], i. e., artificial solid state "atoms" which can serve as single photon emitters for photonic quantum tasks, embedded in photonic nanostructures; and superconducting qubits (Kjaergaard et al. 2020; Arute et al. 2019)[5],[6], where a non-linear inductor—the Josephson junction—breaks the harmonicity of microwave resonator circuits, allowing the ground and first excited states to be operated as an electronically controllable qubit. Of certain interest is *topologically protected* qubits (Das Sarma, Freedman, and Nayak 2006)[7], which will be, if the experiments are successful, much more resilient to decoherence processes, because the quantum state is impervious to local perturbations.

(4) Peter Lodahl, Sahand Mahmoodian, and Søren Stobbe (2015). "Interfacing single photons and single quantum dots with photonic nanostructures". In: *Rev. Mod. Phys.* 87 (2), pp. 347–400.

(5) Morten Kjaergaard et al. (2020). "Superconducting Qubits: Current State of Play". In: *Annual Review of Condensed Matter Physics* 11.1, pp. 369–395.

(6) Frank Arute et al. (2019). "Quantum supremacy using a programmable superconducting processor". In: *Nature* 574 (7779), pp. 505–510.

(7) Sankar Das Sarma, Michael Freedman, and Chetan Nayak (2006). "Topological quantum computation". In: *Physics Today* 59.7, pp. 32–38.

2.1.1 Spin Systems

The single spin embodies perhaps the most quantum mechanical system of all; it is an inherent quantum property, with no direct classical analog. However, due to weak light-spin coupling, to achieve quantum limited interactions between light and spins, steps must be taken to overcome decoherence processes. This enhancement can derive from many different mechanisms, such as cavity enhanced interactions in cavity QED, where single atoms are strongly coupled to the electromagnetic mode of an optical resonator, or, alternatively, by increasing the number of atoms, and interacting not with single spins, but an *ensemble* of spins.

The spin ensemble, covered in Chapter 5, will be the spin system of choice in this thesis. A picture of cell containing such a system, and a typical level scheme for state preparation and readout can be seen in Fig. 2.2. The quantum interface between light and atomic ensembles is reviewed in (Klemens Hammerer, A. S. Sørensen, and Polzik 2010)[8].

(8) Klemens Hammerer, Anders S. Sørensen, and E. S. Polzik (2010). "Quantum interface between light and atomic ensembles". In: *Rev. Mod. Phys.* 82 (2), pp. 1041–1093.

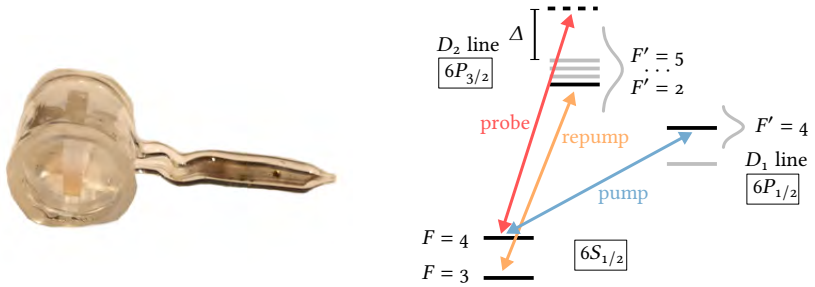

Figure 2.2: Atomic cell (left) and level scheme (right) for dispersive readout of alkali spin ensembles. See Chapter 5 for details, and in particular Fig. 5.10 and Fig. 5.1.

Within this platform, a plethora of quantum effects have been demonstrated. For the research group of Quantop, these results include: entanglement between two spin ensembles (B. Julsgaard, Kozhekin, and Polzik 2001)[9]; squeezing and entanglement of light (Wasilewski, Fernholz, et al. 2009)[10]; quantum limited magnetometry, improved by EPR-type entanglement (Wasilewski, Jensen, et al. 2010)[11]; dissipatively driven entanglement (Hanna Krauter et al. 2011)[12],(Muschik, Polzik,

(9) B. Julsgaard, A. Kozhekin, and E. S. Polzik (2001). "Experimental long-lived entanglement of two macroscopic objects". In: *Nature* 413 (6854), pp. 400–403.

(10) W. Wasilewski, T. Fernholz, et al. (2009). "Generation of two-mode squeezed and entangled light in a single temporal and spatial mode". In: *Opt. Express* 17.16, pp. 14444–14457.

(11) W. Wasilewski, K. Jensen, et al. (2010). "Quantum Noise Limited and Entanglement-Assisted Magnetometry". In: *Phys. Rev. Lett.* 104, p. 133601.

(12) Hanna Krauter et al. (2011). "Entanglement Generated by Dissipation and Steady State Entanglement of Two Macroscopic Objects". In: *Phys. Rev. Lett.* 107 (8), p. 080503.

and J. Ignacio Cirac 2011)[13]; deterministic teleportation (Krauter et al. 2013)[14]; and squeezing of the spin variables by stroboscopic measurement (Vasilakis, Shen, et al. 2015)[15]. Later efforts (Dideriksen et al. 2021)[16] used these room temperature spin ensembles as heralded single photon sources.

Other groups working on similar efforts include that of Michael Romalis, who showed pulsed back-action evasion in a hot alkali vapor system (Vasilakis, Shah, and Romalis 2011)[17], and magnetometry enhanced by QND measurements (Shah, Vasilakis, and Romalis 2010)[18]; Morgan Mitchell, who have demonstrated sub-projection noise sensititivity in magnetometry (Koschorreck et al. 2010)[19], and sub-SQL measurement of spin amplitude and phase noise (Colangelo et al. 2017)[20] in cold rubidium experiments; and Vladan Vuletić, who have demonstrated, e. g., spin squeezing (Leroux, Schleier-Smith, and Vuletić 2010)[21] and heralded entanglment with a negative Wigner function (McConnell et al. 2015)[22], again in cold rubidium. For cold atoms, recent results include things such as the deterministic creation of Schrödinger cat states between light and a single cold rubidium atom (Hacker et al. 2019)[23].

The group of Ofer Firstenberg are doing interesting work on understanding the collective properties of room temperature gasses in dilute or buffer gas filled cells (Shaham, Katz, and Firstenberg 2020)[24].

2.1.2 High-Q Mechanical Oscillators

The second material system covered in this thesis is that of microfabricated mechanical resonators. As depicted in Fig. 2.3, an extremely wide array of different designs exist, with masses ranging from g, for macroscopic mirrors, to zg, where the mechanical resonator is comprised by the motion of cold atoms inside an optical cavity. One could argue that the kg scale mirrors of LIGO (Abbott et al. 2016) should be counted here as well, due to the quantum noise limits encountered in current experiments.

In between these two extremes exists a whole host of resonators which have been painstakingly designed and fabricated using advanced micro- and nanofabrication techniques. Roughly, these fall in two categories: those where only the mechanically compliant element is fabricated, and those where the optical (or electrical) resonator is also fabricated into the same device. Common to all these is the use of advanced fabrication facilities to fabricate micro- and nanoscale features, in some cases interfacing them with other types of systems such a superconducting microwave circuits.

The membrane-in-the-middle geometry was pionerred in the group of Jack Harris (Thompson et al. 2008)[25], after realizing that commercially available silicon nitride films, used as windows for x-ray spectroscopy, showed excellent mechanical properties, with quality factors of 10^7 at cryogenic temperatures.

Since then, a host of different mechanical resonator designs have been proposed and implemented, from trampoline resonators (Kleckner et al. 2011)[26], phononically shielded square membranes (Yu et al. 2014), soft clamped phononic membranes (Yeghishe Tsaturyan et al. 2017)[27], to fractal-like string resonators (Fedorov et al. 2020)[28], etc. The implementation of strain engineering was also sucessfully used to increases mechanical Q (Ghadimi et al. 2018)[29]. Also see Aspelmeyer, Kippenberg, and Marquardt (2014).

(13) Christine A. Muschik, E. S. Polzik, and J. Ignacio Cirac (2011). "Dissipatively driven entanglement of two macroscopic atomic ensembles". In: *Phys. Rev. A* 83 (5), p. 052312.

(14) H Krauter et al. (2013). "Deterministic quantum teleportation between distant atomic objects". In: *Nature Physics* 9 (7), pp. 400–404.

(15) G. Vasilakis, H. Shen, et al. (2015). "Generation of a squeezed state of an oscillator by stroboscopic back-action-evading measurement". In: *Nature Physics* 11 (5), pp. 389–392.

(16) Karsten B Dideriksen et al. (2021). "Room-temperature single-photon source with near-millisecond built-in memory". In: *Nature Communications* 12 (1), p. 3699.

(17) G. Vasilakis, V. Shah, and M. V. Romalis (2011). "Stroboscopic Backaction Evasion in a Dense Alkali-Metal Vapor". In: *Phys. Rev. Lett.* 106 (14), p. 143601.

(18) V. Shah, G. Vasilakis, and M. V. Romalis (2010). "High Bandwidth Atomic Magnetometery with Continuous Quantum Nondemolition Measurements". In: *Phys. Rev. Lett.* 104 (1), p. 013601.

(19) M. Koschorreck et al. (2010). "Sub-Projection-Noise Sensitivity in Broadband Atomic Magnetometry". In: *Phys. Rev. Lett.* 104 (9), p. 093602.

(20) Giorgio Colangelo et al. (2017). "Simultaneous tracking of spin angle and amplitude beyond classical limits". In: *Nature* 543 (7646), pp. 525–528.

(21) Ian D. Leroux, Monika H. Schleier-Smith, and Vladan Vuletić (2010). "Implementation of Cavity Squeezing of a Collective Atomic Spin". In: *Phys. Rev. Lett.* 104 (7), p. 073602.

(22) Robert McConnell et al. (2015). "Entanglement with negative Wigner function of almost 3,000 atoms heralded by one photon". In: *Nature* 519 (7544), pp. 439–442.

(23) Bastian Hacker et al. (2019). "Deterministic creation of entangled atom–light Schrödinger-cat states". In: *Nature Photonics* 13 (2), pp. 110–115.

(24) Roy Shaham, Or Katz, and Ofer Firstenberg (2020). "Quantum dynamics of collective spin states in a thermal gas". In: *Phys. Rev. A* 102 (1), p. 012822.

(25) J. D. Thompson et al. (Mar. 2008). "Strong dispersive coupling of a high-finesse cavity to a micromechanical membrane". In: *Nature* 452 (7183), pp. 72–75.

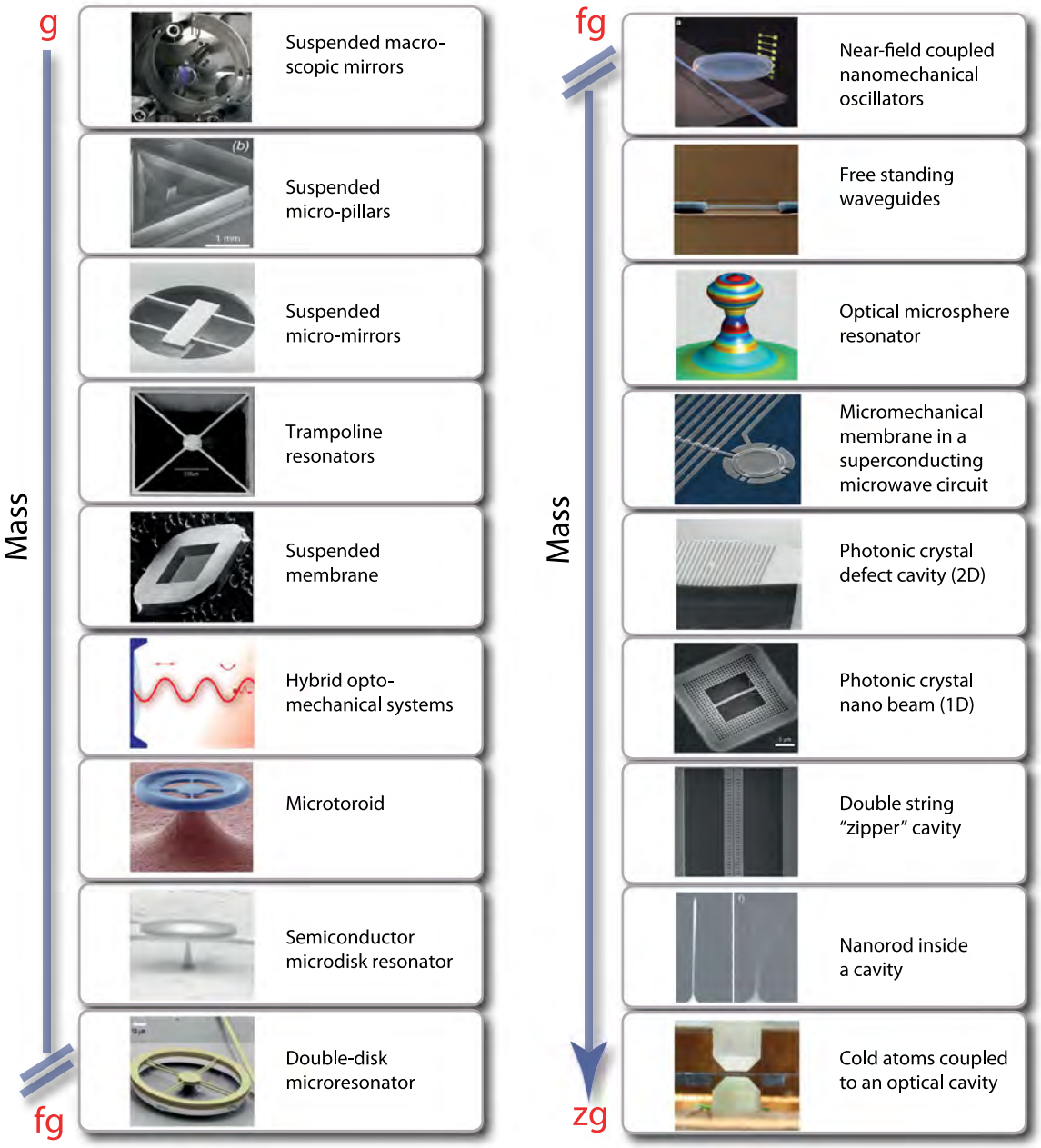

Figure 2.3: Different mechanical oscillators. Reprinted figure with permission from Markus Aspelmeyer, Tobias J. Kippenberg, and Florian Marquardt (2014). "Cavity optomechanics". In: *Rev. Mod. Phys.* 86 (4), pp. 1391–1452. Copyright 2014 by the American Physical Society.

The ultimate reported microresonator mechanical performance reported is that of MacCabe et al. (2020)[30], who reported an ultra-high $Q = 5 \times 10^{10}$, and a Qf-product of 2.6×10^{20}. Here, a nanobeam mechanical resonator at $\omega_m/2\pi = 5\,\mathrm{GHz}$, co-located with an optical micro-cavity ($\lambda = 1550\,\mathrm{nm}$), was fabricated in silicon. Like many other systems, this resonator was limited by effective two-level systems (TLS), fabrication or material defects in amorphous materials, with two nearly degenerate arrangements, with different electric and acoustic (strain) transition dipoles. Investigations into mitigating these effects, for example by saturating the bath of TLSs (Capelle et al. 2020)[31], is an active area of research.

2.1.3 Quantum Optomechanics

With the advent of high-Q resonators detailed above, arose the possibility of pushing the light-resonator interaction squarely into the quantum domain. This development is detailed succinctly in the review paper by Aspelmeyer, Kippenberg, and Marquardt (2014)[32]. Another good review paper, focusing more on the conceptual ideas, and options offered by optomechanics can be found in Y. Chen (2013)[33], where specific suggestions for probing fundamental properties of quantum theory, including quantum gravity are presented.

Various efforts include measurement based cooling and control to an occupation of $n \sim 5$ (D. J. Wilson et al. 2015)[34], and subsequently to the ground state (Rossi, Mason, J. Chen, Yeghishe Tsaturyan, et al. 2018)[35], paving the way for continuous force and displacement measurement below the SQL (Mason et al. 2019)[36]. Wieczorek et al. (2015)[37] implemented Kalman filtering to optimally estimate the quantum state of a mechanical oscillator, which was later improved by Rossi, Mason, J. Chen, and Schliesser (2019)[38], where a variance of 1.29, corresponding to a coherent state purity of $\mathcal{P} = 0.78$ was demonstrated.

The long standing goal of achieving ground state cooling starting from room temperature was demonstrated in Delić et al. (2020)[39], in a system with a levitated nanoparticle as the mechanical object.

Entanglement has also been demonstrated in a number of optomechanical systems, including the motion of macroscopic diamond crystals at room temperature (K. C. Lee et al. 2011)[40], and the creation of entangled light modes from two cavities with a shared mechanically pliable mirror (Barzanjeh et al. 2019)[41], as well as heralded entanglement of two remote micromechanical oscillators (Riedinger et al. 2018)[42]. Noteworthy goals include proposals for steady state entanglement of two membranes in separate cavities (Tan et al. 2013)[43], or the same cavity (Woolley and Clerk 2013)[44].

Other efforts include quantum radiation pressure noise reduction by injection of squeezed light (Yap et al. 2020)[45], optomechanical Bell tests (Marinković et al. 2018)[46], demonstration of Phonon Fock states in a bulk acoustic-wave resonator (Chu et al. 2018)[47] and the creation of a quantum memory at telecom wavelengths (Wallucks et al. 2020)[48] in an optomechanical device.

2.1.4 Hybrid Systems

As noted above, individual quantum systems have different strengths and weaknesses for different quantum tasks. Therefore, demonstrating quantum links be-

(26) Dustin Kleckner et al. (2011). "Optomechanical trampoline resonators". In: *Opt. Express* 19.20, pp. 19708–19716.

(27) Yeghishe Tsaturyan et al. (2017). "Ultracoherent nanomechanical resonators via soft clamping and dissipation dilution". In: *Nature Nanotechnology* 12 (8), pp. 776–783.

(28) S. A. Fedorov et al. (2020). "Fractal-like Mechanical Resonators with a Soft-Clamped Fundamental Mode". In: *Phys. Rev. Lett.* 124 (2), p. 025502.

(29) A. H. Ghadimi et al. (2018). "Elastic strain engineering for ultralow mechanical dissipation". In: *Science* 360.6390, pp. 764–768.

(30) Gregory S. MacCabe et al. (2020). "Nano-acoustic resonator with ultralong phonon lifetime". In: *Science* 370.6518, pp. 840–843.

(31) Thibault Capelle et al. (2020). "Probing a Two-Level System Bath via the Frequency Shift of an Off-Resonantly Driven Cavity". In: *Phys. Rev. Applied* 13 (3), p. 034022.

(32) Markus Aspelmeyer, Tobias J. Kippenberg, and Florian Marquardt (2014). "Cavity optomechanics". In: *Rev. Mod. Phys.* 86 (4), pp. 1391–1452.

(33) Yanbei Chen (2013). "Macroscopic quantum mechanics: theory and experimental concepts of optomechanics". In: *Journal of Physics B: Atomic, Molecular and Optical Physics* 46.10, p. 104001.

(34) D. J. Wilson et al. (2015). "Measurement-based control of a mechanical oscillator at its thermal decoherence rate". In: *Nature* 524 (7565), pp. 325–329.

(35) Massimiliano Rossi, David Mason, Junxin Chen, Yeghishe Tsaturyan, et al. (2018). "Measurement-based quantum control of mechanical motion". In: *Nature* 563 (7729), pp. 53–58.

(36) David Mason et al. (2019). "Continuous force and displacement measurement below the standard quantum limit". In: *Nature Physics* 15 (8), pp. 745–749.

(37) Witlef Wieczorek et al. (2015). "Optimal State Estimation for Cavity Optomechanical Systems". In: *Phys. Rev. Lett.* 114 (22), p. 223601.

(38) Massimiliano Rossi, David Mason, Junxin Chen, and Albert Schliesser (2019). "Observing and Verifying the Quantum Trajectory of a Mechanical Resonator". In: *Phys. Rev. Lett.* 123 (16), p. 163601.

tween different systems is of great interest—an endeavour is known as "hybrid" systems. Limiting ourselves to hybrid systems involving mechanics and either spins or another system, the field of research is still vast.

Cold ion traps, used for quantum computing and simulation (J. I. Cirac and P. Zoller 1995; Gross and Bloch 2017; Brown, Kim, and Monroe 2016)[49],[50],[51], have been at the leading edge of quantum information for more than a decade. Here, the motional and internal states of trapped ions are coupled, and used to implement quantum gates. While only a single material system is involved, such systems do involve both motional and internal degrees of freedom, effectively harnessing two different quantum properties. In a similiar cold atoms setup, negative-mass instability was observed, with the atomic center of mass motion coupling to the collective atomic spin (Kohler et al. 2018)[52].

By employing ultracold atoms to perform sympathethic cooling of a mechanical oscillator, significant performance over feedback cooling alone was shown by (Jöckel et al. 2015; Christoph et al. 2018)[53],[54], with the membrane temperature starting respectively from room temperature and 500 mK. The former group of these two groups, of Philipp Treutlein, later demonstrated strong coupling between their membrane and cold spin ensemble (Karg et al. 2020)[55], in a tuneable fashion, where the effective interaction could be tuned from Hamiltonian (energy-conserving) to dissipative, thereby changing the decay time of the collective excitations, with the effective negative mass of the spin system playing a vital role for the dynamics.

Superconducting qubits, described above, implement excellent candidates for practical qubits, but linking them together across different dilution refrigerators has proven evasive, as it requires electron temperatures that are not compatible with room temperature interconnects. To this end, transducing the quantum signals to the optical domain via an electromechanical interaction has been demonstrated (Higginbotham et al. 2018; Mirhosseini et al. 2020)[56],[57]. In a similar vein, Reed et al. (2017)[58] proposed using a mechanical resonator as a memory for a travelling (photonic) qubit. In a similar line of experiments, coupling a micromechanical oscillator to microwave superconducting qubits allowed for the direct measurement of the mechanical population in different energy levels (Arrangoiz-Arriola et al. 2019)[59].

Finally, the proposal of fabricating integrated devices harnessing the opportunities from both optomechanics, electromechanics and nanophotonics, Nano-Opto-Electro-Mechanics (NOEMS) (Midolo, Schliesser, and Fiore 2018)[60] has been proposed. This endeavour of tightly integrated devices with hybrid characteristics, and others like it, is of great interest.

While the list of examples presented here is in no way exhaustive, I hope that it does convey a sense of the many different directions hybrid quantum systems are evolving, and the opportunities afforded by the intricate interplay of disparate systems.

2.2 Quantop

Turning now to properly understanding the role of this work, we must discuss the scientific experience and status in my research group, Quantop, before 2017, where

(39) Uroš Delić et al. (2020). "Cooling of a levitated nanoparticle to the motional quantum ground state". In: *Science* 367.6480, pp. 892–895.

(40) K. C. Lee et al. (2011). "Entangling Macroscopic Diamonds at Room Temperature". In: *Science* 334.6060, pp. 1253–1256.

(41) S Barzanjeh et al. (2019). "Stationary entangled radiation from micromechanical motion". In: *Nature* 570 (7762), pp. 480–483.

(42) Ralf Riedinger et al. (2018). "Remote quantum entanglement between two micromechanical oscillators". In: *Nature* 556 (7702), pp. 473–477.

(43) Huatang Tan et al. (2013). "Achieving steady-state entanglement of remote micromechanical oscillators by cascaded cavity coupling". In: *Phys. Rev. A* 87, p. 022318.

(44) M. J. Woolley and A. A. Clerk (2013). "Two-mode back-action-evading measurements in cavity optomechanics". In: *Phys. Rev. A* 87 (6), p. 063846.

(45) Min Jet Yap et al. (2020). "Broadband reduction of quantum radiation pressure noise via squeezed light injection". In: *Nature Photonics* 14, pp. 19–23.

(46) Igor Marinković et al. (2018). "Optomechanical Bell Test". In: *Phys. Rev. Lett.* 121 (22), p. 220404.

(47) Yiwen Chu et al. (2018). "Creation and control of multi-phonon Fock states in a bulk acoustic-wave resonator". In: *Nature* 563 (7733), pp. 666–670.

(48) Andreas Wallucks et al. (2020). "A quantum memory at telecom wavelengths". In: *Nature Physics* 16 (7), pp. 772–777.

(49) J. I. Cirac and P. Zoller (1995). "Quantum Computations with Cold Trapped Ions". In: *Phys. Rev. Lett.* 74 (20), pp. 4091–4094.

(50) Christian Gross and Immanuel Bloch (2017). "Quantum simulations with ultracold atoms in optical lattices". In: *Science* 357.6355, pp. 995–1001.

(51) Kenneth R. Brown, Jungsang Kim, and Christopher Monroe (2016). "Co-designing a scalable quantum computer with trapped atomic ions". In: *npj Quantum Information* 2.1, p. 16034.

(52) Jonathan Kohler et al. (2018). "Negative-Mass Instability of the Spin and Motion of an Atomic Gas Driven by Optical Cavity Backaction". In: *Phys. Rev. Lett.* 120 (1), p. 013601.

my Ph.D. started.

2.2.1 The Room Temperature Alkali Spin System

The alkali spin ensemble system was, by the time the hybrid endeavours began, the quantum system of choice in Quantop – supplemented by cold cesium experiments (Appel et al. 2009; H. L. Sørensen et al. 2016). As discussed above, the system had been employed in both CW and pulsed experiments, for experiments ranging from teleportation to quantum enhanced magnetometry.

Common to the previous experiments, however, was the operation in markedly different regimes; in a spin–spin configuration, the Larmor (spin resonance) frequency could be chosen freely, effectively removing the effect of quadratic Zeeman splitting (see Chapter 5). For the hybrid experiment, the Larmor frequency was dictated by the membrane frequency of $> 1\,\mathrm{MHz}$. Furthermore, the cell geometry needed to be modified, to obtain faster motional averaging, commensurate with the decoherence time of the mechanical system, and faster readout rates.

These challenges had been largely overcome by the time I joined the experiment, as manifested by the results presented in Møller et al. (2017).

2.2.2 An Optomechanical System in the Quantum Regime

The optomechanical efforts in Quantop commenced with the arrival of Koji Usami and Dalziel "Dal" Wilziel, who kicked off the optomechanical experiments using commercially available Norcada membranes.

With the arrival of Albert Schließer to the group in 2013 came a stronger focus on fabricating higher quality resonators of our own design. The fabrication efforts were led by Yeghishe Tsaturyan, and focused on the implementation of phononic shields (Yu et al. 2014; Y. Tsaturyan et al. 2014; Yeghishe Tsaturyan et al. 2017). The different membranes are discussed in more detail in Section 4.1.

The first generation of membranes used for *quantum* experiments in our group were phononic bandgap membranes, with the phononic shield embedded in the silicon substrate supporting the silicon nitride membranes. These membranes were used successfully in experiments like Nielsen et al. (2017) and Møller et al. (2017). While ultimate mechanical quality factor was not much higher than those offered by commercial membranes, the phononic shield did alleviate many experimental problems related to clamping. By the time my Ph.D. started, the membranes with the phononic shield embedded in the silicon nitride film (Yeghishe Tsaturyan et al. 2017) were just becoming mature enough for use in experiments, yielding orders of magnitude higher Q, and thereby improved quantum coherence.

2.2.2.1 The Monolithic Cavity Design

Separate, but related to the fabricaiton efforts of membranes, was the development of a cavity design for optomechanics. The final "monolithic" design, so called for the design philosophy of removing all non-essential degrees of freedom from the cavity assembly, is detailed in Nielsen (2016) and was successfully used for the squeezing experiments in Nielsen et al. (2017). This experiment showed up to 2.4 dB of ponderomotive squeezing, from a range of mechanical modes, thus demonstrating that a quantum enabled optomechanical system had been created.

(53) Philipp Christoph et al. (2018). "Combined feedback and sympathetic cooling of a mechanical oscillator coupled to ultracold atoms". In: *New Journal of Physics* 20.9, p. 093020.

(54) Andreas Jöckel et al. (2015). "Sympathetic cooling of a membrane oscillator in a hybrid mechanical–atomic system". In: *Nature Nanotechnology* 10.1, pp. 55–59.

(55) Thomas M. Karg et al. (2020). "Light-mediated strong coupling between a mechanical oscillator and atomic spins 1 meter apart". In: *Science*.

(56) A. P. Higginbotham et al. (2018). "Harnessing electro-optic correlations in an efficient mechanical converter". In: *Nature Physics* 14.10, pp. 1038–1042.

(57) Mohammad Mirhosseini et al. (2020). "Superconducting qubit to optical photon transduction". In: *Nature* 588 (7839), pp. 599–603.

(58) A. P. Reed et al. (2017). "Faithful conversion of propagating quantum information to mechanical motion". In: *Nature Physics* 13 (12), pp. 1163–1167.

(59) Patricio Arrangoiz-Arriola et al. (2019). "Resolving the energy levels of a nanomechanical oscillator". In: *Nature* 571 (7766), pp. 537–540.

(60) Leonardo Midolo, Albert Schliesser, and Andrea Fiore (2018). "Nano-opto-electro-mechanical systems". In: *Nature Nanotechnology* 13, pp. 11–18.

The monolithic cavity is previewed in Fig. 6.1; Chapter 6 will discuss this design, and why it is less than ideal for hybrid experiments.

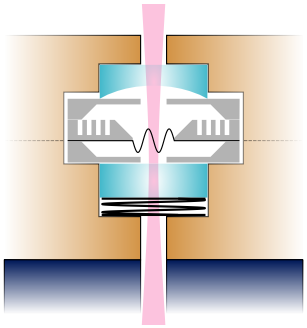

Figure 6.1: (preview) The old, monolithic, cavity design concept. This design was used successfully for "pure" optomechanical experiments, but is less suited for hybrid experiments, due to a lack of tunability. Adapted from Nielsen 2016, with modifications.

2.2.3 The Hybrid System

The hybrid experiment, the marriage of two very different quantum systems, began in Quantop in 2015. By then, the experimental crew consisted of Ph.D. students Christoffer Møller, Rodrigo A. Thomas, and postdoc Georgios Vasilakis, under guidance of Albert Schließer and Eugene Polzik. Møller brought the experience from the optomechanics world, and Thomas and Vasilakis brought the experience from the atomic spin system.

2.2.3.1 *Quantum Backaction-Evasion, QBAE*

These efforts, published in Møller et al. (2017)[(61)], and thoroughly detailed in Møller (2018)[(62)] and to some extent Rodrigo A. Thomas (2020)[(63)], resulted in demonstration of quantum back-action evasion (QBAE) of 1.8 dB relative to the mechanics only, thereby demonstrating the feasibility of using an effective negative mass atomic system as a "noise eater" for mechanical sensors. Fig. 2.4 depictes the observed QBAE, with the atomic system detuned slightly blue of the mechanics. The total signal for respectively positive mass (green) and negative mass (red), compared to the mechanics-only (blue), demonstates the positive and negative interference of the back-action.

A vital experimental hurdle to overcome was that of interfacing the two systems; while previous optomechanical experiments were rather wavelength agnostic, the atomic system forced the optomechanics to operate a very specific optical wavelength. This led to the so-called "semi-monolithic" cavity design; this minimally invasive design change relative to the monolithic cavity did yield successful results, but not without large experimental drawbacks, to which we shall return in Chapter 6.

(61) Christoffer B. Møller et al. (2017). "Quantum back-action-evading measurement of motion in a negative mass reference frame". In: *Nature* 547.7662, pp. 191–195.

(62) Christoffer B. Møller (2018). "Quantum Back-Action Evasion in a Hybrid Spin-Optomechanical System". Ph.D. thesis. University of Copenhagen.

(63) Rodrigo A. Thomas (2020). "Optical spin-mehcanics quantum interface: entanglement and back-action evasion". Ph.D. thesis. University of Copenhagen.

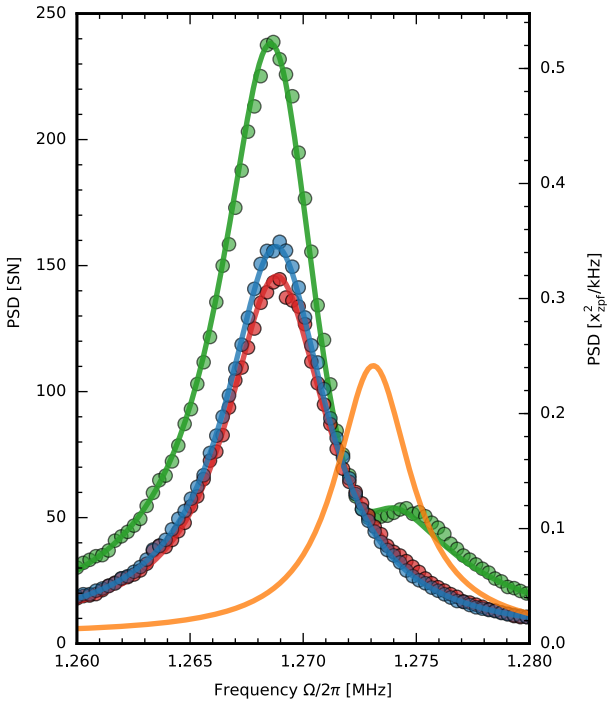

Figure 2.4: QBAE in a hybrid experiment, as reported in Møller et al. (2017). The lines represent respectively mechanics only (blue), inferred spin signal (yellow), and the hybrid signal for positive mass (green) and negative mass (red). The latter demonstrates total noise below that of the mechanics only, proving efficient QBAE of 1.8 dB (relative to the mechanics alone). Figure adapted from Rodrigo A. Thomas (2020).

2.3 Quantum Mechanics-Free Subspaces

One significant possibility made possible by the simultaneous measurement of two quantum systems in a hybrid configuration is that of *quantum mechanics-free subspaces*. The crux of this concept is that by suitable engineering, two inherently quantum mechanical systems may have a subspace of their collective degrees of freedom be, ideally, free from one or more of the usual limitations associated with a single system.

In particular, for quantum sensing applications, a minimum sensitivity exists, the so-called *Standard Quantum Limit* (SQL) for continuous measurement of motion. This is depicted in Fig. 2.5. In the top panels, the ground state (blue), imprecision (orange) and back-action contributions are shown for three different ratios of the readout rate Γ_m to the mechanical linewidth γ_m. As the light power, proportional to the readout rate, is turned up, the imprecision noise is reduced, while the back-action noise increases. In the bottom panel, the total noise[(64)] at the mechanical resonance is shown for varied Γ_m. We see a minimum amount of total (and added) noise, which is the SQL.

K. Hammerer et al. (2009)[(65)] proposed the creation of an Einstein-Poldosky-Rosen (EPR) channel between a mechanical resonator and an atomic ensemble with effective negative mass. The effective negative mass enables QND readout of the EPR

(64) Not the added noise, which is sometimes also shown in graphs like this. Here I include the thermal (ground state) noise.

(65) K. Hammerer et al. (2009). "Establishing Einstein-Poldosky-Rosen Channels between Nanomechanics and Atomic Ensembles". In: *Phys. Rev. Lett.* 102 (2), p. 020501.

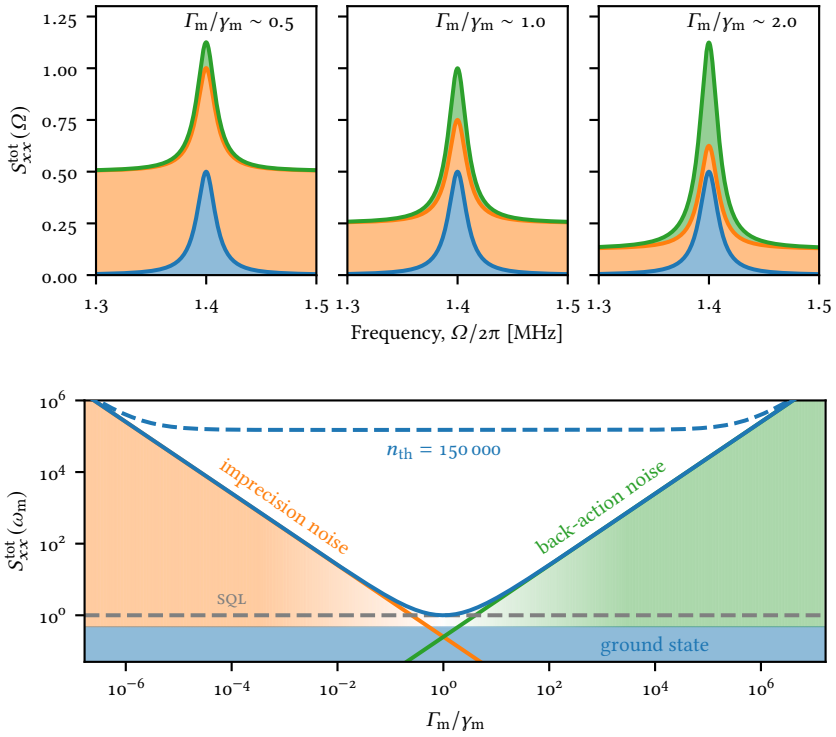

Figure 2.5: The SQL for continuous measurement of a mechanical oscillator. Top panels: ground state noise (blue), phase/imprecision noise (orange) and back-action (green), all normalized so the ground state noise is $1/2$ on resonance, for three different readout rates relative to the decay rate (Γ_m/γ_m). Bottom panel: on-resonance noise contributions for varied Γ_m. The imprecision noise falls off as $1/\Gamma_m$, while the back-action grows as Γ_m^1, leading to an optimum sensitivity for $\Gamma_m = \gamma_m$, where total added noise equals the ground state fluctuations. The dashed blue line shows the total noise for a thermal population of $n_{th} = 1.5 \times 10^5$, corresponding to a temperature of 10 K. $\omega_m/2\pi = 1.4$ MHz, $\gamma_m/2\pi = 20$ kHz, $m_{eff} = 2$ ng, $L_{cav} = 3$ mm. Definitions here follow Aspelmeyer, Kippenberg, and Marquardt (2014).

variables, which effectively prepares the joint system in an entangled state. The authors also proposed the implementation of teleporation from the spin ensemble to the mechanics, based on a Bell-type measurement of the spin and an auxillary spin system, following the EPR entanglement of the mechanics and spin.

Tsang and Caves (2010)[66] seperately suggested a related approach for evading the back-action, based on engineering an effective interaction mimicking a negative mass system. Tsang and Caves (2012)[67] expanded on this idea, providing a general framework for this "negative mass" approach to hybrid quantum system. What Tsang and Caves (2012) calles "Engineering a classical subsystem within a quantum environment", was later phrased as "Trajectories without quantum uncertainties" by Polzik and Klemens Hammerer (2015)[68] in their review of the development of these ideas.

In practice, the idea had already been implemented, for example in B. Juls-

(66) Mankei Tsang and Carlton M. Caves (2010). "Coherent Quantum-Noise Cancellation for Optomechanical Sensors". In: *Phys. Rev. Lett.* 105 (12), p. 123601.

(67) Mankei Tsang and Carlton M. Caves (2012). "Evading Quantum Mechanics: Engineering a Classical Subsystem within a Quantum Environment". In: *Phys. Rev. X* 2 (3), p. 031016.

(68) E. S. Polzik and Klemens Hammerer (2015). "Trajectories without quantum uncertainties". In: *Annalen der Physik* 527.1-2, A15–A20.

gaard, Kozhekin, and Polzik (2001), where two spin ensembles, of opposite effective masses, were entangled, although the language we now use to describe this configuration had not yet been formulated. In a spin-spin setup, the idea was utilized in Wasilewski, Jensen, et al. (2010) to improve a magnetometry experiment.

The concept has received significant theoretical investigation since then, for example by K. Zhang, Pierre Meystre, and W. Zhang (2013)[69], who suggested tailloring the potential for a Bose–Einstein condensate to realize a negative mass oscillator in order to evade back-action; Stannigel, Rabl, and Zoller (2012)[70] investigating preparation of entangled states in cascadede quantum networks; Vasilyev, Muschik, and Klemens Hammerer (2013)[71], invetigating the properties of spin squeezing under different conditions; X. Huang et al. (2018)[72], who investigated coherent noise cancellation for entanglement in hybrid systems; and Khalili and Polzik (2018) and Zeuthen, Polzik, and Khalili (2019)[73],[74], investigating the feasibility of utilizing negative mass oscilators for improving the sensitivity of gravitational wave detectors such as LIGO. A recent proposal for implementing a pulsed QND quantum gate in a entagled spin–mechanics hybrid system was put forward by Manukhova, Rakhubovsky, and Filip (2020)[75].

Other suggestions for avoiding the backaction include detuned paramatric amplification in a setup with two mechanical oscillators (Szorkovszky et al. 2014)[76], thereby entangling them. Two tone driving and read-out was utilized by Delaney et al. (2019)[77] to demonstrate squeezing of mechanical motion by two-tone measurement, and noiseless amplification by Transient Electro-mechanical Amplification.

Fianlly, by driving a cavity with both blue and red detuned pulses, it is possible to engineer a back-action evading measurement, as demonstrated by Shomroni et al. (2019)[78], for a single mechanical oscillator. In a similar scheme, Mika A. Sillanpää and colleagues demonstrated entanglement of two membranes (Ockeloen-Korppi et al. 2018)[79], working as effective end-mirrors in a microwave cavity, with the intracavity radiation correlating and entangling the oscillators. By extending their scheme to a four tone drive, an interaction was engineered where one oscillator behaved as an effectively negative mass oscillator, thereby creating a quantum mechanics–free subspace for the collective variables of the two oscillators (de Lépinay et al. 2021)[80].

Althought many more brilliant researchers have performed interesting and relevant experiments, we must end the discussion of the literature here. We have discussed the field of quantum optics (in the most general sense), the motivation behind hybrid quantum systems, the fields of spin ensembles and optomechanics, previous scientific endeavours in Quantop, and finally the concept of quantum mechanics free subspaces.

(69) Keye Zhang, Pierre Meystre, and Weiping Zhang (2013). "Back-action-free quantum optomechanics with negative-mass Bose-Einstein condensates". In: *Phys. Rev. A* 88 (4), p. 043632.

(70) K Stannigel, P Rabl, and P Zoller (2012). "Driven-dissipative preparation of entangled states in cascaded quantum-optical networks". In: *New Journal of Physics* 14.6, p. 063014.

(71) Denis V. Vasilyev, Christine A. Muschik, and Klemens Hammerer (2013). "Dissipative versus conditional generation of Gaussian entanglement and spin squeezing". In: *Phys. Rev. A* 87 (5), p. 053820.

(72) Xinyao Huang et al. (2018). "Unconditional Steady-State Entanglement in Macroscopic Hybrid Systems by Coherent Noise Cancellation". In: *Phys. Rev. Lett.* 121 (10), p. 103602.

(73) F. Ya. Khalili and E. S. Polzik (2018). "Overcoming the Standard Quantum Limit in Gravitational Wave Detectors Using Spin Systems with a Negative Effective Mass". In: *Phys. Rev. Lett.* 121 (3), p. 031101.

(74) E. Zeuthen, E. S. Polzik, and F. Ya. Khalili (2019). "Gravitational wave detection beyond the standard quantum limit using a negative-mass spin system and virtual rigidity". In: *Phys. Rev. D* 100 (6), p. 062004.

(75) A. D. Manukhova, A. A. Rakhubovsky, and R. Filip (2020). "Pulsed atom-mechanical quantum non-demolition gate". In: *npj Quantum Information* 6.1, p. 4.

(76) A Szorkovszky et al. (2014). "Mechanical entanglement via detuned parametric amplification". In: *New Journal of Physics* 16.6, p. 063043.

(77) R. D. Delaney et al. (2019). "Measurement of Motion beyond the Quantum Limit by Transient Amplification". In: *Phys. Rev. Lett.* 123 (18), p. 183603.

(78) Itay Shomroni et al. (2019). "Optical backaction-evading measurement of a mechanical oscillator". In: *Nature Communications* 10 (1).

(79) C. F. Ockeloen-Korppi et al. (2018). "Stabilized entanglement of massive mechanical oscillators". In: *Nature* 556 (7702), pp. 478–482.

(80) Laure Mercier de Lépinay et al. (2021). "Quantum mechanics–free subsystem with mechanical oscillators". In: *Science* 372.6542, pp. 625–629.

Chapter 3

Basic Optomechanics

> “The easiest way to be on top of the field, is to pick a very small field.
>
> Simone Giertz

Basic optomechanics is introduced. Canonical system, equations of motions, dissipation & noise. Also, some needed math is introduced.

After the very general overview presented in Chapter 1, and the somewhat superficial walk through of the scientific results obtained in QUANTOP until the summer of 2017 in Chapter 2, we now change gears to a somewhat lower, but much more concrete level. We will be covering a rather large amount of material from basic harmonic oscillators, optical cavities, canonical quantum cavity optomechanics to the mapping of membrane-in-the-middle systems to the canonical description.

We start out with the 1D harmonic oscillator in Section 3.1, and move on to how a membrane may be described as one in Section 3.2. In Section 3.3 we treat (classical) dissipation and its relation to thermal noise. The classical harmonic oscillator is quantized in Section 3.4. The basic coupling mechanism between membranes and light, radiation pressure, is covered in Section 3.5, before we move on to our way of enhancing this interaction, optical cavities, in Section 3.6. With these ingredients in place, we are ready to introduce the canonical description of (quantum) cavity optomechanics in Section 3.7. Since our system does not trivially map to this canonical description, Section 3.8 deals with how to treat the membrane-in-the-middle system as a canonical system through the Transfer Matrix Model (TMM). We round off the chapter with a brief overview of a number of cavity optomechanical effects relevant to our discussions in Section 3.9.

The descriptions given here will be somewhat idealized; the true horrors of actually implementing a system such as the one described here will be postponed to Chapter 4 or later.

This chapter borrows extensively from the excellent thesis by Nielsen (2016), especially with regards to the derivations for spectral densities, thermal fluctuations etc. Other good expositions, with emphasis on different aspects, may be found in, e. g., Møller (2018) and Rodrigo A. Thomas (2020).

But, before we dig into the physics, we must, as one is often forced to, start out with a bit of math.

3.0 Transforming to the Frequency Domain

In this section I introduce some needed math and notations, specifically that of Fourier transforms and the Power Spectral Density, PSD.

3.0.1 The Fourier Transform

For a continuous function $f(t)$ we define the Fourier transform as[1]

$$f(\Omega) = \mathcal{F}\left\{f(t)\right\}(\Omega) \equiv \int_{-\infty}^{\infty} f(t)\mathrm{e}^{-\mathrm{i}\Omega t}\,\mathrm{d}t, \tag{3.1}$$

and the inverse transform as

$$f(t) = \mathcal{F}^{-1}\big\{f(\Omega)\big\}(t) \equiv \int_{-\infty}^{\infty} f(\Omega)\mathrm{e}^{+\mathrm{i}\Omega t}\,\frac{\mathrm{d}\Omega}{2\pi}. \tag{3.2}$$

In general, we always use the short hand notation $f(\Omega)$, but sometimes the more explicit $\mathcal{F}\{\cdot\}(\Omega)$ is helpful.

We will often be dealing with time derivatives of Fourier transforms. Luckily, both the Fourier transform and the derivative are *linear* in the mathematical sense[2], so one easily obtains

$$\frac{\mathrm{d}}{\mathrm{d}t}f(t) = \frac{\mathrm{d}}{\mathrm{d}t}\mathcal{F}^{-1}\big\{f(\Omega)\big\}(t) = \mathcal{F}^{-1}\big\{\mathrm{i}\Omega f(\Omega)\big\}(t), \tag{3.3}$$

and by Fourier transforming both sides of this equation we get[3]

$$\mathcal{F}\left\{\frac{\mathrm{d}}{\mathrm{d}t}f(t)\right\}(\Omega) = \mathrm{i}\Omega f(\Omega), \tag{3.4}$$

or in other words, time derivatives in Fourier space is achieved by multiplication by $\mathrm{i}\Omega$ (or, $-\mathrm{i}\Omega$ if the Fourier transform is defined with the opposite sign).

Sometimes we will need to transform not only normal functions, but quantum operators. The definitions for operators are analogous to those for functions, however two different conventions exist and both are in active use in our groups work. Nielsen (2016) and Møller (2018) use one, while Rodrigo A. Thomas (2020), Møller et al. (2017), and Rodrigo A. Thomas et al. (2020) use another.

In the first, and simplest, convention one simply uses the definition of the Fourier transform. The upshot then is that, in general, the conjugate of the Fourier transform of an operator $\hat{A}$ does not equal the Fourier transform of the conjugate:

$$\left(\hat{A}(\Omega)\right)^{\dagger} \neq \hat{A}^{\dagger}(\Omega), \tag{3.5}$$

(1) At least two other options exist. One concerns the normalization, putting $1/\sqrt{2\pi}$ on each transformation, instead of $1/2\pi$ only on the inverse. The other is flipping the sign of $\mathrm{i}\Omega$ to $-\mathrm{i}\Omega$. The latter is used in Rodrigo A. Thomas et al. (2020).

(2) That is, both have the properties of *additivity* and *homogeneity*:

$$f(x) + f(y) = f(x + y)$$
$$f(ax) = af(x).$$

(3) Noting that

$$\mathcal{F}\{\mathcal{F}^{-1}[f(\Omega)](t)\}(\Omega) = f(\Omega).$$

because

$$\left(\hat{A}(\Omega)\right)^\dagger = \left(\int_{-\infty}^{\infty} \hat{A}(t)\mathrm{e}^{-\mathrm{i}\Omega t}\,\mathrm{d}t\right)^\dagger = \int_{-\infty}^{\infty} \hat{A}^\dagger(t)\mathrm{e}^{+\mathrm{i}\Omega t}\,\mathrm{d}t = \hat{A}^\dagger(-\Omega). \tag{3.6}$$

The other convetion, now with the opposite sign convention for the "forward" transform, defines a "new", or flipped, Fourier transform for transposed operators, specifically $\hat{a}^\dagger$, so

$$\mathcal{F}\left\{\hat{a}(t)\right\}(\Omega) = \int_{-\infty}^{\infty} \hat{a}(t)\mathrm{e}^{+\mathrm{i}\Omega t}\,\mathrm{d}t \equiv \hat{a}(\Omega) \tag{3.7}$$

$$\mathcal{F}'\left\{\hat{a}^\dagger(t)\right\}(\Omega) = \int_{-\infty}^{\infty} \hat{a}^\dagger(t)\mathrm{e}^{-\mathrm{i}\Omega t}\,\mathrm{d}t \equiv \hat{a}^\dagger(\Omega). \tag{3.8}$$

In this case we have

$$\left(\hat{a}(\Omega)\right)^\dagger = \left(\int_{-\infty}^{\infty} \hat{a}(t)\mathrm{e}^{+\mathrm{i}\Omega t}\,\mathrm{d}t\right)^\dagger = \int_{-\infty}^{\infty} \hat{a}^\dagger(t)\mathrm{e}^{-\mathrm{i}\Omega t}\,\mathrm{d}t = \hat{a}^\dagger(\Omega), \tag{3.9}$$

i. e., the statement we found was not true in the other convention, cf. Eq. (3.5).

The motivation for this change relates to the case where one considers sidebands around a laser frequency, ω_L. In this "flipped" convention $\hat{a}(\Omega)$ and $\hat{a}^\dagger(\Omega)$ both describe fluctuations at the upper sideband (absolute frequency $\omega_\mathrm{L} + \Omega$), while $\hat{a}(-\Omega)$ and $\hat{a}^\dagger(-\Omega)$ concern the lower sideband—i. e., it relates what one would measure in a homodyne measurement of the upper/lower sideband more naturally.

To make the difference even more concrete, let's end this section by applying the Fourier transform to the sum $\hat{a}(t) + \hat{a}^\dagger(t)$—combinations like these appear for example in expressions describing optomechanical interactions and homodyne detection. We multiply by respectively $\exp(-\mathrm{i}\Omega t)$ and $\exp(+\mathrm{i}\Omega t)$, and integrate over t, with both conventions:

$$\mathcal{F}\left\{\hat{a}(t) + \hat{a}^\dagger(t)\right\} = \int_{-\infty}^{\infty} \mathrm{e}^{-\mathrm{i}\Omega t}\left(\hat{a}(t) + \hat{a}^\dagger(t)\right)\mathrm{d}t = \hat{a}(\Omega) + \hat{a}^\dagger(+\Omega) \qquad \text{(first convention)} \tag{3.10}$$

$$\mathcal{F}\left\{\hat{a}(t) + \hat{a}^\dagger(t)\right\} = \int_{+\infty}^{\infty} \mathrm{e}^{+\mathrm{i}\Omega t}\left(\hat{a}(t) + \hat{a}^\dagger(t)\right)\mathrm{d}t = \hat{a}(\Omega) + \hat{a}^\dagger(-\Omega) \qquad \text{(second convention),} \tag{3.11}$$

where in the last term of Eq. (3.11), we used the fact that we are transforming with $+\mathrm{i}\Omega t$ instead of $-\mathrm{i}\Omega t$.

The situation is kind of a mess, and have led many untrained experimentalists astray. I present both conventions here to hopefully elucidate the situation, as well as to be able to follow the derivations in the respective sources where it is relevant.

3.0.2 Power Spectral Density (PSD)

Next, we move on to the Power Spectral Density (PSD), which is central to our descriptions of oscillators. Following Nielsen (2016) we first define the *finite time*

Fourier transform

$$f_T(\Omega) \equiv \int_{-T/2}^{T/2} f(t) \mathrm{e}^{-\mathrm{i}\Omega t} \, \mathrm{d}t, \tag{3.12}$$

and then define the Power Spectral Density, PSD, from this, as

$$S_{ff}(\Omega) \equiv \lim_{T\to\infty} \frac{1}{T} \left| f_T(\Omega) \right|^2 . \tag{3.13}$$

The PSD is central to a lot of our discussions. It describes the power present in the signal $f(t)$ at the frequency Ω, thus separating spectrally separated signals that are hard to discern in the time domain.

Similarly, we can define the *Cross Spectral Density*, CSD, from two different signals $f(t)$ and $g(t)$

$$S_{fg}(\Omega) \equiv \lim_{T\to\infty} \frac{1}{T} f_T^*(\Omega) g_T(\Omega) \tag{3.14}$$

To gain some understanding of what the CSD tells us, we introduce the cross-correlation function between f and g as

$$f \star g(t) \equiv \lim_{T\to\infty} \int_{-T/2}^{T/2} f(t') g(t'+t) \, \mathrm{d}t'. \tag{3.15}$$

For $f = g$, the cross-correlation becomes the *auto-correlation* function. The Wiener–Khinchin theorem relates the cross-correlation (or equivalently auto-correlation) to the CSD (PSD), by stating

$$S_{fg}(\Omega) = \mathcal{F}\left\{ f \star g(t) \right\}(\Omega). \tag{3.16}$$

In other words, a CSD tells us about the frequencies present in a cross-correlation function.

All of these definitions are made for the continuous time case. The experimentally inclined may already now wish to interject that the data that we acquire is always discretized, in both time and value. We will deal with the discretization of time in Section 9.3. Until then, we will always assume continuous time, or the difference will be immaterial.

With these definitions out of the way, we are armed for the physics. Let's go.

3.1 The Harmonic Oscillator

To start out, we first show how to obtain the *mechanical susceptibility*, $\chi(\Omega)$, i. e., the frequency dependent response of an oscillator[4] to external perturbations. Throughout the thesis we will work almost exclusively in the frequency domain, but recalling at all times that susceptibility is just another way of rephrasing Newton's laws is beneficial.

We start with Newton's second law for an object of mass m, subjected to a number of external forces, such as the one depicted in Fig. 3.1

$$\sum F = ma = m\ddot{x}, \tag{3.17}$$

(4) Some authors make a point of distinguishing things that oscillate by themselves, *oscillators*, from things that resonate due to external perturbations, *reonators*. I will make no such distinction, and simply call them all *oscillators*.

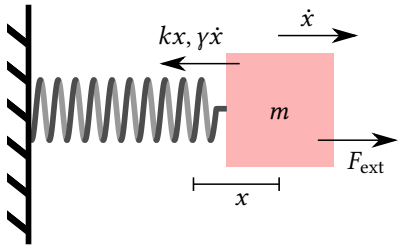

Figure 3.1: The idealized 1D harmonic oscillator. An object of mass m is connected to a rigid suspension point by a spring with spring constant k, and is currently at a position x away from the spring equilibrium. The block is moving with velocity $\dot{x}$, which leads to a velocity damping of size $\gamma\dot{x}$ in the opposite direction. Finally, the mass is subjected to a total external force F_{ext}.

where a and x is understood to be time dependent, e. g., $x(t)$, and the dot(s) denote time derivatives. Identifying the relevant forces and their directions as depicted in Fig. 3.1, we obtain

$$m\ddot{x} = F_{\text{ext}} - kx - \gamma\dot{x}, \tag{3.18}$$

which we rearrange into

$$kx + \gamma\dot{x} + m\ddot{x} = F_{\text{ext}}. \tag{3.19}$$

With no external forces and zero dissipation, the solutions take the form $A\cos(\omega t) + B\sin(\omega t)$, with $\omega^2 = k/m$ being the angular frequency. Hence their name *harmonic oscillators*.

We now go the Fourier domain (see Section 3.0.1 for details), i. e., we Fourier transform the entire equation (3.19), and make an *ansatz* of linearity, such that frequencies do not mix, by which we obtain

$$kx(\Omega) + \mathrm{i}\gamma\Omega x(\Omega) - m\Omega^2 x(\Omega) = F_{\text{ext}}(\Omega). \tag{3.20}$$

We have now transformed the equation for independent ts into an equation for independent Ωs. Dividing through by m, and collecting factors, by which we then divide, we get to spectral response of a harmonic oscillator to a general force

$$x(\Omega) = \frac{1}{m}\frac{1}{\omega^2 - \Omega^2 + \mathrm{i}\gamma\Omega}F_{\text{ext}}(\Omega) = \chi(\Omega)F_{\text{ext}}(\Omega), \tag{3.21}$$

after identifying $\omega^2 = k/m$, as the angular frequency squared of a harmonic oscillator without damping[(5)], and redefining $\gamma/m \to \gamma$.

We plot a set of different susceptibilities in Fig. 3.2. A couple of point to be noted: at very low frequencies, all amplitudes go to one and the phase is zero, i. e., for DC forces, they all react in phase to the external force, and with the same amplitude. For $\Omega \gg \omega$ all traces asymptotically go towards $1/\Omega^2$. and the phase goes towards $-\pi$; i. e., all responses are heavily dampened, and react exactly out of phase to external forces.

(5) We here also note a notational point: Capital omega, Ω, will be reserved for independent variables, while small omegas, ω, will be used for specific angular frequencies, e. g., resonance frequencies, drive frequencies, corner frequencies of filters etc.

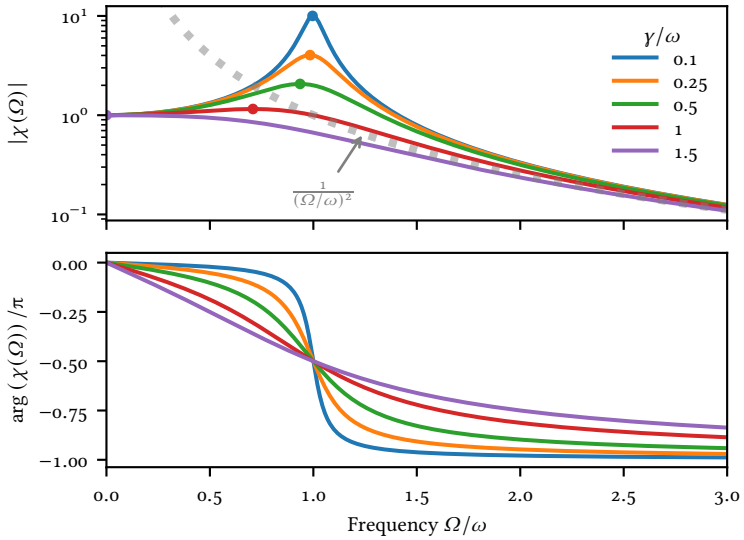

Figure 3.2: Mechanical susceptibilities for different values of γ. Top: Response amplitude, $|\chi(\Omega)|$. Grey dashed line: $1/(\Omega/\omega)^2$. Dots: Maximum response. Bottom: Response phase, $\arg(\chi(\Omega))$, relative to the perturbing force.

Close to the bare resonance frequency, $\Omega/\omega \sim 1$, traces with small damping (γ/ω) show huge enhancement of the response, i. e., resonance. Also, as γ shrinks, so does the difference between the frequency with maximum response and the bare resonance frequency (dots, top panel of Fig. 3.2). Note that all responses lag exactly $\pi/2$ behind the force at the bare resonance frequency, independent of the size of the damping.

3.2 Membranes as Oscillators

Now that we've established some formalism for 1D harmonic oscillators, we must then ask ourselves: how do we successfully use this to describe the very much 3D objects that membranes are? In this section I will give a description of how and why we are able to model the oscillations of membranes as simple harmonic oscillators.

We start by considering first the simple case of square (or slightly rectangular) membrane, rigidly clamped at the edge. We assume that the thickness d is orders of magnitude smaller than the side lengths L_x, L_y.

(6) The oscillation is now in the z-direction - x (and y) is orthogonal to the axis of oscillation.

The governing differential equation for the out-of-plane displacement $w(x, y; t)$[6] of a uniform membrane with uniform in-plane tension is (Nielsen 2016, p. 18)

$$\frac{D}{d}\nabla^4 w(x, y; t) - \mathcal{T}\nabla^2 w(x, y; t) + \rho\frac{\partial^2}{\partial t^2}w(x, y; t) = 0, \tag{3.22}$$

(7) Both of which are material properties, describing respectively the flexural rigidity under compression or tension and (for small compression) the ratio of transverse elongation divided by the axial compression.

where $\mathcal{T}$ is the tensile stress, ρ the material density per volume, and D is the flexural rigidity, which depends on the Young's modulus, E, and the Poisson's ratio, ν[7]:

$$D = \frac{Ed^3}{12(1-\nu^2)}. \tag{3.23}$$

Material constants for Si_3N_4 may be found in Appendix B. The three terms of (3.22) represent respectively the energy associated with bending, the in-plane tension and the kinetic energy. In many regards the first of these terms can be ignored, as it is typically orders of magnitude smaller then the latter two – see Nielsen (2016) for details. Discarding this term, simplifies the problem to a the normal wave equation

$$\nabla^2 w(x,y;t) = -\frac{1}{c^2}\frac{\partial^2}{\partial t^2} w(x,y;t). \tag{3.24}$$

In the simplest description, the modes of a rectangular membrane $w_{mn}(x,y;t)$, with mode indices n and m, can be seperated into an oscillatory term, $z_{mn}(t)$ and a spatial part:

$$w_{nm}(x,y;t) = z_{nm}(t) M_{nm}(x,y) = z_{nm}(t)\sin(nk_x x)\sin\left(mk_y y\right) \tag{3.25}$$

$$z_{nm}(t) = z_0(t)\cos(\omega_{nm} t), \tag{3.26}$$

where z_0 is the slowly varying displacement amplitude, and $k_i = \pi/L_i$ is the wavenumber; it arises directly from the requirement that the displacement is zero at the edge. The spatial part of (3.25) is plotted in Fig. 3.4, for $n, m \in \{1,2,3\}$ and a square membrane.

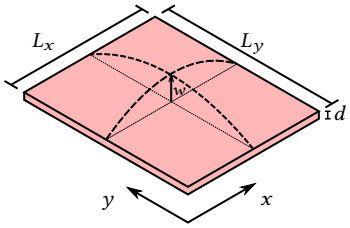

Figure 3.3: A rectangular membrane of sidelengths L_x, L_y and thickness d, with out-of-plane displacement w.

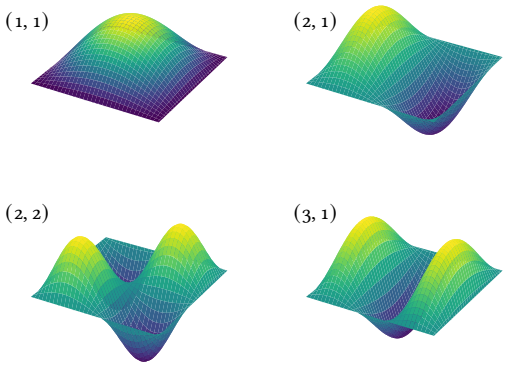

Figure 3.4: Mode shapes, $M_{nm}(x,y)$ of four combinations of (n,m) for a square membrane.

These modes have frequencies

$$\omega_{nm} = c\sqrt{n^2k_x^2 + m^2k_y^2} = \pi\sqrt{\frac{\mathcal{T}}{\rho}}\sqrt{\frac{n^2}{L_x^2} + \frac{m^2}{L_y^2}}, \tag{3.27}$$

where $c = \sqrt{\frac{\mathcal{T}}{\rho}}$ is the speed of sound in the material.

A couple of learning points from this equation that will eventually carry over to our more advanced[8] phononically shielded soft clamped membranes: high

(8) Advanced, but analytically untractable.

tension and small size leads to high frequencies. At the same time, small n and m corresponds to small spatial frequency and small oscillation frequencies. Curiously absent from the equation is the membrane thickness d; a fact originating from the unspoken assumption that we can neglect the energy loss associated with bending—an assumption which turns out to be analytically favorable, but in the end wrong—we shall return to why in a later chapter.

If we instead of considering the spatial part, as depicted in Fig. 3.4, consider the time evolution of a fixed (x_0, y_0), we see that it is entirely harmonic. Neglecting for a moment that we cannot probe the membrane in a *point*, but will always probe some (small) area, our next step in transforming the 3D oscillation to a 1D description will be to simply *require* that the potential energy of a given mode equals the energy of a 1D harmonic oscillator at the same frequency:

$$V_{\text{osc}}(t) = \frac{1}{2} k z^2_{x_0,y_0}(t) = \frac{1}{2}\omega^2_{nm} m_{\text{eff}} z^2_{x_0,y_0}(t). \tag{3.28}$$

If we, on the other hand, integrate the potential energy of each small part of the membrane we get

$$V_{\text{osc}}(t) = \int_0^{L_x}\int_0^{L_y} \frac{1}{2}\omega^2_{nm} w^2(x,y;t)\rho d \,\mathrm{d}x\mathrm{d}y \tag{3.29}$$

$$= \int_0^{L_x}\int_0^{L_y} \frac{1}{2}\omega^2_{nm} z^2_{nm}(t) M^2_{nm}(x,y)\rho d \,\mathrm{d}x\mathrm{d}y \tag{3.30}$$

$$= \frac{1}{2}\omega^2_{nm}\left[\int_0^{L_x}\int_0^{L_y} M^2_{nm}(x,y)\rho d \,\mathrm{d}x\mathrm{d}y\right] z^2_{nm}(t), \tag{3.31}$$

which is mathematically just the 1D harmonic oscillator of (3.28), with an effective mass given by the term in brackets. For a rectangular membrane, this integral evaluates to

$$m_{\text{eff}} = \frac{L_x L_y \rho d}{4} = \frac{1}{4} m_{\text{phys}}, \tag{3.32}$$

independent of n and m, and equal to a quarter of the physical mass. For the general case, the effective mass may be written as (Yeghishe Tsaturyan 2019, p. 9)[9]

$$m_{\text{eff}} = \rho \int \left(\frac{|Q|}{|Q_{\max}|}\right)^2 \mathrm{d}V, \tag{3.33}$$

where Q is the out of plane displacement, and $Q_{\max}$ is the maximum displacement normalizing the mode shape[10].

We have now seen how a manifestly 3D membrane can be effectively treated as a (classical) 1D harmonic oscillator. This abstraction will be used throughout the rest of the thesis. This classical oscillator is the one we will be quantizing in Section 3.4. But first, we turn to the decay term, and its relation to thermal noise.

(9) Yeghishe Tsaturyan (2019). "Ultracoherent soft-clamped mechanical resonators for quantum cavity optomechanics". Ph.D. thesis. University of Copenhagen.

(10) Our choice of M_{nm} is already normalized. Also, don't confuse this Q (displacement) with the quality factor, Q defined in the next section.

3.3 Dissipation & Noise

Having now dealt with harmonic oscillators at some length, we move on to the *dampened* part of harmonic oscillators, as described by γ in the equation of motions for a harmonic oscillator, (3.18).[11]

Focusing for a moment on the time domain, for example by Fourier transforming back from the Fourier domain response described by (3.21), one gets after assuming $x(0) = 0$ and $v(0) = 0$ (Uhlenbeck and Ornstein 1930, p. 834)[12]

$$x(t) = \frac{1}{m_{\text{eff}}\omega_1} \int_0^t F(\tau) e^{-\gamma(t-\tau)/2} \sin\left(\omega_1(t-\tau)\right) \mathrm{d}\tau, \tag{3.34}$$

where $\omega_1 = \sqrt{\omega^2 - \gamma^2/4}$ is the effective oscillation frequency. For our membranes, $\omega_m/\gamma = Q$ is on the order of 10^9, and thus $\omega_1 = \omega_m$ for all practical purposes.

The full solution to Eq. (3.18) is

$$x(t) = \frac{\gamma x_0 + 2\dot{x}_0}{2\omega_1} e^{-\gamma t/2} \sin(\omega_1 t) + x_0 e^{-\gamma t/2} \cos(\omega_1 t) + \frac{1}{m_{\text{eff}}\omega_1} \int_0^t F(\tau) e^{-\gamma(t-\tau)/2} \sin\left(\omega_1(t-\tau)\right) \mathrm{d}\tau, \tag{3.35}$$

where x_0 is the initial position, and $\dot{x}_0$ is the initial velocity. If the force term $F(\tau)$ is sufficiently small, or stochastic, the last term may be ignored for sufficiently large x_0 and small times. In that case, we can rewrite Eq. (3.35) as

$$x(t) = x_X(t)\cos(\omega_1 t) + x_Y(t)\sin(\omega_1 t) \tag{3.36}$$

where $x_X(t)$ and $x_Y(t)$ are the two quadratures of oscillation, which are equal to the prefactors to the harmonics in Eq. (3.35). Measuring $x(t)$ and performing a lock-in detection at ω_1 yields the time-dependent quantity

$$x_R(t) = \sqrt{x_X^2(t) + x_Y^2(t)} = \sqrt{\left(\frac{\gamma x_0 + 2\dot{x}_0}{2\omega_1}\right)^2 + x_0^2} \times e^{-\gamma t/2} \tag{3.37}$$

This quantity decays with a time constant $\tau = 2/\gamma$, which, given that the oscillation frequency is known (which it is, since we just did lock-in detection of the oscillation), allows us to calculate Q as

$$Q = \frac{\omega_m}{\gamma} = \frac{\omega_m \tau}{2}. \tag{3.38}$$

How this measurement is performed in practice will be covered in Section 4.4.

3.3.1 Brownian Noise & the Fluctuation-Dissipation Theorem

After the initial displacement and velocity has decayed, the convolution term of Eq. (3.35) becomes dominant, and we must think about how to describe this force. The most relevant case for us is that of *thermal perturbations*. The *fluctuation-dissipation theorem* states that any dissipation is always accompanied by thermal fluctuations and vice versa. In our case, if there is velocity damping, as postulated

(11) The specifics of what damping model to use is often glossed over—because the one presented here is adequate, so will I. For more details, see, e. g., Dalziel J. Wilson (2012). "Cavity Optomechanics with High-Stress Nitride Films". Ph.D. thesis. California Institute of Technology.

(12) G. E. Uhlenbeck and L. S. Ornstein (1930). "On the Theory of the Brownian Motion". In: *Phys. Rev.* 36 (5), pp. 823–841.

by in our equations of motion, there *must* also be a corresponding thermal force, F_{th} on our oscillator.

If the reservoir responsible for the thermal force F_{th} is at the temperature T, and the oscillator has equilibrated to the reservoir, the power spectral density of the thermal force is

$$S_{F_{\text{th}}F_{\text{th}}}(\Omega) = 4k_{\text{B}}T\gamma m_{\text{eff}}, \tag{3.39}$$

where k_{B} is Boltzmann's constant. This spectral density is *independent of* Ω, and thus has infinite power, which is of course unphysical. Using the Wiener-Khinchin theorem, this can be shown to correspond to a delta-time correlation. In truth, the spectral density falls off for very high frequencies, corresponding to a very short coherence time, much faster than any other process in our system. In this case, the spectrally flat approximation is good.

Using the frequency domain expression for $x(\Omega)$ in Eq. (3.21) and the definition of PSD in Section 3.0.2, the spectrum of displacements arising from this force

$$S_{xx}(\Omega) = S_{FF}(\Omega)|\chi(\Omega)|^2 \tag{3.40}$$

becomes, by insertion of the susceptibility, $\chi(\Omega)$, again from Eq. (3.21), as well as the PSD of the thermal force from Eq. (3.39),

$$S_{xx}(\Omega) = \frac{4\gamma k_{\text{B}}T m_{\text{eff}}^{-1}}{(\omega_{\text{m}}^2 - \Omega^2)^2 + \Omega^2\gamma^2}. \tag{3.41}$$

Since we are almost always interested in the response close to resonance, and not the wings where the response has decayed by many orders of magnitude, we may approximate this expression by a Lorentzian response as

$$S_{xx}(\Omega) \approx \frac{\gamma k_{\text{B}}T}{\omega^2 m_{\text{eff}}} \frac{1}{(\omega - \Omega)^2 + \gamma^2/4}, \tag{3.42}$$

with γ now being the full width half maximum (FWHM) of the Lorentzian. The two equations (3.41) and (3.42) are displayed in Fig. 3.5.

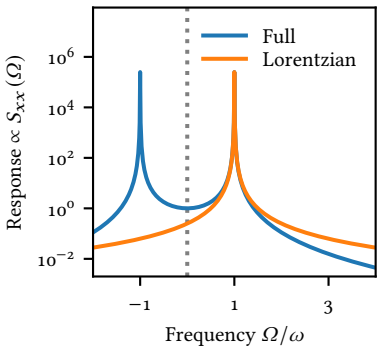

Figure 3.5: Full model of Eq. (3.41) and Lorentzian approximation of Eq. (3.42), normalized so $S_{xx}(0) = 1$ for the full model. Frequency is axis is normalised to the oscillator frequency ω, and $\gamma = 0.002\omega$.

We now invoke Parseval's theorem

$$\int_{-\infty}^{\infty} |f(t)|^2 \, \mathrm{d}t = \frac{1}{2\pi} \int_{-\infty}^{\infty} |f(\Omega)|^2 \, \mathrm{d}\Omega, \tag{3.43}$$

and the knowledge that $\langle x \rangle = 0$, and thus $\mathrm{Var}(x) = \langle x^2 \rangle$ to write

$$\langle x^2 \rangle = \frac{1}{2\pi} \int_{-\infty}^{\infty} |x(\Omega)|^2 \, \mathrm{d}\Omega. \tag{3.44}$$

Since the Hamiltonian for a harmonic oscillator is given by

$$H = \frac{1}{2} m_{\text{eff}} \omega^2 x^2 + \frac{1}{2} m_{\text{eff}} \dot{x}^2 \tag{3.45}$$

and since the equipartition theorem of statistical mechanics states that each quadratic term will have mean energy $k_B T/2$, we also have

$$\langle x^2 \rangle = \frac{k_B T}{m_{\text{eff}} \omega^2}, \tag{3.46}$$

and, therefore

$$\frac{1}{2\pi} \int_{-\infty}^{\infty} |x(\Omega)|^2 \, \mathrm{d}\Omega = \frac{k_B T}{m_{\text{eff}} \omega^2}. \tag{3.47}$$

In words, the variance of motion may be directly found by integrating over the PSD, and the variance is directly proportional to the temperature.

Simulating the effects of Brownian noise can be done by numerical integration of numerical integration of (3.34). We discretize time with the step size Δt, and insert for $F(\tau)$ a Gaussian noise with standard deviation[13] $\sqrt{2 k_B T m_{\text{eff}} / \Delta t}$.

The result of such a simulation is shown in Fig. 3.6 for three different values of Q. In the left hand column the time domain signal $x(t)$ is shown. In the right hand side, the averaged PSD obtained by splitting the time domain signal into 10 equal segments is shown, together with the full oscillator response model of Eq. (3.41) with zero free parameters.

As Q decreases, the response in frequency space becomes wider and lower, while the variance, $\langle x^2 \rangle$, remains the same. In the time domain, the oscillation amplitude changes slower for high Q, and large excursions are rarer than for low Q.

(13) Nielsen (2016) gives a different expression for this standard deviation, which does not have dimensions of force, and scales incorrectly with the choice of Δt.

3.4 Quantum Mechanics

Having dealt, until now, with a purely classical description, it is now time to turn to the *quantum* part of *quantum optomechanics*. Often, when introducing quantum mechanics, one starts from the Schrödinger equation, which can be solved for the particles of interst, and goes on to introduce second quantization with ladder operators. In quantum optomechanics, the approach is different. Quoting again W. Bowen and Milburn (2015, preface)

> A key feature of the theory of engineered quantum systems is how the quantum description is given. One does not solve the Schrödinger equation for every atomic or molecular constituent of the macroscopic system. On the contrary, one begins with a classical description of the relevant macroscopic degrees of freedom — elastic deformations in the case of mechanics and classical current and flux in the case of quantum circuits — and quantises these collective degrees of freedom directly. This works if the macroscopic system can be so designed that the relevant collective degrees of freedom largely de-couple from the microscopic degrees of freedom, which remain only as a source of noise and dissipation.

The authors note further that this approach makes quantum optomechanics 'Essentially (…) an "effective quantum field theory."'

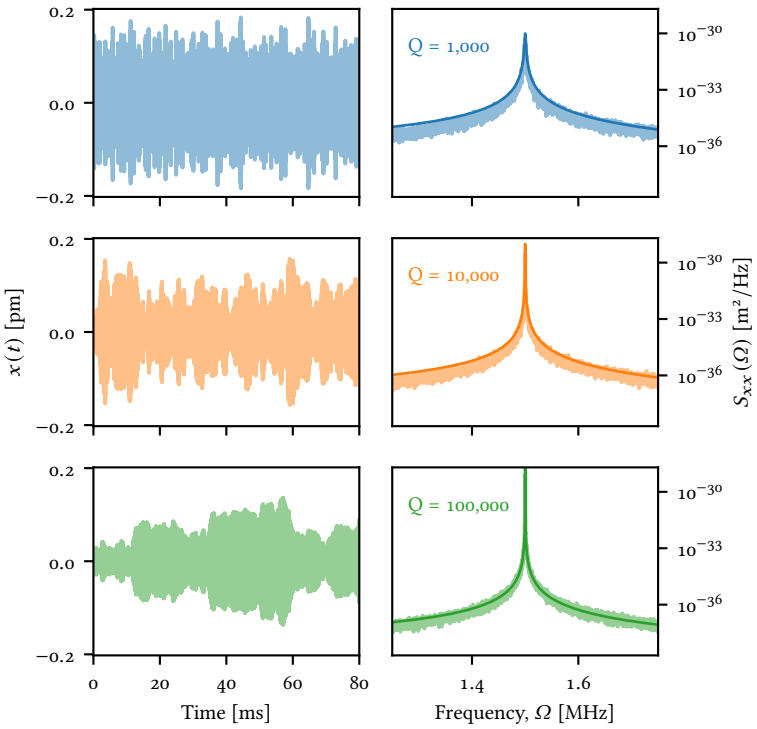

Figure 3.6: Thermal response of harmonic oscillators to a Gaussian/thermal driving force. Left column: position as a function of time, $x(t)$. Right column: PSD of the displacement, $S_{xx}(\Omega)$. $\omega/2\pi = 1.5\,\text{MHz}$, $m_{\text{eff}} = 20\,\text{ng}$, $T = 300\,\text{K}$, $\Delta t = 50\,\text{ns}$. For these parameters $\langle x^2 \rangle = (48\,\text{pm})^2$.

The classical Hamiltonian for a harmonic oscillator, as described in the previous sections, is

$$H = \frac{1}{2}kx^2 + \frac{1}{2m}p^2, \tag{3.48}$$

with the two terms representing respectively the potential and kinetic energy of the oscillator. We now postulate that these degrees of freedom are represented by quantum operators, $\hat{x}$[14] and $\hat{p}$, leading to the Hamiltonian

$$\hat{H} = \frac{1}{2}k\hat{x}^2 + \frac{1}{2m}\hat{p}^2, \tag{3.49}$$

which is the starting point for the quantum mechanical description. These two operators do not commute, $[\hat{x}, \hat{p}] = i\hbar$. Although the equation looks deceptively similar to the one one is bound to encounter in an undergraduate quantum mechanics course (indeed, the math is identical), there is an abstraction here, alluded to in the quote above. While the "undergraduate Hamiltonian" describes a single particle (maybe an electron) in some kind of potential, whose origin we do not know or particularly care about, Eq. (3.49) describes the *collective dynamics* of many atoms, whose collective motion gives rise to a single momentum, and whose internal

(14) Another common choice for the position operator is $\hat{q}$.

stresses and possibly advanced geometrical arrangement gives rise to the spring potential $\frac{1}{2}k\hat{x}^2$. That this approach works relies on a number of things; for example, we have to know that the single mode description is reasonable. A membrane is an inherently multi-mode object, but if the modes are spectrally well separated and the motion does not leave the linear regime, so frequencies do not mix, we may simple choose to care about a single mode only, and quantize the motion of that.

We now define the creation and annihilation operators[15],

$$\hat{a} = (2\hbar m\omega)^{-1/2}\,(\mathrm{i}\hat{p} + \omega\hat{x}) \qquad \hat{a}^\dagger = (2\hbar m\omega)^{-1/2}\,(-\mathrm{i}\hat{p} + \omega\hat{x})\,. \tag{3.50}$$

These *ladder operators* will be used to describe both membranes, spins and light fields throughtout this thesis. They have the well known commutation relation

$$[\hat{a}, \hat{a}^\dagger] = \hat{a}\hat{a}^\dagger - \hat{a}^\dagger\hat{a} = 1. \tag{3.51}$$

We rewrite the Hamiltonian in terms of these, as

$$\hat{H} = \hbar\omega\left(\hat{a}^\dagger\hat{a} + \frac{1}{2}\right). \tag{3.52}$$

For the harmonic oscillator, a set of (energy) eigenstates, $\{\psi_n\}$ or $\{|n\rangle\}$, exists, for which

$$\hat{a}\,|n\rangle = \sqrt{n}\,|n-1\rangle \tag{3.53}$$

$$\hat{a}^\dagger\,|n\rangle = \sqrt{n+1}\,|n+1\rangle\,, \tag{3.54}$$

thus respectively *lowering* or *raising* the *quantum number n*, which counts the number of excitations in the oscillator, since

$$\hat{a}^\dagger\hat{a}\,|n\rangle = n\,|n\rangle\,, \tag{3.55}$$

which leads to the obvious definition $\hat{n} \equiv \hat{a}^\dagger\hat{a}$. The exception is that the lowering operator on the state $|0\rangle$ returns, by definition, nothing; $\hat{a}\,|0\rangle \equiv 0$. The energy of the Fock state $|n\rangle$ is $\hbar\omega(n + \frac{1}{2})$, leading to the identification of the factor $\frac{1}{2}$ in Eq. (3.52) as the *ground state energy*—the lowest energy state, that the oscillator can possibly assume.

Similarly, we can also express the position, $\hat{x}$ and $\hat{p}$, from the ladder operators

$$\hat{x} = x_{\mathrm{zpf}}(\hat{a}^\dagger + \hat{a}) \tag{3.56}$$

$$\hat{p} = p_{\mathrm{zpf}}(\hat{a}^\dagger - \hat{a}), \tag{3.57}$$

with

$$x_{\mathrm{zpf}} = \sqrt{\frac{\hbar}{2m\omega}} \tag{3.58}$$

$$p_{\mathrm{zpf}} = \sqrt{\frac{\hbar m\omega}{2}} = m\omega x_{\mathrm{zpf}}, \tag{3.59}$$

are the *zero point fluctuations* of the oscillator, i. e., the standard deviation of the vacuum state, $|0\rangle$[16]. For our membranes, with effective masses on the order of 2 ng (Yeghishe Tsaturyan et al. 2017) and frequencies around $\omega/2\pi = 1.4\,\mathrm{MHz}$, $x_{\mathrm{zpf}} \sim 50\,\mathrm{am} = 5 \times 10^{-17}\,\mathrm{m}$.

(15) Slightly different variations exist. I follow David J. Griffiths (2005). *Introduction to quantum mechanics*. Pearson Prentice Hall, p. 468.

(16) W. Bowen and Milburn (2015) as well as Gerry and Knight (2005) claim that these zero point fluctuations are a "direct consequence of the zero-point energy". I find this to be a tautology or a misunderstanding—the fluctuations are a result of the non-commutability of the operators, which limits product of variances, c.f. Heisinberg's indeterminacy (uncertainty) relation. The fact that a state with a finite momentum variance has kinetic energy, and vice versa, is not too surprising.

The zero point fluctuations also leads to an obvious way of introducing dimensionless variables, $\hat{X}$ and $\hat{P}$, as

$$\begin{aligned}\hat{X} &= \frac{\hat{x}}{\sqrt{2}x_{\mathrm{zpf}}} = \frac{1}{\sqrt{2}}\left(\hat{a}^\dagger + \hat{a}\right)\\ \hat{P} &= \frac{\hat{p}}{\sqrt{2}p_{\mathrm{zpf}}} = \frac{\mathrm{i}}{\sqrt{2}}\left(\hat{a}^\dagger - \hat{a}\right).\end{aligned} \tag{3.60}$$

These variables are normalized such that

$$\left[\hat{X}, \hat{P}\right] = \mathrm{i}, \tag{3.61}$$

from which we directly conclude

$$\sigma\left(\hat{X}\right)\sigma\left(\hat{P}\right) \geq \frac{1}{2}\left|\left\langle\left[\hat{X}, \hat{P}\right]\right\rangle\right| = \frac{1}{2}. \tag{3.62}$$

or equivalently

$$\mathrm{Var}\left(\hat{X}\right)\mathrm{Var}\left(\hat{P}\right) \geq \frac{1}{4}, \tag{3.63}$$

which leads directly to the lower bound on their sum

$$\mathrm{Var}\left(\hat{X}\right) + \mathrm{Var}\left(\hat{P}\right) \geq 1, \tag{3.64}$$

which holds when $\mathrm{Var}\left(\hat{X}\right) = \mathrm{Var}\left(\hat{P}\right) = \frac{1}{2}$ – any other combination of variances that fulfill Eq. (3.63) will have a sum of variances larger than 1[17]. This single system bound, will become the EPR state boundary that we need to break to demonstrate entanglement in Chapter 10.

(17) When the equality in (3.63) holds

$$\mathrm{Var}(\hat{P}) = 1/4\,\mathrm{Var}(\hat{X}),$$

so

$$\mathrm{Var}(\hat{X}) + \mathrm{Var}(\hat{P}) = \mathrm{Var}(\hat{X}) + 1/(4\,\mathrm{Var}(\hat{X})),$$

which is easily verified to be minimized for $\mathrm{Var}(\hat{X}) = 1/2$.

Since our membranes are coupled to a hot environment, they will not occupy the ground state, or indeed any other low-occupation state if we do nothing to them. Since *phonons*, i. e., mechanical excitations, are bosons, Bose–Einstein statistics apply. If the oscillator has thermalized to an environment at the temperature T, the probability distribution for finding the oscillator in the energy level n is

$$p(n) = \mathrm{e}^{-\frac{\hbar\omega n}{k_{\mathrm{B}}T}}\left[1 - \mathrm{e}^{-\frac{\hbar\omega}{k_{\mathrm{B}}T}}\right], \tag{3.65}$$

with mean occupancy

$$\bar{n} = \langle n\rangle = \sum_{n=0}^{\infty} np(n) = \left[\mathrm{e}^{\frac{\hbar\omega}{k_{\mathrm{B}}T}} - 1\right]^{-1}. \tag{3.66}$$

For a membrane at $\omega/2\pi = 1.4\,\mathrm{MHz}$ held at $4\,\mathrm{K}$, $\bar{n} = 6\times 10^4$, or, in other words, very far from the ground state with $\bar{n} = 0$.

In terms of the ladder operators, the variance of the position and momentum operators for a state in thermal equilibrium is given by

$$\mathrm{Var}\left(\hat{X}\right) = \mathrm{Var}\left(\hat{P}\right) = \bar{n} + 1. \tag{3.67}$$

Instead of representing a state in terms of the position and momentum, it is often beneficial to represent it as a phasor, i. e., by an amplitude and a phase, plus an "uncertainty ball" (W. Bowen and Milburn 2015, p. 7), as depicted in Fig. 3.7.

This picture is especially useful for *coherent states*, which are a special set of states, that are eigenstates of the annihilation operator

$$\hat{a}\,|\alpha\rangle = \alpha\,|\alpha\rangle\,, \tag{3.68}$$

where α is a complex number. It may be shown (Gerry and Knight 2005, p. 44) that the coherent state expressed as a sum of number states is

$$|\alpha\rangle = \mathrm{e}^{-\frac{1}{2}|\alpha|^2} \sum_{n=0}^{\infty} \frac{\alpha^n}{\sqrt{n!}}\,|n\rangle\,. \tag{3.69}$$

The coherent state has the same uncertainty in both $\hat{X}$ and $\hat{P}$ as the ground state, and thus can be thought of also as a displaced ground state. The complex number α can of course be written $|\alpha|\mathrm{e}^{\mathrm{i}\theta}$. This makes the representation as a phasor obvious, as long as one keeps the uncertainty in mind.

In absence of decay and external forces, the coherent state evolves as

$$|\alpha\rangle \to |\mathrm{e}^{-\mathrm{i}\omega t}\alpha\rangle\,, \tag{3.70}$$

i. e., revolves in phase space with the frequency ω going in clockwise circles.

The coherent state amplitude α is directly related to the number of excitations present in the system, as

$$\langle\hat{n}\rangle = \langle\alpha|\,\hat{n}\,|\alpha\rangle = \langle\alpha|\,\hat{a}^\dagger\hat{a}\,|\alpha\rangle = \langle\alpha|\,\alpha^*\alpha\,|\alpha\rangle = |\alpha|^2. \tag{3.71}$$

The probability of finding the system in a given number state is given by

$$P_n = |\,\langle n|\alpha\rangle\,|^2 = \mathrm{e}^{-|\alpha|^2}\frac{|\alpha|^{2n}}{n!} = \mathrm{e}^{-\bar{n}}\frac{\bar{n}^n}{n!}, \tag{3.72}$$

which is a Poisson distribution with mean $\bar{n}$.

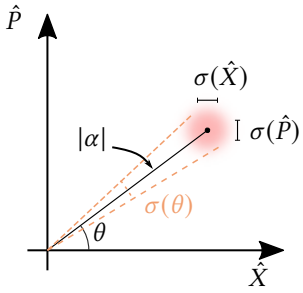

Figure 3.7: A coherent state phase space representation

❧ ❋ ❧

We've now covered the needed material for harmonic oscillators, how to treat membranes as such, and a quantum mechanical description. As such, we're now ready to move onto the *opto*-part of *optomechanics*. We start out with a section on the interaction of light and mechanics, before moving on to the light and optical cavities in more details.

3.5 Radiation Pressure Coupling

The foundation of coupling of light and mechanical degrees of freedom is *radiation pressure*. A stream of photons, each carrying momentum $\hbar k$, with k being the wavenumber, impinging on a (partially) reflective medium, thus exerts a force proportional to the number of photons impinging. If the light is incident normal to the surface, the momentum of a reflected photon is fully reversed, thus imparting a change of

$$\Delta p = 2\hbar k, \tag{3.73}$$

per photon. A picture of the situation is shown in Fig. 3.8. Since $\Delta p = F\Delta t$, we can estimate the force from a beam of light. Take, for example, 1 mW of light at 852 nm, which corresponds to about 4.2×10^{15} photons per second, or in other words

$$F = n_{\text{phot}} \frac{\Delta p}{\Delta t} = 6.7 \times 10^{-12}\ \text{N}. \tag{3.74}$$

This is an absolutely minute force, even compared to the low effective masses of a new ng that we will encounter. In the next section, we will deal with a way of amplifying this force.

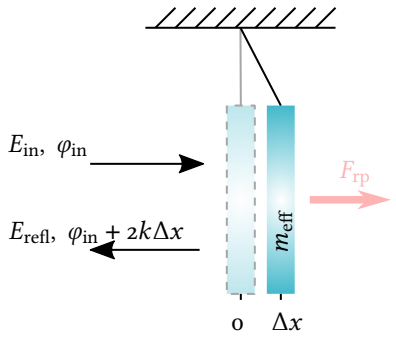

Figure 3.8: Radiation pressure force on a harmonically suspended mirror. The input light leads to a radiation pressure force F_{rp} as it is reflected off the suspended mirror. The reflected beam acquires a phase that depends on the position of the mirror, so the phase of the reflected light $\varphi_{\text{in}} \longrightarrow \varphi_{\text{in}} + 2k\Delta x$.

The motion of the reflecting material modifies the light by changing the *optical phase* of the reflected light[18]. Here, one must consider the phase sensitivity one needs to measure a given displacement. Since a movement of the reflective surface by Δx changes the phase, $\Delta\varphi = k2\Delta x$[19], the smallest detectable change in position is

$$\Delta x = \frac{\Delta\varphi}{2k}. \tag{3.75}$$

A phase sensitivity of 1 mrad and light at $\lambda = 852$ nm leads to a position sensitivity of $\Delta x = 68$ pm. So, even a rather good phase sensitivity leads to minimal detectable displacements that are many orders of magnitude larger than the zero point fluctuations, x_{zpf}.

The message is clear: we need to boost the interaction strength, if we are to have any hope of doing something interesting.

(18) Other mechanisms can be envisioned; for example, a mirror that *tilts* would deflect the beam instead, thus changing the amount of light reflected in a given direction.

(19) The factor of 2 comes from the light going back and forth.

3.6 Optical Cavities

The basic recipe for boosting the light-mechanics interaction will be having the light interact with the mechanics several times. If, for example, the light somehow samples the change in path length N times, the change in phase as well as the radiation pressure on the material will be boosted by a factor N, assuming that all of the interactions happen in a time scale much faster than the motion of the

mechanical object. Our chosen way of "recycling" the photons, will be to build a Fabry–Perot resonator from two highly reflective mirrors, although a host of alternative strategies exist, as described in Chapter 2, especially Fig. 2.3.

We consider the simplest way of constructing an optical resonator, the plano-plano Fabry-Perot cavity, as depicted in Fig. 3.9. The design with two plane mirrors is not stable for practical applications; however, the idealized description essentially holds for the similar case of, e. g., a plano-concave or concave-concave design, where one or two of the plane mirrors are replaced with concave counterparts. The mirrors are placed L apart. Each mirror has a field transmission and reflectivity of (r_i, t_i), which we allow to be complex, to describe an arbitrary phase of the reflected/transmitted beam. The power reflectivity and transmissivity we label (R_i, T_i), with $R_i = |r_i|^2$, $T_i = |t_i|^2$[20].

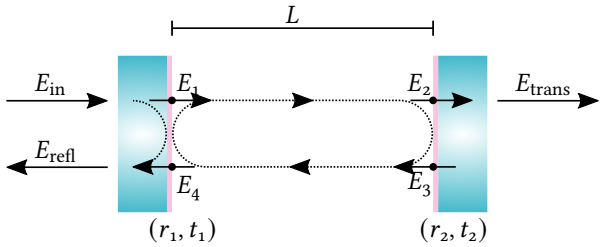

Figure 3.9: A simple optical cavity. The relation of the field at different locations is explained in the main text.

The input beam, E_{in}, is partially reflected into E_{refl} and partially transmitted into E_1. At the same time E_4 is transmitted into E_{refl} and reflected into E_1. Thus,

$$E_1 = t_1 E_{in} + r_1 E_4 \tag{3.76}$$

$$E_{refl} = -r_1 E_{in} + t_1 E_4, \tag{3.77}$$

with the minus sign on the reflection in second line explained in [20].

E_2, E_3 and E_{trans} relate in a similar fashion. Finally, E_2 is simply E_1, upon acquiring a propagation phase of kL, i. e.,

$$E_2 = E_1 e^{ikL} \qquad E_4 = E_3 e^{ikL}, \tag{3.78}$$

and E_3 is simply E_2 reflected on the second mirror:

$$E_3 = r_2 E_2. \tag{3.79}$$

By expressing E_4 from E_3, E_3 from E_2 and finally E_2 from E_1, we obtain an expression for E_1, that depends only on the system parameters and the input field E_{in}:

$$E_1 = t1 E_{in} + r_1 r_2 e^{2ikL} E_1, \tag{3.80}$$

which is easily transformed to

$$E_1 = \frac{t_1}{1 - r_1 r_2 e^{2ikL}} E_{in}. \tag{3.81}$$

(20) I am sweeping some complexity under the rug; one should keep track of which side the beam is coming from, so each surface has four coefficients, r, t and r', t' respectively. With the optical phase referenced at the plane of incidence for both beams, unitarity (essentially energy conservation) requires that

$$t t' = 1 - r^2$$
$$r' = -r.$$

We pick $t = t'$, thus restricting the transmission phases, with little loss of generality, and explicitly insert $-r$ for reflections from high to low refractive index. For details, see Eugene Hecht (2002). *Optics*. 4th International Edition. Addison Wesley, Sec. 4.11..

The corresponding circulating optical power, $|E_{\mathrm{circ}}|^2$, normalized to the input power is plotted in Fig. 3.10, for a symmetric cavity, i. e., $r_1 = r_2 = r$, and different values of r, expressed through the finesse, $\mathcal{F}$, defined below.

When the round trip phase, $2\varphi = 2kL$, equals $n\pi$, the cavity is resonant, and the circulating power builds up to values much larger than the input power – roughly by a factor $\mathcal{F}/\pi$.

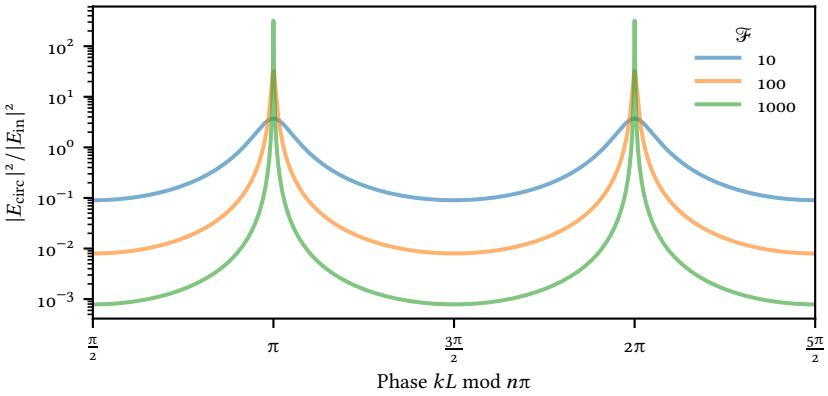

Figure 3.10: Cavity resonances for different values of the finesse, $\mathcal{F}$. The cavity is resonant when $\varphi = kL = n\pi$, i. e., when the intracavity field, E_{circ}, builds up to much larger values than the input field, E_{in}.

Combining the expressions above, we obtain for the transmitted field

$$E_{\mathrm{trans}} = \frac{t_1 t_2 \mathrm{e}^{\mathrm{i}kL}}{1 - r_1 r_2 \mathrm{e}^{2\mathrm{i}kL}} E_{\mathrm{in}}, \tag{3.82}$$

and reflected field

$$E_{\mathrm{refl}} = \left(-r_1 + \frac{r_2 t_1^2 \mathrm{e}^{2\mathrm{i}kL}}{1 - r_1 r_2 \mathrm{e}^{2\mathrm{i}kL}}\right) E_{\mathrm{in}}. \tag{3.83}$$

Since we have ignored losses, it is not too cumbersome to verify that $(|E_{\mathrm{refl}}|^2 + |E_{\mathrm{trans}}|^2)/|E_{\mathrm{in}}|^2 = 1$, or in other words, that all energy is eventually transmitted or reflected. The reflected and transmitted powers are plotted in Fig. 3.11. As the reflectivity goes up, the resonances become narrower,

We now define a number of useful quantities. The first is the *free spectral range*, FSR[21],

$$\mathrm{FSR}_\nu = \frac{c}{2L}, \tag{3.84}$$

which quantifies the separation in frequency between consecutive resonances. This is only a property of the separation between the mirrors, L. It is also equal to the inverse of the round trip time of the light, i. e., $\tau_{\mathrm{RT}} = \mathrm{FSR}_\nu^{-1}$. The next is the *cavity finesse*,

$$\mathcal{F} = \frac{2\pi}{-\ln R_1 R_2}. \tag{3.85}$$

(21) The FSR is sometimes labeled with a subscript to denote the units used. If no label is present it is almost always safe to assume that real (non-angular) frequencies are assumed.

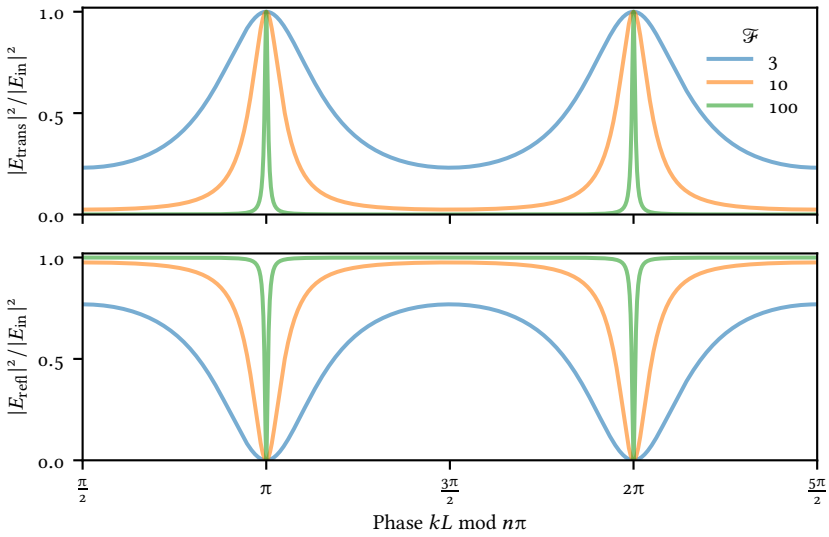

Figure 3.11: Reflection and transmission through a lossless cavity, for different values of the finesse, $\mathcal{F}$. The sum of normalized transmitted and reflected power equals 1, since we have neglected all losses. Note the linear y-scale, as opposed to Fig. 3.10.

The finesse quantifies the ratio between the width of the resonances and the FSR

$$\mathcal{F} = \frac{\text{FSR}}{\kappa/2\pi}. \tag{3.86}$$

In Fig. 3.12, I plot the Finesse for a symmetric cavity, for different mirror reflectivities, R. In the left panel, the finesse is plotted on a semi-logarithmic axis, while in the right panel, for small transmissivities, $(1-R)$, the axes are *log-log*. For the sake of calculating the finesse, only R matters—whether the rest is transmission or loss does not matter—and thus this graph may be used to infer the finesse for a total loss plus transmission of some size. For example, 10 ppm transmission and loss on both mirrors, gives a finesse of $\sim 3 \times 10^5$, or an enhancement of the circulating power of $\sim 10^5$.

The cavity linewidth κ quantifies simultaneously the width of the cavity resonance features as a function of detuning of the input light frequency, as well as the *loss rate* of light from the optomechanical cavity. It can be expressed as the loss per roundtrip divided by the round trip time, and the different loss mechanisms add linearly

$$\kappa = \kappa_1 + \kappa_2 + \kappa_L, \tag{3.87}$$

where κ_i describes the loss of photons from the cavity at mirror 1 & 2 or though some loss-process, subscripted L. The mirror loss rates equals

$$\kappa_1 = \frac{1}{\tau}|t_1|^2 \qquad \kappa_2 = \frac{1}{\tau}|t_2|^2 \tag{3.88}$$

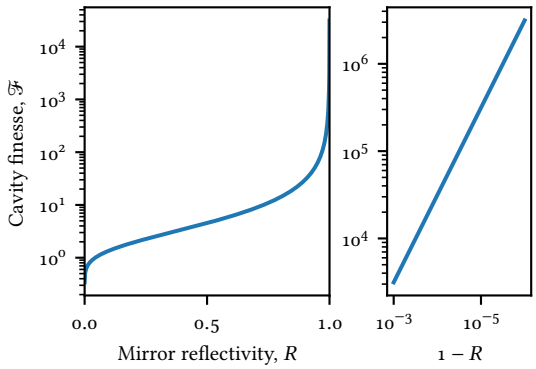

Figure 3.12: Cavity finesse, $\mathcal{F}$, for a symmetric cavity, with $R_1 = R_2 = R$. Left: As a function of $R \in [0, 1]$. Right: As a function of $1 - R \in [10^{-3}, 10^{-6}]$. Notice the peculiar choice of x-axis, such that low values of $1 - R$ is to the right, to agree with the figure to the left. Note different y-axes.

Since it is useful to describe where light is going, we define the *overcoupling*, η, which is simply a given loss rate divided by the total cavity loss rate

$$\eta_i = \frac{\kappa_i}{\kappa}. \tag{3.89}$$

People use this terminology slightly differently, but in general three different situations exist; $\eta < 1/2$, $\eta = 1/2$ and $\eta > 1/2$, called respectively *under-*, *critically* and *over-coupled*[22].

(22) Yes, it is rather confusing that the *overcoupling parameter* describes both cavities that are undercoupled and overcoupled. Such is life.

From the point of a beam of light impinging on a cavity, η describes how much of the beam will enter the cavity, as well as how much light is reflected. For $\eta = 1/2$ *no* light is reflected off the cavity – it is either lost or transmitted. At the extremes, low η means that little light enters the cavity, but the beam is simply reflected, while high η means that a lot of light enter the cavity, but is transmitted out through the same port. In more quantifiable terms, the ratio of the input power to the transmitted power, on cavity resonance and for no loss, $\kappa_L = 0$, is

$$\frac{P_{\text{trans}}}{P_{\text{in}}} = \frac{4T_1T_2}{(T_1 + T_2)^2} = 4\eta_{\text{trans}}(1 - \eta_{\text{trans}}) = 4(1 - \eta_{\text{in}})\eta_{\text{in}}, \tag{3.90}$$

which is plotted in Fig. 3.13. This also highlights that cavities are linear, in the sense that the transmission is independent of which direction you send light through them, although the intracavity field may vary.

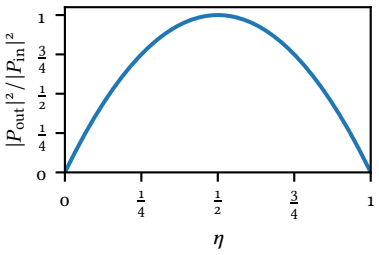

Figure 3.13: Relative power transmission as a function of the cavity coupling parameter, η. Because we want to maximize the detection of the light that has interacted with the membrane, we typically operate our system as close to $\eta = 1$ as practically possible, leading to low overall power transmission.

From the point of view of an intracavity field, the *different* η's describe transmission in different directions. It is then said that the cavity is undercoupled (or overcoupled) in either transmission or reflection, depending on which mirror serves as the input mirror.

Having discussed optical resonators in some depth now, we are ready for the holy marriage of cavities and mechanics.

3.7 Canonical Cavity Optomechanics

We consider the *canonical cavity optomechanical* setup, as depicted in Fig. 3.14. Here a single, perfectly reflective and *mechanically compliant* mirror ("membrane") is is used to form a Fabry–Perot cavity with another, stationary, mirror, the allows for light to enter and exit the cavity.

The *canonical* setup is in many ways the conceptually simplest way of depicting a optomechanical setup, and independent of the actual implementation one is dealing with, it is often helpful to map the specific system to the canonical case. We will deal with a more realistic model for our setup in Section 3.8.

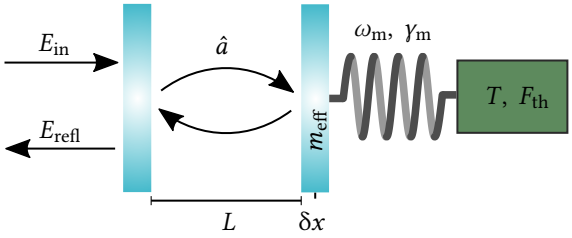

Figure 3.14: Canonical optomechanical system. A mechanically compliant mirror forms a Fabry–Perot cavity of length L together with another mirror. The moving mirror, with resonance frequency ω_{m} and mass m_{eff}, moves δx and thus modulates the cavity resonance frequency, and is coupled to a reservoir at temperature T with the rate γ_{m}, giving rise to a fluctuating thermal force, F_{th}. The cavity field is described by the field operator $\hat{a}$, and the input and output electrical fields E_{in} and E_{refl}.

We restrict ourselves to the case where only a single optical cavity mode is populated, and describe the electrical field by the (quantum) operator $\hat{a}$—as strongly indicated by this notation, we will see that the description of a bosonic degree of freedom applies not only to the membrane, but also to the optical field. The membrane, with frequency ω_{m} and mass m_{eff} is coupled to a bath at temperature T at the rate γ_{m}, giving rise to thermal forces F_{th}. The cavity is L long, and the mechanical motion away from equilibrium is δx.

The strength of the optomechanical coupling is quantified by the *coupling parameter*,

$$G \equiv \frac{\partial \omega_{\mathrm{cav}}}{\partial x_{\mathrm{m}}}. \tag{3.91}$$

For a canonical system like the one discussed here, the resonance frequency of the cavity is given by $\omega_{\mathrm{cav}} = 2\pi nc/2L$, with n some integer. Evaluating the derivative at the equilibrium position as $L \longrightarrow L + x_{\mathrm{m}}$, we get

$$G = \frac{\partial}{\partial x_{\mathrm{m}}} \frac{2\pi nc}{2(L + x_{\mathrm{m}})}\bigg|_{x_{\mathrm{m}}=0} = \frac{\omega_{\mathrm{cav}}}{L}. \tag{3.92}$$

For a resonance frequency corresponding to a wavelength of 852 nm and a typical cavity length of 2 mm, $G = 1.1 \times 10^{18}\ \mathrm{m^{-1}\,s^{-1}}$. This is of course a number that bears

little relevance to reality – we will never be able to change the length of a cavity by one metre, from the original length of a couple of millimetres, without fundamentally changing the cavity; further, any rate that are three orders of magnitude faster than the hundreds of THz optical frequency showing up in your calculations should be reason for, if not concern, then at least attention.

For optomechanics, the obvious way to get rid of this horrible PHz-scale frequency, is to multiply the rate by a characteristic length scale of the movement, to wit, the zero point fluctuations, x_{zpf},

$$g_0 \equiv G x_{\mathrm{zpf}}, \tag{3.93}$$

which takes a much more reasonable size. With $G = 1.1 \times 10^{18}\ \mathrm{m^{-1}\ s^{-1}}$ and $x_{\mathrm{zpf}} = 5 \times 10^{-17}\ \mathrm{m}$ we get a rough estimate of g_0 being on the order of $6 \times 10^{1}\ \mathrm{s^{-1}}$, if we were to use a membrane as the compliant mirror and somehow made it perfectly reflecting.

The *dispersive coupling* described above, where the membrane motion changes the cavity resonance frequency is by far the most common. It is however not the only scheme for cavity optomechanics. The most prominent alternative option is that of *dissipative optomechanics*, where the membrane motion modulates the cavity linewidth, κ. One then defines a dissipative coupling rate $H = \frac{\mathrm{d}\kappa}{\mathrm{d}x}$ as a direct analog of G[23]. As we will see in Section 3.8.1, our membrane-in-the-middle setup actually does have dissipative coupling, albeit at lower rate than the dissipative coupling. Dissipative coupling in a membrane-at-the-edge system (closely related to a membrane-in-the-middle) was explored theoretically in Dumont et al. (2019)[24], as well as in an system with a highly reflecting membrane *outside the cavity* in Tagantsev and Polzik (2021)[25]. Although dissipative optomechanics is an interesting field, we will focus on the dispersive interaction from now on.

(23) And, analogously with what will be defined for the dissipative coupling, $h_0 = H x_{\mathrm{zpf}}$ and $h = \sqrt{n_{\mathrm{cav}}} h_0$

(24) Vincent Dumont et al. (2019). "Flexure-tuned membrane-at-the-edge optomechanical system". In: *Opt. Express* 27.18, pp. 25731–25748.

(25) A. K. Tagantsev and E. S. Polzik (2021). "Dissipative optomechanical coupling with a membrane outside of an optical cavity". In: *Phys. Rev. A* 103 (6), p. 063503.

3.7.1 The Optomechanical Hamiltonian

Turning to the Hamiltonian describing the optomechanical interaction, we see that we must have two harmonic oscillators, the optical field and mechanical element respectively, a coupling term plus driving term for the optical field:

$$\hat{H} = \hat{H}_{\mathrm{opt}} + \hat{H}_{\mathrm{mech}} + \hat{H}_{\mathrm{int}} + \hat{H}_{\mathrm{drive}}, \tag{3.94}$$

where the individual terms are given by

$$\hat{H}_{\mathrm{opt}} = \hbar\omega_{\mathrm{cav}} \left(\hat{a}^\dagger \hat{a} + \frac{1}{2} \right) \tag{3.95}$$

$$\hat{H}_{\mathrm{mech}} = \frac{1}{2m_{\mathrm{eff}}} \hat{p}^2 + \frac{m_{\mathrm{eff}} \omega_{\mathrm{m}}^2}{2} \hat{x}^2 = \hbar\omega_{\mathrm{m}} \left(\hat{b}^\dagger \hat{b} + \frac{1}{2} \right) \tag{3.96}$$

$$\hat{H}_{\mathrm{int}} = \hbar G \hat{x} \hat{a}^\dagger \hat{a} \tag{3.97}$$

$$\hat{H}_{\mathrm{drive}} = \hbar\sqrt{\kappa_{\mathrm{in}}} \left(\bar{s}_{\mathrm{in}} \hat{a}^\dagger \mathrm{e}^{-\mathrm{i}\omega_{\mathrm{L}} t} - \bar{s}_{\mathrm{in}}^* \hat{a} \mathrm{e}^{\mathrm{i}\omega_{\mathrm{L}} t} \right). \tag{3.98}$$

The optical and mechanical Hamiltonians should come as no big surprise – they are simply the harmonic oscillators we introduced already, albeit with $\hat{a}, \hat{a}^\dagger$ reserved for the optical field, and $\hat{b}, \hat{b}^\dagger$ for the mechanical oscillator. The interaction Hamilton follows the form introduced above; radiation pressure displaces the membrane, and thus the number of optical excitations must show up ($\hat{a}^\dagger \hat{a}$), and the

membrane position ($\hat{x}$) changes the optical resonance with the rate G. The drive term has mean photon flux $\bar{S}_{\text{in}}$, and couples in with a rate $\sqrt{\kappa_{\text{in}}}$, and we have explicitly written the time evolution of the optical drive field[26].

The interaction Hamiltonian may be re-written as

$$\hat{H}_{\text{int}} = \hbar G x_{\text{zpf}} \left(\hat{b}^\dagger + \hat{b}\right) \hat{a}^\dagger \hat{a} = \hbar g_0 \left(\hat{b}^\dagger + \hat{b}\right) \hat{a}^\dagger \hat{a}. \tag{3.99}$$

If the optical field inside the cavity is strong, it is often useful to separate the field into the mean field and the fluctuations around this value as[27]

$$\hat{a} \longrightarrow \alpha + \hat{a}. \tag{3.100}$$

giving us

$$\hat{H}_{\text{int}} = \hbar g_0 (\hat{b}^\dagger + \hat{b}) \left(\alpha^* + \hat{a}^\dagger\right) (\alpha + \hat{a}) \tag{3.101}$$

$$= \hbar g_0 (\hat{b}^\dagger + \hat{b}) \left(|\alpha|^2 + \alpha \hat{a}^\dagger + \alpha^* \hat{a}\right) \tag{3.102}$$

The first term is a constant shift of the mechanical equilibrium position, which we simply absorb into $\hat{x}$ (and since $\hat{x}$ changes, also the detuning, Δ). We have also dropped the term containing the product $\hat{a}^\dagger \hat{a}$, which is quadratic in the fluctuations, and thus small compared to the terms enhanced by α. Defining the *field enhanced coupling rate*[28]

$$g = g_0 |\alpha| = g_0 \sqrt{\langle \hat{n} \rangle}, \tag{3.103}$$

we arrive at the *linearized interaction Hamilton*,

$$\hat{H}_{\text{int}} = \hbar g \left(\hat{a} + \hat{a}^\dagger\right) \left(\hat{b}^\dagger + \hat{b}\right). \tag{3.104}$$

The phase choice above is that of *real* α, i. e., that we are referencing other phases to the phase of the intracavity field, which we pick to be real, without loss of generality. This is the standard choice for optomechanics; however, for hybrid systems, it is sometimes beneficial to use the input field as the phase reference. In that case, the intracavity alpha is *not* real, but rotated depending on the cavity detuning, as discussed in Section 3.6. This leads to a Hamiltonian of the form

$$\hat{H}_{\text{int}} = \hbar g \left(\hat{a} e^{-i\phi} + \hat{a}^\dagger e^{i\phi}\right) \left(\hat{b}^\dagger + \hat{b}\right). \tag{3.105}$$

The drive, or input, term describes an input field, denoted $\bar{s}_{\text{in}}$ to denote 1) that it is a classical field, and 2) to differentiate propagating fields, which have dimension of flux (square root of photons per time), from localized fields, which count a number of photons. The linearization performed above gets rid of the mean cavity occupation, so for large fields, $\hat{H}_{\text{drive}}$ is often found only implicitly in the field enhanced coupling rate, g. For other scenarios, for example when driving the optomechanics with a modulated light beam, the fluctuating part of $\bar{s}_{\text{in}}$ reappears in our equations, although sometimes with the classical part suppressed as before. Later, we will also encounter this term where it is labeled $\hat{a}$, and the fact that it is a propagating field must be inferred from the subscripts instead.

(26) The drive term is often seen with a prefactor of i, owing to a different convention for the cavity input/output relations.

(27) The fluctuations are sometimes introduced as $\delta\hat{a}$, and then later renamed back to $\hat{a}$. Here we take the full step straight away.

(28) A word of caution: this definition is the *standard* definition used in the field of optomechanics. Later, we will encounter a redefined version of g.

To get rid of the terms evolving at optical frequencies, we transform to a frame rotating at the frequency of the optical drive laser. With the detuning $\Delta = \omega_L - \omega_{cav}$, the needed transformation is (W. Bowen and Milburn 2015, chapter 1)

$$\hat{H} \to \hat{U}^\dagger \hat{H} \hat{U} - \hat{T}, \quad \text{where } \hat{T} = \hbar\omega_L \hat{a}^\dagger \hat{a} \text{ and } \hat{U} = e^{-i\hat{T}t/\hbar}. \tag{3.106}$$

In the end, we obtain a total Hamiltonian

$$\hat{H}/\hbar = -\Delta \hat{a}^\dagger \hat{a} + \omega_m \hat{b}^\dagger \hat{b} + g\left(\hat{a}^\dagger + \hat{a}\right)\left(\hat{b}^\dagger + \hat{b}\right) + \sqrt{\kappa_{in}}\left(\bar{s}_{in}\hat{a}^\dagger - \bar{s}_{in}^*\hat{a}\right), \tag{3.107}$$

where we have also dropped the zero point energies.

A note on the field operators: after transformation to the rotating frame, they are defined in terms of the quantum amplitudes

$$\hat{a}(t) = \frac{1}{2\pi}\int_{-\infty}^{\infty} d\Omega\, e^{-i\Omega t}\hat{a}(\Omega) \qquad \hat{a}^\dagger(t) = \frac{1}{2\pi}\int_{-\infty}^{\infty} d\Omega\, e^{+i\Omega t}\hat{a}^\dagger(\Omega), \tag{3.108}$$

where $\hat{a}$ is the field in a rotating frame with respect to the relevant optical carrier frequency, ω_L, so that $\hat{a}(\Omega)$ represents the field at absolute frequency $\Omega + \omega_{laser}$. This expression is valid for Fourier frequencies close to the optical carrier, $|\Omega| \ll \omega_{laser}$.

3.7.2 Heisenberg–Langevin Formalism

Armed with the Hamiltonian describing the interaction and systems, we are ready to introduce dissipation in our quantum mechanical description. The approach is that of the Heisenberg–Langevin formalism[29]; a deeper exposition of this formalism may be found in Gardiner and P. Zoller (2000, chapter 3)[30], or for our case the more relevant formulation found in W. Bowen and Milburn (2015, section 1.4).

(29) With the obvious other approach being that of the Master equation approach.

(30) C. W. Gardiner and P. Zoller (2000). *Quantum Noise*. 2nd edition. Springer-Verlag.

For a general system operator $\hat{A}$, the time evolution in the Heisenberg picture is given by

$$\dot{\hat{A}} = \frac{i}{\hbar}\left[\hat{H}, \hat{A}\right]. \tag{3.109}$$

Now, if the total Hamiltonian contains a coupling term to a thermal bath (of harmonic oscillators, index by j), this coupling term will contribute to the time evolution of the system operators. If the bath interacts with the system through the position degree of freedom, we may write

$$\hat{H}_{sys-bath} = \sum_j \left[\frac{\hat{p}_j}{2m_j} + \frac{k_j}{2}\left(\hat{x}_j - \hat{x}\right)^2\right]. \tag{3.110}$$

This coupling to a large number of oscillators turns out to lead to exactly the kind of fluctuating zero mean force described in Section 3.3. Mathematically, the noise operator takes the form

$$\hat{f}(t) = \sum_j k_j \hat{q}_j^h(t), \tag{3.111}$$

where $\hat{q}_j^h = \hat{q}_j(0)\cos(\omega_j t) + \frac{\hat{p}_j(0)}{\omega_j m_j}\sin(\omega_j t)$. If the initial displacements and momenta are random and of zero mean, it is easy to convince oneself that $\hat{f}$ is zero

mean also; that the large number of independent oscillators lead to a fluctuating, seemingly stochastic, signal also seems intuitively appealing.

The mathematical definition of the noise operator, $\hat{f}$, is not very easy to use in practice; instead, the statistical properties, expressed through the PSD can be found as

$$\begin{aligned} S_{f,f}(\Omega) &= 2m\gamma\hbar\Omega\big(\bar{n}(\Omega)+1\big) \\ S_{f,f}(-\Omega) &= 2m\gamma\hbar\Omega\ \ \bar{n}(\Omega), \end{aligned} \tag{3.112}$$

where we have already made the *first Markovian approximation* $\gamma(t) = \gamma\delta(t)$, or equivalently $\gamma(\Omega) = \gamma$, and where

$$\bar{n}(\Omega) = \frac{1}{e^{\hbar\Omega/K_B T} - 1}. \tag{3.113}$$

We may also define the *symmetrized* PSD as

$$\bar{S}_{f,f} = \frac{S_{f,f}(\Omega) + S_{f,f}(-\Omega)}{2} = m\gamma(\Omega)\hbar\Omega(2\bar{n}+1). \tag{3.114}$$

After a set of lengthy derivations, the *Markov quantum Langevin equation* can be found as

$$\dot{\hat{A}} = \frac{i}{\hbar}\left[\hat{H}_{sys}, \hat{A}\right] - \frac{1}{i\hbar}\left[\hat{A}, \hat{x}\right]\hat{f}(t) + \frac{m_{eff}}{2i\hbar}\left\{\left[\hat{A}, \hat{x}\right], \gamma\dot{\hat{x}}(t)\right\}, \tag{3.115}$$

where $\{A, B\} = AB + BA$ is the *anti-commutator*. As we will often work with dimensionless quantities, $\hat{X}, \hat{P}$, it is useful to express Eq. (3.115) in terms of $\hat{X}$ instead of $\hat{x}$. This leads to a rescaled noise operator

$$\hat{P}_{in}(t) = \frac{x_{zpf}\hat{f}(t)}{\hbar\sqrt{\gamma}}, \tag{3.116}$$

and the total equation taking the form

$$\dot{\hat{A}} = \frac{i}{\hbar}\left[\hat{H}_{sys}, \hat{A}\right] + i\sqrt{2\gamma}\left[\hat{A}, \hat{X}\right]\hat{P}_{in}(t) + \frac{1}{2iQ}\left\{\left[\hat{A}, \hat{X}\right], \dot{\hat{X}}\right\}. \tag{3.117}$$

We notice here, that the last term is suppressed by the oscillator Q, and so will be repressed for most practical purposes in our experiment.

The equation looks unwieldy, but may be tackled by first finding $\dot{\hat{X}}$. We use the Hamiltonian Eq. (3.107) and ignore the optical parts for now. Since an operator commutes with itself, the two last terms of Eq. (3.117) vanish, and we are left with

$$\dot{\hat{X}} = \frac{i}{\hbar}\left[\hat{H}_{sys}, \hat{X}\right] = \frac{i}{\hbar}\left[\hbar\omega_m\hat{b}^\dagger\hat{b}, \hat{X}\right], \tag{3.118}$$

which by recalling the definition of $\hat{X}$ and $\hat{P}$ as well as the commutator relation $[\hat{b}, \hat{b}^\dagger] = 1$, can be easily evaluated to

$$\dot{\hat{X}} = \omega_m\hat{P}. \tag{3.119}$$

Once $\dot{\hat{X}}$ is known, one then similarly finds

$$\dot{\hat{P}} = -\omega_m\hat{X} - \gamma\hat{P} + \sqrt{2\gamma}\hat{P}_{in}. \tag{3.120}$$

These equations take exactly the form one would expect from the classical description. The two variables rotate into one another at the frequency ω_m. In the momentum variable, we find the decay term, proportional to the momentum itself, as well as a noise operator term, responsible for the thermal perturbations.

As a final note, one sometimes encounters the quantum Langevin equation in the rotating wave approximation, where non-energy conserving terms have been neglected, by inserting the ladder operators forms of $\hat{x}$ and $\hat{x}_j$ into Eq. (3.110) and neglecting quickly oscillating terms such as $\hat{b}^\dagger_{(j)}\hat{b}^\dagger_{(j)}$ and $\hat{b}_{(j)}\hat{b}_{(j)}$. Here, the Langevin equation takes the form

$$\dot{\hat{A}} = \frac{\mathrm{i}}{\hbar}\left[\hat{H}_\mathrm{sys}, \hat{A}\right] - \left[\hat{A}, \hat{b}^\dagger\right]\left(\frac{\gamma}{2}\hat{b} - \sqrt{\gamma}\hat{\ell}(t)\right) + \left(\frac{\gamma}{2}\hat{a}^\dagger - \sqrt{\gamma}\hat{\ell}^\dagger(t)\right)\left[\hat{A}, \hat{b}\right], \tag{3.121}$$

where the noise operator now has the following properties

$$\left[\hat{b}_\mathrm{in}(t), \hat{b}^\dagger_\mathrm{in}(t')\right] = \delta(t-t') \tag{3.122}$$

$$\left[\hat{b}_\mathrm{in}(t), \hat{b}_\mathrm{in}(t')\right] = \left[\hat{b}^\dagger_\mathrm{in}(t), \hat{b}^\dagger_\mathrm{in}(t')\right] = 0 \tag{3.123}$$

$$\left\langle \hat{b}^\dagger_\mathrm{in}(t)\hat{b}_\mathrm{in}(t')\right\rangle = \quad \bar{n}\delta(t-t') \tag{3.124}$$

$$\left\langle \hat{b}_\mathrm{in}(t)\hat{b}^\dagger_\mathrm{in}(t')\right\rangle = (\bar{n}+1)\delta(t-t'). \tag{3.125}$$

The rotating wave approximation "smears out" the bath interaction over the entire oscillation, leading to the appearance of decay and noise operators also in the position operator.

3.7.3 Input–output Formalism

The effective interaction Hamilton above, Eq. (3.107), describes the intracavity field, the optomechanics and their interaction. The interaction term couples the amplitude quadrature of the light, $\hat{X}_\mathrm{L} \propto \hat{a}^\dagger + \hat{a}$, to the membrane position $\hat{X}_\mathrm{m} \propto \hat{b}^\dagger + \hat{b}$. However, we have no access to the intracavity field, only what leaks out of the cavity, and this depends on the cavity parameters.

Fig. 3.15 displays the effect of a cavity on resonance and detuned by some amount $\pm\Delta$. We consider the effect a vibrating membrane has on the intracavity field. On resonance, the cavity light field phase is modulated by the dispersive shift induced by membrane motion, while the amplitude is not changed to first order. For a detuning $\pm\Delta$, the phase modulation is reduced, because the slope of the phase response is lower, and a direct amplitude modulation of the field appears. Note that the phase responses are in phase, while the amplitude responses are out of phase, for the different detunings.

The trick now appears: by virtue of time reversal symmetry, we may infer that for a detuned cavity the membrane motion couples to *both* amplitude and phase noise of the beam outside of the cavity.

This motivates a rotation of the intracavity field operators[31] by $\psi_\mathrm{in} = \arctan(2\Delta/\kappa)$, leading to a Hamilton of the form

$$\hat{H}/\hbar = \frac{\omega_\mathrm{m}}{2}\left(\hat{X}^2_\mathrm{m} + \hat{P}^2_\mathrm{m}\right) - \Delta\left(\hat{X}^{\mathrm{cav}\,2}_{\mathrm{L,m}} + \hat{P}^{\mathrm{cav}\,2}_{\mathrm{L,m}}\right) - 4g\left(\hat{X}^\mathrm{cav}_{\mathrm{L,m}}\cos\psi_\mathrm{in} + \hat{P}^\mathrm{cav}_{\mathrm{L,m}}\sin\psi_\mathrm{in}\right)\hat{X}_\mathrm{m}, \tag{3.126}$$

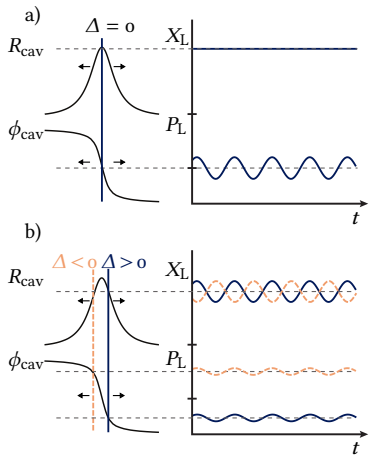

Figure 3.15: Cavity rotations. On resonance (a), the membrane motion modulates the intracavity field phase. For finite detuning $\pm\Delta$ (b), the membrane motion modulates the optical phase *and* amplitude. By time reversal, we may infer that the membrane couples to both amplitude and phase noise of light impinging on the cavity. Figure reproduced from Rodrigo A. Thomas (2020).

(31) Alternatively, this can be thought of as a change of the phase reference for the intracavity field with respect to the input field, so $\hat{a} \to \hat{a}e^{-\mathrm{i}\psi_\mathrm{in}}$.

where the factor of 4 comes in part (a factor $2\sqrt{2}$) from the change to quadrature operators instead of ladder operators, with the light quadrature operators

$$\begin{aligned}\hat{X}_{\mathrm{L}} &= \frac{\hat{a}+\hat{a}^{\dagger}}{2}\\ \hat{P}_{\mathrm{L}} &= \frac{\hat{a}-\hat{a}^{\dagger}}{2\mathrm{i}},\end{aligned} \tag{3.127}$$

which should be contrasted with Eq. (3.60), where the light operators carry an extra factor $1/\sqrt{2}$. The remaining factor $\sqrt{2}$, by virtue of elimination, arises from a redefinition of $g \to g/\sqrt{2}$. This non-standard choice is used in our work Rodrigo A. Thomas et al. (2020), and I preserve it here for consistency between the letter and this thesis. Further, the definitions of the light operators above enforces a commutator $[\hat{X}_{\mathrm{L}}, \hat{P}_{\mathrm{L}}] = \mathrm{i}/2$, in contrast to the mechanical quadratures, for which $[\hat{X}_{\mathrm{m}}, \hat{P}_{\mathrm{m}}] = \mathrm{i}$. We have also introduced the subscripts $\langle\cdot\rangle_{\mathrm{L,m}}$, which will become relevant with the introduction of the spins in Chapter 5 – here we will need to label, for example, the optical operators at the spin systems with $\langle\cdot\rangle_{\mathrm{L,s}}$.

In the rest of this section, I will follow the notation and derivations found in our paper Rodrigo A. Thomas et al. (2020) and its Supplementary Information. Here we find that the rotation of the optical quadratures with the Heisenberg–Langevin equations and the Hamiltonian above leads to a set of equations of motions, which in the frequency domain and steady state regime become

$$\begin{pmatrix} \kappa/2 - \mathrm{i}\Omega & \Delta & 2g\sin\psi_{\mathrm{in}} \\ -\Delta & \kappa/2 - \mathrm{i}\Omega & -2g\cos\psi_{\mathrm{in}} \\ -4g\cos\psi_{\mathrm{in}} & -4g\sin\psi_{\mathrm{in}} & \chi_{\mathrm{moo}}^{-1} \end{pmatrix} \begin{pmatrix} \hat{X}_{\mathrm{L,m}}^{\mathrm{cav}} \\ \hat{P}_{\mathrm{L,m}}^{\mathrm{cav}} \\ \hat{X}_{\mathrm{m}} \end{pmatrix} = \begin{pmatrix} \sqrt{\kappa_{\mathrm{in}}}\hat{X}_{\mathrm{L,m}}^{\mathrm{in}} + \sqrt{\kappa_{\mathrm{ex}}}\hat{X}_{\mathrm{L,m}}^{\mathrm{ex}} \\ \sqrt{\kappa_{\mathrm{in}}}\hat{P}_{\mathrm{L,m}}^{\mathrm{in}} + \sqrt{\kappa_{\mathrm{ex}}}\hat{P}_{\mathrm{L,m}}^{\mathrm{ex}} \\ \hat{f}_{\mathrm{m}} \end{pmatrix}, \tag{3.128}$$

(32) Usually pronounced "chi-moo".

where $\chi_{\mathrm{moo}}^{-1} \equiv (\omega_{\mathrm{mo}}^2 - \Omega^2 - i\Omega\gamma_{\mathrm{mo}})/\omega_{\mathrm{mo}}$[32] is the bare susceptibility for the dimensionless position (without optical spring and broadening effects, introduced in the following section).

The optical noise operators are respectively related to the input light field, which couples into the cavity at rate $\sqrt{\kappa_{\mathrm{in}}}$, and the noise related to light coupling out of the second cavity mirror as well as intracavity losses, with a total rate of $\kappa_{\mathrm{ex}} = \kappa_{\mathrm{ex}}^{\mathrm{HR}} + \kappa_{\mathrm{ex}}^{\mathrm{loss}}$.

Absent from these equations is $\hat{P}_{\mathrm{m}}$; this variable is eliminated with the Fourier-domain Heisenberg–Langevin equation for $\hat{X}_{\mathrm{m}}$,

$$-\mathrm{i}\Omega\hat{X}_{\mathrm{m}} = \omega_{\mathrm{mo}}\hat{P}_{\mathrm{m}}. \tag{3.129}$$

The solution for $\hat{P}_{\mathrm{m}}$ can thus be inserted, which leads to decay (contained in χ_{m}) and the noise operator $\hat{f}_{\mathrm{m}}$ showing up in the position variable. The momentum variable can be found via Eq. (3.129), but we do not need to explicitly carry it throughout the calculations.

These equations of motion may be written in a more compact form, which we shall use to a high degree throughout the rest of the thesis. We define certain

submatrices of Eq. (3.128) as the matrices

$$\begin{aligned} \boldsymbol{A} &= \begin{pmatrix} \kappa/2 - i\Omega & \Delta \\ -\Delta & \kappa/2 - i\Omega \end{pmatrix} \qquad \boldsymbol{B} = \begin{pmatrix} 0 \\ -2g \end{pmatrix} \\ \boldsymbol{C} &= \begin{pmatrix} -4g & 0 \end{pmatrix} \qquad\qquad \hat{\boldsymbol{X}}^{j}_{\mathrm{L,m}} = \begin{pmatrix} \hat{X}^{j}_{\mathrm{L,m}} \\ \hat{P}^{j}_{\mathrm{L,m}} \end{pmatrix}, \end{aligned} \tag{3.130}$$

with $j \in \{\mathrm{cav}, \mathrm{in}, \mathrm{ex}\}$ labeling the different optical fields. Further, defining a general 2D rotation matrix

$$\boldsymbol{O}_{\alpha} = \begin{pmatrix} \cos\alpha & -\sin\alpha \\ \sin\alpha & \cos\alpha \end{pmatrix} \tag{3.131}$$

we also define $\boldsymbol{O}_{\psi_{\mathrm{in}}}$ for the input cavity rotation.

Noting that the cavity response matrix $\boldsymbol{A}$ is invariant under quadrature rotations, $\boldsymbol{O}_{\psi}\boldsymbol{A}\boldsymbol{O}_{\psi}^{\mathsf{T}} = \boldsymbol{A}$, we find the intracavity field and the mechanical variable as a function of the input fluctuations and thermal bath

$$\hat{\boldsymbol{X}}^{\mathrm{cav}}_{\mathrm{L,m}} = \boldsymbol{A}^{-1}\left(\sqrt{\kappa_{\mathrm{in}}}\hat{\boldsymbol{X}}^{\mathrm{in}}_{\mathrm{L,m}} + \sqrt{\kappa_{\mathrm{ex}}}\hat{\boldsymbol{X}}^{\mathrm{ex}}_{\mathrm{L,m}}\right) - \boldsymbol{A}^{-1}\boldsymbol{O}_{\psi_{\mathrm{in}}}\boldsymbol{B}\hat{X}_{\mathrm{m}}, \tag{3.132}$$

$$\hat{X}_{\mathrm{m}} = \chi_{\mathrm{m}}\left[-\boldsymbol{C}\boldsymbol{A}^{-1}\boldsymbol{O}^{\mathsf{T}}_{\psi_{\mathrm{in}}}\left(\sqrt{\kappa_{\mathrm{in}}}\hat{\boldsymbol{X}}^{\mathrm{in}}_{\mathrm{L,m}} + \sqrt{\kappa_{\mathrm{ex}}}\hat{\boldsymbol{X}}^{\mathrm{ex}}_{\mathrm{L,m}}\right) + \hat{f}_{\mathrm{m}}\right], \tag{3.133}$$

in which $\chi_{\mathrm{m}} = (\chi^{-1}_{\mathrm{moo}} - \boldsymbol{C}\boldsymbol{A}^{-1}\boldsymbol{B})^{-1}$ is the effective mechanical susceptibility in the presence of optomechanical coupling,

$$\chi_{\mathrm{m}} = \frac{\omega_{\mathrm{mo}}}{(\omega^2_{\mathrm{m}} + 2\Omega\delta\omega_{\mathrm{m}} - \Omega^2 - \mathrm{i}\Omega\gamma_{\mathrm{m}})} \tag{3.134}$$

where the modified resonance frequency, $\omega_{\mathrm{m}} = \omega_{\mathrm{mo}} + \delta\omega_{\mathrm{m}}$, and line width, $\gamma_{\mathrm{m}} = \gamma_{\mathrm{mo}} + \delta\gamma_{\mathrm{m}}$ are changed as

$$\delta\omega_{\mathrm{m}(\Omega)} = \frac{4g^2\omega_{\mathrm{m}}}{\kappa\Omega}\left[\frac{(\Delta+\Omega)\kappa/2}{(\Delta+\Omega)^2 + (\kappa/2)^2} + \frac{(\Delta-\Omega)\kappa/2}{(\Delta-\Omega)^2 + (\kappa/2)^2}\right] \tag{3.135}$$

$$\delta\gamma_{\mathrm{m}}(\Omega) = \frac{8g^2\omega_{\mathrm{m}}}{\kappa\Omega}\left[\frac{(\kappa/2)^2}{(\Delta+\Omega)^2 + (\kappa/2)^2} - \frac{(\kappa/2)^2}{(\Delta+\Omega)^2 + (\kappa/2)^2}\right], \tag{3.136}$$

which are called respectively the *optical spring shift* and *optical damping rate*[33]. The optical spring and damping are plotted in Fig. 3.16, for an experimentally relevant set of paramters. We see that the optical spring shift is on the order of a couple of kilohertz; compared to our bare mechanical frequencies of $\omega_{\mathrm{m}}/2\pi \sim 1.4\,\mathrm{MHz}$, this is a small effect. The optical damping rate also easily reaches several kilohertz, but comparing that of the intrinsic damping rate of $\gamma_{\mathrm{mo}} \sim 2\,\mathrm{mHz}$ this effect very quickly dominates other decay terms.

(33) For $\Delta > 0$ the rate can be negative, i. e., anti-damping. For practical reason the, by far, most often encountered situation is that of $\Delta < 0$, for which the optics dampen the mechanics.

The optical cooling may be understood by considering the picture in Fig. 3.17. For two different ratios of the cavity line width, κ, to the mechanical frequency, ω_{m}, we depicted the cavity envelope in blue. Detuned from the cavity resonance, is a carrier at ω_{L}. The optomechanical interaction supports processes that scatter photons out of the carrier, to higher (anti-Stokes, $\omega_{\mathrm{L}} + \omega_{\mathrm{m}}$) and lower (Stokes, $\omega_{\mathrm{L}} - \omega_{\mathrm{m}}$) frequencies by the simultaneous annihilation and creation of a phonon in the mechanics, plus the inverse processes (creation of carrier photon plus creation/annihilation of phonon). If the cavity is *narrow* ($\kappa \ll \omega_{\mathrm{m}}$), the cavity is said

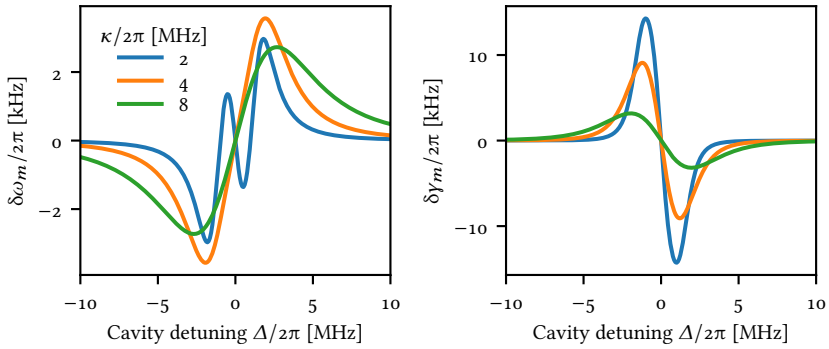

Figure 3.16: Optical spring, $\delta\omega_\mathrm{m}$, (left) and damping, $\delta\gamma_\mathrm{m}$, (right) for different cavity widths. Other parameters: $\omega_\mathrm{mo}/2\pi = 1.4\,\mathrm{MHz}$, $g/2\pi = 100\,\mathrm{kHz}$.

to be *resolved*, and one scattering process is enhanced by the cavity response. If the cavity is *wide* ($\kappa \gg \omega_\mathrm{m}$), it is *unresolved*, and the two different processes happen with almost identical rates. Since the process that destroys phonons removes energy from the mechanical system, the oscillator is cooled by the interaction with light. For blue detuning, the process is reversed, and the membrane is heated. Once the total line width $\gamma_\mathrm{mo} + \delta\gamma_\mathrm{m}$ crosses o, the mechanical motion is parametrically amplified, and grows exponentially, quickly leading to a runaway process.

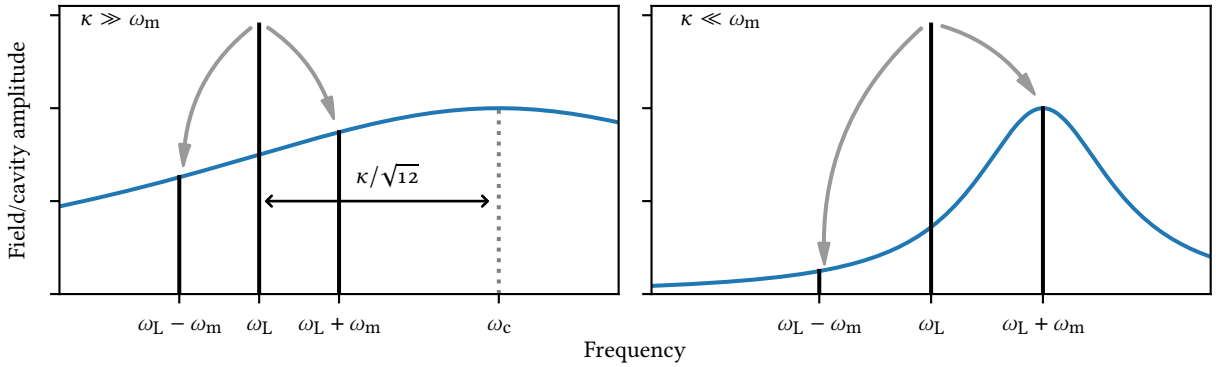

Figure 3.17: Sideband resolution in the unresolved (left) and resolved (right) regime. In the unresolved case, the cavity enhancement of scattering to the Stokes and anti-Stokes sidebands are almost the same. Placing the carrier at the steepest point of the cavity envelope, at $\Delta = \mp\kappa/\sqrt{12}$, maximizes the asymmetry. For the resolved case, the asymmetry of scattering rates is maximized when $\Delta = \mp\omega_\mathrm{m}$. The sideband heights are not to scale with the carrier height.

Substituting Eq. (3.133) in Eq. (3.132) solves the system for the cavity field

$$\hat{X}^\mathrm{cav}_\mathrm{L,m} = \boldsymbol{O}_{\psi_\mathrm{in}} Y^{-1} \boldsymbol{O}^\intercal_{\psi_\mathrm{in}} \left(\sqrt{\kappa_\mathrm{in}}\hat{X}^\mathrm{in}_\mathrm{L,m} + \sqrt{\kappa_\mathrm{ex}}\hat{X}^\mathrm{ex}_\mathrm{L,m} \right) - \boldsymbol{O}_{\psi_\mathrm{in}} Y^{-1} \boldsymbol{B} \chi_\mathrm{moo} \hat{F}_\mathrm{m}, \tag{3.137}$$

where $Y = \boldsymbol{A} - \boldsymbol{B}\chi_\mathrm{moo}\boldsymbol{C}$ is the effective cavity response matrix in the presence of optomechanical coupling. The solution uses the *Schur complement* detailed in

Appendix E, for the 3×3 matrix in Eq. (3.128), and the definition of the sub-matrices in Eq. (3.130). This solution for the cavity field can also be used to express the mechanical response, Eq. (3.133), as

$$\hat{X}_{\mathrm{m}} = -\chi_{\mathrm{moo}} C Y^{-1} \boldsymbol{O}_{\psi_{\mathrm{in}}}^{\intercal} \left(\sqrt{\kappa_{\mathrm{in}}} \hat{\boldsymbol{X}}_{\mathrm{L,m}}^{\mathrm{in}} + \sqrt{\kappa_{\mathrm{ex}}} \hat{\boldsymbol{X}}_{\mathrm{L,m}}^{\mathrm{ex}} \right) + \chi_{\mathrm{m}} \hat{f}_{\mathrm{m}}. \tag{3.138}$$

Finally, the field leaking out of the cavity can be detected, and the mechanical motion inferred from this light. The phase of the outgoing classical carrier field with respect to the cavity field is given by $\psi_{\mathrm{out}} = \arctan(2\Delta/(\kappa_{\mathrm{in}} - \kappa_{\mathrm{ex}}))$. Overall, the total phase shift with respect to the input field is $\psi_{\mathrm{out}} + \psi_{\mathrm{in}}$. The cavity input-output relations, taking into account the acquired phase shift with respect to the input, from Eq. (3.137), is

$$\begin{aligned} \hat{\boldsymbol{X}}_{\mathrm{L,m}}^{\mathrm{out}} &= \boldsymbol{O}_{\psi_{\mathrm{in}}+\psi_{\mathrm{out}}}^{\intercal} (-\hat{\boldsymbol{X}}_{\mathrm{L,m}}^{\mathrm{in}} + \sqrt{\kappa_{\mathrm{in}}} \hat{\boldsymbol{X}}_{\mathrm{L,m}}^{\mathrm{cav}}) && (3.139) \\ &= \boldsymbol{O}_{\psi_{\mathrm{out}}}^{\intercal} (\kappa_{\mathrm{in}} Y^{-1} - \mathbb{1}_2) \boldsymbol{O}_{\psi_{\mathrm{in}}}^{\intercal} \hat{\boldsymbol{X}}_{\mathrm{L,m}}^{\mathrm{in}} + \sqrt{\kappa_{\mathrm{in}}\kappa_{\mathrm{ex}}} \boldsymbol{O}_{\psi_{\mathrm{out}}}^{\intercal} Y^{-1} \boldsymbol{O}_{\psi_{\mathrm{in}}}^{\intercal} \hat{\boldsymbol{X}}_{\mathrm{L,m}}^{\mathrm{ex}} \\ &\quad - \sqrt{\kappa_{\mathrm{in}}} \boldsymbol{O}_{\psi_{\mathrm{out}}}^{\intercal} Y^{-1} \boldsymbol{B} \chi_{\mathrm{moo}} \hat{f}_{\mathrm{m}}, && (3.140) \end{aligned}$$

where in the second line we have inserted the expression for the intracavity field from Eq. (3.137).

These equations, describing respectively the intracavity field, mechanical response and the output light are the full solutions, on which the final modelling of our system will be based. However, they are also somewhat unwieldy and not overly transparent – as often, however, a suitable set of simplifying assumptions can be made, which will serve to highlight the most crucial features of the scheme.

We note first that the cavity response matrix can be expressed in terms of the complex Lorentzian sideband amplitudes

$$\mathcal{L}(\Omega) \equiv \frac{(\kappa/2)}{\kappa/2 - \mathrm{i}(\Omega + \Delta)} \tag{3.141}$$

with phase $\Theta(\Omega) \equiv \mathrm{Arg}[\mathcal{L}(\Omega)]$, and where the dependence on Δ is suppressed for notational brevity. This allows us to write $\boldsymbol{A}^{-1}$ as

$$\begin{aligned} \boldsymbol{A}^{-1} &= \frac{1}{\kappa} \begin{pmatrix} \mathcal{L}(\Omega) + \mathcal{L}^*(-\Omega) & \mathrm{i}[\mathcal{L}(\Omega) - \mathcal{L}^*(-\Omega)] \\ -\mathrm{i}[\mathcal{L}(\Omega) - \mathcal{L}^*(-\Omega)] & \mathcal{L}(\Omega) + \mathcal{L}^*(-\Omega) \end{pmatrix} && (3.142) \\ &= \frac{|\mathcal{L}(\Omega)|+|\mathcal{L}(-\Omega)|}{\kappa} \mathrm{e}^{\mathrm{i}[\Theta(\Omega)-\Theta(-\Omega)]/2} \boldsymbol{O}_{[\Theta(\Omega)+\Theta(-\Omega)]/2} \left[\mathbb{1}_2 + \mathrm{i} \frac{|\mathcal{L}(\Omega)|-|\mathcal{L}(-\Omega)|}{|\mathcal{L}(\Omega)|+|\mathcal{L}(-\Omega)|} \boldsymbol{O}_{-\pi/2} \right]. && (3.143) \end{aligned}$$

If the response of the cavity, $\mathcal{L}(\Omega)$, is sufficiently flat over the relevant frequency band, we can substitute the response evaluated at the mechanical frequency, $\mathcal{L}(\pm\Omega) \approx \mathcal{L}(\pm\omega_{\mathrm{m}})$, which also fixes $\Theta(\pm\Omega) \approx \Theta(\pm\omega_{\mathrm{m}})$. This motivates the rotation of input light quadratures as

$$\boldsymbol{X}_{\mathrm{L,m}}^{\mathrm{in(ex)}\prime} \equiv \mathrm{e}^{\mathrm{i}[\Theta(\omega_{\mathrm{m}})-\Theta(-\omega_{\mathrm{m}})]/2} \boldsymbol{O}_{[\Theta(\omega_{\mathrm{m}})+\Theta(-\omega_{\mathrm{m}})]/2} \boldsymbol{O}_{\psi_{\mathrm{in}}}^{\intercal} \boldsymbol{X}_{\mathrm{L,m}}^{\mathrm{in(ex)}}, \tag{3.144}$$

which, using Eqs. (3.143) and (3.144) to reexpress the light (QBA) force on the mechanical mode (i.e., Eq. (3.133), 1st term in square brackets), we find

$$-C\boldsymbol{A}^{-1} \boldsymbol{O}_{\psi_{\mathrm{in}}}^{\intercal} \left(\sqrt{\kappa_{\mathrm{in}}} \hat{\boldsymbol{X}}_{\mathrm{L,m}}^{\mathrm{in}} + \sqrt{\kappa_{\mathrm{ex}}} \hat{\boldsymbol{X}}_{\mathrm{L,m}}^{\mathrm{ex}} \right) \approx 2\sqrt{\Gamma_{\mathrm{m}}} \begin{pmatrix} 1 \\ \mathrm{i}\zeta_{\mathrm{m}} \end{pmatrix}^{\intercal} \left(\sqrt{\kappa_{\mathrm{in}}/\kappa} \hat{\boldsymbol{X}}_{\mathrm{L,m}}^{\mathrm{in}\prime} + \sqrt{\kappa_{\mathrm{ex}}/\kappa} \hat{\boldsymbol{X}}_{\mathrm{L,m}}^{\mathrm{ex}\prime} \right),$$

(3.145)

where we have introduced the mechanical readout rate and sideband asymmetry parameter,

$$\Gamma_\mathrm{m} \equiv \frac{4g^2}{\kappa}(|\mathcal{L}(\omega_\mathrm{m})| + |\mathcal{L}(-\omega_\mathrm{m})|)^2, \quad \zeta_\mathrm{m} \equiv \frac{|\mathcal{L}(\omega_\mathrm{m})| - |\mathcal{L}(-\omega_\mathrm{m})|}{|\mathcal{L}(\omega_\mathrm{m})| + |\mathcal{L}(-\omega_\mathrm{m})|}, \tag{3.146}$$

respectively, remembering that $\mathcal{L}$ depends on Δ. The readout rate and sideband asymmetry are plotted in Fig. 3.18. For narrow cavities, we see that the sideband asymmetry is high, and maximized for $\Delta = \omega_\mathrm{m}$, while for wider cavities the point of maximum ζ_m moves to larger detunings, in line with the heuristical description above. We also see that the readout rate has some interesting features. For low κ, the shape has three local maxima, at $\Delta \in \{\pm\omega_\mathrm{m}, 0\}$, while for large κ the shape is smooth. Further, evidently the maximally achievable readout rate for fixed g has a maximum for intermediate κ; as a function of growing κ, for fixed Δ, Γ_m first grows and then falls off again.

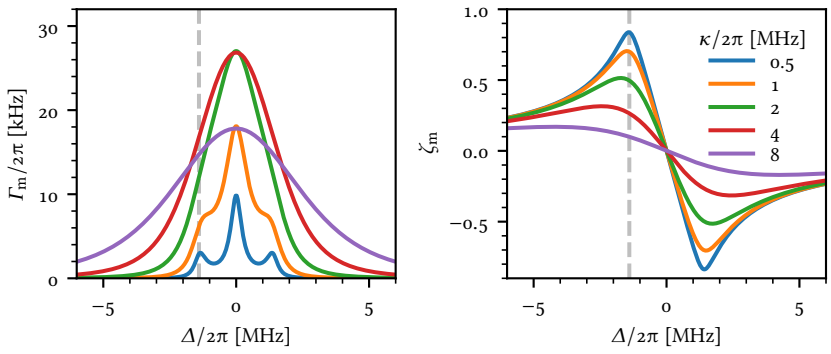

Figure 3.18: Optical readout rate, Γ_m, (left) and sideband asymmetry, ζ_m, (right) for varied κ. $g/2\pi = 100\,\mathrm{kHz}$, $\omega_\mathrm{m} = 1.4\,\mathrm{MHz}$. Vertical dashed lines indicate $\Delta = -\omega_\mathrm{m}$.

Returning to the equations above, we make the final approximation, and ignore the finite overcoupling by setting $\kappa_\mathrm{in} = \kappa$, i. e., ignoring losses and outcoupling through the high reflector mirror. Inserting this approximation into Eq. (3.145) we arrive at the final, simplified response of $\hat{X}_\mathrm{m}$.

$$\hat{X}_\mathrm{m} = \chi_\mathrm{m}[\hat{f}_\mathrm{m} + 2\sqrt{\Gamma_\mathrm{m}}(\hat{X}^\mathrm{in}_\mathrm{L,m} + \mathrm{i}\zeta_\mathrm{m}\hat{P}^\mathrm{in}_\mathrm{L,m})], \tag{3.147}$$

where we now have for the effective, Fourier-domain susceptibility

$$\chi_\mathrm{m}(\Omega) = \frac{\omega_\mathrm{mo}}{(\omega_\mathrm{m}^2 - \Omega^2 - \mathrm{i}\Omega\gamma_\mathrm{m})} \tag{3.148}$$

with dynamical broadening/damping $\delta\gamma_\mathrm{m} \equiv \gamma_\mathrm{m} - \gamma_\mathrm{mo} = 2\zeta_\mathrm{m}\Gamma_\mathrm{m}$, parametrized by ζ_m and Γ_m.

Noting that $-\mathbb{1}_2 + \kappa\boldsymbol{A}^{-1} = \mathrm{e}^{\mathrm{i}[\Theta(\omega_\mathrm{m})-\Theta(-\omega_\mathrm{m})]}\boldsymbol{O}_{\Theta(\omega_\mathrm{m})+\Theta(-\omega_\mathrm{m})}$, we find in this limit that the rotated output quadrature

$$\boldsymbol{X}^{\mathrm{out}\prime}_\mathrm{L,m} \equiv \mathrm{e}^{-\mathrm{i}[\Theta(\omega_\mathrm{m})-\Theta(-\omega_\mathrm{m})]/2}\boldsymbol{O}^\mathsf{T}_{[\Theta(\omega_\mathrm{m})+\Theta(-\omega_\mathrm{m})]/2}\boldsymbol{O}^\mathsf{T}_{\psi_\mathrm{in}}\boldsymbol{X}^\mathrm{out}_\mathrm{L,m}, \tag{3.149}$$

obeys

$$X^{\mathrm{out}\prime}_{\mathrm{L,m}} = X^{\mathrm{in}\prime}_{\mathrm{L,m}} + \sqrt{\Gamma_{\mathrm{m}}} \begin{pmatrix} \mathrm{i}\zeta_{\mathrm{m}} \\ 1 \end{pmatrix} \hat{X}_{\mathrm{m}}, \tag{3.150}$$

as follows from $\hat{X}^{\mathrm{out}}_{\mathrm{L,m}} = -\hat{X}^{\mathrm{in}}_{\mathrm{L,m}} + \sqrt{\kappa_{\mathrm{in}}}\hat{X}^{\mathrm{cav}}_{\mathrm{L,m}}$ combined with Eq. (3.132), again assuming $\kappa_{\mathrm{in}} = \kappa$.

This concludes the derivation of the main equations governing the mechanical system and its interaction with light. We will meet these equations again in the following sections, as well as in Chapter 10, and a similar set of relations for the spin system in Chapter 5. For now, we turn our attention to mapping of our specific optomechanical setup, the membrane-in-the-middle concept, to the canonical optomechanical system described thus far.

3.8 Membrane-in-the-Middle (MIM) Optomechanics

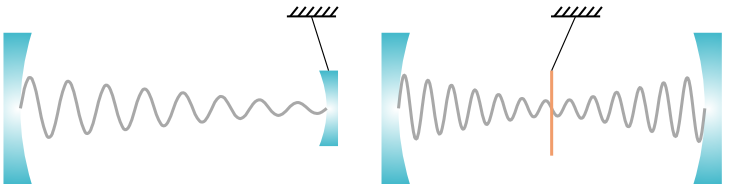

Figure 3.19: Canonical (left) and MIM optomechanical (right) systems. In the canonical setup, one end mirror is mechanically pliable. In a MIM setup a membrane is placed inside the standing wave of a resonator with (ideaelly) stationary mirrors.

In Fig. 3.19 a canonical optomechanical system and a membrane-in-the-middle (MIM) setup are displayed. In the canonical system, the mechanically compliant element is one of the end mirrors, forming the optical resonator; in the MIM setup, the mechanical element is placed within the optical mode of a "normal" Fabry–Perot resonator; the membrane dividies the cavity into two *subcavities*. This approach offers several distinct advantages, as well as some disadvantages. In this section, we will deal not so much with *why* one would be interested in MIM optomechanics, but in *how* to map such a system to the canonical model.

3.8.1 The Transfer Matrix Model (TMM)

The Transfer Matrix Model (TMM) is our daily workhorse for evaluating things like the effect of the membrane position in the standing wave of the unperturbed cavity (what we will later call "$2kz$ modulation"), g_0, cavity overcoupling η and so on. Introduced by Jayich et al. (2008)[34] and expanded in, e. g., Dalziel J. Wilson (2012)[35], it consists of a conceptually rather straightforward model, shown in Fig. 3.20. Two flat mirrors with field reflection and transmission coefficients (r_1, t_1)

(34) A M Jayich et al. (2008). "Dispersive optomechanics: a membrane inside a cavity". In: *New Journal of Physics* 10.9, p. 095008.

(35) Dalziel J. Wilson (2012). "Cavity Optomechanics with High-Stress Nitride Films". Ph.D. thesis. California Institute of Technology.

and (r_2, t_2) are placed L apart, with a dielectric membrane (with (r_m, t_m)) placed z away from one mirror.

The reflected and transmitted fields, as well as properties like the overcoupling in transmission and reflection, the ratio of powers in the two subcavities, etc., may then be numerically evaluated.

Although the model is very crude, ignoring all sorts of complicating factors such as non-flat mirrors, higher order modes, etc., it has proven extremely robust and accurate in describing a variety of different MIM optomechanical designs.

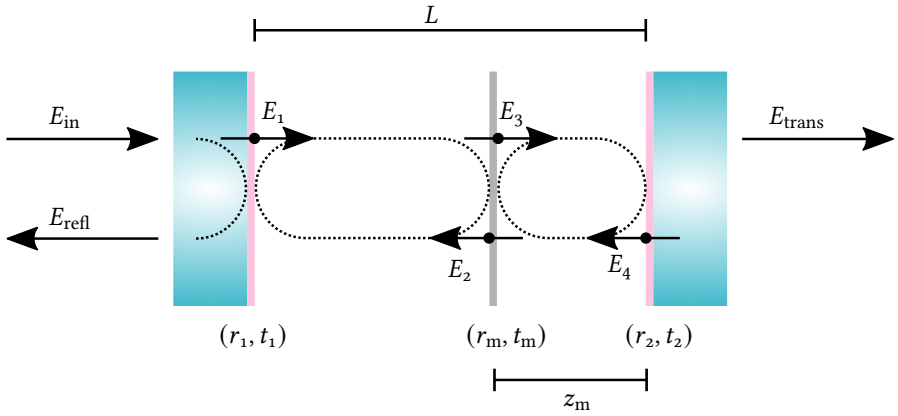

Figure 3.20: TMM concept. Two mirrors, placed L apart, and with field reflection and transmission coefficients (r_i, t_i) form a cavity, containing a dielectric membrane (r_m, t_m). By solving for E_{trans}, E_{refl} in terms of E_{in} for varying values of the membrane position z, we can calculate different properties of the optomechanical system.

The model starts by writing the relations connecting the electrical fields at different places, just like we did for the Fabry–Perot cavity in Section 3.6. This time, we use a different convention for the transmission and reflection coefficients than the one explained in footnote [20] on page 37. We do this to keep the notation in line with the one in Jayich et al. (2008), and reproduced in Nielsen (2016), Møller (2018) and so on. The transformation connecting the input and output fields must still be unitary, but by allowing the plane of reference for the phases of the optical fields to not co-incide, it is possible to obtain a notation that gets rid of the awkward minus-sign on one reflection. The trick is to let $t \to it$ and $r' = r$, such that the scattering matrix, $\mathbf{S}$, connecting the input fields to the output fields takes the form

$$\begin{pmatrix} E_{\text{refl},1} \\ E_{\text{refl},2} \end{pmatrix} = \begin{pmatrix} r & it \\ it & r \end{pmatrix} \begin{pmatrix} E_{\text{in},1} \\ E_{\text{in},2} \end{pmatrix} = \mathbf{S} \begin{pmatrix} E_{\text{in},1} \\ E_{\text{in},2} \end{pmatrix} \tag{3.151}$$

as opposed to

$$\begin{pmatrix} E_{\text{refl},1} \\ E_{\text{refl},2} \end{pmatrix} = \begin{pmatrix} r & t \\ t & -r \end{pmatrix} \begin{pmatrix} E_{\text{in},1} \\ E_{\text{in},2} \end{pmatrix}. \tag{3.152}$$

Verifying that both of these matrices are unitary (i. e., that $\mathbf{S}^\dagger \mathbf{S} = \mathbb{1}$) is easy, as long as $r^* t - r t^* = 2\Im(r^* t) = 0$[36]; hence, they both conserve energy. The convention used

(36) Which is true in particular for real r and t.

here, with it, has the virtue of being independent of which side the beam is coming from, but does introduce a slightly artificial shift of the phase reference point. A longer discussion of this phase convention may be found in Siegman (1986, chapter 11.1)[37].

(37) A.E. Siegman (1986). *Lasers*. University Science Books.

The set of equations we must solve is

$$\begin{aligned} E_1 &= \mathrm{i}t_1 E_{\mathrm{in}} &&+ r_1 E_2 \mathrm{e}^{\mathrm{i}k(L-z_{\mathrm{m}})} \\ E_2 &= \mathrm{i}t_m E_4 \mathrm{e}^{\mathrm{i}kz_{\mathrm{m}}} &&+ r_{\mathrm{m}} E_1 \mathrm{e}^{\mathrm{i}k(L-z_{\mathrm{m}})} \\ E_3 &= \mathrm{i}t_m E_1 \mathrm{e}^{\mathrm{i}k(L-z_{\mathrm{m}})} &&+ r_{\mathrm{m}} E_4 \mathrm{e}^{\mathrm{i}kz_{\mathrm{m}}} \\ E_4 &= &&\ r_2 E_3 \mathrm{e}^{\mathrm{i}kz_{\mathrm{m}}} \\ E_{\mathrm{refl}} &= \mathrm{i}t_1 E_2 \mathrm{e}^{\mathrm{i}k(L-z_{\mathrm{m}})} &&+ r_1 E_{\mathrm{in}} \\ E_{\mathrm{trans}} &= \mathrm{i}t_2 E_3 \mathrm{e}^{\mathrm{i}kz_{\mathrm{m}}}. \end{aligned} \tag{3.153}$$

The membrane transmission and reflection coefficients are covered in Section 4.1.3. These coefficients are not real, but do respect the condition $\Im(r * t) = 0$.

By setting $E_1 = 1$, the set of equations in Eq. (3.153) can be solved, yielding a set of analytically cumbersome expressions, which are however easily solved numerically for a given set of parameters $\{ t_1, r_1, t_2, r_2, t_{\mathrm{m}}, r_{\mathrm{m}}, L, z_{\mathrm{m}} \}$[38] for arbitrary optical wavenumber k.

(38) Or, for the membrane, equivalently refractive index n and thickness d.

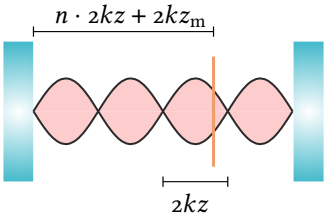

Figure 3.21: Membrane position in the cavity field, $2kz$. The field of the unperturbed cavity (red), has a node every $\lambda/2 = \pi/k$, and is therefore periodic in $2kz$. The membrane is positioned z_{m} into the nth bubble.

The MIM model can obviously be thought of as two coupled cavities, with the membrane acting as the coupling mirror. It should therefore come as no big surprise as the resonance condition of each subcavity matters, or in other words, that the system is sensitive to displacements of the membrane by distances smaller than half an optical wavelength, the distance between two nodes of a standing wave. The same conclusion can be drawn from imagining the membrane as a very transmissive element moving in the unperturbed standing wave of a cavity, as depicted in Fig. 3.21. In this picture, as the membrane is moved $\delta z_{\mathrm{m}} = \pi/k$ starting from a node, it moves from one node to the next, sampling an entire "bubble" of light. Since, $L, z_{\mathrm{m}} \gg \lambda$, this system is approximately periodic in $kz = \pi$, and not 2π like normal periodic functions, it is customary to work with the quantity $2kz$, which is then 2π-periodic.

For a lossless cavity ($r = 1$, n purely real), the resonance condition of the cavity is modfied by the membrane as

$$|r_{\mathrm{m}}| \cos(2k_{\mathrm{res}}\Delta z) = \cos(k_{\mathrm{res}}L + \phi), \tag{3.154}$$

where $\Delta z = z_{\mathrm{m}} - L/2$ denotes the membrane distance from the center of the cavity, and $\phi = \arg(r_{\mathrm{m}})$, and k_{res} is the resonant wavenumber. Neglecting the constant phase ϕ, and approximating the left hand side expression for k_{res} by the bare (unperturbed) wavenumber, $k_{\mathrm{o},n} = n\pi/L$, one arrives at an expression for the resonant wavenumbers

$$k_{\mathrm{res}} = \frac{1}{L} \cos^{-1}\left(|r_{\mathrm{m}}| \cos(2k_{\mathrm{o},n})\right) + k_{\mathrm{o},n} \tag{3.155}$$

$$\approx \frac{1}{L} |r_{\mathrm{m}}| \sin\left(2k_{\mathrm{o},n} z_{\mathrm{m}}\right) + k_{\mathrm{o},n}. \tag{3.156}$$

In this picture, where we imagine the geometry to be frozen and the wavelength (and thus wavenumber) varied, we see that the membrane modulates the resonances in a periodic fashion. The periodic part can be turned into a frequency

change, $\frac{c}{2\pi}\frac{1}{L}|r_m|\sin(2k_{0,n}z_m)$, which when plotted against the resonant wavenumber folded into a single $2kz$ bubble leads to the picture in Fig. 3.22. Recalling the definition of our dispersive coupling, this change of the resonance frequency with membrane position is exactly what we are after; the derivative of the curves are directly proportional to the coupling G. The curves are further vertically offset by subtraction of the maximum values, such that we only plot negative frequency shifts – first, a small offset has little impact on our system, and secondly, adding a material with $n > 1$ should only *increase* the optical path length, thus reducing the resonance frequency.

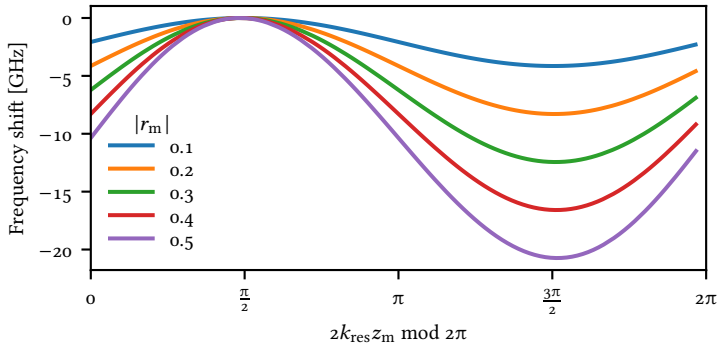

Figure 3.22: Frequency shift as a function of $2kz$, for varied membrane reflectivity. The curves are offset vertically so that only negative changes are allowed. $L = 2.3\,\text{mm}$, $\Delta z_m = -0.12\,\text{mm}$.

The rest of the model is mostly based on the numerical simulations, but a few points can still be made. First, the cavity transmission and reflection is now not only a function of the mirrors transmissions – the amount of light in the two subcavities also matter, and thus

$$T_{cav} = \frac{|E_{trans}|^2}{|E_{in}|^2} = \frac{|t_2E_3|^2}{|E_{in}|^2} \qquad R_{cav} = \frac{|E_{refl}|^2}{|E_{in}|^2}. \tag{3.157}$$

Similarly, the overcoupling parameters now also reflect the different amount of light in the two subcavities. For no loss, we get

$$\eta_{trans} = \frac{|t_2|^2|E_3|^2}{|t_2|^2|E_3| + |t_1|^2|E_2|^2} \qquad \eta_{refl} = \frac{|t_1|^2|E_2|^2}{|t_2|^2|E_3| + |t_1|^2|E_2|^2}. \tag{3.158}$$

With the addition of losses, the denominator must be modified in a suitable manner to reflect *where* the losses happen, since more light at a lossy element means more total effective loss.

The cavity linewidth is modified in a similar manner. Dumont et al. (2019) gives an analytical expression for the linewidth as

$$\kappa = \frac{(1-|r_m|^2)c|t_1|^2 + (1+2|r_m|\cos(2k_{res}z_m+\varphi_r) + |r_m|^2)c|t_2|^2}{2z_m(1-|r_m|^2) + 2(L-z_m)(1+2|r_m|\cos(2k_{res}z_m+\varphi_r) + |r_m|^2)}. \tag{3.159}$$

While this equation is nice, it is not particularly transparent, so in practice we evaluate the linewidth numerically with the TMM. Nielsen (2016) notes that the

(39) I. e., a weighted sum $\sum \alpha_i\kappa_i$, with $\alpha_i \geq 0$ and $\sum_i \alpha_i = 1$.

linewidth should always be a convex combination[39] of the decay rates of two subcavities, assuming a perfectly reflecting membrane,

$$\kappa_1 = \frac{c|t_1|^2}{2(L - z_m)} \qquad \kappa_2 = \frac{c|t_2|^2}{2z_m}, \tag{3.160}$$

which can provide a sanity check, as the total linewidth must lie between these two values.

The last point is that of the interpretation of the dispersive shift arising from an effective radiation pressure force. In the MIM setup, the membrane feels not one, but *two* radiation pressure forces, one from each of the subcavities. Recalling the radiation pressure force from Section 3.5, for the canonical system, we have

$$F_{can} = \frac{2\hbar k \bar{n}_{cav}}{\tau_{RT}} = \hbar G \bar{n}_{cav}. \tag{3.161}$$

With two different forces, we simply add them together while keeping track of their directions, and obtain

$$F_{MIM} = F_1 - F_2 = 2\hbar k \left(\frac{\bar{n}_1}{\tau_1} - \frac{\bar{n}_2}{\tau_2} \right) = 2\hbar k \frac{\bar{n}_2}{\tau_2} \left(\frac{\bar{n}_1 \tau_2}{\bar{n}_2 \tau_1} - 1 \right) \equiv \hbar G \bar{n}_{cav,eff}. \tag{3.162}$$

This *defines* the effective number of cavity photons such that the MIM expression matches that of the canonical system. Isolating G, we get

$$G = 2k \frac{\bar{n}_1/\tau_1 - \bar{n}_2/\tau_2}{\bar{n}_1 + \bar{n}_2}, \tag{3.163}$$

or when expressed through the electrical fields (which are fluxes, so $n_{1/2} = \tau_{1/2}(|E_{1/3}|^2 + |E_{2/4}|^2)$), and scaling with x_{zpf}

$$g_0 = \frac{2kx_{zpf}}{2\pi} \frac{|E_1|^2 + |E_2|^2 - \left(|E_3|^2 + |E_4|^2\right)}{\tau_1 \left(|E_1|^2 + |E_2|^2\right) + \tau_2 \left(|E_3|^2 + |E_4|^2\right)}. \tag{3.164}$$

Thus, it is clear that the optomechanical coupling is proportional to the difference of photons in the two subcavities, or when $L_1 \sim L_2$ so $\tau_1 \sim \tau_2$, the ratio $(n_1/n_2) - 1$.

Putting all this together, we plot in Fig. 3.23 the TMM evaluated for the optomechanical assembly used in Chapter 10 – the parameters are listed in Table 3.1.

We see here that all important parameters are modulated by the movement of the membrane in $2kz$. Starting from the top plot, two distinct high-coupling points exist, with near-identical amplitude and different sign. This sign difference is immaterial for practical purposes, as we almost ways encounter g_0-*squared*. However, the cavity linewidth, κ, and the overcoupling in reflection η, is modulated in a similar fashion as g_0. Since we are interested in maximizing η, we choose to work on the high-κ high-coupling point. This also minimizes the transmission (and conversely maximizes the reflection). g_0^2/κ and g_0^2/κ^2 can be useful in estimating the ratio of coherent interactions to loss mechanisms, such as for calculation of cooperativities, C.

This concludes the derivation of the Transfer Matrix Model (TMM), which effectively maps our membrane-in-the-middle optomechanical system to the canonical system. For a given choice of parameters (transmissions, losses, lengths etc.), we obtain direct parallels to the parameters describing the canonical system, including the optomechanical coupling, G, and have derived a method for predicting other important system parameters.

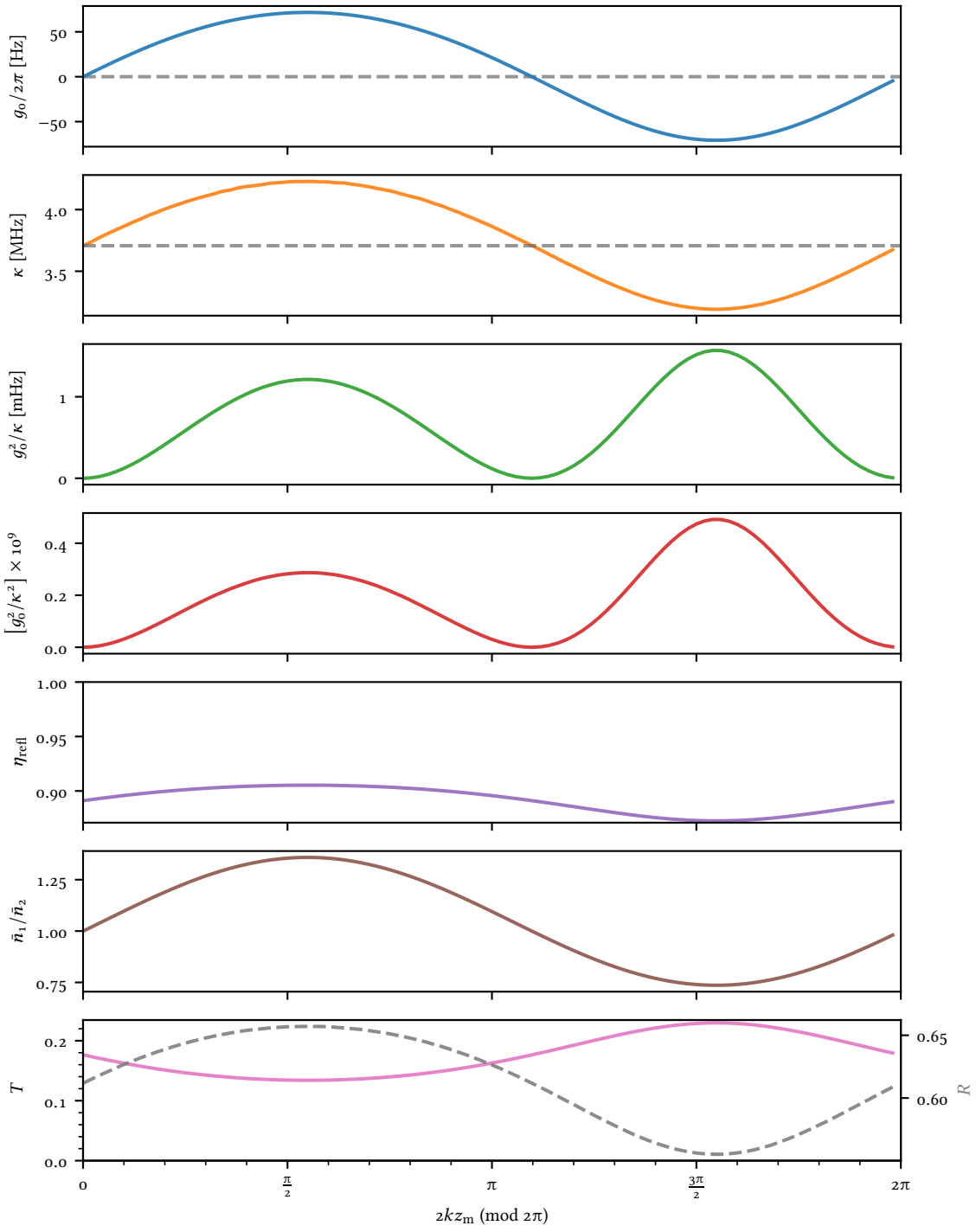

Figure 3.23: Transfer matrix model, evaluated for experimentally relevant parameters, as listed in Table 3.1.

Parameter	Symbol	Value
Membrane effective mass	m_{eff}	2 ng
Membrane frequency	$\omega_{\text{m}}/2\pi$	1.4 MHz
Input mirror transmission	T_1	360 ppm
Input mirror loss	δ_1	20 ppm
Back mirror transmission	T_2	20 ppm
Back mirror loss	δ_2	4 ppm
Cavity length	L	2.6 mm
Membrane position	z_{m}	1.25 mm
Membrane thickness	d	14 nm

Table 3.1: Parameters for the TMM.

3.9 Cavity Optomechanical Effects

As a last point of action in this chapter, we will briefly discuss a couple of interesting or important processes or effects in our optomechanical system.

3.9.1 OMIT

OptoMechanically Induced Transparency (OMIT), analogously to the atomic physics predecessor, Electromagnetically Induced Transparency (EIT), is both an interesting and important physical process in its own right, as well as an important experimental tool.

The effect was first proposed in the context of optomechanics in Schliesser (2009)[40], and shortly thereafter in Agarwal and S. Huang (2010)[41], and successfully implemented and reported in Weis et al. (2010)[42]. Quoting the abstract of original paper, OMIT is performed in the following manner:

> A control optical beam tuned to a sideband transition of a micro-optomechanical system leads to destructive interference for the excitation of an intracavity probe field, inducing a tunable transparency window for the probe beam.

The "control optical beam" here refers to a strong, classical beam tuned below the resonance of the cavity. This driving beam will by itself drive the mechanics. If we introduce a second beam to the cavity, for example by suitable modulation of the strong classical beam, the response of the mechanics to the strong beam may interfere with the weak "probe" beam. The original formulation is valid for system well into the resolved sideband regime, where the lower sideband can easily be ignored. For our case, in the intermediate regime, between resolved and unresolved, the description must include both modulation sidebands, if the probe beam is generated by modulation of the carrier – such treatments can be found in Nielsen (2016), Yeghishe Tsaturyan (2019) and Møller (2018). Further, the original implementation was for a whispering gallery mode resonator, where light was coupled in from a tapered optical fiber, the transmission of which served as the detection path. This change of the relevant input-output relations leads to a shift from *transparency* to *opaqueness*; had we probed in reflection, we would observe a transparency window.

(40) Albert Schliesser (2009). "Cavity Optomechanics and Optical Frequency Comb Generation with Silica Whispering-Gallery-Mode Microresonators". Ph.D. thesis. Ludwig–Maximilians–Universität München.

(41) G. S. Agarwal and Sumei Huang (2010). "Electromagnetically induced transparency in mechanical effects of light". In: *Phys. Rev. A* 81 (4), p. 041803.

(42) Stefan Weis et al. (2010). "Optomechanically Induced Transparency". In: *Science* 330.6010, pp. 1520–1523.

OMIT is quantum interference effect, originating with the discretized energy levels, but is classical in the sense that no quantum noise is involved; we are observing classical mean values and the driving fields are classical. The scheme is depicted in Fig. 3.24.

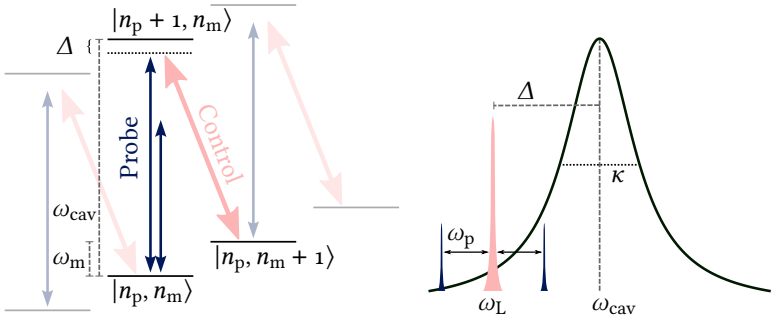

Figure 3.24: OMIT level scheme. The two-photon detuning, $\delta = \omega_p - \omega_L - \omega_m$, is chosen $\delta = 0$.

We start with a strong, coherent field at frequency ω_L, which we phase modulate at frequency ω_p (p for probe) with modulation index β. We then split the field into a strong part and fluctuations. Using the Jacobi–Anger expansion, and terminating at first order in β, we get

$$a_{in}(t) = \alpha_{in} e^{i\omega_L t + \beta \sin(\omega_p t)} \tag{3.165}$$

$$= \alpha_{in} e^{i\omega_L t} \left[1 + \frac{\beta}{2} \left(e^{i\omega_p t} - e^{-i\omega_p t} \right) \right] = (\alpha_{in} + \delta a)\, e^{i\omega_L t} \tag{3.166}$$

$$\delta a(t) = \alpha_{in} \frac{\beta}{2} \left(e^{i\omega_p t} - e^{-i\omega_p t} \right) = \alpha_{in} i\beta \sin(\omega_p t). \tag{3.167}$$

Note that if the input field is chosen real, $\alpha_{in} = \alpha_{in}^*$, the modulation sidebands are purely imaginary. The phase of the modulation ($\sin(\omega_p t)$ vs. $\cos(\omega_p t)$) is arbitrary in practice, and one might have started as well with any harmonic modulation. What *is* important is that β is small, so the sidebands are much weaker than the carrier.

In the simplest scheme, we perform direct detection of the total output field from the cavity, detecting the amplitude fluctuations of the light, i. e., X_L^{out}. The resulting photocurrent is then demodulated at the modulation frequency, and we obtain an OMIT amplitude and phase.

In our quadrature language, and since we will be demodulating output field at the modulation frequency, the input field takes the form

$$\hat{X}_L^{in}(\omega_p) = \begin{pmatrix} 0 \\ G \end{pmatrix} \tag{3.168}$$

where G is the *effective* modulation strength, proportional to β and α (the larger the classical input field, the larger the size of the sidebands).

We find the intra-cavity field by starting with Eq. (3.137), the final expression for the intracavity field, and dropping all terms containing only noise operators, which are irrelevant compared to our classical drive. This gives

$$\boldsymbol{X}_{L,m}^{cav} = \boldsymbol{O}_{\psi_{in}} \boldsymbol{Y}^{-1} \boldsymbol{O}_{\psi_{in}}^{\mathsf{T}} \sqrt{\kappa_{in}} \boldsymbol{X}_{L,m}^{in}, \tag{3.169}$$

where the hats have been dropped, due to the classical nature of the fields.

If performed in transmission, and assuming a lossless cavity, the output optical quadratures is related to the intracavity quadratures by the input-output relation

$$\boldsymbol{X}_{\mathrm{L}}^{\mathrm{out,ex}} = \sqrt{\kappa_{\mathrm{ex}}}\boldsymbol{X}_{\mathrm{L}}^{\mathrm{cav}}. \tag{3.170}$$

However, these quadratures are defined with respect to the phase of the *input* optical field, while we are using the transmitted beam as the detection LO. Since the phase of the output field $\arg[\alpha_{\mathrm{ex,out}}] = \arg[\alpha_{\mathrm{cav}}] = \arg[\alpha_{\mathrm{in}}] + \psi_{\mathrm{in}}$, performing direct detection $\propto \hat{a}_{\mathrm{nl}}^{\dagger}\hat{a}_{\mathrm{nl}} = (\alpha^* + \hat{a}^{\dagger})(\alpha + \hat{a})$ (with "nl" denoting the non-linearized ladder operators) measures not only X_{L}, but $X_{\mathrm{L}}\cos\psi_{\mathrm{in}} + P_{\mathrm{L}}\sin\psi_{\mathrm{in}}$; this is equivalent to the rotation

$$\boldsymbol{X}_{\mathrm{L}}^{\mathrm{out,eff}} = \boldsymbol{O}_{\psi_{\mathrm{in}}}^{\mathsf{T}}\boldsymbol{X}_{\mathrm{L}}^{\mathrm{out,ex}}, \tag{3.171}$$

and detection of the X_{L}. Collecting these expressions we get an expression for the detected light

$$X_{\mathrm{L}}^{\mathrm{out,eff}} = \begin{pmatrix} 1 & 0 \end{pmatrix}\sqrt{\kappa_{\mathrm{in}}\kappa_{\mathrm{ex}}}Y^{-1}\boldsymbol{O}_{\psi_{\mathrm{in}}}\boldsymbol{X}_{\mathrm{L}}^{\mathrm{in}}, \tag{3.172}$$

which we easily evaluate to

$$X_{\mathrm{L}}^{\mathrm{out,eff}} = \frac{-\Delta\cos\psi_{\mathrm{in}} + (\kappa/2 - \mathrm{i}\Omega)\sin\psi_{\mathrm{in}}}{(\kappa/2 - \mathrm{i}\Omega)^2 + \Delta^2 + 8g^2\Delta\chi_{\mathrm{moo}}}\sqrt{\kappa_{\mathrm{in}}\kappa_{\mathrm{ex}}}G, \tag{3.173}$$

or, by inserting the definition of $\psi_{\mathrm{in}} = \arctan(2\Delta/\kappa)$,

$$X_{\mathrm{L}}^{\mathrm{out,eff}} = \frac{-8\Delta\mathrm{i}\Omega}{\sqrt{1 + \frac{4\Delta^2}{\kappa^2}}\kappa\left(4\Delta\left[\Delta + 8g^2\chi_{\mathrm{moo}}\right]\right) + 2\left(\kappa/2 - \mathrm{i}\Omega\right)}\sqrt{\kappa_{\mathrm{in}}\kappa_{\mathrm{ex}}}G. \tag{3.174}$$

These equations can be factored into equations of the form

$$X_{\mathrm{L}}^{\mathrm{out,eff}} = \frac{C(\Omega)}{1 - M(\Omega)}G, \tag{3.175}$$

which leads to the following interpretations: first, the entire equation for the signal can be thought of as a (complex) transfer function of the input modulation, $X_{\mathrm{L}}(\Omega) = T(\Omega)G(\Omega)$, and our goal is now to find T, independent of G. Secondly, since the mechanics appear only in the term $M(\Omega)$, the entire response can be though of as the bare cavity response, divided by $(1 - M(\Omega))$.

In practical experiments, frequency-dependent delays in the acquisition electronics make precise measurements of the phase of $T(\Omega)$ impractical, and we almost always measure and fit the magnitude (absolute square) of the transfer function $|T(\Omega)|^2$, which I define as the OMIT signal, $\mathrm{OMIT} = |T(\Omega)|^2$[43].

Finally, this derivation was performed for a single mechanical mode. In practice, our systems are highly multi-mode, so we need to explicitly include all coupled modes (which are broadened such that they can not be smoothed out of the data) to our fit. This is done by modifying $M(\Omega)$ by

$$g^2\chi_{\mathrm{moo}} \rightarrow \sum_i g_i^2\chi_{\mathrm{moo},i}, \tag{3.176}$$

(43) Derivations in, e. g., Yeghishe Tsaturyan (2019) and Møller (2018) displays the non-squared response. In practice, we all fit the squared version.

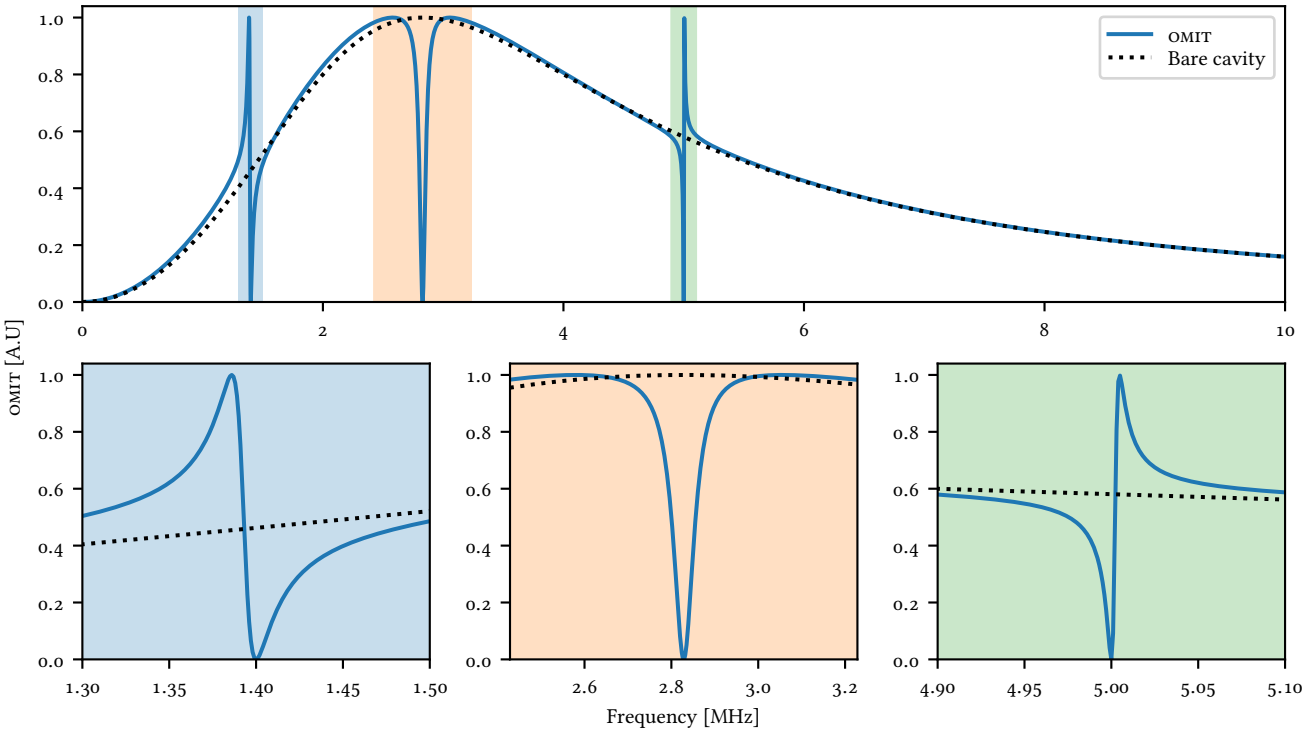

Figure 3.25: OMIT signal. Top panel: bare cavity ($g_i = 0$, dotted line) and full OMIT response with three mechanical modes. Bottom row: zoom in on the resonances. All traces are normalized to the maximum response for the empty cavity. $\kappa/2\pi = 4\,\text{MHz}$, $\Delta/2\pi = -2\,\text{MHz}$, $\gamma_{0,i}/2\pi = 1\,\text{mHz}$, $g_i/2\pi = 200\,\text{kHz}$, $\omega_0/2\pi \in \{ 1.4\,\text{MHz}, \sqrt{\Delta^2 + (\kappa/2)^2}/2\pi \sim 2.83\,\text{MHz}, 5\,\text{MHz} \}$.

as discussed in Nielsen (2016, section 2.3.7).

The final expression is plotted in Fig. 3.25, for a case with three mechanical modes. The three modes have frequencies that are respectively below, at, and above the frequency with highest response of the bare cavity, at $\omega = \sqrt{\Delta^2 + (\kappa/2)^2}$. The lowest frequency mode shows a dispersive-like feature with first a peak below the mechanical resonance, and a dip at the mechanical frequency. For the highest frequency peak the dispersive feature is mirrored, with the peak landing to the right of the dip. The peak at the maximum of the response curve of the OMIT feature is a symmetrical dip with only small but wide peaks on either side of the resonance.

OMIT measurements are used extensively in the experiments to measure predominantly κ and Δ, i. e., properties of the cavity. In that sense, OMIT itself, which is a mechanical effect interesting in its own right, for practical purposes is often a correction to the cavity response $C(\Omega)$[44].

(44) This is true to a degree, where, in our group, the term "OMIT" is used colloquially to mean simply a measurement of the cavity parameters with phase modulation – the optomechanical parameters are ignored.

3.9.2 Ponderomotive Squeezing

The driven coherent response discussed in the last section, OMIT, is related to a quantum (and therefore more dignified) process, called *ponderomotive squeezing*,

where the optomechanical interaction squeezes the (amplitude) fluctuations of the output light below those of the coherent (and groundstate) optical fields. Where OMIT was driven by a classical modulation, ponderomotive squeezing arises solely from the interference of the light-induced quantum backaction with the shot noise itself.

As noted by P. Meystre et al. (1985)[45], there is a one-to-one correspondence between a (canonical) optomechanical system, and a cavity with a medium whose refractive index changes with the intensity of the light, i. e., a *Kerr* medium or $\chi^{(3)}$ non-linear material. Later that year, the first ever squeezing of light was reported in a Kerr-type system, consisting of sodium (Na) atoms in a cavity (Slusher et al. 1985)[46], albeit at the very modest level of 0.3 dB.

Since then, a very large number of physical systems have been shown to facilitate squeezing of light below the shot noise level. Most prominently, systems with $\chi^{(2)}$ non-linear crystals in cavities, hold the current record of 15 dB of optical squeezing (Vahlbruch et al. 2016)[47]. However, since the squeezing generated by $\chi^{(2)}$ non-linearities occur at an optical frequency different (usually twice that) from the pumping field, $\chi^{(3)}$ type squeezers are still interesting for many applications, where the squeezing close the pumping frequency is desired. In the context of optomechanics, squeezing has been reported by, e. g., Brooks et al. (2012)[48], Purdy et al. (2013)[49], Safavi-Naeini et al. (2013)[50], and Nielsen et al. (2017).

The derivation found in Nielsen (2016)[51] gives a clear exposition of the physics at play; the intracavity field quadratures are expressed through the input quadratures and cavity transduction functions plus the optomechanical coupling, the mechanical response is eliminated by insertion of the expressions for the mechanical $\hat{X}$ quadrature, and finally the PSD is calculated from the output optical quadratures. This derivation thus essentially mirrors the derivation of the general output field of Eq. (3.140) – in essence, we just need to evaluate this equation and we're done; in practice some insights can be gleamed by a set of simplifications. The expressions that I obtain here are not as analytically nice – instead, this section serves as a demonstration of how to apply our formalism to quantum noise driven processes.

Starting from Eq. (3.140) and assuming a perfectly one-sided lossless cavity probed in reflection, i. e., $\kappa = \kappa_{\mathrm{in}}$ and $\kappa_{\mathrm{ex}} = 0$, and thus $\psi_{\mathrm{in}} = \psi_{\mathrm{out}} = \psi$, we have

$$\hat{\boldsymbol{X}}^{\mathrm{out}}_{\mathrm{L,m}} = \boldsymbol{O}^{\mathsf{T}}_{\psi}(\kappa \boldsymbol{Y}^{-1} - \mathbb{1}_2)\boldsymbol{O}^{\mathsf{T}}_{\psi}\hat{\boldsymbol{X}}^{\mathrm{in}}_{\mathrm{L,m}} - \sqrt{\kappa}\boldsymbol{O}^{\mathsf{T}}_{\psi}\boldsymbol{Y}^{-1}\boldsymbol{B}\chi_{\mathrm{moo}}\hat{f}_{\mathrm{m}}. \tag{3.177}$$

Assuming further that the output field is detected without any loss, and that we either perform direct detection, or homodyne detection of the optical $\hat{X}$ quadrature, we have

$$\hat{X}^{\mathrm{det}}_{\mathrm{L}} = \hat{X}^{\mathrm{out}}_{\mathrm{L}}, \tag{3.178}$$

or in other words, the first component of Eq. (3.177). By making these assumptions we have reduced the number of inputs to our equation to the optical input quadratures and the mechanical noise operator. The expression for the detected optical quadrature is

$$\hat{X}^{\mathrm{det}}_{\mathrm{L}} = \frac{\left[\left\{(4\Delta^2+\kappa^2)\left(\kappa^2 + 4\Delta(\Delta + 8g^2\chi_{\mathrm{moo}})\right) - 4(4\Delta^2-\kappa^2)\Omega^2\right\}\hat{X}^{\mathrm{in}}_{\mathrm{L}}\right] + 16\Delta\kappa\Omega\left(-\mathrm{i}g\sqrt{1+\frac{4\Delta^2}{\kappa^2}}\sqrt{\kappa}\chi_{\mathrm{moo}}\hat{f}_{\mathrm{m}} + \Omega\hat{P}^{\mathrm{in}}_{\mathrm{L}}\right)}{(4\Delta^2+\kappa^2)\left[4\Delta\left(\Delta + 8g^2\chi_{\mathrm{moo}}\right) + (\kappa - 2\mathrm{i}\Omega)^2\right]}. \tag{3.179}$$

(45) P. Meystre et al. (1985). "Theory of radiation-pressure-driven interferometers". In: *J. Opt. Soc. Am. B* 2.11, pp. 1830–1840.

(46) R. E. Slusher et al. (1985). "Observation of Squeezed States Generated by Four-Wave Mixing in an Optical Cavity". In: *Phys. Rev. Lett.* 55 (22), pp. 2409–2412.

(47) Henning Vahlbruch et al. (2016). "Detection of 15 dB Squeezed States of Light and their Application for the Absolute Calibration of Photoelectric Quantum Efficiency". In: *Phys. Rev. Lett.* 117 (11), p. 110801.

(48) Daniel W.C. Brooks et al. (2012). "Non-classical light generated by quantum-noise-driven cavity optomechanics". In: *Nature* 488 (7412), pp. 476–480.

(49) T. P. Purdy et al. (2013). "Strong Optomechanical Squeezing of Light". In: *Phys. Rev. X* 3 (3), p. 031012.

(50) Amir H. Safavi-Naeini et al. (2013). "Squeezed light from a silicon micromechanical resonator". In: *Nature* 500 (7461), pp. 185–189.

(51) And followed closely by Møller (2018) and Yeghishe Tsaturyan (2019).

Since all input variables are, by definition, zero mean stochastic variables, we cannot evaluate the equation directly. Instead, following the procedure lined out in Section 10.2.2, we note that Eq. (3.179) is linear in the noise operators, allowing us to write is as a matrix equation,

$$\boldsymbol{Q}_{\text{out}} = \boldsymbol{U}\boldsymbol{Q}_{\text{in}}, \tag{3.180}$$

with $\boldsymbol{Q}_{\text{out}} = (\hat{X}_{\text{L}}^{\text{det}})$, and $\boldsymbol{Q}_{\text{in}} = (\hat{X}_{\text{L}}^{\text{in}}, \hat{P}_{\text{L}}^{\text{in}}, \hat{f}_{\text{m}})^{\intercal}$, which allows us to calculate the (symmetrized) output power spectral density as

$$\bar{S}_{X_{\text{L}}X_{\text{L}}} = \boldsymbol{U}^{\dagger}\bar{\boldsymbol{S}}_{\text{in}}\boldsymbol{U}, \tag{3.181}$$

where $\bar{\boldsymbol{S}}_{\text{in}}$ is the (diagonal) matrix containing the noise spectral densities of the inputs, i. e., $\bar{\boldsymbol{S}}_{\text{in}} = \text{diag}\big(1/4, 1/4, \gamma_{\text{o}}\,(n_{\text{th}} + 1/2)\big)$.

The output (detected light PSD) is displayed in Fig. 3.26. We here see a prominent dip below the shot noise level (dotted line) for frequencies below the mechanical resonance frequency of $\omega_{\text{o}}/2\pi = 1.37\,\text{MHz}$. As the coupling rate, g, is increased, the dip broadens, becomes deeper and the minimum moves to a lower frequency.

In Fig. 3.27, the spectrum is displayed for varied bath temperature, T. We here see that the overall shape of the squeezing curve is unaffected, but the dip depth is reduced for higher temperatures.

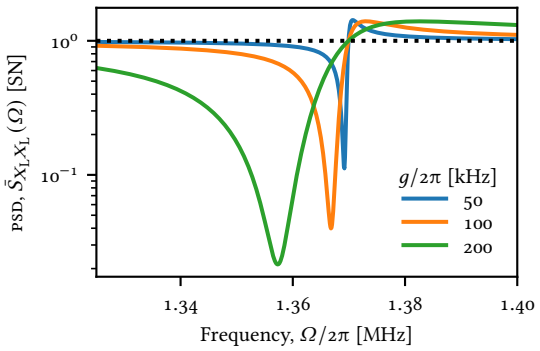

Figure 3.26: Ponderomotive squeezing in reflection for varied g. $\omega_{\text{o}}/2\pi = 1.37\,\text{MHz}$, $\kappa/2\pi = 4.2\,\text{MHz}$, $\Delta/2\pi = -0.5\,\text{MHz}$, $T = 10\,\text{K}$, $Q = 650 \times 10^{6}$.

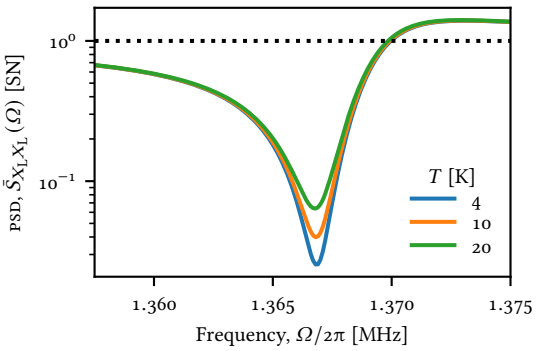

Figure 3.27: Ponderomotive squeezing in reflection for varied T. Other parameters like Fig. 3.26, $g/2\pi = 100\,\text{kHz}$.

Including the finite detection efficiency, η, modifies the detected light as

$$\hat{X}_{\text{L}}^{\text{det}} = \sqrt{\eta}\hat{X}_{\text{L}}^{\text{out}} + \sqrt{1-\eta}\hat{X}_{\text{L},\eta}^{\text{in}}, \tag{3.182}$$

effectively replacing part of the squeezed output light with uncorrelated shot noise, reducing the detected squeezing, as depicted in Fig. 3.28. Here, entire trace is reduced in amplitude; evidently, though both finite detection efficiency and temperature limits the attainable squeezing, the two effects can be distinguished in a fit.

Finally, including the finite overcoupling into our model leads to the full model needed to fit experimental traces. The finite overcoupling leads to different input

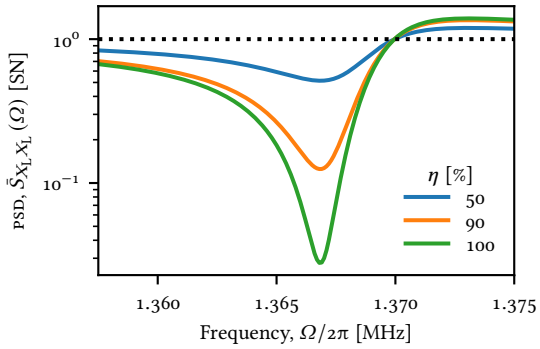

Figure 3.28: Ponderomotive squeezing in reflection for varied T. Other parameters like Fig. 3.26, $g/2\pi = 100\,\mathrm{kHz}$.

and output rotations $\psi_{\mathrm{in}} \neq \psi_{\mathrm{out}}$, effectively sending some of the phase response of the light into the detected quadrature, enhancing the peak above resonance and limiting squeezing.

In Fig. 3.29 an experimental squeezing trace is shown. Δ and κ have been separately measured by an OMIT-style measurement; further $\gamma_{\mathrm{mo}}/2\pi = 2.15\,\mathrm{mHz}$ and cavity overcoupling in reflection $\eta_{\mathrm{refl}} = 0.91$ are fixed by separate calibrations. Because the squeezing is limited by detection efficiency, the fit is insensitive to T, which is fixed at 10 K. The light blue trace is the raw data, while the dark blue trace is a smoothened version of the data. The solid orange line depicts the fit of our full squeezing model (to the *unsmoothened* data). Finally, the fit is evaluated with a detection efficiency of $\eta = 95\,\%$, showing that a large increase in squeezing efficiency is realistically attainable by improving the detection efficiency. Even without an increased detection efficiency, the observed squeezing of $(3.92 \pm 0.12)\,\mathrm{dB}$ over a 3 kHz region around the minimum (and fitted squeezing of 4.34 dB) is higher than reported elsewhere for optomechanical squeezing.

By detecting the transmitted beam, instead of the reflected, the squeezing signal is essentially flipped around the resonance, such that the squeezing appears above the mechanical resonance. Experimentally, for us, the transmitted beam has significantly higher detection efficiency, of $\eta \sim 0.9$, which means that sensitivity to temperature is higher. Such two squeezing traces are shown in Fig. 3.30

3.9.3 Static Bistability

A feature of the optomechanical system, which sets practical limitations to the achievable coupling rates is *static bistability*. In essence, when increasing the intracavity power, a regime is reached where more than one quasistable configuration exists; the mean displacement of the membrane in the cavity shifts the cavity resonance, which changes the intracavity power.

The effect may be explained in several ways – I here follow that in Aspelmeyer, Kippenberg, and Marquardt[52]. This description assumes that the light force reacts instantaneously to the mechanical motion, i.e., that the cavity bandwidth is significantly larger than the mechanical frequency, $\kappa \gg \Omega_m$.

(52) Markus Aspelmeyer, Tobias J. Kippenberg, and Florian Marquardt (2014). "Cavity optomechanics". In: *Rev. Mod. Phys.* 86 (4), pp. 1391–1452.

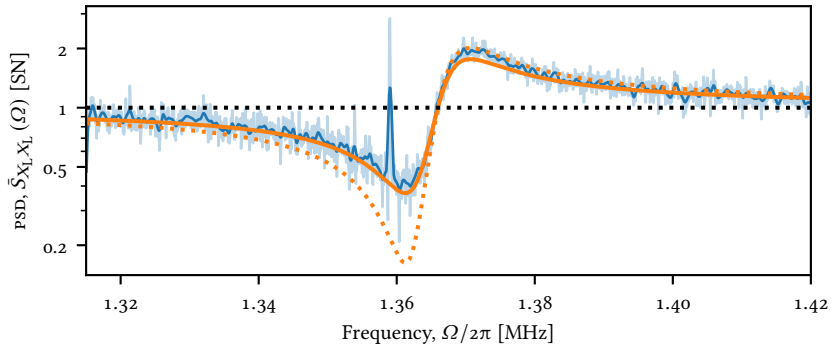

Figure 3.29: Ponderomotive squeezing in reflection. Light blue trace is data. Dark blue line is smoothed data. Solid orange line is a fit of the full squeezing model to the unsmoothed data. Dotted orange line shows the fit evaluated with an increased detection efficiency, $\eta_{\text{det}} = 0.95$, predicting close to 8 dB of squeezing. The peak at 1.36 MHz is laser phase noise; it is not removed from the data before fitting.

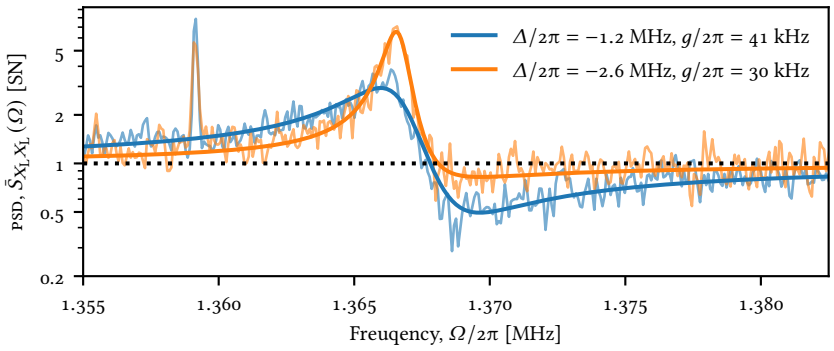

Figure 3.30: Ponderomotive squeezing in transmission. The two traces are fit collectively, with $\eta_{\text{det}} = 0.9$, $\eta_{\text{trans}} = 0.09$, $\gamma_{\text{mo}} = \omega_{\text{mo}}/Q \sim 2\pi \times 2.1$ mHz, $\kappa/2\pi = 3.3$ MHz. The fitted temperature is $T = 10.4$ K.

The two forces acting on the membrane is the spring force, $F = -kx$, and the radiation-pressure force, $F_{\text{rad}} = \hbar G \bar{n}_{\text{cav}}(x)$. Both depend on membrane position x; the spring force directly, the radiation-pressure force through the position dependence of the number of photons $\bar{n}_{\text{cav}}(x)$.

Since both these forces are conservative, a corresponding potential may be defined:

$$F(x) = F_{\text{spring}}(x) + F_{\text{rad}}(x) = -\frac{\partial V(x)}{\partial x} = -\frac{\partial V_{\text{rad}}(x)}{\partial x} - \frac{\partial V_{\text{spring}}(x)}{\partial x}. \tag{3.183}$$

In the regime where only a single optical mode needs to be included ($\kappa \ll \Delta\nu_{\text{FSR}}$), the number of circulating photons is

$$\bar{n}_{\text{cav}}(x) = \frac{\bar{n}_{\text{cav}}^{\text{max}}}{1 + [2(Gx + \Delta)/\kappa]^2}, \tag{3.184}$$

where $\bar{n}_{\mathrm{cav}}^{\mathrm{max}}$ is the number of photons on resonance, and proportional to the incoming optical power. Integrating $F_{\mathrm{rad}}(x)$ we find

$$V_{\mathrm{rad}}(x) = -\tfrac{1}{2}\hbar\kappa\bar{n}_{\mathrm{cav}}^{\mathrm{max}} \arctan\left[\frac{2(Gx+\Delta)}{\kappa}\right], \tag{3.185}$$

leading to a total potential of

$$V(x) = \frac{m_{\mathrm{eff}}\omega_{\mathrm{m}}^2}{2}x^2 - \tfrac{1}{2}\hbar\kappa\bar{n}_{\mathrm{cav}}^{\mathrm{max}} \arctan\left[\frac{2(Gx+\Delta)}{\kappa}\right]. \tag{3.186}$$

This potential is plotted in Fig. 3.31 for increasing optical power. While the first term is dependent on the mechanical mode, for our system G is roughly independent of the mode shape, as long as the mode has a maximum at the same point as our normal mode of interest.

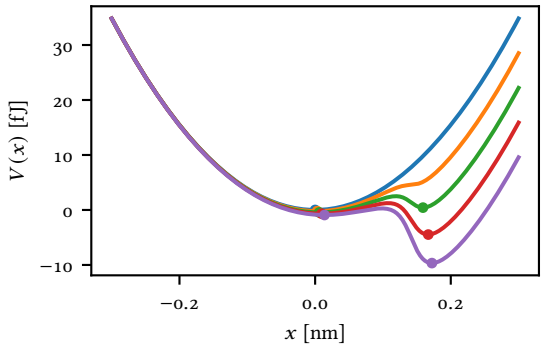

Figure 3.31: Static bistability. As the optical power is increased, a second minimum appears for positive x. The system can thus assume two stable configurations, with two circulating optical powers. Random perturbations can lead to switching between the two states.

Static bistability is not observed for our normal mode of interest; instead it becomes more of a technical limitation, as lower frequency modes of our membranes (discussed in the next chapter) reach the point of static bistability first, which sets the cavity into random oscillations between the two stable points, effectively making locking the cavity impossible.

This concludes the chapter about theoretical descriptions of optomechanics. We started out with a simple 1D description of classical harmonic oscillators. We then mapped 3D membranes to the 1D description, before considering the effects of dissipation and thermal noise, before quantizing the motion of the membrane.

We then turned from pure mechanics to light-matter interaction, specifically radiation pressure forces, and position measurements by phase measurements. Since those effects are small, we introduced the concept of optical resonators, to boost the interaction between light and mechanics.

With the interaction mechanism in place, we turned to the canonical optomechanical description, followed by the transfer matrix model, which maps our membrane-in-the-middle system to the canonical case. Finally, we explored a small number of optomechanical effects with relevance to our experiment.

The descriptions in this chapter have been highly idealized. The world, unfortunately, is never quite as simple as introductory chapters would have you believe, and so in the following chapter we will turn to some of the complexities that have been, so far, swept under the rug.

Chapter 4

Optomechanics in Practice

> “Possibly the most common error of a smart engineer, is to optimize a thing that should not exist.
>
> Elon Musk

Practical implementation details of a membrane-in-the-middle optomechanical system. Cryostats, Q-measurements, membrane fabrication & other dirty details.

4.1 Membrane Fabrication

4.1.1 Membrane Generations

The field of cavity optomechanics took off with the realization that commercially available Si_3N_4-membranes used as windows for X-ray applications also possessed excellent mechanical properties (Jayich et al. 2008; Dalziel J. Wilson et al. 2009; Dalziel J. Wilson 2012)[1]. These membranes are fabricated by (amongst others, but for optomechanics primarily) Norcada Inc. and almost universally referred to as simply “Norcada membranes” – such a membrane is depicted in Fig. 4.1 (left).

(1) Dalziel J. Wilson et al. (2009). “Cavity Optomechanics with Stoichiometric SiN Films”. In: *Phys. Rev. Lett.* 103 (20), p. 207204.

Norcada membranes suffer from a number of experimental challenges, though. The most serious one is that the mechanical qualities turned out to depend very sensitively on the clamping of the membrane, and because cryogenic cooling is simultaneously a requirement, softly suspending the membranes is also not a solution.

The solution chosen in our group is to use phononic bandgaps. These offer a twofold advantage: it severely reduces sensitivity to clamping, thus allowing for much more repeatable characteristics, and it shields the mechanical mode from radiative losses and external perturbations in the frequency region of interest.

Three major generations of membranes were developed, with the last being divided into 4 sub-generations, as this design concept has been proven to be the superior one by far.

The first generation (not depicted) used a 1D phononic shield, where a single beam of Si_3N_4 was shaped (Y. Tsaturyan et al. 2014)[2]. This was abandoned due to the entire patterned beam supporting low frequency modes with too large excursions – Møller (2018) calls them "too floppy". The second generation (pictured in Fig. 4.1, middle) used a 2D phononic shield, with a central defect supporting a suspended slightly rectangular membrane (Yu et al. 2014)[3]. This membrane design offered a big step up in experimental relevance for quantum applications, as the susceptibility to changing clamping was essentially eliminated, and the introduction of a bandgap allowed for very good isolation of the mechanical mode, leading to $Q \sim 10^7$ for $d = 60\,\mathrm{nm}$.

The third major generation of membranes took a different approach. Instead of embedding the phononic pattern in the supporting silicon, now the Si_3N_4 material was patterned. This came with a series of advantages, mainly a orders-of-magnitude increase in Q due to a reduction of losses related to bending of the membrane at rigid membrane–support interface (Yeghishe Tsaturyan et al. 2017; Yeghishe Tsaturyan 2019)[4,5].

The phononically patterned Si_3N_4 membranes exist in four major generations: the first one, published in Yeghishe Tsaturyan et al. (2017), Gen I, supported a simple defect at the center. Gen II added small holes to the membrane defect, thus reducing the effective mode mass, increasing the mode frequency, and thereby pushing the mode of interest further into the bandgap region. Gen III slightly adjusted these holes, sacrificing some bandgap–mode separation for even higher Qs, and the appearance of a second order bandgap. Gen IV is currently being developed in the group of Albert Schließer, primarily by postdoc Eric Langman. These new membranes, among other things, use a pattern of non-circular holes, and a modified defect, which better distributes the internal stress of the Si_3N_4, at the cost of a reduced membrane pad defect size.

(2) Y. Tsaturyan et al. (2014). "Demonstration of suppressed phonon tunneling losses in phononic bandgap shielded membrane resonators for high-Q optomechanics". In: *Opt. Express* 22.6, pp. 6810–6821.

(3) P.-L. Yu et al. (2014). "A phononic bandgap shield for high-Q membrane microresonators". In: *Applied Physics Letters* 104.2, p. 023510.

(4) Yeghishe Tsaturyan et al. (2017). "Ultracoherent nanomechanical resonators via soft clamping and dissipation dilution". In: *Nature Nanotechnology* 12 (8), pp. 776–783.

(5) Yeghishe Tsaturyan (2019). "Ultracoherent soft-clamped mechanical resonators for quantum cavity optomechanics". Ph.D. thesis. University of Copenhagen.

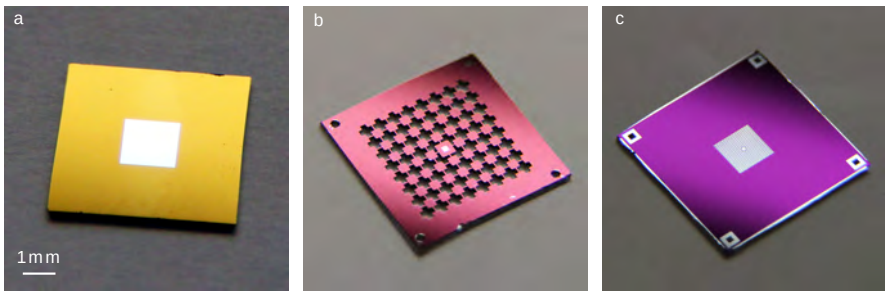

Figure 4.1: Membrane generations. a) Commercially available square membranes from Norcada Inc. b) Membranes with a 2D phononic pattern embedded in the Si. c) Membrane with the phononic pattern embedded in the Si_3N_4. The thickness of the Si_3N_4 layer determines the color through normal thin-film interference.

The second major generation membranes, i. e., the ones with the 2D phononic shield embedded in the silicon, was used for Nielsen et al. (2017) and Møller et al. (2017). When I joined the experiment in Summer 2017, the third major generation of phonically patterned membranes were just maturing enough to be utilized in quantum experiments, having been only recently well understood enough for publication (Yeghishe Tsaturyan et al. 2017). For the results reported in Chapter 10 Gen II of these membranes were utilized.

Of course such a change in membrane design leads to a number of new challenges and potentially very different optimum parameters choices. Some of these experiences led to an overall redesign of our optomechanical cavities, as described in Part II. The most important driver for this change was the reduction of the optically clear area of the membrane pad. As shown in Fig. 4.2, the defect pad at the center of the membrane is around 200 µm across, leading to significantly higher chances of increased cavity losses if the optical mode of the cavity is not perfectly aligned to the membrane – see Fig. 4.9 for a relatively well aligned mode.

4.1.2 Modes of the Phononic Bandgap Membranes

The mode shapes of these soft clamped phononic bandgap silicon nitride membranes is of course very far from the description in Section 3.2, where we discussed the oscillation patterns of uniform, rectangular plates.

For the soft clamped membranes the rectangular geometry is replaced with a hexagonal grid of holes, breaking both uniformity and also leading to things such non-uniform in-plane tension. By simple virtue of everything being static in the plane, the tension in thinner tethers must be higher than in the wider sections. The hexagonal pattern is terminated in a square hole of a supporting silicon frame. These things conspire to making analytical treatment of these membranes untractable, and we must therefore resort to numerical methods such as the *finite element method* (FEM).

In Quantop, the FEM software of choice is COMSOL Multiphysics®. This software is a very powerful tool for simulating a very wide variety of physical problems, with excellent simulation of cross-couplings between different physical parameters. For the purpose of this thesis, mainly the mechanical part is of major interest – both in this section, where we concern ourselves with mechanical mode shapes of membranes, and in section Chapter 8 where we are interested in simulating the mechanical spectrum and mode shapes of mirrors.

The simulated mode shapes of the Gen II are depicted in Fig. 4.2. The mode in the top frame, labeled A, is the lowest frequency mode within the phononic bandgap, and the mode with which we will be working. This is sometimes called the "fundamental" mode because it is the only mode in the bangdap with approximate rotational symmetry, although one can readily see that the radial mode profile has several nodes.

The four other modes in the bandgap, labeled B-E with increasing frequency, are pictured below. These all have zero displacement amplitude at the center of the defect, and are not even approximately rotationally symmetric. These modes are high Q and by themselves not uninteresting for optomechanics. For example, modes C and D are near-degenerate, which may be an interesting feature. From a more mundane point of view, measuring the coupling rates to these four modes

can be used to infer the mode position on the membrane; this was done in a systematic way for rectangular membranes in Nielsen et al. (2017) and Nielsen (2016). In practice we most often use it as a rough gauge; as long as the coupling to mode A is significantly higher than that with any other mode, the beam is relatively well centered on the membrane defect pad.

In Fig. 4.3 the displacement amplitude of mode A is shown along x and y. We observe that the mode amplitude decays exponentially with the distance from the center. The drastically reduced amplitude close to the clamping edges leads to suppression of sharp bends of the membrane, which leads to the drastic improvement of Q for these soft-clamped membranes, compared to the rectangular membranes with the phononic shield embedded in the silicon frame. The energy associated with the (now reduced) bending at the edges of the membrane is exactly the term we ignored in the wave equation for the membrane in Chapter 3; including it into the physical description explains why the membrane Q could be boosted by orders of magnitude by this design change.

4.1.3 Membrane Thickness

4.1.3.1 Membrane Reflection

Membrane reflection is a very important parameter, since it forms the basic mechanism for light-membrane coupling. The phenomenon is essentially thin film interference, in a simple boundary: normal incidence, input medium with $n = 1$, and monochromatic input. Solving the Fresnell equations combined with a simple geometric model, leads directly to the following expression for the membrane field reflectivity and transmission:

$$r_m = \frac{(n^2 - 1)\sin(knd)}{2in\cos(knd) + (n^2 + 1)\sin(knd)} \tag{4.1}$$

$$t_m = \frac{2n}{2in\cos(knd) + (n^2 + 1)\sin(knd)}. \tag{4.2}$$

n is the refractive index of the membrane material. For Si_3N_4 and a wavelength of $\lambda = 852\,\text{nm}$, $n = 2$.

The amplitude of the reflection coefficient is plotted in Fig. 4.4 for varied thickness. In the left panel the reflection is plotted for $\lambda \in \{ 780\,\text{nm}, 852\,\text{nm}, 920\,\text{nm} \}$. For thicknesses smaller than 100 nm the three curves are almost identical. Only for d larger than ~150 nm do the curves dephase, and we see significantly different reflections for the different wavelengths.

Since the optomechanical coupling is proportional to both reflection and, through the zero points fluctuations, $x_{\text{zpf}} \propto m_{\text{eff}}^{-1/2}$, the total coupling rate g_0 has a nontrivial shape, with especially the first maximum displaced towards smaller thickness, compared to the reflection curves, with the maximum g_0 for $d \sim 60\,\text{nm}$. I plot g_0 and a curve $\propto d^{-1/2}$ to guide the eye in the right panel of Fig. 4.4.

4.1.3.2 Effect on Q

As discussed in Yeghishe Tsaturyan et al. (2017), the overall scaling of mechanical Q with thickness depends on which damping mechanism dominates. For our membranes, the dominating loss term is associated with surface losses (as opposed to

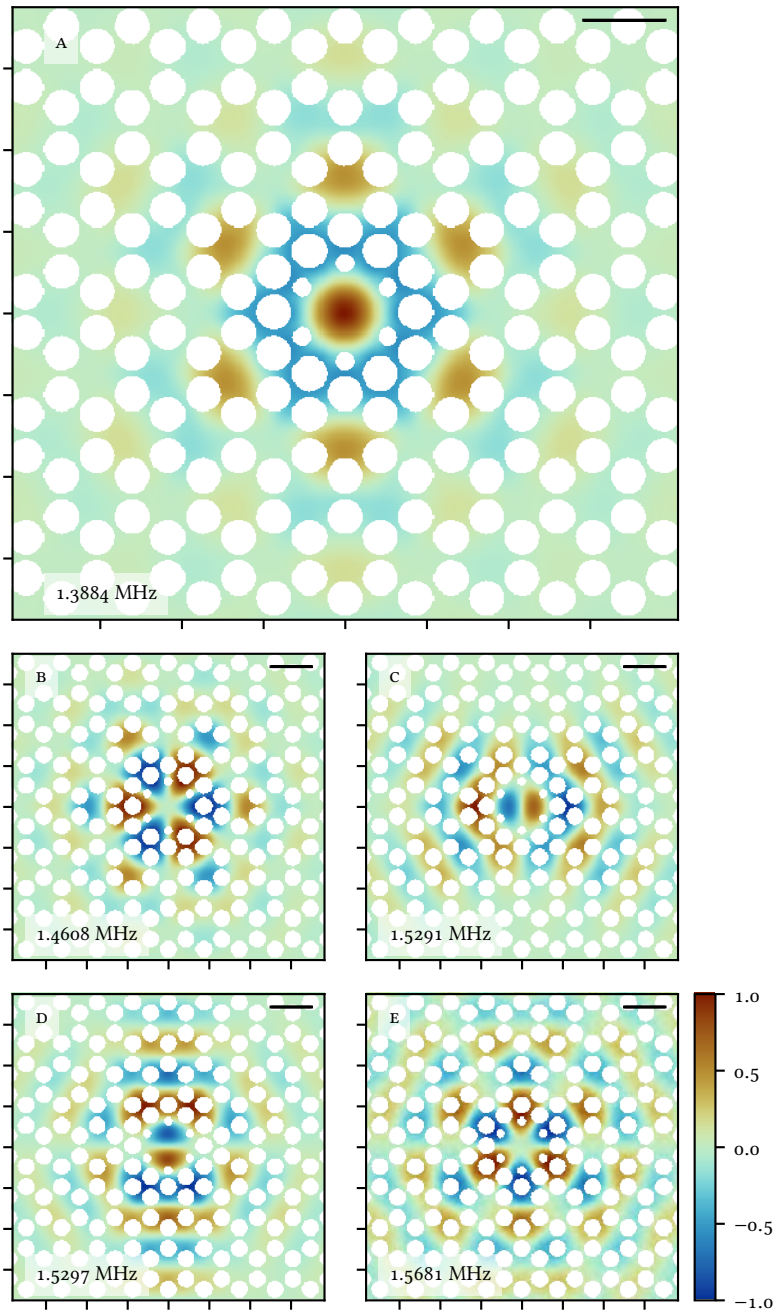

Figure 4.2: Normalized out of plane displacement for the five different modes in the bandgap for a Gen II membrane. Scale bars and tick spacings are 200 µm.

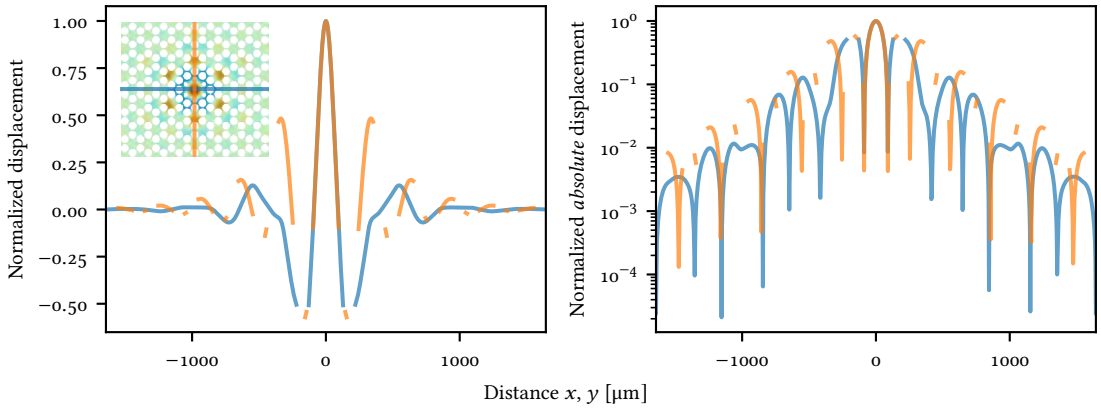

Figure 4.3: Cuts of the displacement of mode A. Left: Displacement along the x and y direction (see inset for direction). Right: Absolute displacement on a logarithmic scale.

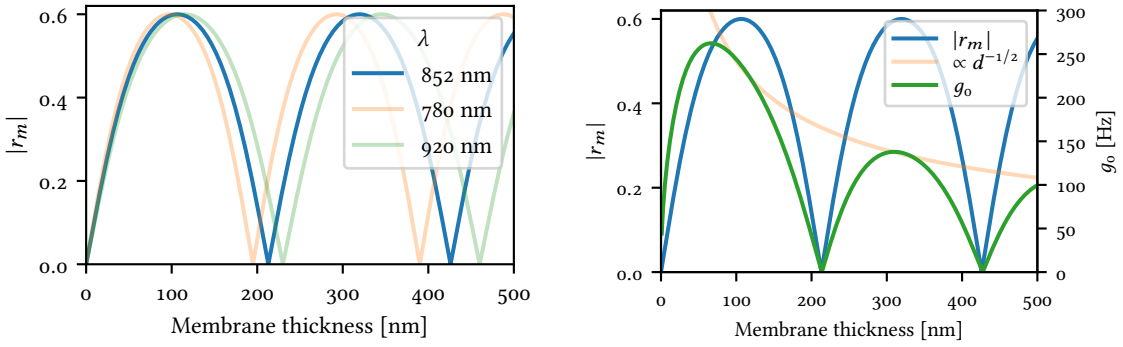

Figure 4.4: Membrane reflection and g_0 as a function of thickness. Left: Membrane reflection amplitude for $\lambda = 780\,\text{nm}, 852\,\text{nm}, 920\,\text{nm}$. For $d < 100\,\text{nm}$ the three curves essentially overlap, so reflection is insensitive to wavelength. For $d \gtrsim 150\,\text{nm}$ the curves dephase, and significant differences appear. Right: Reflection for $\lambda = 852\,\text{nm}$ and resulting g_0, which falls off as $\propto d^{-1/2}$ due to higher effective mass, m_{eff}. g_0 is maximized for $d \sim 60\,\text{nm}$. I assume $n = 2$ for all wavelengths. g_0 is calculated for a square membrane with $\omega = 1.28\,\text{MHz}$.

volume losses), as long as the membrane is kept below ~100 nm. This is always the case for us, in which case the membrane Q scales as

$$Q = \frac{a^2}{d}, \tag{4.3}$$

where a is the lattice constant, and can be thought of as an overall scale parameter for the membrane. Since the membrane frequency scales with a^{-1}, we expect Q to scale with f^{-2} and d^{-1}, as was observed in Yeghishe Tsaturyan et al. (2017). If one then wants maximize Q without regard to any other parameter, low frequencies and thin membranes are the way to go; however, as the coupling scales with the reflectivity, there is a trade-off to be made, and since low frequencies are problematic

in terms of things like laser noise (see Chapter 9), the choice of frequency is also limited by other factors.

4.2 Optical Cavities in Practice

Optical cavities as presented in Section 3.6 are not actually feasibly in reality. First of all, a set of two plane mirror do not form a stable resonator in practice; only for perfectly parallel mirrors – see Milonni and Eberly (2010, chapter 7)[6]. Instead at least one of the mirrors is almost always replaced by a curved (concave) mirror.

(6) Peter W. Milonni and Joseph H. Eberly (2010). *Laser physics*. Wiley.

While a longer exposition on optical modes in cavities is outside of the scope of this thesis, a number of relevant properties must be treated.

First, the question of resonator stability. This essentially describes whether a geometric configuration of mirrors (their curvatures, the distance between them and their tilt with the axis connecting them) is stable, i. e., whether they support stable modes. Ignoring the tilt, one can, using geometrical optics, calculate a stability criterion

$$0 \leq g_1 g_2 \leq 1, \tag{4.4}$$

where g_1 and g_2 are parameters describing the geometry through the relations

$$g_1 = 1 - \frac{L}{R_1} \qquad g_2 = 1 - \frac{L}{R_2}, \tag{4.5}$$

with R_i being the radius of curvature of the two mirrors[7], and L is the separation between them. Since flat mirrors have $R = \infty$, for a plano-plano cavity, $g_1 g_2 = 1$ independent of L. Thus, the resonator is marginally stable - any tilt will ruin the stability.

(7) Concave mirrors have $R > 0$, while convex mirrors have $R < 0$ in this convention.

The general stability criterion may be represented graphically as in Fig. 4.5 from the extremely nice paper by Kogelnik and Li (1966)[8]. For two identical curved mirrors with $R_1 = R_2 = R$, a stable cavity is formed for $0 < L \leq 2R$, and for a flat mirror one one end, $R_1 = \infty$, $0 < L \leq R$.

(8) H. Kogelnik and T. Li (1966). "Laser Beams and Resonators". In: *Appl. Opt.* 5.10, pp. 1550–1567.

4.2.1 Gaussian Modes

Following Milonni and Eberly (2010) (a similar derivation may be found in Kogelnik and Li (1966)), the general solution to the paraxial wave equation is that of *Gaussian* modes, i. e., modes whose intensity decay radially as Gaussian. For a geometry with rectangular geometry, the solutions to the governing equations is that of Hermite–Gaussian modes

$$\boldsymbol{E}(x,y,z) = \boldsymbol{E}_0 \frac{w_0}{w(z)} H_m\left[\sqrt{2}\frac{x}{w(z)}\right] H_n\left[\sqrt{2}\frac{y}{w(z)}\right] \times e^{i[kz-(m+n+1)\arctan(z/z_0)} e^{ik(x^2+y^2)/(2R(z))} e^{-(x^2+y^2)/w^2(z)}. \tag{4.6}$$

Taking the terms one at a time, we ahove the electric field amplitude and polarization $\boldsymbol{E}_0 = E_x \mathbf{e}_x + E_y \mathbf{e}_y$[9], followed by a term normalizing the field amplitude with the ratio of beam size $w(z)$ to the minimum beam size (waist), w_0. After that follows two Hermite polynomials $H_j[x]$. The three exponential function represent

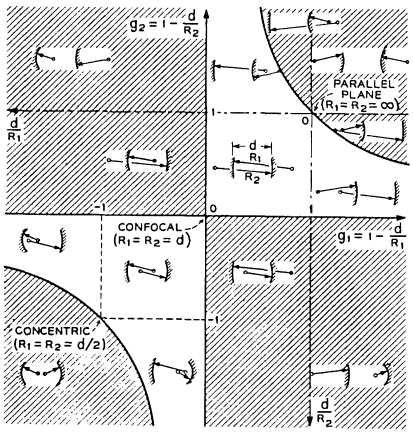

Figure 4.5: Resonator stability diagram. Note the dual axes with g_1, g_2 growing towards $+x, +y$ and $d/R_1, d/R_2$ growing towards $-x, -y$ respectively. Reprinted from Kogelnik and Li (1966).

(9) The polarization is assumed orthogonal to the cavity axis z.

respectively a mode-dependent propagation phase, the phase curvature and the radial decay.

The mode waist size at the minimum is given by

$$w_0 = \sqrt{\frac{\lambda L}{\pi}} \left[\frac{g_1 g_2 (1 - g_1 g_2)}{g_1 + g_2 - 2 g_1 g_2} \right]^{1/4} = \sqrt{\frac{\lambda}{\pi}} \left[\frac{L(R_1 - L)(R_2 - L)(R_1 + R_2 - L)}{(R_1 + R_2 - 2L)^2} \right]^{1/4}, \quad (4.7)$$

and evolves as

$$w(z) = w_0 \sqrt{1 + \frac{z^2}{z_R^2}}, \quad (4.8)$$

where z_R is the *Rayleigh range*

$$z_R = \frac{\pi w_0^2}{\lambda}, \quad (4.9)$$

and the curvature $R(z)$ given by

$$R(z) = z + \frac{z_R^2}{z}. \quad (4.10)$$

The waist position relative to the end mirrors is given by

$$z_1 = \frac{-L g_2 (1 - g_1)}{g_1 + g2 - 2 g_1 g_2} \qquad z_2 = \frac{L g_1 (1 - g_2)}{g_1 + g_2 - 2 g_1 g_2} = z_1 + L. \quad (4.11)$$

Restricting ourselves to the case of a symmetric cavity, i. e., where $R_1 = R_2 = R$, we can plot the cavity waist size and the beam size at the mirrors as a function of L, as seen in Fig. 4.6. The waist size, w_0, is symmetric around $L = R$, and tends to zero for $L \to 0$ and $L \to 2R$. For small L the beam size at the mirrors, w_1, follows w_0, but deviates substantially for $L \gtrsim R/2$, and diverges as $L \to 2R$. Choosing the geometry of the optomechanical cavity is important, because a too large waist size leads to scattering on the phononic pattern, which leads to excess intracavity losses. In general, it is therefore advisable to have a cavity with L close to either 0 or $2R$, to minimize scattering losses.

Computing the stability for the range of lengths, shows that the cavity is only marginally stable for $L \sim 0$, $L \sim 2R$, and (perhaps more surprising) for $L \sim R$. This means that any mirror tilt or difference in mirror ROCs, will render the cavity unstable; avoiding the latter configuration is therefore a good idea for optomechanics.

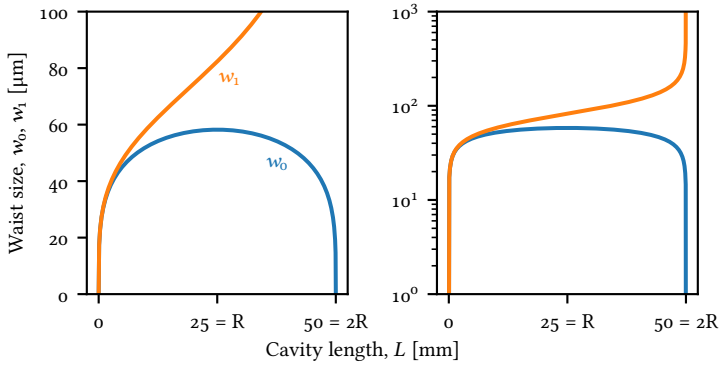

Figure 4.6: Cavity waist size, w_0, and beam size at the mirrors, w_1, as a function of cavity length, L, for a symmetric cavity, $R_1 = R_2 = R = 25\,\text{mm}$. Left panel: linear scale. Right panel: Logarithmic scale. For small L the sizes are almost identical, while for large L the waist size is small and the spot size at the mirrors diverges.

The mode-dependent *Gouy phase* in Eq. (4.6) gives rise to a mode-dependent resonance condition, splitting the different modes according to $m + n + 1$ as well as the longitudinal mode number q, as

$$\nu_{mnq} = \text{FSR}\left[q + \frac{1}{\pi}(m + n + 1)\arccos\left(\sqrt{g_1 g_2}\right)\right], \tag{4.12}$$

with the FSR defined in Section 3.6, and the *transverse mode spacing*, TMS, given by

$$\text{TMS} = \frac{\text{FSR}}{\pi}\arccos\left(\sqrt{g_1 g_2}\right). \tag{4.13}$$

The FSR, TMS and the ratio TMS/FSR is plotted in Fig. 4.8. The FSR drops off as $\propto L^{-1}$, as expected, while the TMS in absolute frequency has a non-trivial shape; comparing the TMS to the FSR reveals a simpler relation. For short cavities the splitting between consecutive modes is small (TMS is small). For $L = R$, $\text{TMS} = \text{FSR}/2$, so equal order modes overlap with equal order modes of other axial modes (q), and odd modes overlap with odd modes. For $L \to 2R$, $\text{TMS} \to \text{FSR}$, but this limit is not practical due to the diverging beam size at the mirrors and the lack of stability of the resonator. In Fig. 4.7 an example spectrum is shown, for $\text{TMS}/\text{FSR} \sim 1/3.5$.

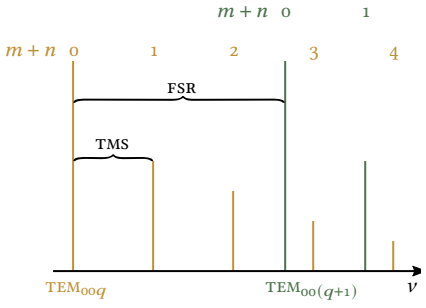

Figure 4.7: Free Spectral Range, FSR, and Transverse Mode Spacing, TMS. The modes with longitudinal mode number q are split by the TMS for every increase in $m + n$, the transverse mode numbers. The distance between two consecutive longitudinal modes, TEM_{00q} and $\text{TEM}_{00(q+1)}$, is the FSR. Peak heights are arbitrary but represent a typical spectrum for a misaligned cavity. Each peak represents $(m + n + 1)$ degenerate modes.

4.2.2 Mode Matching to a Cavity

While the usual solution for a Fabry–Perot cavity with round mirrors is not the one given above, in Eq. (4.6), but rather that of Laguerre–Gaussian modes (which will be covered in Chapter 7), which have rotational symmetries, inserting an ever so slightly tilted membrane into a cavity breaks this symmetry and effectively splits the mode of equal $m + n$ slightly. In practice, completely eliminating tilt is almost impossible, so the basis most relevant to us is indeed the Hermite–Gaussian modes.

In Chapter 3 we derived a model under the assumption of only a single optical mode being populated. The frequency of different longitudinal modes serves a a

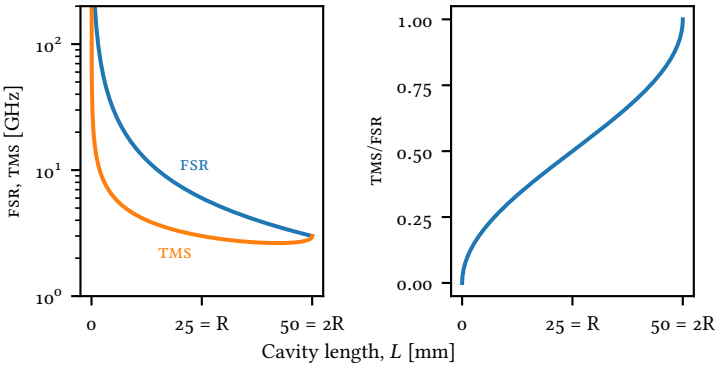

Figure 4.8: Free Spectral Range, FSR, and Transverse Mode Spacing, TMS, and their ratio, TMS/FSR, for a symmetric cavity with $R = 25$ mm.

discriminator in this case, but with potentially much smaller transverse mode spacing, we have to work a little harder to ensure that only a single mode is populated. Here, the spatial overlap of the input optical beam with the transverse cavity mode of interest will serve as a spatial discriminator, ensuring that light is only coupled into a single mode, and with as high an efficiency as possible; this procedure is known as mode matching.

Modematching of optical beams to cavities is covered excellently in Anderson (1984)[10]. As noted there, the set of Hermite–Gaussian (or, equivalently, Laguerre–Gaussian) modes forms a complete set. The approach is therefore to decompose the input optical beam onto this set of modes; this is most easily done at the waist, where the modes take their most simple form – the beam has the smallest size, and the phase fronts are flat. In total, six parameters determine the overlap of the input beam with a given cavity mode: two describing transverse translation, two describing relative rotations of the cavity axis and input beam propagation direction and finally the waist axial position and size.

(10) Dana Z. Anderson (1984). "Alignment of resonant optical cavities". In: *Appl. Opt.* 23.17, pp. 2944–2949.

It is almost always easiest to perform mode matching of an input beam by measuring the transmitted intensity; in reflection the size of the dips in the reflection depends heavily on the cavity overcoupling, whereas in transmission the overall gain on the detector can be adjusted to a suitable level (or the input beam attenuated with a neutral density filter). One then scans either the laser frequency or a piezo in the cavity by at least one FSR, which is often easily identified by a repeated pattern in the transmission peaks, and detects the transmitted intensity with a suitable photodetector and an oscilloscope.

If the input beam is close to aligned (correct transverse position and rotation) and close to mode matched (correct waist position and size), Anderson (1984) shows that the mismatched mode couples only to transverse modes with $m + n > 2$, i. e., which are spectrally offset from the fundamental by $2 \times$ TMS. The other four parameters couple to the first higher order family with $m + n = 1$. In practice, this means that it is possible to isolate the effects of misalignment and suboptimal modematching; by iteratively removing the coupling of the input beam to the $\mathrm{TEM}_{10}/\mathrm{TEM}_{01}$ family, offset by 1TMS from the fundamental (which can be done

solely by displacing and rotating the beam axis relative to the cavity axis), the mode mismatch can be assessed. The beam waist size and position can then be adjusted by moving one or more lenses in the beam path, and the alignment re-optimised.

To assess which direction the beam is mis-aligned, a camera imaging the transmitted intensity is often helpful. By scanning the cavity over a full FSR and imaging the output beam, it is possible to infer which axis (x or y) is most mis-aligned, and adjust the beam steering mirrors before the cavity accordingly. Such a picture, for a well-aligned TEM_{00} mode, can be seen in Fig. 4.9.

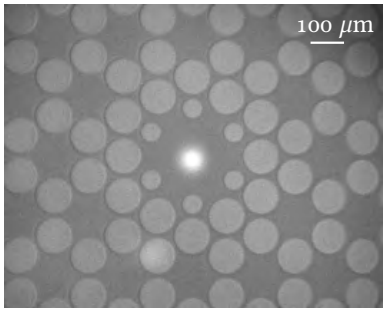

Figure 4.9: The optical mode on the membrane.

4.3 The Cryostat

Since thermal perturbations is our main enemy in terms of decoherence, it is absolutely necessary to cool the optomechanical assembly to cryogenic temperatures. Broadly speaking, three options exist: liquid nitrogen (LN, 77 K), liquid helium (LHe, 4 K) and helium dilution fridges (~50 mK).

In practice, LN turns out to be not cold enough, and some kind of helium based cooling is needed. In Section 4.3.1 I discuss our choice of cryostat, the Janis ST-100. Then, in Section 4.3.2, I discuss why we did not, despite its many potential advantages, buy a closed cycle cryostat or a dilution refrigerator.

4.3.1 Janis ST-100 LHe Crystat

The cryostat used in our experiment is the Janis[11] ST-100 flow cryostat, depicted in Fig. 4.10. The cryostat uses either LHe or LN, which is supplied to the cryostat from the topmost flange, into which a transfer tube can be inserted. The cryogenic then evaporates, and is vented to the environment through the KF flange on the top tube.

(11) Janis has since been acquired by Lake Shore Cryotronics, Inc.

The cryostat can be mounted either vertically, as depicted, or horizontally – we exclusively use it in the vertical orientation. In the science chamber, at the bottom, a cold finger with attachment points (see Fig. 4.11) for out optomechanical assembly is found.

Optical access to the cryostat is provided through up to four windows. We have no use for two of these, so they are masked off with aluminium blanks. Janis supplies only windows without optical coatings. To minimize optical losses, 1 in windows with high quality anti-reflection coatings for 852 nm have been epoxied into aluminium blanks.

The cryostat can operate in two main modes: push and pull. In the push mode, a slight overpressure in the cryogenic dewar pushes the liquid and gas through the transfer tube, into the cryostat, while in pull-mode a vacuum pump enhances the pressure differential across the cryostat, effectively sucking, or pulling, the cryogenic through the system. We most often use the system in push mode, relying solely on the pressure in the dewar for getting the flow running. On rare occasions, starting the flow with a pump can aid the process. Once flow is established, the pump can be turned off – much like how a chimney sucks better once it has been heated.

Running the pump on the cryogenic line does have one main advantage: it lowers the boiling point of the cryogenic liquid, thus reducing the lowest attainable

Figure 4.10: The ST-100 cryostat. Gas/vacuum ports from top to bottom: LHe inlet port, LHe outlet/vent, science chamber vacuum port with valve. Total height: 60 cm.

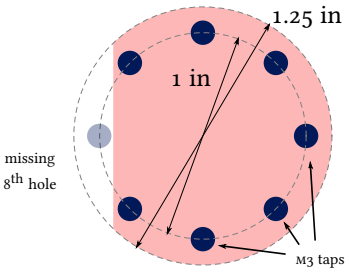

Figure 4.11: Approximate geometry of the cold finger. 7 M3 holes on a 1 in diameter, spaced at 45° intervals, with a flattened edge. The overall diameter is 1.25 in. When the cryostat is mounted in the orientation shown in Fig. 4.10 the depicted plane and holes point towards the floor. Scale 1:1.

temperature. For our cryostat around 2 K can be achieved at the cold finger in pull mode. The sacrifice one makes is mechanical vibrations associated with the pumping action, and an increase in consumption (with a corresponding reduction in operating time).

The cryostat also supplies a means of reducing the gas pressure at the membrane. We evacuate the cryostat with a Pfeiffer HiCube eco 80 pumping station, which includes both a small turbo pump, backing pump and integrated controls for push-button operation. The ST-100 is by no means a high vacuum system. At room temperature, we never observe much below 10^{-3} mbar[12], measured with a sensor placed at the pump – so the pressure in the chamber is probably even somewhat worse. However, at cryogenic conditions, *cryo pumping*, the action of condensation of gas particles onto cold surfaces, reduces the chamber pressure to levels where we are no longer limited by gas damping, and routinely observe $Q \sim 10^9$. In this regime, the measurements at the pump reach around 10^{-6} mbar, which is probably *higher* than the chamber pressure.

The turbo pump runs at 90 000 rpm, or with a frequency of 1.5 kHz. If the pump is connected directly to the cryostat, this vibration completely prevents any locking of the optomechanical cavity, due to the size of the excursions. This is solved by the introduction of what Nielsen (2016) calls a *impedance mismatch* along the vacuum line. In practice, this means embedding a section of the vacuum tube in a suitably large chunk of cement. This extra mass effectively dampens all vibrations, allowing us to lock the cavity with the pump running.

The mounting and mechanical design of the cryostat has a couple of drawbacks, related to the length. One, the central part of the cryostat itself contracts by more than a mm upon cooldown. This is by no means a showstopper, as the length is stable almost as soon as a cryogenic temperature has been reached, but it does completely mis-align the cavity from the input optical beams. This means that coupling the beam into the cavity has to be re-optimized continuously when changing between room temperature and cryogenic operation. Secondly, and worse, suspending the ~60 cm long cryostat vertically entails equally long supports standing on the optical table. For the experiments in Chapter 10, we used Bosch Rexroth aluminium profiles, which are good for many things, but whose thermal expansion of around 23 ppm/K means that a 1 K change of temperature of a 60 cm beam will displace the cavity by around 14 µm, which should be compared to the beam waist of around 50 µm. Differential heating of the two beams supporting the cryostat is even worse, as this effectively tilts the membrane, with a cantilever effect, amplifying the mis-alignment. We have since upgraded the vertical beams to Invar[13], which drops the thermal expansion coefficient to around 1.2 ppm/K.

4.3.2 Why Not Closed Cycle?

The choice of using a flow cryostat raises the obvious question: why not closed cycle? A lot of the problems related to flow cryostats can be solved[14] by buying a closed cycle cryostat. One might even consider going for a dilution refrigerator, instead of a 4 K cryostat.

The primary advantage of using a closed cycle cryostat is the continuous operation of cryogenic temperatures. With 4 K operating times are limited to a handful of days, before a typical 100 l dewar is depleted. With closed cycle, samples can be

(12) Better known as "kitchen vacuum".

(13) An iron-nickel alloy with approximately 64 % iron and 36 % nickel. Also known as FeNi36.

(14) Given enough grant money can be acquired.

kept cold for practically unlimited time.

The main disadvantage of closed cycle systems is the presence of recondensers, used to re-liquefy the helium. These typically involve a displacer unit operating at at frequency of 1 Hz, periodically modulating the gas pressure at the cold head. The slow but sudden change of gas pressure leads to periodic wideband mechanical noise, perturbing the optomechanics. While the displacements are small, even minute forces resonant with, e. g., a low-frequency membrane mode, may completely hamper optomechanical operation. A *Montana Cryostation C2* was tested in our labs in the spring of 2016, and found to have unacceptable excursions for our needs.

The possibility of reducing the bath temperature from 4 K to mK range in a dilution fridge poses the same mechanical disadvantage, but would be very beneficial in relaxing requirements for optomechanical cooling. However, as will be discussed later, we do not observe thermalization to even 4 K of our membranes; instead they thermalize to somewhere around 10 K. The mechanism leading to this elevated temperature is not understood at present—it seems, most importantly, to be independent of probe light power—rendering thermalization anywhere close to mK temperatures wishful at best. In our sister group of Albert Schließer (see Rossi (2020, appendix C)[15]), a Bluefors LD-250 dilution refrigerator has been used with some success, albeit only for pure interferometric measurements of bare membranes (no cavities), and with no free space optical access—laser light is guided trough fibers, rendering such a cryostat unusable for our needs—or, as reported in Seis (2021)[16] for electro-mechanics, where the optical beams are replaced by microwave electrical drives.

In summary, closed cycle cryostats would, if mechanical disturbances can be alleviated, provide a significant experimental improvement, especially if the question of thermalization can be solved, and the membrane bath temperature reduced by order(s) of magnitude. However, cashing out the money for such a device is a large investment, considering the amount of unknowns.

(15) Massimiliano Rossi (2020). "Quantum Measurement and Control of a Mechanical Resonator". Ph.D. thesis. University of Copgenhagen.

(16) Yannick Seis (2021). "Ultra-Coherent Electro-Mechanics in the Quantum Regime". Ph.D. thesis. University of Copenhagen.

4.4 Q-measurements

A central figure of merit of membranes is, as stated the *quality factor* or Q-factor, i. e., the ratio of oscillation frequency to damping :

$$Q = \frac{\omega}{\gamma}. \tag{4.14}$$

This quantity shows up again and again, e. g., in the coherence time of the oscillator, and is therefore of vital importance for our experiments. In general, the Q is limited by several different factors, that all add up like (Aspelmeyer, Kippenberg, and Marquardt 2014)

$$Q_{\text{total}}^{-1} = \sum_i Q_i^{-1}, \tag{4.15}$$

where i labels the individual loss mechanisms, which include things like:

- gas damping
- clamping losses

- anharmonic effects, including thermoelastic damping and phonon-phonon interactions
- material-induced losses, including losses induced by fabrication or material defects; this is often modeled by so-called two-level defects

Longer discussions of these loss mechanisms can be found in, e. g., Yeghishe Tsaturyan (2019), Møller (2018) or in the review article Aspelmeyer, Kippenberg, and Marquardt (2014).

For a square membrane, the gas damping for the (n, m) mode is (Bao et al. 2002)[17]

$$Q_{\text{gas}} = \rho d \omega_{nm} \sqrt{\frac{\pi RT}{32 m_{\text{molar}}}} \frac{1}{p}, \tag{4.16}$$

where R is the gas constant, m_{molar} is the molar weight of the residual gas and p is the gas pressure, which we seek to lower with our vacuum equipment. Q_{gas} can be seen for room and cryogenic temperatures in Fig. 4.12. This equation also neglects an effect know as *squeeze damping*, which starts to matter when membranes are positioned close to large objects, like mirrors. For details see Bao et al. (2002) and Møller (2018, p. 54).

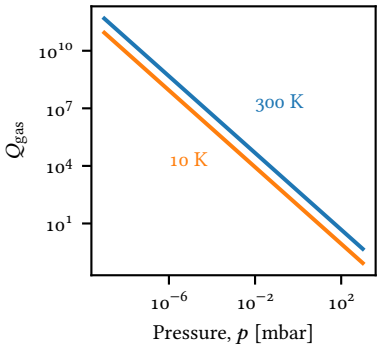

Figure 4.12: Q_{gas} as a function of pressure p, for $T = 300\,\text{K}$ and $10\,\text{K}$. $d = 20\,\text{nm}$, $\omega/2\pi = 1.3\,\text{MHz}$, $\rho = 3.17\,\text{g/cm}^3$, $m_{\text{molar}} = 29\,\text{g/mol}$.

(17) Minhang Bao et al. (2002). "Energy transfer model for squeeze-film air damping in low vacuum". In: *Journal of Micromechanics and Microengineering* 12.3, pp. 341–346.

In general, we seek to measure the *quality*[18] of our samples. While things like internal and clamping losses are something that can be alleviated or minimized in the design and fabrication steps, once a device leaves the cleanroom, the only two real handles we, as experimentalists, have are the sample temperature and the pressure of the surrounding gas. Because cryogenic cooldown of entire wafers of samples[19] is unfeasible, primary characterization needs to happen at room temperature. Once a given membrane has been installed into an optomechanical assembly, its Q can be checked *in situ* and at cryogenic temperatures, as long as one ensures that dynamical optomechanical effects can be neglected.

Since the Q is, per Eq. (4.14), a ratio of resonance frequency to linewidth, the temptation might fall upon the researcher to simply try to go and measure both of these quantities. However, for our membrane where Q routinely falls in the range of 100 million to a billion ($10^8 - 10^9$), and for frequencies around 1 MHz, the linewidth is only on the order of mHz. Getting this kind of spectral resolution is very hard. We therefore need a different approach.

(18) Both the Q and in a more general sense

(19) Typically 21 samples on a 6 inch wafer, which absolutely does not fit in our cryostats.

4.4.1 Ringdown Measurements

The way we measure Qs can be summarized rather simply: excite the membrane to a large, classical amplitude, and measure the exponential decay. In practice, this excitation can be performed with either a piezo, mechanically shaking the entire membrane and frame, or by the application of a modulated radiation pressure force. The two methods offer slightly different advantages, but for our purposes can be considered essentially identical – for purposes such as measuring the displacement profile of a membrane, the difference between local and global excitation of the mode becomes important. Details about our specific setup for Q characterization can be found in Barg (2014)[20].

(20) Andreas Barg (2014). "Optical Characterization of Micromechanical Membranes". M.Sc. thesis. University of Copenhagen & University of Hamburg.

Recalling Eq. (3.37), the lock-in detection of a large oscillation amplitude decaying, and rewriting it in a simpler form, the large initial oscillation amplitude x_{R0}, decays as

$$x_R(t) = x_{R0} e^{-\gamma t/2}. \tag{4.17}$$

By detecting the decay, and fitting it with a function ae^{-bt}, we can then infer $\gamma = 2b$, and obtain

$$Q = \frac{\pi \nu_m}{b} = \frac{\omega_m}{2b}. \tag{4.18}$$

Importantly, a does not enter into the equation, so we do not have to worry about transduction efficiencies or other complicating factors; as long as the amplitude is large enough to be reliably detected above the noise floor and the excitation is large enough to dwarf out thermal motion we should be fine. With frequencies of $\sim$1.4 MHz and Q of $\sim 1 \times 10^8$, $b \sim 4 \times 10^{-2}$, or a time constant $\tau = b^{-1}$ of $\tau \sim 22$ s for the signal to decay to 1/e.

The read out scheme is very close to the one described in Section 3.5, with the membrane motion inducing an optical phase shift $\Delta\varphi(t) = k2\Delta x_R(t)$, which we then detect interferometrically in a Michelson-type interferomter, as depicted in Fig. 4.13. Where a normal Michelson interferometer uses a non-polarizing beamsplitter, we use a PBS and half wave plates in each arm, and perform polarization homodyning of the combined beams. A piezo in the reference arm stabilizes the interferometer with the sum of of the photocurrents from the detectors.

A lock-in amplifier[21] drives either an AOM, leading to a modulated radiation pressure force, or a piezo. The same lock-in amplifier then demodulates the detected photocurrent at the modulation frequency, and yields $x_R(t)$. Since the membranes have linewidths of on a couple of mHz, very fine control of the excitation frequency is needed.

A typical data trace for a ringdown measurement is shown in Fig. 4.14. During the times marked in red, the excitation force is turned on, and the amplitude of the oscillations grow. As soon as the excitation is turned off, the amplitude decays like a simple exponential. By knowing the exciting frequency and fitting the decay time, Q can be measured.

Once the membrane has been assembled into a full optomechanical cavity and placed in our ST-100 cryostat, we need to measure the Q again. However, as noted above, the gas pressure in our cryostat at room temperature leaves a lot to be desired, and we are therefore gas damping limited at room temperature. Here we can only assess whether things are *potentially ok* or *very much not ok*, i. e., if the Q is gas damping limited or *very low*, $Q \lesssim 10^{-6}$. At cryogenic temperatures, gas damping is no longer a limitation, but we have to consider optomechanical effects. If we probe the cavity red detuned we can dampen the membrane, and blue detuned we can reduce the effective damping, both of which are obviously bad estimates of the intrinsic Q.

In practice, our approach is to detune the laser close to the lower limit of the Ti:Sapph tuning range, approximately 780 nm. At this wavelength, the mirror coatings are dramatically less reflective, and the cavity finesse is reduced to a number close to unity, reducing cavity intensity build-up, reducing g, and thus optomechanical effects like optical damping. To further ensure that optical damping plays no

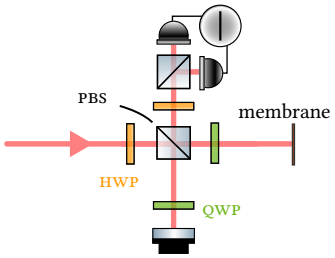

Figure 4.13: Michelson type interferometer for membrane Q measurements.

(21) Typically a ZURICH INSTRUMENTS HF2LI.

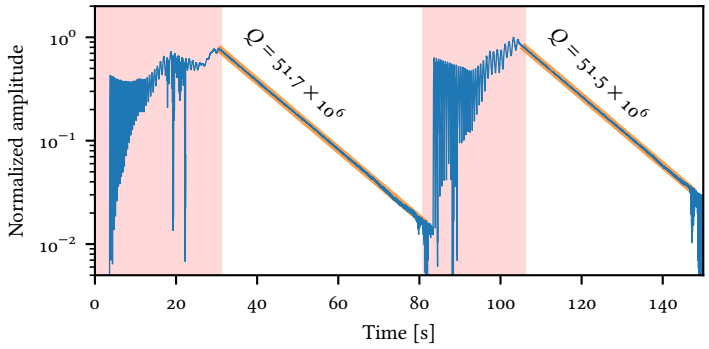

Figure 4.14: Ringdown measurement example. The red regions are excluded from the fits, and used for exciting the membrane. Data (blue) is fitted by a simple exponential ae^{-bt} (orange), and the Q is calculated with Eq. (4.18). This membrane has $\nu_m = 1.26\,\text{MHz}$, and $Q \sim 51 \times 10^6$ at room temperature.

role, we measure the Q through ringdown measurements with laser detuned *both red and blue* (typically at the half-max transmission point on both sides), arguing that if the measured Qs and thus linewidths are equal, i. e., $\gamma_{mo} + \gamma_{opt} \cong \gamma_{mo} - \gamma_{opt}$, then γ_{opt} is very small, and can be ignored.

4.5 Membrane Temperature Calibrations

Calibrating the membrane temperature is important, as it determines the thermal decoherence rate and membrane occupation for a given optical damping rate.

One standard way of measuring the effective bath temperature T follows Gorodetsky et al. (2010)[22]. This procedure is also described in detail in Nielsen (2016, chapter 3.8). The method uses the fact that the integrated displacement spectrum of Eq. (3.47) is directly proportional to the temperature, as well as to the quantity $g_0^2 n_{eff}$, with n_{eff} being the effective occupation of the membrane. Assuming g_0 is constant for a range of temperatures, one can measure at number of effective temperatures, while keeping $C_q \ll 1$ to minimize quantum backaction, and fit the relationship between cold finger temperature and effective temperature.

(22) M. L. Gorodetsky et al. (2010). "Determination of the vacuum optomechanical coupling rate using frequency noise calibration". In: *Opt. Express* 18.22, pp. 23236–23246.

However, this method is cumbersome in practice. It involves stabilizing the cryostat at a number of temperatures, and for each ensuring you are operating at the same $2kz$ point, before taking a number of spectra with varied detuning. Once this process has been performed once for a given membrane geometry and cavity assembly, easier (but somewhat less precise) methods usually suffice. Consistent observations across time and different setups with identical membranes serves as a sanity check for these methods.

The most used method for our setup is to measure ponderomotive squeezing in transmission, from which the effective bath temperature can be extracted through the $\gamma_m(n + 1/2)$-term in the denominator

$$C_q = \frac{4g^2}{\kappa\gamma_m(n + 1/2)}, \tag{4.19}$$

and by knowing the other parameters separately, because the amount of squeezing observed scales with (Møller 2018, sec. 4.4)

$$\frac{S^{\text{out}}_{X_\text{L}X_\text{L}}}{\text{SN}} = 1 - \frac{C_\text{q}}{C_\text{q} + 1}. \tag{4.20}$$

In Chapter 10 we fit our full model to squeezing traces in transmission, and deduce an effective bath temperature of 11 K, in line with what is reported elsewhere, for similar membranes. This is somewhat higher than the approximately 7 K reported for the previous generation of membranes, such as in Møller et al. (2017).

Chapter 5

Alkali Spin Systems

> “When physicists don’t understand something, they do what everyone else does: give it a name. That helps them talk about it, but don’t confuse that with understanding.
>
> Richard A. Muller

The physics of alkali atomic spin systems.

The second material system in our hybrid setup is formed by the collective spin of a large number ($N \sim 10^9$) of room temperature cesium atoms, confined in a glass cell. In this chapter we will cover the short version of spin systems; the interested reader may consult, e. g., Brian Julsgaard (2003)[1] and Rodrigo A. Thomas (2020)[2]; a number of the figures in this chapter is reproduced with permission from the latter. The main goal is to describe how a collection of atomic spins may serve as one effective harmonic oscillator.

We end the section with a section about CIFAR, a novel spin readout rate calibration method, reported in Rodrigo A. Thomas et al. (2021)[3].

5.1 Spin Ensembles

5.1.1 Cesium

Our spin ensemble consists of cesium-133. Cesium is the heaviest, stable[4] alkali metal. Cesium-133 is the only stable isotope, and as such only trace amounts of other isotopes occur in cesium samples; cesium-137, a fission product of uranium-235, being the most prominent.

Cesium is an attractive choice of atom for a number of reasons: a relatively simple electronic level structure, owing to the single electron in the outermost shell, high vapor pressure at room temperature, and widely available laser sources,

(1) Brian Julsgaard (2003). “Entanglement and Quantum Interactions with Macroscopic Gas Samples”. Ph.D. thesis. University of Aarhus.

(2) Rodrigo A. Thomas (2020). “Optical spin-mehcanics quantum interface: entanglement and back-action evasion”. Ph.D. thesis. University of Copenhagen.

(3) Rodrigo A. Thomas et al. (2021). “Calibration of spin-light coupling by coherently induced Faraday rotation”. In: *Opt. Express* 29.15, pp. 23637–23653.

(4) The heavier francium is radioactive; the most stable isotope is francium-223 and has a half-life of 22 min.

to name some. Other noteworthy alternative alkali metals are potassium and rubidium. For cesium, the standard reference for any kind of data is Steck (2019)[5].

Cesium has a nuclear spin of $I = 7/2$, which together with the electron spin of $S = 1/2$, gives the two possible ground state spin amplitudes $F = \{3, 4\}$. For the first electronically excited state, $L' = 1$, so $J' = L' + S'$ assumes the values $\{1/2, 3/2\}$. The two excited states thus have $F' \in \{3, 4\}$ and $F' \in \{2, 3, 4, 5\}$ respectively[6]. Cesium has the electron structure $[\mathrm{Xe}]6s^1$, with the first excited state being $[\mathrm{Xe}]6p^1$, and thus the two transitions are $6^2S_{1/2} \rightarrow 6^2P_{1/2}$ and $6^2S_{1/2} \rightarrow 6^2P_{3/2}$[7]. These two transitions are referred to respectively as the D_1 and D_2 transitions, and have transition wavelengths of $\lambda_{D_1} = 894.592\,\mathrm{nm}$ and $\lambda_{D_2} = 852.347\,\mathrm{nm}$. This large scale level structure is depicted in Fig. 5.1, together with our optical probing, pumping and repumping scheme.

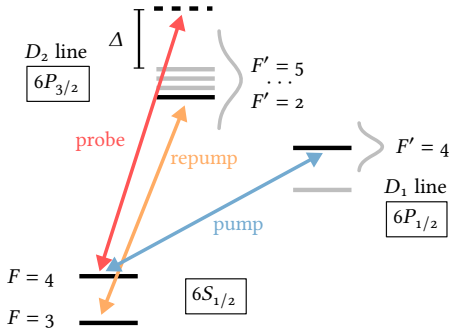

Figure 5.1: Level scheme of cesium, with our optical probing, pumping and repumping scheme. Δ is our probing detuning from the $F = 4 \rightarrow F' = 5$.

Due to the large energy separation between the ground state manifold and the two excited states, essentially all atoms will be somewhere in the ground state unless actively pumped to an excited state. Therefore, we will concern ourselves mainly with the dynamics of the spins in the ground state manifold, and the effects of external magnetic fields. The different spins (nuclear, orbital angular, and electron) each have their own magnetic moment μ, and all interact with each other via the fine and hyperfine couplings. If the energy shifts induced by an external magnetic field $\mathbf{B}$ are small compared to the hyperfine splittings[8], the good quantum numbers are F and the projection on our chosen quantization axis, m_F; the latter is, since we're always dealing with the F, m_F quantization, sometimes simply denoted m. The total level structure involved in the D_2 transition is shown in Fig. 5.2. The energy of a state with total angular momentum F and projection m_F, $E_{F,m}$ is given by the *Breit–Rabi forumla* (Steck 2019)

$$E_{F,m} = -\frac{h\nu_{\mathrm{hfs}}}{2(2I+1)} + g_I\mu_B mB \pm \frac{h\nu_{\mathrm{hfs}}}{2}\sqrt{1 + \frac{4m}{2I+1}x + x^2}, \tag{5.1}$$

where h is Planck's constant, ν_{hfs} is the hyperfine splitting, the sign $\pm$ is the same as $F = I \pm 1/2$, $B = |\mathbf{B}|$, $\mu_B = h \cdot 1.4\,\mathrm{MHz/G}$ is the Bohr Magneton, and x quantifies the relative strength of the Zeeman effect (second term in (5.1)) to the hyperfine

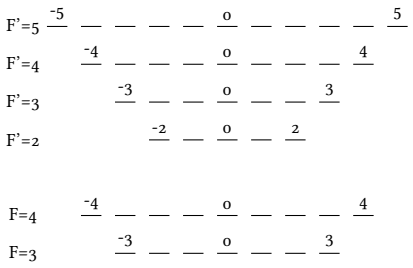

Figure 5.2: Cesium D_2 levels in both the upper and lower manifolds. The numbers above the lines denote the m_F quantum number. There are 16 states in the lower manifold and 32 in the upper.

(5) Daniel A. Steck (2019). *Cesium D Line Data.* available online at http://steck.us/alkalidata (revision 2.2.21, 21 November 2019).

(6) We will use primes to denote spin values for the electronically excited states, and unprimed for the ground state. Usually, we put the prime on the letters (e. g., F'), but sometimes one may encounter a shorthand like $5'$.

(7) Notation is

$$n^{2S+1}L_J,$$

with n the electron shell number, S the spin (and thus $2S+1$, or *spin multiplicity*, the number of available spin states J, if $L \geq S$; for $L > S$ the available number of Js is $2L + 1$), L the orbital angular momentum and J the total angular momentum $J = L + S$.

(8) An assumption that will always hold in this thesis.

splitting

$$x = \frac{(g_J - g_I)\mu_B B}{h\nu_{hfs}}. \tag{5.2}$$

The spin-orbit and nuclear g-factors are approximately $g_J \approx 2$ and $g_I \approx -4 \times 10^{-4}$[9]. For the magnetic fields relevant to our experiment, $B < 10\,\mathrm{G} = 1\,\mathrm{mT}$, which gives $x \sim 10^{-3}$.

(9) See Steck (2019) for exact values

Expanding Eq. (5.1) around $x = 0$, and keeping only the first and second order terms, gives us a suitable expression for the energies in the low-field limit. For the $F = 4$ levels,

$$E_{4,m} = \hbar\omega_s m + \frac{\hbar\omega_{qzs}}{2}m^2, \tag{5.3}$$

where ω_s is the *Larmor frequency* and ω_{qzs} is the *quadratic Zeeman splitting*, given respectively by

$$\frac{\omega_s}{2\pi} = \frac{g_F\mu_B B}{h} = \nu_s \tag{5.4}$$

$$\frac{\omega_{qzs}}{2\pi} = \frac{2\nu_s^2}{\nu_{hfs}}. \tag{5.5}$$

The hyperfine Landé g-factor is given by

$$g_F = g_J\frac{F(F+1)-I(I+1)+J(J+1)}{2F(F+1)} + g_I\frac{F(F+1)+I(I+1)-J(J+1)}{2F(F+1)} = \begin{cases} 0.250390 & \text{for } F = 4 \\ -0.251194 & \text{for } F = 3. \end{cases} \tag{5.6}$$

In the end, the Larmor frequency scales as $350\,\mathrm{kHz/G} \cdot B$; to match the mechanical frequencies of $1.4\,\mathrm{MHz}$, we therefore need magnetic fields around $4\,\mathrm{G}$ - a rather modest requirement[10]. For $B = 4\,\mathrm{G}$, $\omega_{hfs}/2\pi = 428\,\mathrm{Hz}$. This is on the order of the spin linewidths that we have, so some cancellation of this shift will be needed.

(10) For comparison, the earth magnetic field in Copenhagen is around 0.5 G, highlighting that magnetic shield will be important for us

The quadratic Zeeman shift is positive for all values of m_F, and the frequency difference between two adjacent m_F-levels, where $\Delta m = m' - m = 1$, is

$$\frac{E_{m'} - E_m}{\hbar} = \frac{E_{m+1} - E_m}{\hbar} = \omega_s + \omega_{qzs}\left(m + \frac{1}{2}\right), \tag{5.7}$$

so for the extreme levels, the effect is larger by a factor 4 or 3, depending on F. The quadratic Zeeman splitting may also be used to spectrally separate the different transitions in the limit where $\omega_s \gg \gamma_s$; we will use this fact to measure the spin polarization with MORS, as explained in Section 5.6.

In the experiments, laser light or radio frequency radiation will drive transitions between different m_F-levels. Due to selection rules, only transitions with $\Delta m_F \in \{0, \pm 1, \pm 2\}$ can be driven, and we will mostly be interested in those where $\Delta m_F = \pm 1$. We will be driving these transitions when the radio frequency field is tuned to $\omega_{rf} \sim \omega_s$, and the difference in spin frequencies will show up in our signals at ω_s. The $2F + 1$ levels will give rise to $2F$ different peaks in the regime where the levels are split by the quadratic term.

Putting what we know about the energies, and restricting ourselves to transitions within a single sub-manifold of the ground state (in practice, $F = 4$), we write

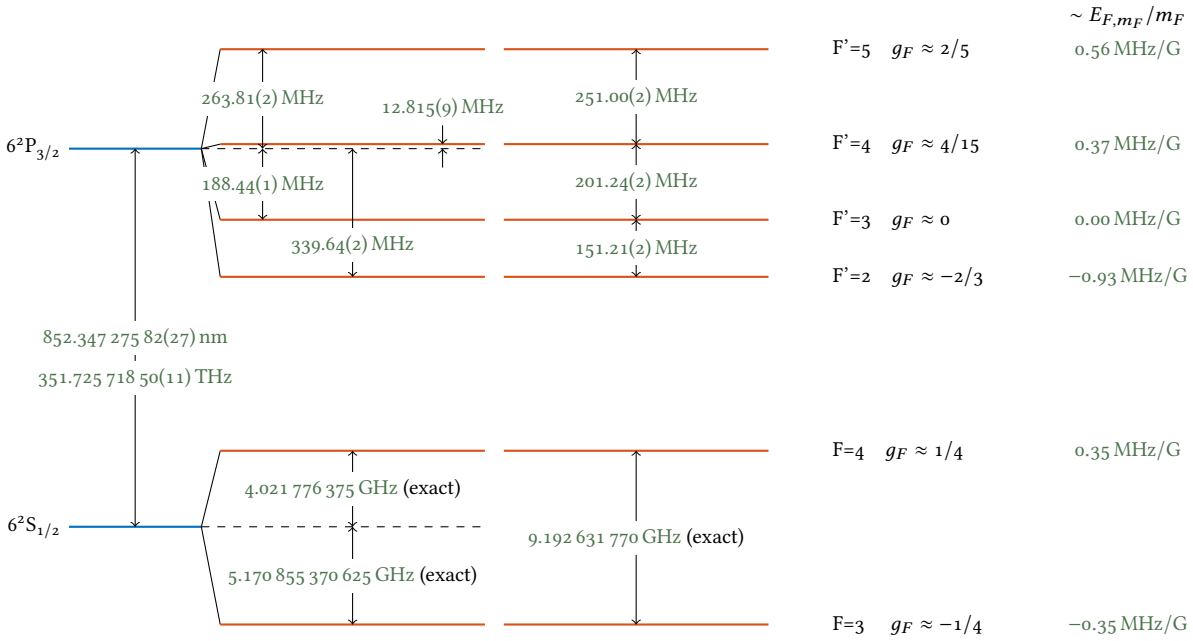

Figure 5.3: Cesium D_2 level structure. The lower manifold is split by the hyperfine splitting into two sub-manifolds with $F \in \{3, 4\}$, and the upper manifold into $F' \in \{2, 3, 4, 5\}$. Figure produced with inspiration from Steck (2019).

the Hamiltonian

$$H_B = \hbar \sum_m \left[\omega_s m \left|m\right\rangle \left\langle m\right| + \frac{\omega_{qzs} m^2}{2} \left|m\right\rangle \left\langle m\right| \right], \tag{5.8}$$

where $|m\rangle$ is a shorthand notation for the state $|F, m_F\rangle$.

Our chosen basis until now has been the energy eigenstates of the atom in an external magnetic field. We now change into a basis of angular momenta. At the same time, we depart from the single atom description thus far, and move explicitly to collective degrees of freedom of our N atoms. The individual atoms have angular momentum $f^{(i)}_{\{x,y,z\}}$, with i indexing the atoms. To preserve consistency with the notation used in other works from my group (see, e. g., Brian Julsgaard (2003), Rodrigo A. Thomas (2020)), the chosen quantization axis is along x, as opposed to the conventional choice of z[11]. In total,

(11) Further, in Rodrigo A. Thomas et al. (2020) the collective spin is labeled $J_{\{x,y,z,0\}}$. I here use the notation from Rodrigo A. Thomas (2020).

$$\begin{aligned}
\hat{F}_x &= \sum_{i=0}^{N} \hat{f}_x^{(i)} = \sum_{i=0}^{N} \sum_{m=-4}^{4} m\hat{A}_{mm}^{(i)} \\
\hat{F}_y &= \sum_{i=0}^{N} \hat{f}_y^{(i)} = \frac{1}{2} \sum_{i=0}^{N} \sum_{m=-4}^{3} c(F,m) \left(\hat{A}_{m+1,m}^{(i)} + \hat{A}_{m,m+1}^{(i)} \right) \\
\hat{F}_z &= \sum_{i=0}^{N} \hat{f}_z^{(i)} = \frac{1}{2\mathrm{i}} \sum_{i=0}^{N} \sum_{m=-4}^{3} c(F,m) \left(\hat{A}_{m+1,m}^{(i)} - \hat{A}_{m,m+1}^{(i)} \right) \\
\hat{F}_0 &= \sum_{i=0}^{N} \hat{f}_z^{(i)} = \sum_{i=0}^{N} \sum_{m=-4}^{4} \hat{A}_{mm}^{(i)},
\end{aligned} \tag{5.9}$$

where $c(F,m) = \sqrt{F(F+1) - m(m+1)}$ and the operator $\hat{A}_{ab}^{(i)} \equiv |a\rangle \langle b|^{(i)} = |F,a\rangle \langle F,b|^{(i)}$ define the weight of the atomic coherences. The sums include respectively the diagonal and the first off-diagonal elements of the total matrix $\sum_n \sum_m |n\rangle \langle m|^{(i)}$.

The four spin operators thus describe the total ensemble spin along the three spatial directions, and the total spin length. We further define $\hat{F}_+ = \hat{F}_y + \mathrm{i}\hat{F}_z$ and $\hat{F}_- = \hat{F}_y - \mathrm{i}\hat{F}_z$, the ladder operators in the angular momentum basis.

The equation here assumes homogeneous coupling to all atoms; in practice this is not the case in any given instant. I will ignore this for now, and refer the interested reader to Brian Julsgaard (2003). The spin operators have the commutator $[\hat{F}_k, \hat{F}_l] = \mathrm{i}\epsilon_{klm}\hat{F}_m$, with ϵ_{xyz} being the Levi–Civita symbol.

In this basis, the energy of the collective spin, neglecting the quadratic Zeeman shift, can be written as

$$H_\mathrm{B} = \hbar\omega_\mathrm{s}\hat{F}_x, \tag{5.10}$$

which takes the form of a classical dipole in an external magnetic field along the x-axis, for which $H \propto \mathbf{B} \cdot \mathbf{F}$.

5.1.2 The Holstein–Primakoff Approximation

In the hybrid experiment we will be working always with a highly spin-polarized ensemble of atoms, i. e., where most of the atoms have their spin aligned along (or anti-parallel to) the magnetic field. In that limit, we may treat the spin along x as a classical variable of size $F_x \sim |\langle \hat{F}_x \rangle|$, with the transverse spin components $\hat{F}_y$ and $\hat{F}_x$ having only small fluctuations.

We now apply the *Holstein–Primakoff transformation* or *approximation* (Holstein and Primakoff 1940)[12]. This allows us to introduce bosonic ladder operators for the collective spins, $\hat{b}$ and $\hat{b}^\dagger$, respectively with $[\hat{b}, \hat{b}^\dagger] = 1$. Following Klemens Hammerer (2006)[13] and Rodrigo A. Thomas (2020), we write the spin component

$$\hat{F}_x = F_x - \frac{\hat{b}^\dagger \hat{b}}{2}, \tag{5.11}$$

i. e., we express it as a mean value plus some small number of fluctuations, that always decrease the total spin length. In the low excitation (high polarization) limit $\langle \hat{b}^\dagger \hat{b} \rangle \ll F_x$, the ladder operators are given by

$$\hat{F}_+ \simeq \sqrt{F_x}\hat{b} \qquad \hat{F}_- \simeq \sqrt{F_x}\hat{b}^\dagger, \tag{5.12}$$

(12) T. Holstein and H. Primakoff (1940). "Field Dependence of the Intrinsic Domain Magnetization of a Ferromagnet". In: *Phys. Rev.* 58 (12), pp. 1098–1113.

(13) Klemens Hammerer (2006). "Quantum Information Processing with Atomic Ensembles and Light". Ph.D. thesis. Technische Universität München.

allowing us to write

$$\hat{b}^\dagger \hat{b} = \frac{\hat{F}_- \hat{F}_+}{F_x} = \frac{\hat{F}_y^2 + \hat{F}_z^2 + \mathrm{i}[\hat{F}_y, \hat{F}_z]}{F_x} \approx \frac{\hat{F}_y^2 + \hat{F}_z^2}{F_x}, \tag{5.13}$$

where the term with the commutator, $[\hat{F}_y, \hat{F}_z] = \mathrm{i}\hat{F}_x$, evaluates to $-\hat{F}_x/F_x$, which is constant, and can be ignored.

Putting this together, we can write the Hamiltonian from Eq. (5.10) as

$$\hat{H}_\mathrm{B}/\hbar = \omega_\mathrm{s}\hat{F}_x \approx \omega_\mathrm{s}F_x - \frac{\omega_\mathrm{s}}{2}\left(\hat{X}_\mathrm{s}^2 + \hat{P}_\mathrm{s}^2\right), \tag{5.14}$$

with the dimensionless spin conjugate variables

$$\begin{aligned} \hat{X}_\mathrm{s} &= \hat{F}_z/\sqrt{\hbar F_x} \\ \hat{P}_\mathrm{s} &= \pm\hat{F}_y/\sqrt{\hbar F_x}, \end{aligned} \tag{5.15}$$

where the ± sign foreshadows the choice of negative or positive effective mass. The conjugate variables have the usual commutator $[\hat{X}_\mathrm{s}, \hat{P}_\mathrm{s}] = \mathrm{i}$. The constant energy term $\omega_\mathrm{s}F_x$, as all constant energy offsets, will contribute nothing to the overall dynamics of the system, and can be disregarded.

5.2 Negative Effective Mass

As alluded to many times already, the spin system will assume the role of an oscillator with negative effective mass. We will now see how this comes about. For a general introduction to the question of quantum frames of reference, with positive or negative mass, see Giacomini, Castro-Ruiz, and Brukner (2019)[14].

The idea is depicted in Fig. 5.4. The state $|0\rangle$ describes the fully polarized state, where all atoms are pointing towards x or $-x$, with the magnetic field B being aligned towards x. If B and F_x are pointing in opposite directions, the state with zero excitations, $|0\rangle$, has the lowest total energy possible. If, on the other hand, the spin is aligned parallel to the magnetic field, the energy is maximized. Which spin polarization one obtains can be chosen, by changing the polarization of the pumping and re-pumping light; σ_+ polarization drives the atoms towards $|4, +4\rangle$ (parallel to B), while σ_- polarized light drives them towards $|4, -4\rangle$ (anti-parallel to B).

If the system starts out in $|0\rangle$, we can add an excitation to the system with $\hat{b}^\dagger|0\rangle = |1\rangle$. This collective operator either *adds* or *subtracts* adds a single quantum of energy ω_s from the system, depending on whether the state is spin and magnetic field is aligned in parallel or anti-parallel, while also increasing the fluctuations in the transverse quadratures, $\hat{X}_\mathrm{s}, \hat{P}_\mathrm{s}$. The feature that *increasing fluctuations in the relevant quadratures* corresponds to *decreasing* the energy is what makes this oscillator effectively negative mass.

In Fig. 5.5 we show a driven measurement of the spin with positive mass ($+\omega$, in blue) and negative mass ($-\omega$, in orange)[15]. The top panel shows the size of the driven responses, which are virtually identical for the two orientations. In the bottom panel, the phase of the responses are shown. Apart from a slight background originating in electrical delays, the blue line fits very well with the expected shape

(14) Flaminia Giacomini, Esteban Castro-Ruiz, and Časlav Brukner (2019). "Quantum mechanics and the covariance of physical laws in quantum reference frames". In: *Nature Communications* 10, p. 494.

(15) The astute reader may have noticed that the convention for the sign on ω_s is a bit messy. My apologies. Sometimes, like here, the negative mass system is represented with frequency $-\omega_\mathrm{s}$ (i. e., $\omega_\mathrm{s} > 0$, so *minus a positive value*), and sometimes we define it as a negative frequency $\omega_\mathrm{s} < 0$. I hope context is enough to devulge which notation is being used at a given time.

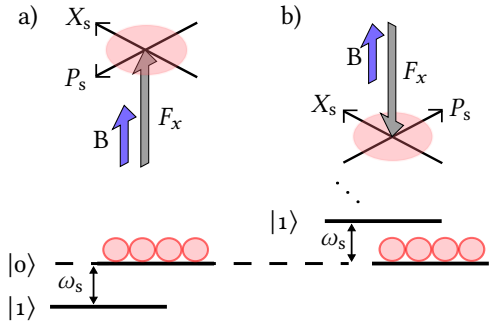

Figure 5.4: Positive and negative mass configurations of the spin. All spins are idealized as residing in the extreme m_F level, which has minimum tranverse fluctuations, which we label $|0\rangle$. Adding an excitation bring the collective spin to the $|1\rangle$ state, while adding (positive mass) or removing (negative mass) $\hbar\omega_s$ of energy. Figure reproduced, with changes, from Rodrigo A. Thomas (2020).

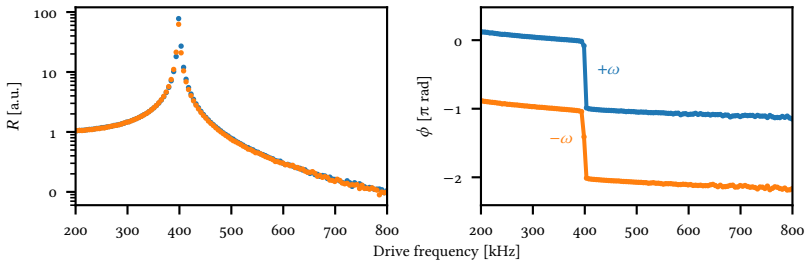

Figure 5.5: Driven response of the spin oscillator with positive and negative mass. The amplitudes of the responses are virtually identical, but the phases are out of phase for the postive mass (blue, $+\omega$) and negative mass (orange, $-\omega$) configurations. Figure reproduced, with changes, from Rodrigo A. Thomas (2020).

of a normal harmonic oscillator: in phase for low frequency, π out of phase for high frequency. The negative mass case shows the exact opposite response: π out of phase for low drive frequency, and $2\pi = 0$ phase, i. e., in phase, for high drive frequency. This perfect π fundamentally says that the spin responds to an external perturbation exactly oppositely of a normal oscillator.

The term "negative mass" is perhaps better called "negative frequency" – there is after all no mass in Eq. (5.14). The term arises from analogy to the normal harmonic oscillator with mass m,

$$H = \frac{m\omega^2}{2}\hat{X}^2 + \frac{1}{2m}\hat{P}^2, \tag{5.16}$$

where flipping the sign of m changes the sign of both terms. Flipping the sign of ω_s has the same role for us.

5.3 Stokes Parameters

We divert our attention now, from that of atoms and spins, to the topic of the polarization of light. The motivation for this is the effect on light of our atoms; for a linearly polarized beam of light, propagating along an axis orthogonal to the mean spin/magnetic field direction, the main effect will be a rotation of the light polarization.

If we consider a wave propagating in the z-direction, we may write any general field at a given point in space as

$$\mathbf{E}(t) = \mathbf{e}_x \underbrace{e_x \cos(\omega t + \varphi_x)}_{E_x} + \mathbf{e}_y \underbrace{e_y \cos(\omega t + \varphi_y)}_{E_y} . \tag{5.17}$$

With E_x and E_y being the electric field in the x and y directions. The polarization state is determined by the relative size of the field strengths, and their relative phase $\delta\varphi = \varphi_x - \varphi_y$. Instead of the pair of orthogonal basis vectors $\{ \mathbf{e}_x, \mathbf{e}_y \}$, we may have picked any number of other bases: $\{ \mathbf{e}_{+45}, \mathbf{e}_{-45} \}$ or $\{ \mathbf{e}_{\sigma_+}, \mathbf{e}_{\sigma_-} \}$, being the two most obvious alternatives.

Alternatively, to describe light polarization, one may define the *Stokes vectors*; instead of keeping track of $e_{\{x,y\}}$ and their phases $\{ \varphi_x, \varphi_y \}$, one can instead choose to track four (possibly normalized) intensities—the *Stokes parameters*. These are sometimes labeled $S_{\{0,1,2,3\}}$, but we will use a notation more closely related to a spatial interpretation[16]:

- S_x: The intensity polarized along x minus that along y
- S_y: The intensity along 45° w.r.t. the x-axis minus that along -45°
- S_z: The intensity of right hand circularly polarized light minus that of left hand polarized light
- S_0: The total intensity

(16) Nota bene! A given Stokes vector does not point in the direction of its label; indeed $S_x = -S_0$ describes light fully polarized along y.

The first three of these are depicted in Fig. 5.6, with S_0 defining the radius of the sphere, such that a vector $[S_x, S_y, S_z]$ falls on the surface or within the sphere at all times.

Writing the electric field of Eq. (5.17) in quantized form, we get

$$\hat{\mathbf{E}}(z,t) = \mathbf{e}_x e_x \left(\hat{a}_x e^{i\phi_x(t)} + \hat{a}_x^\dagger e^{-i\phi_x(t)} \right) + \mathbf{e}_y e_y \left(\hat{a}_y e^{i\phi_y(t)} + \hat{a}_y^\dagger e^{-i\phi_y(t)} \right), \tag{5.18}$$

where we have written the time evolution of the field operators explicitly as $\phi_i(t) = kz - \omega t + \varphi_i$.

Given the definitions of Stokes parameters and the quantized electrical field, the quantum version of the Stokes parameters become (Møller 2018)

$$\hat{S}_x(z,t) = \frac{1}{2} \left(\hat{a}_x^\dagger \hat{a}_x - \hat{a}_y^\dagger \hat{a}_y \right) = \frac{1}{2} \left(\hat{n}_x - \hat{n}_y \right) \tag{5.19a}$$

$$\hat{S}_y(z,t) = \frac{1}{2} \left(\hat{a}_x^\dagger \hat{a}_y + \hat{a}_y^\dagger \hat{a}_x \right) = \frac{1}{2} \left(\hat{n}_{+45} - \hat{n}_{-45} \right) \tag{5.19b}$$

$$\hat{S}_z(z,t) = \frac{1}{2i} \left(\hat{a}_x^\dagger \hat{a}_y - \hat{a}_y^\dagger \hat{a}_x \right) = \frac{1}{2} \left(\hat{n}_R - \hat{n}_L \right) \tag{5.19c}$$

$$\hat{S}_0(z,t) = \frac{1}{2} \left(\hat{a}_x^\dagger \hat{a}_x + \hat{a}_y^\dagger \hat{a}_y \right) = \frac{1}{2} \left(\hat{n}_x + \hat{n}_y \right) . \tag{5.19d}$$

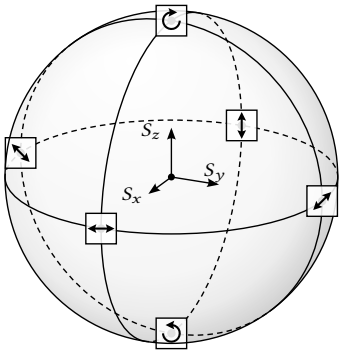

Figure 5.6: Poincare sphere. Modified figure, original by Geek3, published under CC BY 3.0.

The Stokes operators fulfill commutation relations similar to that for angular momentum operators, $\hat{J}$, i. e.

$$\begin{aligned}[\hat{S}_j, \hat{S}_k] &= \mathrm{i}\varepsilon_{jkl}\hat{S}_l \\ [\hat{S}_0, \hat{S}_j] &= 0, \;\; j \in \{x, y, z\} \\ \hat{S}_0(\hat{S}_0 + 1) &= \hat{S}_x^2 + \hat{S}_y^2 + \hat{S}_z^2\end{aligned} \tag{5.20}$$

We may already now consider the time evolution of the Stokes operators in a given medium. If the interaction Hamilton between the light and the medium is described by $\hat{H}_{\text{int}}$, we may write the evolution as (Møller 2018, p. 18)

$$\left(\frac{\partial}{\partial t} + c\frac{\partial}{\partial z}\right)\hat{S}_j(z,t) = \frac{\mathrm{i}}{\hbar}\left[\hat{H}_{\text{int}}, \hat{S}_j(z,t)\right]. \tag{5.21}$$

Our material systems, atomic cells, generally have a length of 10 mm; if the atomic sample had a refractive index of $n = 1$, this would mean that a pulse of light would transverse the length of the cell in 33 ps. On the other hand, the dynamics of interest happens much slower, at timescales of around ~1 µs. Møller (2018) argues that we may therefore ignore the faster of these evolutions, because the light does not appreciably retard during the passage of the cell, and thus

$$c\frac{\partial}{\partial z}\hat{S}_j(z,t) \approx \frac{\mathrm{i}}{\hbar}\left[\hat{H}_{\text{int}}, \hat{S}_j(z,t)\right] \tag{5.22}$$

If the sample is located from $z = 0$ to $z = L$, the input and output stokes operators are given by

$$\hat{S}_j^{\text{in}}(t) \equiv \hat{S}_j(z = 0, t) \tag{5.23}$$

$$\hat{S}_j^{\text{out}}(t) \equiv \hat{S}_j(z = L, t). \tag{5.24}$$

5.3.1 Measuring the Stokes Parameters

The Stokes parameters may be measured with the aid of two photodetectors, one polarizing beam-splitter (PBS), and a set of half and quarter waveplates (HWP and QWP). The idea is depicted in Fig. 5.7, and detailed in W. P. Bowen et al. (2002)[17] and Brian Julsgaard (2003). Also see Agarwal and Chaturvedi (2003)[18].

In this idealized description, the perfect PBS reflects all light polarized in the plane (x), and transmits all light polarized out of the plane (y). The total power is measured by adding the photocurrents on the two detectors together, since $S_0 = (n_x + n_y)/2$.

The three remaining operators are measured by taking the difference of the photocurrents. The waveplates transform the input polarization of interest to the x and y linearly polarized fields just before the PBS. S_x is just the input fields.

S_y neccesitates the prescense of a HWP set to rotate the fields by 45°, which means that the fast axis must be set to $\pi/8$[19].

Measuring S_z comes with some degree of freedom. If the input light is circularly polarized, adding a quarter wave plate will turn it into a linear polarization, independent of the waveplate rotation. Adding a QWP with the axis aligned along x rotates a circularly polarized input to a linear polarization at ±45°, which is then rotated to the x, y-basis by a following HWP. Alternatively, a QWP rotated to $\pi/4$ directly rotates circularly polarized light to the same linear polarization.

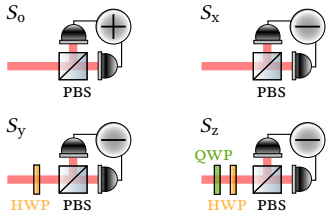

Figure 5.7: Stokes parameter measurements. The polarizing beam splitter (PBS) reflects x-polarized and transmits y-polarized light. The Half (HWP) and Quarter (QWP) waveplates rotate the input light as described in the main text.

(17) Warwick P. Bowen et al. (2002). "Polarization Squeezing of Continuous Variable Stokes Parameters". In: *Phys. Rev. Lett.* 88 (9), p. 093601.

(18) G. S. Agarwal and S. Chaturvedi (2003). "Scheme to measure quantum stokes parameters and their fluctuations and correlations". In: *Journal of Modern Optics* 50.5, pp. 711–716.

(19) The HWP and flip the polarization around the fast axis, and the polarization is thus rotated by $2\pi/8 = \pi/4 = 45°$.

5.4 The Faraday Interaction

The interaction between the collective spin and our light is described by the Faraday interaction; a linearly polarized beam of light will have its polarization rotated around the axis of propagation by an amount proportional to the spin projection along the propagation direction.

Detailed derivations and descriptions of the process may be found in, e. g., Brian Julsgaard (2003) or Rodrigo A. Thomas (2020). Also see Geremia, Stockton, and Mabuchi (2006)[20] for a good reference on dispersive readout of multilevel atoms. In this thesis we will skip very lightly over the derivations and justifications.

(20) J. M. Geremia, John K. Stockton, and Hideo Mabuchi (2006). "Tensor polarizability and dispersive quantum measurement of multilevel atoms". In: *Phys. Rev. A* 73 (4), p. 042112.

As usual, we are interested only in the highly spin polarized case, with close to all atoms pumped to the $|F = 4, m_F = 4\rangle$ state, and in timescales slower than the excited state lifetime, such that the upper states can be adiabatically eliminated. Further, we operate the laser far detuned (several GHz), as to remain far below saturation.

For $F = 4$ and high detuning, $\Delta \gg \gamma_{\mathrm{Cs}}$, the effective atom-light interaction Hamiltonian (Rodrigo A. Thomas (2020, p. 30)) is

$$\hat{H}/\hbar = g_{\mathrm{Cs}} \left(a_0 \hat{S}_0 \hat{\mathbb{1}}_9 + a_1 \hat{S}_z \hat{F}_z + a_2 \left[\hat{S}_0 \hat{F}_z^2 - 2\hat{S}_x(\hat{F}_x^2 - \hat{F}_y^2) - 2\hat{S}_y(\hat{F}_x\hat{F}_y + \hat{F}_y\hat{F}_x) \right] \right), \quad (5.25)$$

where

$$g_{\mathrm{Cs}} = -\frac{c\gamma_{\mathrm{Cs}}}{8A_B\Delta} \frac{\lambda_{\mathrm{Cs}}^2}{2\pi} \quad (5.26)$$

is the effective single photon-single atom coupling rate and the a_i parameters describe the relative strengths of the scalar, vector, and tensor light interactions respectively, and equal

$$a_0 = \frac{1}{4}\left(\frac{1}{1 - \Delta_{35}/\Delta} + \frac{7}{1 - \Delta_{45}/\Delta} + 8 \right) \quad \to 4 \quad (5.27)$$

$$a_1 = \frac{1}{120}\left(-\frac{35}{1 - \Delta_{35}/\Delta} - \frac{21}{1 - \Delta_{45}/\Delta} + 176 \right) \to 1 \quad (5.28)$$

$$a_2 = \frac{1}{240}\left(\frac{5}{1 - \Delta_{35}/\Delta} - \frac{21}{1 - \Delta_{45}/\Delta} + 16 \right) \quad \to 0, \quad (5.29)$$

where the $\to$ denotes the asymptotic value as $\Delta \to \pm\infty$, and $\Delta_{35}/2\pi = 452$ MHz, $\Delta 45/2\pi = 251$ MHz is the frequency difference between the excited state levels $F' = 3/4$ and $F' = 5$, respectively. For our typical detuning of $\Delta/2\pi \sim 3$ GHz, $a_0 \sim 3.83$, $a_1 \sim 1.05$ and $a_2 \sim 0.004$.

The three terms in Eq. (5.25) represent, like stated above, respectively the scalar, vector and tensor light shifts. The first involves only the total light intensity and the identity operator, simply counting the atoms; it is an overall phase retardation, which can be ignored for most relevant situations. The vector interaction involves $\hat{S}_z$ and $\hat{F}_z$, which in our chosen basis of Stokes vectors and with the spin quantized along x and light propagating along z involves a rotation of the spin variable around the z axis, as well as a rotation of the light variables around $\hat{S}_z$, i. e., a circular birefringence, which leaves circular polarizations unchanged, and

rotates linear polarizations around the real propagation axis. The tensor light shift involves products of Stokes operators to the first power and quadratic terms of spin variables, $\hat{F}$. A geometric interpretation is less obvious here, especially for the spin, but for the light, the first term is another overall retardation, while for the last two terms the effect is a linear birefringence around the $\hat{S}_x$ vector and linear birefringence around $\hat{S}_y$, respectively. For more details see Deutsch and Jessen (2010)[21].

(21) Ivan H. Deutsch and Poul S. Jessen (2010). "Quantum control and measurement of atomic spins in polarization spectroscopy". In: *Optics Communications* 283.5. Quo vadis Quantum Optics?, pp. 681–694.

The tensor light shift carries the dual role of being itself a deviation from our nice harmonic oscillator description, and the recipe for fixing the imperfection introduced by the quadratic Zeeman shift. The tensor Stark shift, ω_{tss}, induces a m_F dependent energy shift, which changes the spectral response of our ensemble. Allowing now the input field propagating along z to be polarized not along the magnetic field direction, but any axis perpendicular to the propagation direction, the electric field,

$$\mathbf{E}/E_0 = \mathbf{e}_x \cos\alpha + \mathbf{e}_y \sin\alpha, \tag{5.30}$$

is angled α away from the magnetic field $\mathbf{B} = B\mathbf{e}_x$. The average normalized Stokes parameters for such a field are

$$\begin{aligned} S_x/S_0 &= E_x^* E_x - E_y^* E_y = \cos 2\alpha \\ S_y/S_0 &= 2\Re(E_x E_y^*) \quad\; = \sin 2\alpha \\ S_z/S_0 &= 0 \end{aligned} \tag{5.31}$$

Inserting into Eq. (5.25) and performing first order perturbation theory, one finds that the splitting between adjacent Zeeman levels is changed by

$$\omega_{\text{tss}} = \frac{E_{m+1} - E_m}{\hbar} = \frac{\gamma_{\text{Cs}}}{8A_B\Delta}\frac{\lambda_{\text{Cs}}^2}{2\pi} a_2 S_0 \frac{1 + 3\cos 2\alpha}{2}. \tag{5.32}$$

For $\cos 2\alpha = 1/3$, or $\alpha \approx 54.7^\circ$, the whole term cancels out. On the other hand, the quadratic Zeeman shift may be compensated for a well polarized ensemble by tuning α; this effect is used extensively in our experiment.

Skipping again the details, in the limit of all atoms in a stretched magnetic level, $|F = 4, m_F = \pm 4\rangle$, assuming that the quadratic Zeeman shift has been cancelled by the tensor Stark shift, and canceling the terms proportional to $\hat{F}_x$ and $\mathbb{1}$ by adjusting the magnetic field, we are left with an effective spin-$^1/_2$ description of the magnetic precession plus the interaction with light,

$$\hat{H}_{1/2}/\hbar = \omega_s \hat{F}_x + g_{\text{Cs}}\left(a_1 \hat{S}_z \hat{F}_z \pm 14 a_2 \hat{S}_y \hat{F}_y\right). \tag{5.33}$$

Since we have used the tensorial shift to compensate the quadratic Zeeman shift, it makes sense to rotate the Stokes operators accordingly, and we define

$$\begin{pmatrix} \hat{S}_\parallel \\ \hat{S}_\perp \\ \hat{S}_z \\ \hat{S}_0 \end{pmatrix} = \begin{pmatrix} \hat{S}_x \cos 2\alpha - \hat{S}_y \sin 2\alpha \\ \hat{S}_x \sin 2\alpha + \hat{S}_y \cos 2\alpha \\ \hat{S}_z \\ \hat{S}_0 \end{pmatrix}. \tag{5.34}$$

The classical driving field is along $\hat{S}_\parallel$, so $\langle \hat{S}_\parallel \rangle = \langle \hat{S}_o \rangle = S_\parallel$, and the variables $\hat{S}_\perp$ and $\hat{S}_z$ remain quantum variables. These we redefine as

$$\hat{X}_L = \frac{\hat{S}_z}{\sqrt{S_\parallel}} \quad \hat{P}_L = -\frac{\hat{S}_\perp}{\sqrt{S_\parallel}} \tag{5.35}$$

with $[\hat{X}_L, \hat{P}_L] = \frac{i}{2}$.

Using the definitions of the spin quadrature operators in Eq. (5.15), we write Eq. (5.33) as

$$\hat{H}_s/\hbar = \frac{\omega_s}{2}\left(\hat{X}_s^2 + \hat{P}_s^2\right)^2 - 2\sqrt{\Gamma_s}\left(\hat{X}_s\hat{X}_L + \zeta_s\hat{P}_S\hat{P}_L\right), \tag{5.36}$$

where $\zeta_s = -14\frac{a_2}{a_1}\cos 2\alpha$ quantifies the ratio of the tensor interaction to the vector interation, and we have defined the spin readout rate

$$\Gamma_s = g_{Cs}^2 a_1^2 S_\parallel F_x \tag{5.37}$$

For the usual detuning in our experiments, $\Delta \sim 3\,\text{GHz}$, and the angle used to cancel the quadratic Zeeman shift, $\alpha \sim 60°$, the tensor interaction is small, on the order of $\zeta_s \sim 0.01$, which brings the total spin interaction close to a QND interaction.

5.5 Input-output Relations

With the effective quadrature language Hamiltonian in Eq. (5.36), and the Heisenberg–Langevin equations introduced in Section 3.7.2, the equations of motion for the spin and optical operators evolve as

$$\frac{d}{dt}\begin{pmatrix}\hat{X}_s\\ \hat{P}_s\end{pmatrix} = \begin{pmatrix}-\gamma_{so}/2 & \omega_s\\ -\omega_s & -\gamma_{so}/2\end{pmatrix}\begin{pmatrix}\hat{X}_s\\ \hat{P}_s\end{pmatrix} + 2\sqrt{\Gamma_s}\begin{pmatrix}-\zeta_s\hat{P}_L\\ \hat{X}_L\end{pmatrix} + \begin{pmatrix}\hat{f}_s^X\\ \hat{f}_s^P\end{pmatrix} \tag{5.38}$$

$$\begin{pmatrix}\hat{X}_{L,s}^{out}\\ \hat{P}_{L,s}^{out}\end{pmatrix} = \begin{pmatrix}\hat{X}_{L,s}^{in}\\ \hat{P}_{L,s}^{in}\end{pmatrix} + \sqrt{\Gamma_s}\begin{pmatrix}0 & -\zeta_s\\ 1 & 0\end{pmatrix}\begin{pmatrix}\hat{X}_s\\ \hat{P}_s\end{pmatrix} \tag{5.39}$$

Again, following the derivations in Rodrigo A. Thomas et al. (2020) and its Supplementary Information, we go to the Fourier domain, where we find

$$\begin{pmatrix}\gamma_{so}/2 + \zeta_s\Gamma_s - i\Omega & -\omega_s\\ \omega_s & \gamma_{so}/2 + \zeta_s\Gamma_s - i\Omega\end{pmatrix}\begin{pmatrix}\hat{X}_s\\ \hat{P}_s\end{pmatrix} = 2\sqrt{\Gamma_S}\begin{pmatrix}0 & -\zeta_s\\ 1 & 0\end{pmatrix}\begin{pmatrix}\hat{X}_{L,s}^{in}\\ \hat{P}_{L,s}^{in}\end{pmatrix} + \begin{pmatrix}\hat{f}_s^X\\ \hat{f}_s^P\end{pmatrix}, \tag{5.40}$$

$$\begin{pmatrix}\hat{X}_{L,s}^{out}\\ \hat{P}_{L,s}^{out}\end{pmatrix} = \begin{pmatrix}\hat{X}_{L,s}^{in}\\ \hat{P}_{L,s}^{in}\end{pmatrix} + \sqrt{\Gamma_s}\begin{pmatrix}0 & -\zeta_s\\ 1 & 0\end{pmatrix}\begin{pmatrix}\hat{X}_s\\ \hat{P}_s\end{pmatrix}, \tag{5.41}$$

where $\hat{f}_s^X, \hat{f}_s^P$ are the effective forces acting on the spins via the thermal bath. We note here that where a mechanical oscillator usually decays on in the $\hat{P}$-quadrature, the spin oscillator naturally has decay in both $\hat{X}$ and $\hat{P}$; the underlying spin quadratures $\hat{F}_y$ and $\hat{F}_z$ decay in the same way after all.

Wishing again to find a more compact notation, we define like in Section 3.7.3, a number of matrices

$$\begin{aligned} \boldsymbol{Z} &= \begin{pmatrix} 0 & -\zeta_s \\ 1 & 0 \end{pmatrix}, \quad \boldsymbol{L} = \begin{pmatrix} \gamma_{s0}/2 + \zeta_s\Gamma_s - i\Omega & -\omega_s \\ \omega_s & \gamma_{s0}/2 + \zeta_s\Gamma_s - i\Omega \end{pmatrix}^{-1}, \\ \hat{\boldsymbol{X}}_{L,s}^{in(out)} &= \begin{pmatrix} \hat{X}_{L,s}^{in(out)} \\ \hat{P}_{L,s}^{in(out)} \end{pmatrix}, \quad \hat{\boldsymbol{X}}_s = \begin{pmatrix} \hat{X}_s \\ \hat{P}_s \end{pmatrix}, \quad \hat{\boldsymbol{f}}_s = \begin{pmatrix} \hat{f}_s^X \\ \hat{f}_s^P \end{pmatrix}. \end{aligned} \tag{5.42}$$

With these definitions, we write Eq. (5.40) and Eq. (5.41) as

$$\hat{\boldsymbol{X}}_s = 2\sqrt{\Gamma_s}\boldsymbol{L}\boldsymbol{Z}\hat{\boldsymbol{X}}_{L,s}^{in} + \boldsymbol{L}\hat{\boldsymbol{f}}_s \tag{5.43}$$

$$\hat{\boldsymbol{X}}_{L,s}^{out} = \hat{\boldsymbol{X}}_{L,s}^{in} + \sqrt{\Gamma_s}\boldsymbol{Z}\hat{\boldsymbol{X}}_s = (\mathbb{1}_2 + 2\Gamma_s\boldsymbol{Z}\boldsymbol{L}\boldsymbol{Z})\hat{\boldsymbol{X}}_{L,s}^{in} + \sqrt{\Gamma_s}\boldsymbol{Z}\boldsymbol{L}\hat{\boldsymbol{f}}_s, \tag{5.44}$$

where in the last line we have inserted the expression for $\hat{\boldsymbol{X}}_s$ we just found.

Turning our attention to $\boldsymbol{L}$, describing the spin oscillator response to external forces, can be written in a more transparent form as (Rodrigo A. Thomas 2020, chapter 3)

$$\boldsymbol{L} = \begin{pmatrix} \rho_s(\Omega) & \chi_s(\Omega) \\ -\chi_s(\Omega) & \rho_s(\Omega) \end{pmatrix}, \tag{5.45}$$

with the two susceptibilities

$$\chi_s(\Omega) = \frac{\omega_s}{\omega_s^2 - \Omega^2 - i\Omega\gamma_s + (\gamma_s/2)^2} \tag{5.46}$$

$$\rho_s(\Omega) = \frac{\gamma_{s/2-i\Omega}}{\omega_s^2 - \Omega^2 - i\Omega\gamma_s + (\gamma_s/2)^2}, \tag{5.47}$$

where $\gamma_s = \gamma_{s0} + 2\zeta_s\Gamma_s$ is the total spin linewidth. For the limit of narrow spins, $\gamma_s \ll \omega_s$, and close to resonance, we can approximate the susceptibilities as

$$\begin{aligned} \chi_s(\Omega) &\approx \frac{1}{2}\frac{1}{\omega_s - \Omega - i\gamma_s} \\ \rho_s(\Omega) &\approx -i\chi_s(\Omega). \end{aligned} \tag{5.48}$$

Just like for the mechanics, where we track only $\hat{X}_m$, and calculate $\hat{P}_m$ from it using a simple Fourier domain relation, we can do the same for the spins. We seek approximate versions of Eq. (5.43) and (5.44), valid in the limit $|\omega_s| \gg \gamma_s, |\Omega - |\omega_s||$, i. e., for a narrow spin system, and only close to the resonance. In this limit, the effective thermal forces $\hat{f}_s^X$ and $\hat{f}_s^P$ can be combined into the single thermal force term $\hat{f}_s \approx i\hat{f}_s^X + \hat{f}_s^P$. In this limit, the evolution equation for $\hat{X}_s$ in terms of the susceptibility $\chi_s(\Omega)$ arises from Eq. (5.43)) (setting $\omega_{s0} \equiv \omega_s$),

$$\hat{X}_s = \chi_s\left[2\sqrt{\Gamma_s}\begin{pmatrix} 1 \\ -i\zeta_s \end{pmatrix}^T \hat{\boldsymbol{X}}_{L,s}^{in} + \hat{f}_s\right] = \chi_s\left[2\sqrt{\Gamma_s}(\hat{X}_{L,s}^{in} - i\zeta_s\hat{P}_{L,s}^{in}) + \hat{f}_s\right]. \tag{5.49}$$

Noting that $\hat{P}_s \approx -\text{sign}(\omega_{s0})i\hat{X}_s$ for $\Omega/|\omega_s| \sim 1$, the simpler input-output relation finally becomes,

$$\boldsymbol{X}_{L,s}^{out} = \boldsymbol{X}_{L,s}^{in} + \sqrt{\Gamma_s}\begin{pmatrix} -i\zeta_s \\ 1 \end{pmatrix}\hat{X}_s, \tag{5.50}$$

which follows from Eq. (5.44).

We now have our final expression for the equations of motions of our spin oscillator, and the input-output relation describing the interaction with light. We have made a number of approximations, reducing the complex physics of a large number of atoms down to a harmonic oscillator, interacting with two light quadratures. This mapping into a harmonic oscillator language, puts the spin system on effectively equal footing as our mechanical oscillator in Chapter 3. The spin response will be investigated in certain conditions in the rest of this chapter, before we encounter it again in Chapter 10.

5.6 Magneto-Optical Resonance Spectroscopy (MORS)

An important backbone in our calibrations of the atomic system is the Magneto-Optical Resonance Spectroscopy, MORS, described in B. Julsgaard, Sherson, et al. (2004)[22], and elaborated in Brian Julsgaard (2003) and Rodrigo A. Thomas (2020), this method allows us to measure the population differences between neighboring m_F-levels, as well as the coherence times of the individual transitions and the differential Stark shifts.

(22) B. Julsgaard, J. Sherson, et al. (2004). "Characterizing the spin state of an atomic ensemble using the magneto-optical resonance method". In: *Journal of Optics B: Quantum and Semiclassical Optics* 6.1, pp. 5–14.

In the end, we are after the *spin polarization*, p, defined as

$$p = \frac{|F_x|}{F} = \frac{1}{F}\,\mathrm{Tr}\left[\rho F_x\right], \tag{5.51}$$

which describes how well we have managed to pump the atoms towards a single extreme m_F-level.

The MORS is a driven measurement, with a small RF magnetic field. The RF field is polarized orthogonal to the large DC magnetic field, as induces a precession around the mean spin direction. The RF frequency is stepped across the atomic Zeeman resonances, and for each frequency, the detected signal is demodulated to extract the response amplitude and phase.

Skipping all pretenses of a derivation, the signal of the 8 Zeeman lines is given by

$$\mathrm{MORS}(\omega_{\mathrm{rf}}) = c_0 \left| N \sum_{m=-F}^{F-1} \frac{\left(F(F+1) - m(m+1)\right)\left(P_{m+1} - P_m\right)\gamma_{m+1,m}}{\left(\omega_{m+1,m} - \omega_{\mathrm{rf}}\right) - \mathrm{i}\gamma_{m+1,m}/2} \right|^2 \tag{5.52}$$

where c_0 is an arbitrary proportionality constant, P_m is the population in the mth level, $\gamma_{m+1,m}$ is the decoherence rate of the coherence between levels $m+1$ and m, and the frequencies are labeled similarly. In other words, the MORS signal is the absolute square of the sum of 8 complex Lorentzians, with weight proportional to the population differences between levels.

This is a rather large number of parameters (25 to be exact, if we combine c_0 and N to $c_0 N^2$); luckily a number of simplifying assumptions can be made. First, we can restrict all linewidths to be the same, γ_0; this assumption is rather crude, and not consistent with experimental observations in many conditions (see Rodrigo A. Thomas (2020, chapter 7)). Secondly, we can constrain the frequency differences to $\omega_{m+1,m} = \omega_s + m\omega_{\mathrm{qzs}}$. These simplifications reduce the number of free parameters by 7 and 6 respectively. Lastly, we can introduce the so-called *spin temperature distribution* (Vasilakis, Shah, and Romalis 2011)[23], which states that

(23) G. Vasilakis, V. Shah, and M. V. Romalis (2011). "Stroboscopic Backaction Evasion in a Dense Alkali-Metal Vapor". In: *Phys. Rev. Lett.* 106 (14), p. 143601.

the density matrix describing the optically pumped state may be written as

$$\hat{\rho} = \mathrm{e}^{\beta F_x}/Z, \tag{5.53}$$

where Z is the partition function, and

$$\beta = \ln\left[\frac{1+p}{1-p}\right], \tag{5.54}$$

where p is the spin polarization. Note, that this β is dimensionless, as opposed to the usual β encountered in the expressions for normal thermal distributions. The "spin temperature" is then proportional to β^{-1}, but the overall scale is not set. This assumption leads directly to the populations in the different Zeeman levels being

$$P_m = \mathrm{e}^{\beta m}/Z, \tag{5.55}$$

allowing us to calculate the spin polarization easily as

$$p = \frac{\langle F_x \rangle}{F} = \frac{1}{F}\sum_m m\mathrm{e}^{\beta m}. \tag{5.56}$$

Following S.-K. Lee (2008)[24], the spin temperature can be given an absolute scale and unit of kelvin, by *defining*[25] $\beta = \hbar\omega_\mathrm{s}/k_\mathrm{B}T$. Lee notes that the temperature *is* physical, because of its direct relation to adiabatic demagnetization cooling.

In the end, this reduces the 8 population differences to one single parameter, bringing us to 5 total: $\{\, c_0 N^2, \beta, \gamma_0, \omega_\mathrm{s}, \omega_\mathrm{qzs} \,\}$, and a simplified expression

$$\textsc{mors}_0(\omega_\mathrm{rf}) = \frac{c_0 N^2}{Z^2}\left|\sum_{m=-F}^{F-1}\frac{(F(F+1)-m(m+1))\left(\mathrm{e}^{\beta(m+1)}-\mathrm{e}^{\beta m}\right)\gamma_0}{(\omega_\mathrm{s}+m\omega_\mathrm{qzs}-\omega_\mathrm{rf})-\mathrm{i}\gamma_0/2}\right|^2. \tag{5.57}$$

Fitting the $\textsc{mors}_0$ model can be done without further assumptions, while for the MORS model, one other assumption needs to be made: since we are only fitting *population differences*, 8 peaks does not contain enough information to nail down 9 populations. We therefore assume that the population in $|4,-4\rangle$ is 0. This is probably a small error, due to the presence of our optical pump.

The two models are fitted to experimental data in Fig. 5.8. We observe that the full model present a significantly better fit at the low population end, where the simplified model underestimates the populations. For the same reason, the full model estimates a slightly lower spin polarization. It is remarkable, however, *how well* the simplified model fits the data, with much fewer free parameters.

5.7 Spin Coated Microcells

Our spin cells deserve a section of their own—albeit a short one; more detail may be found in Rodrigo A. Thomas (2020) or Zugenmaier (2018)[26]. A typical cell is shwown in Fig. 5.10. It consists of a circular glass tube, closed off at each end by an anti-reflection coated window, with the windows clamping between them a "chip", i. e., a piece of glass with a square channel along its length, and a microchannel (μ-channel) on one face, connecting the small channel to the larger volume of the cylindrical cell, as depicted in Fig. 5.9, allowing atoms to slowly leak in and out of the channel, thus slowly changing the number of atoms. A stem is connected to the encapsulating cylinder, partly for fabrication reasons, and in part as a place to position a drop of cesium.

(24) S.-K. Lee (2008). "Spin noise at an arbitrary spin temperature". In:

(25) This ignores the quadratic Zeeman splitting, which is small compared to the Larmor frequency.

(26) Michael Zugenmaier (2018). "Towards a Room Temperature Single Photon Source Based on Atomic Vapour". Ph.D. thesis. University of Copenhagen.

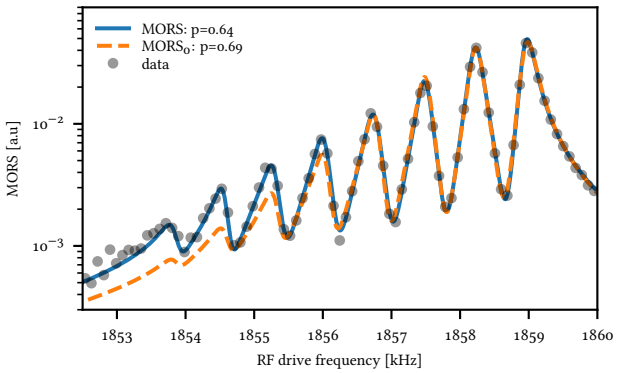

Figure 5.8: MORS and MORS$_0$ models fitted to experimental trace. The full model fits the data better, especially for the peaks with low population differences, where the simplified model undershoots the experimental data, leading to a slight overestimation of the spin polarization, p.

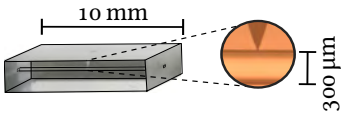

Figure 5.9: Cell chip photograph with lines to guide the eye, and inset with close up of the microchannel connecting the channel to the reservoir of atoms outside the chip. Reproduced from Rodrigo A. Thomas (2020).

An end-view of the cell is shown in Fig. 5.10, along with a concept drawing. The cell is illuminated so the channel and microchannel light up. A faint ring roughly half the diameter of the encapsulating cell marks the AR coated region of the end windows.

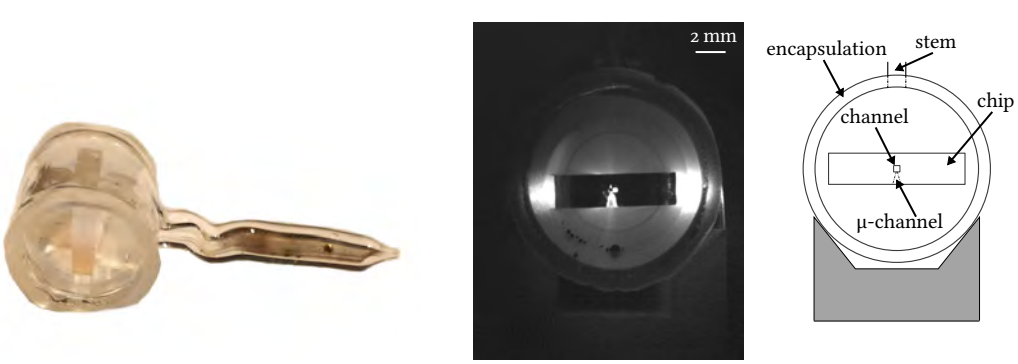

Figure 5.10: Microcell photograph and end view drawing. Reproduced from Rodrigo A. Thomas (2020).

The glass chips are purchased commercially, but all other cell fabrication is performed exclusively by Mikhail Balabas (see Balabas, Jensen, et al. (2010)[27], Balabas, Karaulanov, et al. (2010)[28]). Apart from mastering the craft of glassblowing of scientific grade glassware, Balabas is also *the* expert on coating these cells with spin-preserving coatings. These alkene or paraffin coated cells dramatically increase the spin lifetime of the atomic ensemble, effectively preserving the spin over a very large number of wall collisions. Alkene coated cells show superior spin lifetimes, but degrades when the cells are heated to increase the number of atoms in the cell. Paraffin, in our case C30, is therefore the coating material of choice for

(27) M. V. Balabas, K. Jensen, et al. (2010). "High quality anti-relaxation coating material for alkali atom vapor cells". In: *Opt. Express* 18.6, pp. 5825–5830.

(28) M. V. Balabas, T. Karaulanov, et al. (2010). "Polarized Alkali-Metal Vapor with Minute-Long Transverse Spin-Relaxation Time". In: *Phys. Rev. Lett.* 105 (7), p. 070801.

us, as it allows us to raise the temperature as high as ~60 °C, boosting the number of atoms.

Our cell channels are typically 300 µm × 300 µm × 10 mm, which means that atoms with mean thermal velocity

$$v_{\text{th}} = \sqrt{\frac{8k_{\text{B}}T}{\pi m}}, \tag{5.58}$$

which for $T = 60\,°\text{C}$ and with $m_{\text{Cs}} = 132.9\,\text{u} = 2.2 \times 10^{-25}\,\text{kg}$[29] evaluates to $v_{\text{th}} = 220\,\text{m/s}$. In other words, an average atom traverses the cell in around $300\,\mu\text{m}/220\,\text{m/s} = 1.3\,\mu\text{s}$. Given that we observe spin lifetimes of more than 1 ms, we conclude that a single atomic spin preserves its spin for *thousands* of wall collisions[30]—more elaborate arguments than this crude estimate usually puts the number of collisions a spin survives at ~10^4 (Balabas, Karaulanov, et al. 2010).

(29) With u being the atomic mass unit, equivalent to 1/12 the mass of an unbound neutral carbon-12 atom. Also known as the Dalton, Da.

(30) This should be compared to the 10^6 collision reported for rubidium in an alkene coated cell (Balabas, Karaulanov, et al. 2010).

5.8 Motional Averaging

The atoms are confined to the small channel of 300 µm × 300 µm × 10 mm. Probing of the atoms is performed with a normal Gaussian beam, which means that uniformly filling the channel with light is not possible, without incurring serious scattering losses and beam deformation with the light hitting the edge of the channel, the chip, etc. Typically we use a beam with waist size $w_0 \sim 80\,\mu\text{m}$ ($1/e^2$ radius), which limits optical losses to an acceptable level and optimally covers the channel.

This strongly non-uniform coupling is directly at odds with the assumption of *uniform* coupling we made in the preceding section. We need some kind of mechanism to remedy this; luckily the thermal motion of the atoms discussed, provides such a mechanism known as *motional averaging* (Borregaard et al. 2016)[31]. Very loosely speaking, an individual atom will experience an instantaneous coupling $g_i(t)$, proportional to the light intensity at its position at a given time; if the probing is *slow* enough $\tau_{\text{read}} \propto \Gamma_{\text{s}}^{-1} \ll \tau_{\text{transit}}$, all atoms will cross through the beam many times and the time-averaged interaction strengths should tend towards a narrow unimodal distribution.

(31) J. Borregaard et al. (2016). "Scalable photonic network architecture based on motional averaging in room temperature gas". In: *Nature Communications* 7.1, p. 11356.

The two-time autocorrelation function of the coupling strengths is given in Borregaard et al. (2016) as

$$\langle g_i(0)g_i(t)\rangle = \langle g_i(0)^2\rangle\, e^{-t/\tau_b} + \langle g_i(0)\rangle^2 \left(1 - e^{-t/\tau_b}\right) \tag{5.59}$$

where the brackets denote the ensemble average. The two terms represent the short-time correlations, proportional to the variance of coupling strengths and the long time correlations proportional only to the mean values. Rodrigo A. Thomas (2020, chapter 7) gives a longer exposition and experimental investigation of this effect, but I here summarize only the main effect: the presence of short-time correlations leads to the presence of a broad spectral feature from the atoms. The feature has a spectral width of

$$\frac{\gamma_{\text{s,b}}}{2\pi} = \frac{1}{\pi\tau_b}. \tag{5.60}$$

Borregaard et al. (2016) simulated the movement of atoms in a cell and a beam of width $2w_0 = 110\,\mu\text{m}$ and found $\tau_b = 0.26\,\mu\text{s}$, corresponding to $\gamma_{\text{s,b}} = 1.24\,\text{MHz}$, which is well well in line with our measurements.

While more detailed investigations of spin noise is interesting, see for example Tang et al. (2020)[32], Shaham, Katz, and Firstenberg (2020)[33] or Rodrigo A. Thomas (2020), we here limit ourselves mostly to a phenomenological model, and simply introduce the broadband spin mode as an uncorrelated spin mode with the same resonance frequency as the normal spin resonance, but with a (much) larger linewidth and independent readout rate. We write the broad spin mode as

$$\hat{\boldsymbol{X}}_{\mathrm{s,b}} = 2\sqrt{\Gamma_{\mathrm{s,b}}}\boldsymbol{L}_{\mathrm{b}}\boldsymbol{Z}\hat{\boldsymbol{X}}^{\mathrm{in}}_{\mathrm{L,s}} + \boldsymbol{L}_{\mathrm{b}}\hat{\boldsymbol{\rho}}_{\mathrm{s,b}}, \tag{5.61}$$

where $\boldsymbol{L}_{\mathrm{b}}$ is defined as $\boldsymbol{L}$ with $\gamma_{\mathrm{so}} \to \gamma_{\mathrm{b}}$ and $\Gamma_{\mathrm{s}} \to \Gamma_{\mathrm{s,b}}$. The input-output relation for this total spin system is further modified to

$$\hat{\boldsymbol{X}}^{\mathrm{out}}_{\mathrm{L,s}} = \hat{\boldsymbol{X}}^{\mathrm{in}}_{\mathrm{L,s}} + \sqrt{\Gamma_{\mathrm{s}}}\boldsymbol{Z}\hat{\boldsymbol{X}}_{\mathrm{s}} + \sqrt{\Gamma_{\mathrm{s,b}}}\boldsymbol{Z}\hat{\boldsymbol{X}}_{\mathrm{s,b}}. \tag{5.62}$$

We further assume that the narrow and broad are uncorrelated, which will factor into how we model the broad spin mode in Chapter 10.

The scaling of the broadband spin mode strength with beam size is shown in Fig. 5.11. In the left hand panel we plot the full response close to resonance; the narrow peak is essentially unchanged with beam size. In the right hand panel, the broad response only is shown, where we see a clear dependence on the peak amplitude with changing beam size. As discussed in Rodrigo A. Thomas (2020, chapter 7), the linewidth of the broad mode also depends on the beam size, and the peak height in shot noise units also changes with beam size.

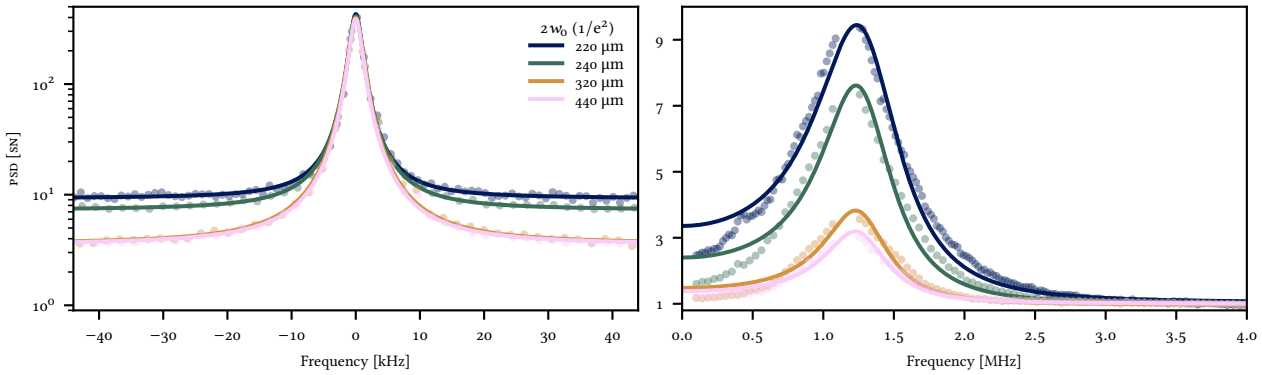

Figure 5.11: Spin noise a function of beam size. Left hand panel: response close to resonance. Right hand panel: Broad response, with the narrow response masked out. The panels are fitted independently. Reproduced from Rodrigo A. Thomas 2020.

5.9 Practical Implementation Details

5.9.1 Experimental Setup

A simplified experimental setup for atoms-only measurements is shown in Fig. 5.12. The full hybrid experimental setup is detailed in Chapter 9, but for now we discuss a couple of things relevant only to the spin system.

(32) Yuanjiang Tang et al. (2020). "Spin-noise spectrum of hot vapor atoms in an anti-relaxation-coated cell". In: *Phys. Rev. A* 101 (1), p. 013821.

(33) Roy Shaham, Or Katz, and Ofer Firstenberg (2020). "Quantum dynamics of collective spin states in a thermal gas". In: *Phys. Rev. A* 102 (1), p. 012822.

The atomic sample (black dots) sits in the middle of a magnetic shield (solid black rectangles), which contains also a set of coils producing a large DC magnetic field, B_{dc}, and two time-varying magnetic fields, B_{rf} and B_{mw}, at microwave and radio frequency ranges respectively. The microwave tone can be used to drive transitions from the $|3\rangle$ manifold to the $|4\rangle$ manifold (and vice versa), and is not used for anything contained in this thesis, but the option is a nice experimental tool; Rodrigo A. Thomas (2020) used these fields to investigate microwave assisted state preparation. The RF field is used to drive Zeeman transitions, such as for MORS (see Section 5.6).

The optical beams are respectively the pump and re-pump beams (green arrow), detailed in Section 5.9.3, and the probe beam (red). For most spin-only experiments, the probe interacts with the spins a single time, before reaching the polarization self-homodyning setup depicted on the right. As shown in Chapter 9, the detection setup can be flipped out of the optical path for hybrid experiments; instead a mirror retro-reflects the beam through the cell for a second interaction, increasing the interaction.

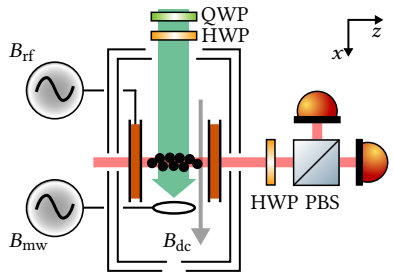

Figure 5.12: Spin system experimental setup concept.

5.9.2 The Magnetic Shield

The magnetic shield surrounding the atomic cell shields the cell from the earth and laboratory magnetic fields. Since cesium has a Larmor frequency of around 350 kHz/G, we typically work with $B \sim 4$ G. This should be compared to the earth magnetic field of around $B_{earth} \approx 0.5$ G in a somewhat unfeasible direction (angled roughly 70° with the horizontal, *World Magnetic Model 2020*.[34]).

(34) NCEI Geomagnetic Modeling Team and British Geological Survey (2019). *World Magnetic Model 2020*. NOAA National Centers for Environmental Information. DOI: 10.25921/11v3-da71. (Visited on 08/12/2022).

Further, any electromagnetic radiation from laboratory sources can directly perturb the various magnetic coherences, so RF magnetic noise must also be shielded for. The magnetic shield therefore consists of a number of layers of μ-metal and aluminium, which are effective against low and high-frequency fields respectively.

Since a gradient of the magnetic field across the cell would lead to a broadening of the resonance, and we require roughly that

$$\frac{\Delta B}{B_0} \ll \frac{\gamma_s}{\omega_s}, \tag{5.63}$$

which for the typical values of γ_s and ω_s means less than 1 ppm magnetic field variation/inhomogeneity. Since our cells are relatively short, this is not too difficult

to obtain, but some care has to be taken in de-Gaussing (de-magnetizing) the shield, and tuning the magnetic coils.

5.9.3 Optical (re-)Pumping

As shown in Fig. 5.1, we prepare the spin ensemble in the spin polarized state by the application of pump and repump light.

The repump light is responsible for moving atoms in the $|F = 3\rangle$ manifold to the $|F = 4\rangle$ manifold. Just the task of pumping between manifolds is most efficiently achieved by pumping on the $|3\rangle \rightarrow |4'\rangle$ transition; $|3\rangle \rightarrow |5'\rangle$ is not an allowed transition due to selection rules, and of the three options $|2'\rangle$, $|3'\rangle$ and $|4'\rangle$, $|4'\rangle$ has the most beneficial branching ratio of the spontaneous decay, i. e., most of the pumped atoms end up in $|4'\rangle$.

However, because we want to minimize the use of optical pumping, which destroys coherences in the $|4\rangle$ manifold, we want to use the repump to perform as much optical pumping as possible. We achieve this by pumping resonantly on the $|3\rangle \rightarrow |2'\rangle$ transition with σ_+ polarized light. Because decay from $|2'\rangle$ all goes back to the $|3\rangle$ manifold, the repump laser essentially works first as a pump for the $|3\rangle$ manifold, collecting atoms in $|F = 3, m_F = 3\rangle$, before off-resonantly[35] repumping to (ideally) $|4, 4\rangle$.

(35) Or resonantly with atoms in a given velocity class, Doppler shifting atoms into resonance with the repump light.

The difference between repumping on $|2'\rangle$ or $|4'\rangle$, measured by MORS, is shown in Fig. 5.13. We observe an increase in the spin polarization from $p = 0.54$ to $p = 0.65$, when changing the repump from $|4'\rangle$ to $|2'\rangle$.

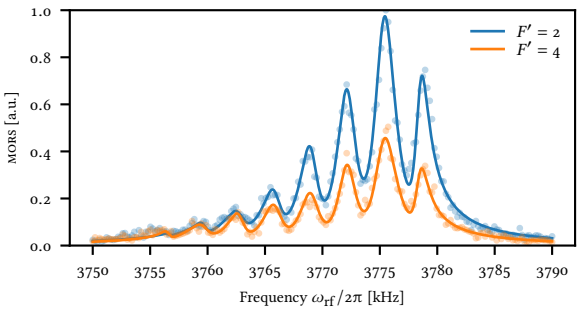

Figure 5.13: Repumping on $F' = 2$ or $F' = 4$. The spin polarization p increases from $p = 0.54$ to $p = 0.65$, when changing the repump from $|4'\rangle$ to $|2'\rangle$.

Pumping within the $|4\rangle$ manifold is performed with a circularly polarized laser tuned to the D_1 resonance. Here we are left with the choice of pumping on $|4\rangle \rightarrow |4'\rangle$ or $|4\rangle \rightarrow |3'\rangle$. The first is most efficient in transferring atoms to the stretched state, but directly couples to atoms in $|4, 3\rangle$, thus destroying the $|4, 3\rangle \langle 4, 4|$ coherence. Pumping on the latter leaves the coherence unchanged, but also has $|4, 3\rangle$ population untouched, limiting the attainable polarization. The power broadening of the $|4, 3\rangle \langle 4, 4|$ coherence is shown in Fig. 5.14, where the detrimental effect of the two can be seen. While the $|3'\rangle$ repump should leave the coherence completely untouched, some broadening is observed in practice, origi-

nating either with off-resonant coupling to the other excited manifold, or from a non-perfect optical polarization.

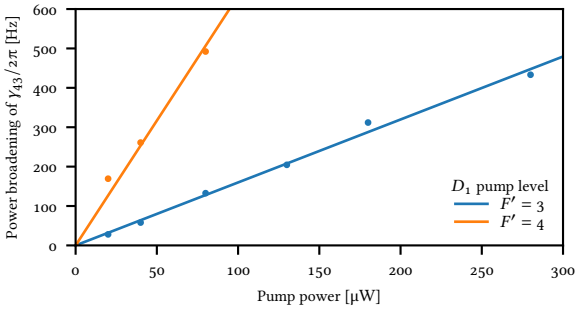

Figure 5.14: Power broadening of the γ_{43} linewidth, as a function of pump power on the D_1 line. Tuning the repump laser to the $F' = 4$ resonance significantly broadens the line, while tuning to the $F' = 3$ line significantly reduces this broadening effect.

5.9.3.1 Spin Temperature

Relating the spin polarization measured with MORS to an effective occupation of the spin oscillator involves relating the transverse fluctuations, related to the effective spin Langevin force, to the occupation n_s. This is covered in more detail in Rodrigo A. Thomas (2020, chapter 5). We can examine the extremes easily.

For a perfectly polarized ensemble, $|p| = 1$, the Heisenberg relation gives

$$|\hat{F}_y^2||\hat{F}_z^2| = \frac{1}{4}\left|\left\langle\left[\hat{F}_y, \hat{F}_z\right]\right\rangle\right|^2 = \frac{1}{4}\left|\left\langle\hat{F}_x\right\rangle\right|^2 = \frac{F^2}{4}, \tag{5.64}$$

and further noting that the two variances are identical, unless the spin state is squeezed.

For the unpolarized case, $|p| = 0$, We use the angular momentum relation $\langle\hat{\boldsymbol{F}}^2\rangle = F(F+1)$, to write

$$\left\langle\hat{F}_x^2\right\rangle + \left\langle\hat{F}_y^2\right\rangle + \left\langle\hat{F}_z^2\right\rangle = F(F+1). \tag{5.65}$$

Noting that for the completely mixed state the variances in all directions are identical, we get

$$\langle\hat{F}_j^2\rangle = \frac{F(F+1)}{3}, \qquad j \in \{x, y, z\}. \tag{5.66}$$

So, for $F = 4$, the transverse variances varies from 2 to $\frac{20}{3}$, or normalized to F, from $\frac{1}{2}$ to $\frac{5}{3}$, as depicted in the left hand panel of Fig. 5.15.

Mapping these transverse fluctuations to an effective occupation happens under the same assumptions as the Holstein–Primakoff approximation, namely high spin polarization. Rodrigo A. Thomas (2020) gives

$$n_s = \frac{\left\langle\hat{F}_y^2\right\rangle + \left\langle\hat{F}_z^2\right\rangle}{\left\langle\hat{F}_x\right\rangle} - \frac{1}{2}. \tag{5.67}$$

which I plot in Fig. 5.15, right panel.

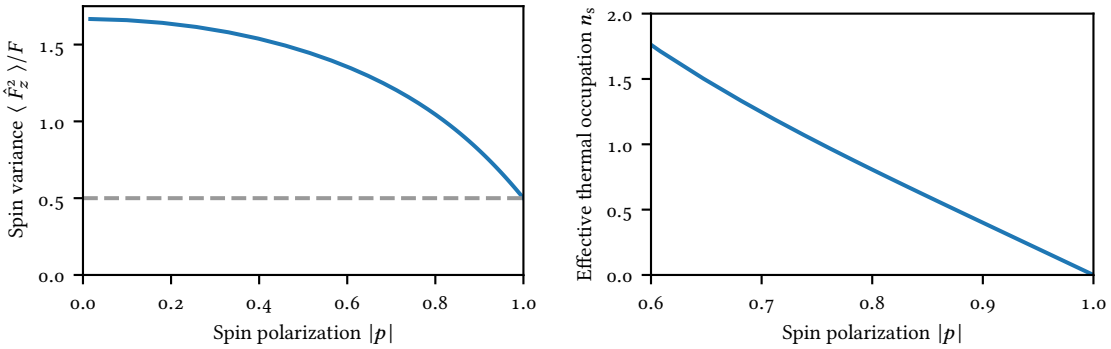

Figure 5.15: Spin transverse variance and thermal occupations as a function of spin polarization, $|p|$. Left: transverse spin component fluctuation for $F = 4$. Right: Effective thermal spin occupations, n_s.

5.9.4 Optical Readout

The optical field at our detector is related to the output field from the atoms by a rotation related to the settings of the waveplates described in Section 5.3.1, as long as we restrict ourselves to the polarizations corresponding to $\hat{X}_{L,s}$ and $\hat{P}_{L,s}$. The effective homodyning angle φ leads to

$$\hat{\boldsymbol{X}}_L^{det} = \begin{pmatrix} \hat{X}_L^{det} \\ \hat{P}_L^{det} \end{pmatrix} = \boldsymbol{O}_\varphi \hat{\boldsymbol{X}}_{L,s}^{out} = \begin{pmatrix} \cos\varphi \hat{X}_{L,s}^{out} - \sin\varphi \hat{P}_{L,s}^{out} \\ \sin\varphi \hat{X}_{L,s}^{out} + \cos\varphi \hat{P}_{L,s}^{out} \end{pmatrix}. \tag{5.68}$$

By varying φ we can thus access both output quadratures from the spins. Similarly, we need only derive expressions for one quadrature, as the two can be rotated freely into one another.

We are interested in the PSD of the light, which is given by the symmetrized correlation function[36]

$$\begin{aligned} \bar{S}_{\boldsymbol{XX}}^{det} \delta(\Omega - \Omega') &= \tfrac{1}{2} \left\langle \hat{X}_L^{det}(\Omega) \hat{X}_L^{det,\dagger}(\Omega') + \hat{X}_L^{det,*}(\Omega') \hat{X}_L^{det,\intercal}(\Omega) \right\rangle \\ &= \boldsymbol{O}_\varphi \bar{S}_{\boldsymbol{XX}}^{out} \boldsymbol{O}_\varphi^\intercal, \end{aligned} \tag{5.69}$$

This 2×2 matrix contains the power and cross spectral densities in the detected light.

Specifying in the input noise operators

$$\bar{S}_{\boldsymbol{XX}}^{in} \delta(\Omega - \Omega') = \tfrac{1}{4} \begin{pmatrix} 1 & 0 \\ 0 & 1 \end{pmatrix} \delta(\Omega - \Omega') \qquad \bar{S}_{\boldsymbol{\ell\ell}} \delta(\Omega - \Omega') = \begin{pmatrix} 1 & 0 \\ 0 & 1 \end{pmatrix} \gamma_s \left(n_s + \tfrac{1}{2} \right) \delta(\Omega - \Omega'), \tag{5.70}$$

and restricting ourselves to the QND case, one finds the output field as

$$\bar{S}_{\boldsymbol{XX}}^{out} = \tfrac{1}{4} \begin{pmatrix} 1 & 2\Gamma_s \chi_s^* \\ 2\Gamma_s \chi_s & 1 + 4\Gamma_s^2 |\chi_s|^2 \end{pmatrix} + \Gamma_s \left(|\chi_s|^2 + |\rho_s|^2 \right) \begin{pmatrix} 0 & 0 \\ 0 & 1 \end{pmatrix} \gamma_{so} \left(n_s + \tfrac{1}{2} \right), \tag{5.71}$$

(36) Reminding ourselves that $\langle \cdot \rangle^*$ denotes complex conjugation of the entries, $\langle \cdot \rangle^\intercal$ denotes the transpose and $\langle \cdot \rangle^\dagger$ denotes transposition *and* complex conjugation.

where new the thermal contribution from X_S in X_L is suppressed by the QND readout, expressed in $Z_{QND} = \left(\begin{smallmatrix} 0 & 0 \\ 1 & 0 \end{smallmatrix}\right)$. The off-diagonal terms represent correlations between the X and P light quadratures, induced by the interaction with the light; the light X_L quadrature drives the spin, and the motion is written into P_L. Restricting ourselves to detection of the P_L^{det} quadrature, i. e., the $(2, 2)$ entry in $\bar{S}_{XX}^{det}$ matrix, one finds (still in the QND case)

$$\frac{S_{PP}^{det}}{SN} = 1+4\Gamma_s^2|\chi_s|^2\cos^2\varphi+4\Gamma_s\Re[\chi_s]\sin\varphi\cos\varphi+4\gamma_{so}\Gamma_s\left(|\chi_s|^2+|\rho_s|^2\right)\cos^2\varphi\left(n_s+\tfrac{1}{2}\right), \tag{5.72}$$

where $SN = 1/4$ is the shot noise level, to which we normalize the output spectrum.

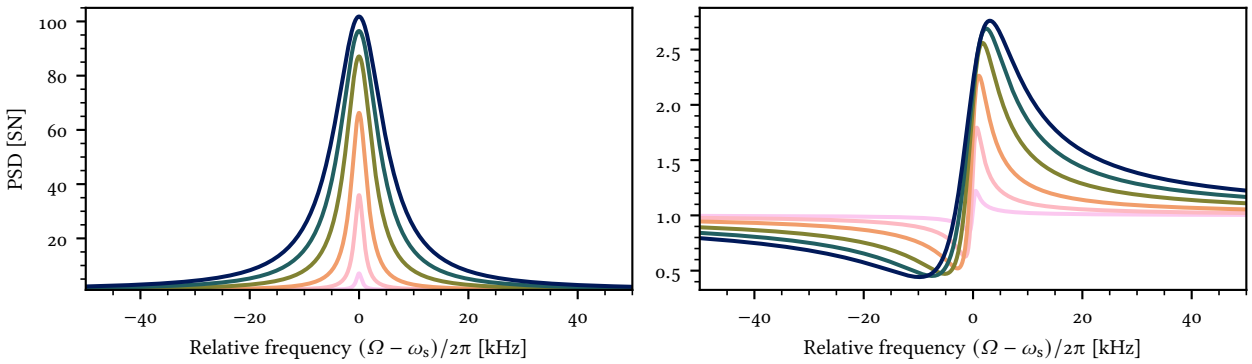

Figure 5.16: Theoretical spin noise curves, Eq. (5.72), evaluated for $\varphi = 0°$ (left) and $\varphi = -84°$. $C_q^s = 5$, $\gamma_{s,dark} = 1\,kHz$, $n_s = 0$. Γ_s varied from 1 kHz to 50 kHz. Peak heights and linewidths for the left hand panel are displayed in Fig. 5.17.

Using the definition of the spin quantum cooperativity[37]

$$C_q^s = \frac{\Gamma_s}{2\gamma_{so}\left(n+\frac{1}{2}\right)} \tag{5.73}$$

we can evaluate Eq. (5.72) for constant C_q^s and no thermal population, $n_s = 0$. We evaluate the model for $\varphi = 0°$ and $\varphi = -84°$. displayed respectively left and right in Fig. 5.16. The spin response in the left hand panel grows with the increase in Γ_s in two ways: first, the peak height increases, and secondly the *area* of the peak grows because the spin linewidth is increased by power broadening. The peak height and linewidth is plotted versus Γ_s in in Fig. 5.17.

The righthand panel, $\bar{S}_{PP}^{det}$ evaluated for $\varphi = -84°$ displays squeezing, originating from the correlations between $\hat{X}_L^{out}$ and $\hat{P}_L^{out}$. As Γ_s is increased, the squeezing becomes stronger (the minimum becomes lower), and the point of maximum squeezing moves away from the resonance. For these parameters, we calculate about 3 dB of optical squeezing. At last, we note that setting $\varphi = \pm 90°$ leads to no atomic contributions in the signal; for QND readout the spin signal is not present in the optical $\hat{X}_L$ quadrature.

(37) While recalling that γ_{so} includes power broadening but not dynamical broadening (which is 0 for QND readout).

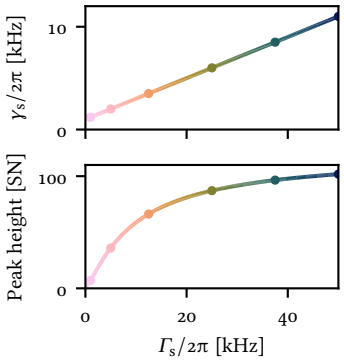

Figure 5.17: Peak height and linewidths from Fig. 5.16. Dots indicate correspond to traces, while the line displays the behaviour for other values of Γ_s.

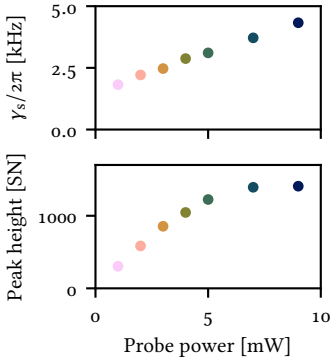

Figure 5.18: Spin LW and peak signal size as a function of probe power, as displayed in Fig. 5.19.

These overall predictions can be observed experimentally. In Fig. 5.19 we plot the spin signal for $\varphi \sim 0^\circ$, and $\varphi \sim 90^\circ$, for varied optical power probing the atoms. However, a number of simplifying assumptions are not applicable to our system in practice.

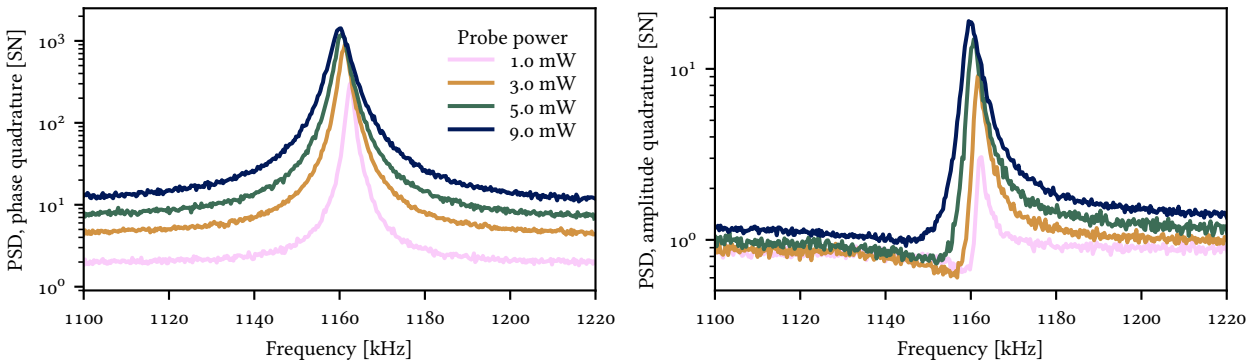

Figure 5.19: Spin signal vs. probe power. Optical phase quadrature (left) and amplitude quadrature (right) PSDs for varied optical power. As the power is increased, the broadband noise mode is read out more strongly, effectively increasing the noise floor, which for the right hand panel washes out the observed squeezing. Peak heights and linewidths for the left hand panel are displayed in Fig. 5.18.

First, we note that the noise level observed away from resonance in the left hand panel is always above the shot noise level, and increases with optical power. This extra noise is the broadband mode, which is read out more effectively as we increase the power. Extracting the peak height and fitting the linewidths leads to the results in Fig. 5.18, which follows the expected behavior well: the linewidth increases linearly, and the peak height saturates for high power. Further, we see the resonance shift a little bit with power, arising from a need to re-balance the LO

angle, α to minimize the quadratic Zeeman splitting, which in turn shifts the whole resonance.

The left hand panel displays the optical squeezing expected, but as Γ_s is increased, so is the broadband noise contribution to the signal, effectively drowning out the quantum correlations allowing us to observe optical squeezing. The increased readout of the broadband noise, masking the "good" correlations turned out to be of vital importance for us; whereas early understanding of the physics involved would imply "high C_q is always better", the concomitant uncorrelated noise originating from higher Γ_s turned out detrimental to our entanglement efforts, and the spin readout rate had to be lowered, reducing C_q^s.

5.10 Coherently Induced Faraday Rotation (CIFAR)

An important experimental task related to atoms is measuring the readout rate Γ_s. This has previously been measured in various ways, which all shared the common disadvantage of necessitating changes to the optical setup, compared to the configuration used for quantum experiments. Since any changes to an optical setup comes with the potential of changes the conditions of the readout process, this is severely disadvantageous. To this end we developed a new technique for spin readout rate calibration, which does not require any changes to our optical setup. Furthermore, the method is insensitive to optical losses and calibration of detection efficiency.

The method is reminiscent of OMIT, in that it measures the interference of a weak probe beam with the driven system response. Since we read out the spins via the Faraday effect, we call the method Coherently Induced FAraday Rotation, or CIFAR. The method was used in Rodrigo A. Thomas et al. (2020) and expanded in the dedicated article Rodrigo A. Thomas et al. (2021)[38], where most of the figures also appear.

(38) Rodrigo A. Thomas et al. (2021). "Calibration of spin-light coupling by coherently induced Faraday rotation". In: *Opt. Express* 29.15, pp. 23637–23653.

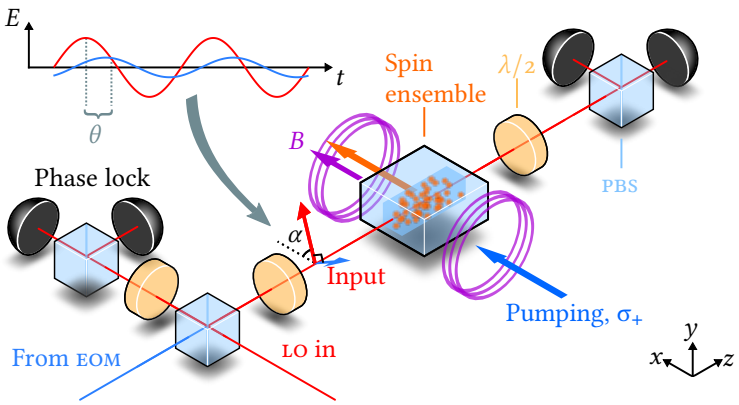

Figure 5.20: CIFAR setup. The strong linearly polarized pump (red) is combined with a much weaker phase modulated beam (blue), with relative phase difference between the beams θ. The beams are rotated such that the strong LO is polarized with angle α to the magnetic field. After interacting with the spin system, the beam is detected in a polarization self-homodyning setup.

We start with the needed experimental setup, depicted in Fig. 5.20. Compared to the normal spin setup (discussed in detail in Chapter 9), the PBS before the spin system is now used not for splitting of LO_1 and LO_2, but for injecting a (phase) modulated beam in an orthogonal polarization to the spin LO. The other port of the PBS is used for locking the relative phase of the modulated beam and the LO, θ. After interacting with the spin system the light is detected in polarization self-homodyning setup, with rotation angle ϕ. We sweep the input modulation frequency ω_{rf} across the spin resonance, and demodulate the output at the same frequency.

Turning to the model, we start with the simplified collective spin Hamiltonian in the quadrature operator formulation for the highly polarized ensemble,

$$\hat{H}_{\text{s}}/\hbar = \frac{-\omega_{\text{s}}}{2}\left(\hat{X}_{\text{s}}^2 + \hat{P}_{\text{s}}^2\right) - 2\sqrt{\gamma_{\text{s}}}\left(\hat{X}_{\text{s}}\hat{X}_{\text{L}} + \zeta_{\text{s}}\hat{P}_{\text{s}}\hat{P}_{\text{L}}\right), \tag{5.74}$$

and the time evolution of spin variables

$$\frac{\text{d}}{\text{d}t}\begin{pmatrix}\hat{X}_{\text{s}}\\ \hat{P}_{\text{s}}\end{pmatrix} = \begin{pmatrix}-\gamma_{\text{s}}/2 & \omega_{\text{s}}\\ -\omega_{\text{s}} & -\gamma_{\text{s}}/2\end{pmatrix}\begin{pmatrix}\hat{X}_{\text{s}}\\ \hat{P}_{\text{s}}\end{pmatrix} + 2\sqrt{\Gamma_{\text{s}}}\begin{pmatrix}0 & -\zeta_{\text{s}}\\ 1 & 0\end{pmatrix}\begin{pmatrix}\hat{X}_{\text{L}}^{\text{in}}\\ \hat{P}_{\text{L}}^{\text{in}}\end{pmatrix}. \tag{5.75}$$

Since CIFAR is a driven measurement, with a sinusoidal drive input in $\boldsymbol{X}_{\text{L}}^{\text{in}}$, we make the ansatz that the spin will be oscillating at the drive frequency, i. e., that other drive and noise terms can essentially be neglected,

$$\boldsymbol{X}_{\text{s}} = \begin{pmatrix}X_{\text{s}}(\omega_{\text{rf}})\\ P_{\text{s}}(\omega_{\text{rf}})\end{pmatrix}\text{e}^{-\text{i}\omega_{\text{rf}}t}, \tag{5.76}$$

where $X_{\text{s}}(\omega_{\text{rf}})$ and $P_{\text{s}}(\omega_{\text{rf}})$ are complex numbers.

The normal input-output relations hold, i. e.

$$\boldsymbol{X}_{\text{L}}^{\text{out}} = \boldsymbol{X}_{\text{L}}^{\text{in}} + \sqrt{\Gamma_{\text{s}}}\boldsymbol{Z}\boldsymbol{X}_{\text{s}} = (\mathbf{1}_2 + 2\Gamma_{\text{s}}\boldsymbol{Z}\boldsymbol{L}\boldsymbol{Z})\boldsymbol{X}_{\text{L}}^{\text{in}}, \tag{5.77}$$

where we see that the input is allowed to interfere with the response of the system. The expression can be evaluated to become

$$\begin{pmatrix}X_{\text{L}}^{\text{out}}\\ P_{\text{L}}^{\text{out}}\end{pmatrix} = \begin{pmatrix}1 - 2\Gamma_{\text{s}}\zeta_{\text{s}}\left(\frac{\gamma_{\text{s}}}{2} - \text{i}\omega_{\text{rf}}\right)\chi_{\text{s}} & -2\Gamma_{\text{s}}\zeta_{\text{s}}^2\omega_{\text{s}}\chi_{\text{s}}\\ 2\Gamma_{\text{s}}\omega_{\text{s}}\chi_{\text{s}} & 1 - 2\Gamma_{\text{s}}\zeta_{\text{s}}\left(\frac{\gamma_{\text{s}}}{2} - \text{i}\omega_{\text{RF}}\right)\chi_{\text{s}}\end{pmatrix}\begin{pmatrix}X_{\text{L}}^{\text{in}}\\ P_{\text{L}}^{\text{in}}\end{pmatrix}. \tag{5.78}$$

(39) Note the difference between φ and ϕ.

The input light is assumed to be pure phase modulation $G = |G|\text{e}^{\text{i}\varphi}$, which we can rotate into an arbitrary light quadrature by adjusting the phase, θ, between the LO and the modulated light. Similarly, we can detect an arbitrary component of the output light by rotation with the phase ϕ[39], giving us

$$\begin{pmatrix}X_{\text{L}}^{\text{in}}\\ P_{\text{L}}^{\text{in}}\end{pmatrix} = \begin{pmatrix}\cos\theta & -\sin\theta\\ \sin\theta & \cos\theta\end{pmatrix}\begin{pmatrix}G\\ 0\end{pmatrix} = \begin{pmatrix}\cos\theta\\ \sin\theta\end{pmatrix}G, \tag{5.79}$$

$$\begin{pmatrix}X_{\text{L}}^{\text{det}}\\ P_{\text{L}}^{\text{det}}\end{pmatrix} = \begin{pmatrix}\cos\phi & -\sin\phi\\ \sin\phi & \cos\phi\end{pmatrix}\begin{pmatrix}X_{\text{L}}^{\text{out}}\\ P_{\text{L}}^{\text{out}}\end{pmatrix}. \tag{5.80}$$

By combining these expressions, and choosing the detected light quadrature to be $P_{\mathrm{L}}^{\mathrm{out}}$, we arrive at an expression for CIFAR,

$$\begin{aligned}|\mathrm{CIFAR}|^2 \equiv \left|P_{\mathrm{L}}^{\mathrm{det}}\right|^2 &= \left|P_{\mathrm{L}}^{\mathrm{out}}\cos\phi + X_{\mathrm{L}}^{\mathrm{out}}\sin\phi\right|^2 \\ &= \Big|\left(1 - 2\Gamma_{\mathrm{s}}\zeta_{\mathrm{s}}\left(\tfrac{\gamma_{\mathrm{s}}}{2} - \mathrm{i}\omega_{\mathrm{rf}}\right)\chi_{\mathrm{s}}\right)\sin(\theta+\phi) \\ &\quad + \Gamma_{\mathrm{s}}\omega_{\mathrm{s}}\chi_{\mathrm{s}}\left[\left(1-\zeta_{\mathrm{s}}^2\right)\cos(\theta-\phi) + \left(1+\zeta_{\mathrm{s}}^2\right)\cos(\theta+\phi)\right]\Big|^2 |G|^2.\end{aligned} \tag{5.81}$$

Because we are only considering the coherent interactions, and not various noise driven terms, the broadband noise is added trivially as

$$\boldsymbol{X}_{\mathrm{L}}^{\mathrm{out}} = (\mathbf{1}_2 + 2\Gamma_{\mathrm{s}}\boldsymbol{Z}\boldsymbol{L}\boldsymbol{Z} + 2\Gamma_{\mathrm{s,b}}\boldsymbol{Z}\boldsymbol{L}_{\mathrm{b}}\boldsymbol{Z})\boldsymbol{X}_{\mathrm{L}}^{\mathrm{in}}, \tag{5.82}$$

allowing for the interference between the probe, the broadband and the narrowband response. For the fits of the model, the broadband mode is included in fits etc., but we now ignore it again for a while, while we consider what insights can be made analytically.

We first consider the case of $\theta = 45^\circ$ and $\phi = 0^\circ$, which corresponds to driving with equal amounts of modulation in the two optiacl quadratures, and detection of $\hat{P}_{\mathrm{L}}$. In this case, Eq. (5.81) simplifies to

$$|\mathrm{CIFAR}(\theta = 45^\circ, \phi = 0^\circ)|^2 = |1 - 2\Gamma_{\mathrm{s}}(-\omega_{\mathrm{s}} + \zeta_{\mathrm{s}}(\gamma_{\mathrm{s}}/2 - \mathrm{i}\omega_{\mathrm{rf}}))\chi_{\mathrm{s}}|^2\,|G|^2. \tag{5.83}$$

The two terms, one constant and one proportional to $\Gamma_{\mathrm{s}}\chi_{\mathrm{s}}$, add coherently to give the total CIFAR signal. The readout rate appears prominently, determining the strength of the second term.

For high spin oscillator Q, i. e., when $\gamma_{\mathrm{s}} \ll \omega_{\mathrm{s}}$, the spin susceptibility can be approximated by

$$\chi_{\mathrm{s}} \approx \frac{-\chi_{\mathrm{so}}}{\omega_{\mathrm{s}}}, \tag{5.84}$$

where

$$\chi_{\mathrm{so}} = \frac{1}{2}\left(\Delta_{\mathrm{rf}} + \mathrm{i}\gamma_{\mathrm{s}}/2\right)^{-1}, \tag{5.85}$$

with $\Delta_{\mathrm{rf}} = \omega_{\mathrm{rf}} - \omega_{\mathrm{s}}$ denoting the detuning of the modulation tone from the spin resonance. With these approximations, the signal, normalized to the input amplitude G, becomes

$$|\mathrm{CIFAR}|^2/|G|^2 \sim |1 - 2\Gamma_{\mathrm{s}}(1 + \mathrm{i}\zeta_{\mathrm{s}})\chi_{\mathrm{so}}|^2 = 1 + \frac{\Gamma_{\mathrm{s}}^2(1+\zeta_{\mathrm{s}}^2) - 2\Gamma_{\mathrm{s}}(\Delta_{\mathrm{rf}} + \zeta_{\mathrm{s}}\gamma_{\mathrm{s}})}{\Delta_{\mathrm{rf}}^2 + (\gamma_{\mathrm{s}}/2)^2}. \tag{5.86}$$

Restricting ourselves to the QND case, where $\zeta_{\mathrm{s}} = 0$, we make the final approximation to arrive at

$$|\mathrm{CIFAR}_0|^2/|G|^2 = 1 + \frac{\Gamma_{\mathrm{s}}^2 - 2\Gamma_{\mathrm{s}}\Delta_{\mathrm{rf}}}{\Delta_{\mathrm{rf}}^2 + (\gamma_{\mathrm{so}}/2)^2}. \tag{5.87}$$

This signal is a combination of three terms: a constant, a Lorentzian and a dispersive feature, representing respectively the drive, the spin response and *the interference* between the two terms. In the limit of strong coupling, one finds that the

maximum and minimum of the signal are separated by approximately $\sqrt{\Gamma_s^2 + \gamma_s^2}$, which in the high-$Q$ limit is approximately Γ_s. In the simplest case, the readout rate can therefore be estimated simply by measuring the frequency difference between the maximum and minimum response.

For the case when $\zeta_s \neq 0$, equation (5.86) leads to a correction of the separation, as the maximum and minimum are separated by $\sim \sqrt{(1+\zeta_s^2)(\Gamma_s^2(1+\zeta_s^2) + \gamma_s^2 - 2\Gamma_s\gamma_s\zeta_s)}$. In the high-coupling limit, $\Gamma_s \gg \gamma_s$, this simplifies to $\sim \Gamma_s(1+\zeta_s^2)$. For our case, when $\zeta_s \sim 0.03$, the correction from the QND case is small. Even though the QND result was derived under a set of approximations, the rule of thumb applies surprisingly well to the full model as well (for $\theta = \pm 45^\circ$ and $\phi = 0^\circ$).

The full CIFAR model is presented in Fig. 5.21, for the QND case, and without the broadband mode included. In the left hand panel, the response is shown for detection of the phase quadrature ($\phi = 0^\circ$), and with varied input modulation angle. For $\theta = \pm\pi/4 = \pm 45^\circ$, we see that the signal is essentially flipped around the resonance, and the minimum response is found at $\pm\Gamma_s/2\pi = \pm 10\,\text{kHz}$.

In the righthand panel, the input angle is fixed at $\theta = \pi/4$, and Γ_s varied from 1 kHz to 20 kHz; we see that the minimum moves to large detunings, and that the interference becomes stronger, leading to a deeper dip.

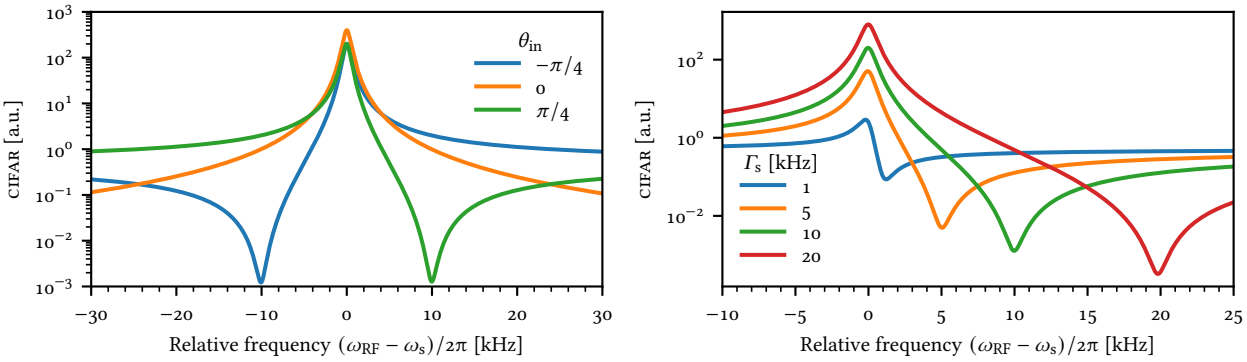

Figure 5.21: CIFAR simple theory. Left: CIFAR for varied input modulation angle, θ. Right: CIFAR for varied Γ_s. $\zeta_s = 0$ (QND case), $\omega_s/2\pi = 1\,\text{MHz}$, $\gamma_s/2\pi = 1\,\text{kHz}$. The broadband mode is not included.

Next, we turn to experimental investigations of the CIFAR signal. In Fig. 5.22 we plot the signal for $\theta = 45^\circ$, $\phi = 0^\circ$, for a range of different RMS drive voltages sent to the EOM, effectively changing G. We plot the amplitude and phase of the CIFAR signal, instead of the amplitude squared discussed in the text. First, we see the thermal response in gray at the bottom; except for the very lowest drive voltage, the signals are all orders of magnitude above the thermal background, and ignoring it is justified. For the lowest drive voltage displayed, we are on the brink of needing to include the thermals directly, to accurately model the response at the dip.

Second, we see that the data is overall well described by the model. The residuals of the fits in Fig. 5.22 is shown in Fig. 5.23. We here see that for low drives, the residuals are flat, and gaussianly distributed; as G is increased, we start to see

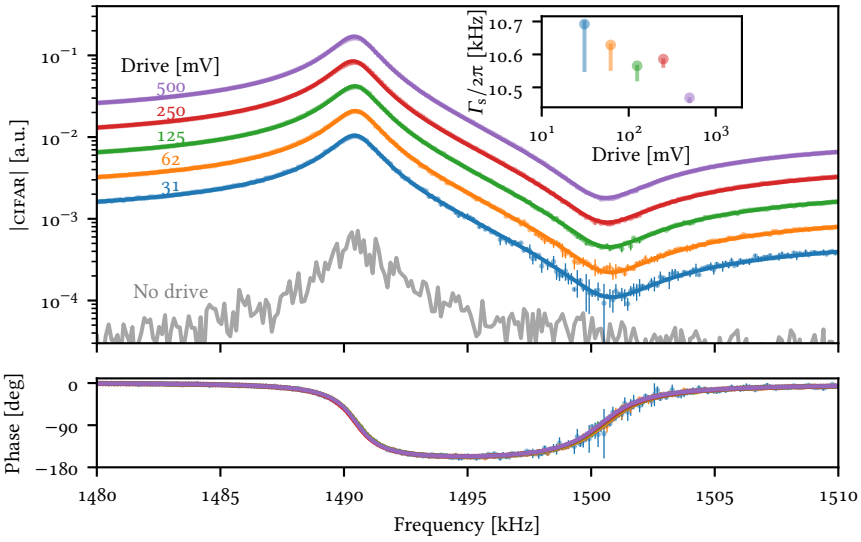

Figure 5.22: CIFAR as a function of modulation amplitude. Average of 3 scans, with 1σ statistical error bars. The CIFAR amplitude (top panel) scales with the EOM modulation depth, G, proportional to the drive voltage, while the phase response (bottom panel) is insensitive to the drive amplitude. The model (solid lines) is fit collectively to the amplitude and phase curves, but separately for each drive voltage. Grey line: response with no drive. Inset: fitted readout rates, Γ_s with asymmetrical error bars – see main text for details. The broadband mode is included in the model. $\theta = 45°$, $\phi = 0°$. Fit residuals are displayed in Fig. 5.23.

structure in the residuals, a deviation from the Gaussian distribution of the residuals. We also observe a trend of higher reduced χ-square value, χ^2_{ref}, indicating a worse fit. Data errors is the statistical error from repeated measurements, and the amplitude and phase traces are fitted collectively for each trace.

The fitted readout rates are displayed in the inset in Fig. 5.22, with their *asymmetrical* 68.27 % confidence interval, corresponding to a 1σ uncertainty for the symmetric uncertainties. The confidence interval is evaluated with the `conf_interval` function of our fitting package `lmfit` (Newville et al. 2021)[40]. The function returns the parameter values for which $\chi^2 = \chi^2_{\text{min}} + 1$. At first sight, the is a clear trend that higher G leads to a lower fitted Γ_s. Here we note that the four results corresponding to the lowest drive voltages all agree statistically, and that only the result for a drive voltage of 500 mV disagrees—and here the clear structure in the residuals and overall worse fit quality indicate that the fit should not be trusted too much. Furthermore, the variation seen in the inset is on the percent scale, despite the order-of-magnitude change in G. Indeed, the fitted value is rather resilient to changes in G, not obviously dependent on it, as long as the fit is good.

To verify the scaling with readout rate, we need to vary either the amount of light or the mean spin. The minimally invasive method is to change the spin, because changing the readout rate effectively also changes our detection. We therefore vary the cell temperature, which changes the number of atoms, and thereby

(40) Matt Newville et al. (2021). *LMFIT: Non-Linear Least-Square Minimization and Curve-Fitting for Python*. zenodo.org/record/4516651. Version 1.0.2.

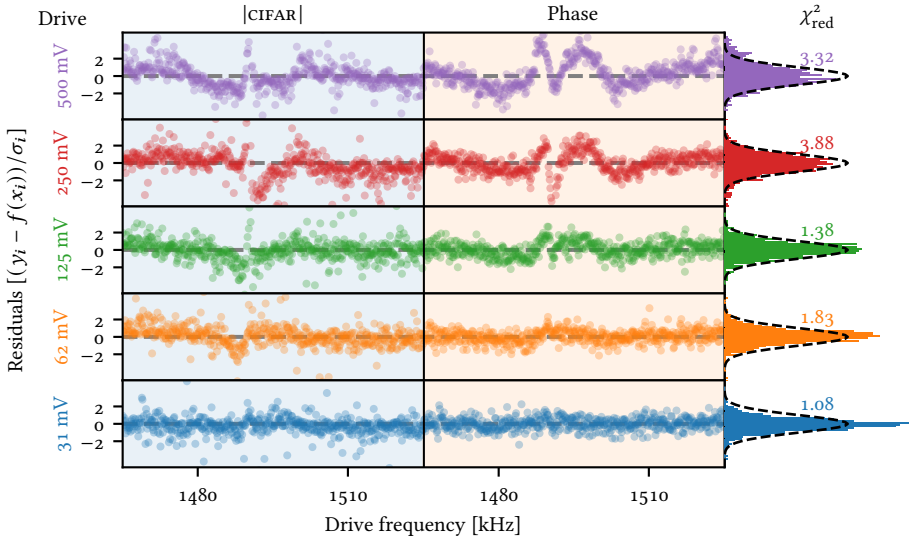

Figure 5.23: Scaled fit residuals from Fig. 5.22. Residuals between the model and data, both in CIFAR amplitude (left column) and phase (right column), scaled with the data uncertainty, for the various drive voltages shown in Fig. 5.22. In the right-most column we show the histogram of the residuals along with a unity width Gaussian curve (dashed lines) to guide the eye. We also print the reduced χ^2. Some outliers are not shown.

J_x. The result of this measurement is shown in Fig. 5.24. Because the change of gas pressure and thermal velocity leads to a slight change in the atomic linewidth, the results are normalized to the respective values of γ_s.

The results in Fig. 5.24 should be compared to the single-mode theoretical curves in the right hand panel of Fig. 5.21. Overall, the experimentally observed behaviour is very well described by the model, as also witnessed by the overall good quality fits. The most obvious discrepancy between the experimental results and Fig. 5.21 is that while the simple model predicts that the CIFAR response amplitude at the minimum keeps getting lower and lower, experimentally we seem to observe a floor below which the peaks do not drop, even for larger readout rates. We ascribe this behaviour to the presence of the broadband mode.

The inset of Fig. 5.24 depicts the rule of thumb that the point of the minimum of the CIFAR curves being located Γ_s away from the maximum, by plotting the separation from maximum to minimum values, Δ_{rf}, normalized to the spin linewidth, γ_s, versus the fitted readout rate Γ_s.

We turn now to the role of the LO angle, α, which controls the tensor coupling, ζ_s as

$$\zeta_s = -14\frac{a_2}{a_1}\cos(2\alpha), \tag{5.88}$$

which means that the size of the tensor coupling is maximized for $\alpha = n \times 90°$, and turned off for $\alpha = 45°$. To reduce the quadratic Zeeman splitting we reduce ω_s to 400 kHz, and turn down the probe power to 250 µW to reduce power broadening.

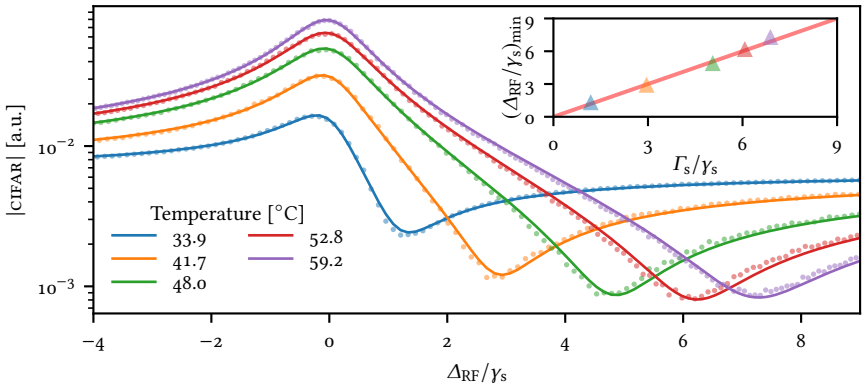

Figure 5.24: CIFAR as a function of cell temperature, effectively changing Γ_s/γ_s. We vary the readout rate by changing the temperature of the cell from ~34 °C to ~59 °C. Inset: The location of the minimum of the CIFAR response in units of Δ_{rf}/γ_s as a function of the normalized readout rate Γ_s/γ_s. Solid line: line with slope 1.

We perform the measurement for two different setting of the input modulation and θ, displayed in Fig. 5.25; in the top panel we display the curves for $\theta = 45^\circ$, as above, while in the bottom panel we display the corresponding curves for $\theta = 90^\circ$. According to equation (5.81), the detected signal goes as

$$|\text{CIFAR}(\theta = 90^\circ, \phi = 0^\circ)/G|^2 = \left|1 - 2\Gamma_s\zeta_s\left(\tfrac{\gamma_s}{2} - i\omega_{rf}\right)\chi_s\right|^2 \tag{5.89}$$

$$\sim 1 - \frac{\zeta_s\Gamma_s\gamma_s}{\Delta_{rf}^2 + (\gamma_s/2)^2}, \tag{5.90}$$

where in the second line we used the high-Q ($\gamma_s \ll \omega_s$ and $\omega_{rf} \sim \omega_s$), and the small tensor coupling ($\zeta_s \ll 1$) limits.

The top panel shows curves essentially looking like those presented in Fig. 5.22. The change in ζ_s does lead to a slightly modified spin linewidth and resonance frequency, but all with a readout rate of $\Gamma_s = 4.9$ kHz.

For $\theta = 90^\circ$, we directly measure the input modulation, which dominates the signal. The spin system responds only with addition ($\zeta_s < 0$) or subtraction ($\zeta_s > 0$) of signal close to the spin resonance. We fit the tensor terms to

$$\begin{aligned}\zeta_s^{0^\circ} &= -0.045 \pm 0.002\\ \zeta_s^{90^\circ} &= 0.040 \pm 0.003,\end{aligned} \tag{5.91}$$

which should be compared to the calculated value for a perfectly spin polarized ensemble of $|\zeta_s|_{max} = 0.053$. For $\alpha = 45^\circ$, the theory predicts zero tensor coupling, reflected in the flat response in Fig. 5.25; here we fit $\zeta_s^{45^\circ} = 0.000 \pm 0.001$.

Finally we present measurements of the broadband mode contribution to the CIFAR signal, in Fig. 5.26. We increase the scan range from the 30 kHz displayed in Fig. 5.22 to ~600 kHz, thus probing the broadband mode shape more effectively, but otherwise run the experiment under the same conditions as the 62 mV trace.

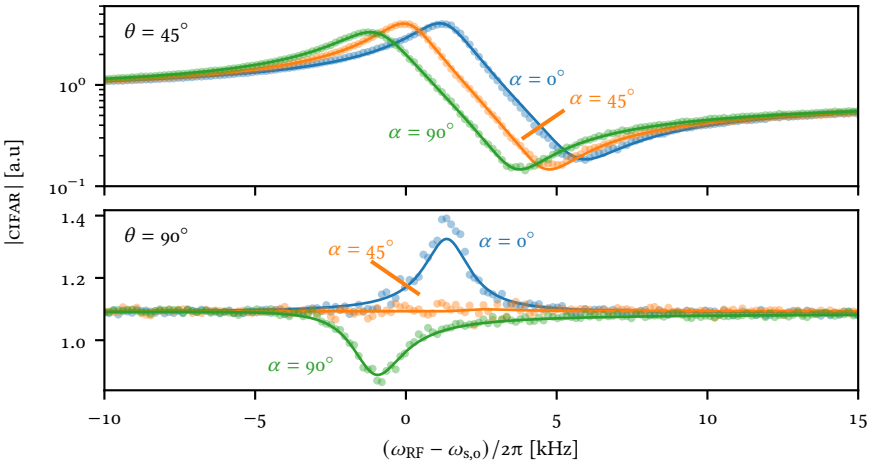

Figure 5.25: CIFAR signal for different tensor coupling parameters ζ_s. The overall response of the spin oscillator to light depends on ζ_s, here controlled by the angle α between the input linear polarization LO and the direction of the magnetic bias field B. The CIFAR signals for input modulation with $\theta = 45^\circ$ (top panel, logarithmic scale) and with $\theta = 90^\circ$ (bottom panel, linear scale), and $\alpha = \{0^\circ, 45^\circ, 90^\circ\}$ are shown in blue, orange and green, respectively.

We perform these measurements for $\theta \in \{-45^\circ, 0^\circ, 45^\circ\}$, and plot the amplitude responses (top panel) and phase responses (bottom panel).

Comparing the $\pm 45^\circ$ traces (green and blue, respectively), we see that flipping θ flips the CIFAR signal around the resonance, and send the phase from "zero plus a peak" to "180 degrees minus a dip". Insets show the narrow phase responses.

For $\theta \sim 0^\circ$, we observe a near-Lorentzian peak, with the asymmetry arising from a slightly wrong θ. For this trace we split the fitted model (dark orange line) into the narrow (light orange line) and broadband (dashed) responses, by evaluating the model with $\Gamma_{s,b} = 0$ and $\Gamma_s = 0$ respectively. For the amplitude we observe how the narrow mode is dominated by the broadband response away from resonance. For the phase response, we see how the expected shift from 180° to 0° is added together with the much more slowly varying broadband mode phase, leading to the non-trivial shape which undergoes a full 180° flip on resonance, but deviates from the light solid line away from resonance. We fit the broadband readout rate $\Gamma_{s,b} = 33.4\,\text{kHz}$ and $\gamma_{s,b} = 0.93\,\text{MHz}$, which should be compared to the readout rate for the narrow mode of $\Gamma_s = \sim 10.6\,\text{kHz}$, and $\gamma_{so} = 1.3\,\text{kHz}$. The experimental traces are very well described by the model over a very wide range of frequencies, despite the highly simplified two-mode model used, thus reinforcing our belief in this simplification for CIFAR and other experiments.

***

This concludes the chapter on spin systems, as well as the entire first part of this thesis.

In this chapter we saw how to effectively map the collective spin of an ensemble of alkali atoms to a harmonic oscillator picture (potentially with a negative effective mass). We started by considering the single-atom Hamiltonian, and de-

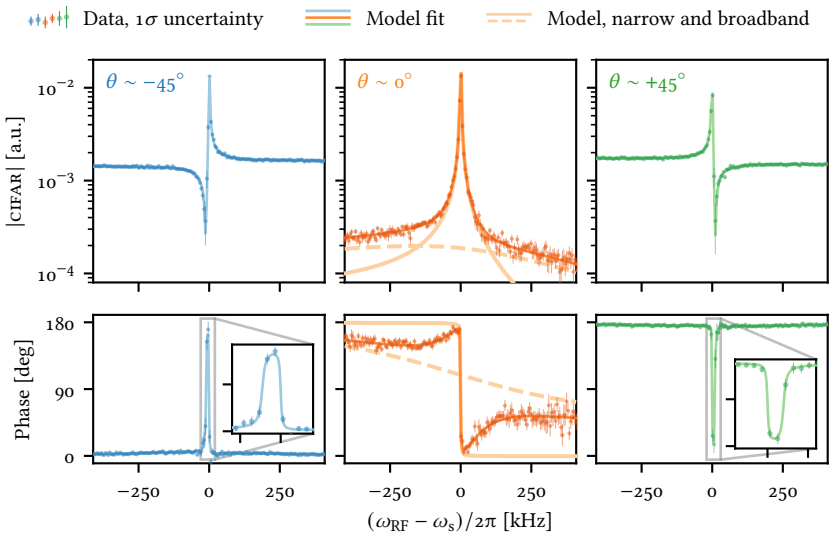

Figure 5.26: Coherent interference between the responses of the narrow and broadband spin modes. CIFAR response amplitude (top row) and phase (bottom row) data (points with error bars) and fits (dark solid lines) as a function frequency detuning for three different modulation phases, $\theta \in \{-45°, 0°, 45°\}$. The data was taken under the same experimental conditions as the 62 mV drive trace (orange curve) in Fig. 5.22. For $\theta = 0°$ we also plot the fit result evaluated with the broadband readout rate set to $\Gamma_{s,b} = 0$ (solid light orange curves, top and bottom panels) and narrowband readout rate $\Gamma_s = 0$ (dashed light orange curves).

scribing the effect of (weak) magnetic fields in the energy-eigenstate basis, before going to the collective angular momentum operator basis.

With the collective spin variables, we performed the Holstein–Primakoff approximation, which maps the transverse spin components of the large collective spin to a harmonic oscillator picture. By flipping the relative orientation of the collective spin and the external magnetic field, we saw how the system can be prepared either in the maximum energy state or the minimum energy state, which corresponds to effective negative and positive mass, respectively.

We then turned to the interaction of light with the spin ensemble. After introducing the Stokes parameters, describing the polarization state of light, before discussing how light reads out the spin projection on the light propagation axis through the Faraday effect, and we saw a corresponding back-action drives the spin. We then derived a set of input–output relations for the spin system.

With the theory in place, we turned to a set of practical tasks: how to actually implement a suitable spin system in practice, how to calibrate it, and a number of important aspect left out of the description so far, most importantly the motional averaging. We finished the chapter by a longer exposition of CIFAR, our novel method for efficiently measuring the spin readout rate.

❖ ❖

With these words we close this Part, having discussed the field of quantum optics, in which this work is set, and the relevant physics of both optomechanics

and ensemble spin systems. In Part II we will discuss a new optomechanical cavity design, relevant to hybrid optomechanics.

Part II

A NEW HYBRID CAVITY

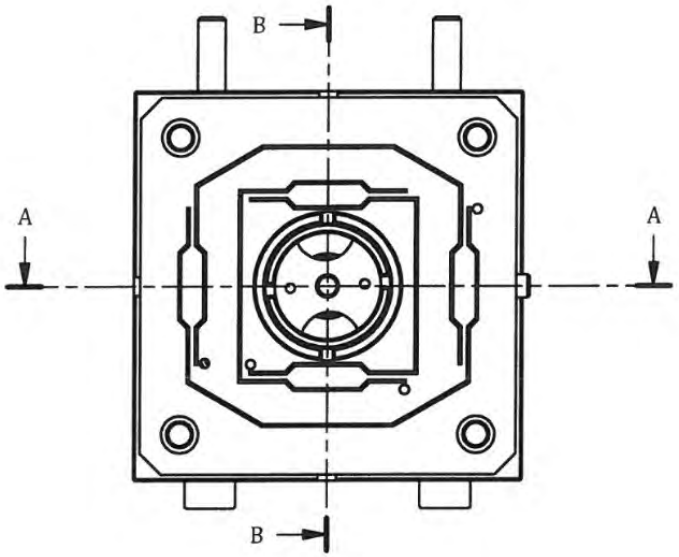

B-B (2 : 1)

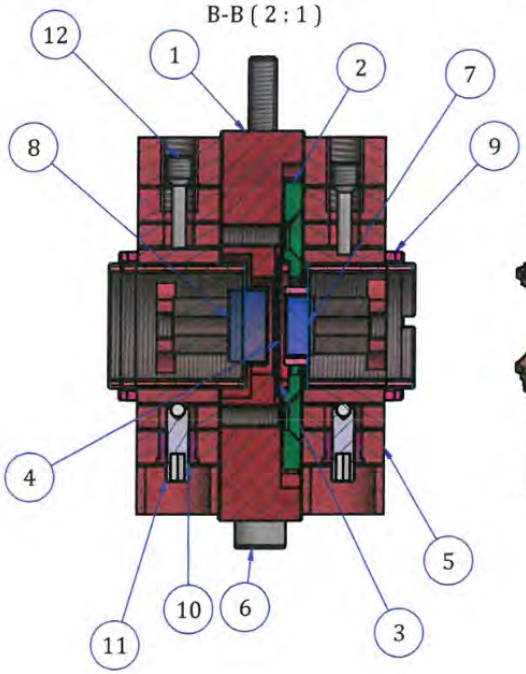

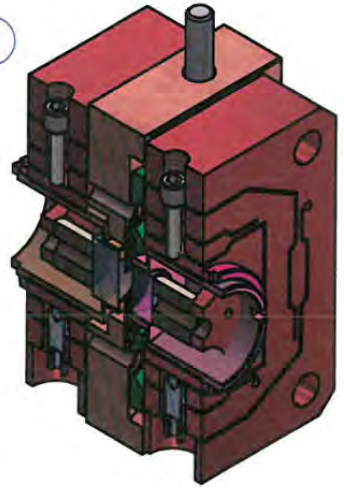

A-A (2 : 1)

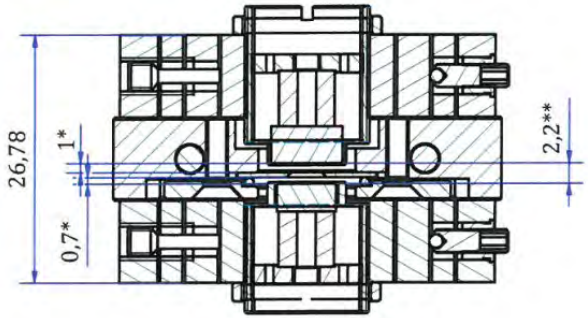

*Mirror to Wafer
**Mirror to Mirror

ITEM	PART NUMBER	QTY	DESCRIPTION	MATERIAL
1	QT-000187v2.0	1	Outer Membraneholder	Copper
2	QT-000188v2.0	1	Inner membrane holder	Copper
3	QT-000192v2.0	1	o-ring_11.5x1.0	Generic
4	QT-000196v2.0	1	SiN_patterned_membrane_1.3MHz	Generic
5	QT-000177v2.0	2	XY Stage	Copper
6	ISO 4762 - M3 x 30	2	Hexagon Socket Head Cap Screw	Stainless Steel, 440C
7	QT-000202v2.0	1	Assembly_layertec_cup	
8	QT-000201v2.0	1	Assembly_supermirror_cup	
9	QT-000197v2.0	2	SM05RR_outside retainer ring	Copper
10	F2D5ESN1P_cut	4	Custom fine pitch bushing	Generic
11	F2D5ES8	4	Thorlabs fine pitch screw	Generic
12	QT-000177-Custom M3 spring screw	4	Custom M3 spring screw	Stainless Steel, 440C

Part name: QT-000200v2.0.iam	Rev.:	Pcs:	**Niels Bohr Institute** **Technical Support Group** Mechanical Department University of Copenhagen
Description: Membrane Holder Assy			
Material:			
Surface treatment:			
Department: Quantop			Date 22-08-2018
Project: Hybrid Sample Holder v2.0 Elmedur			Scale 2 : 1
Initiator: Christoffer Østfeldt			Sheet Size A3
Designed by: user			Page no. 1
All dim. without tolerances ISO 2768-1 (fine)		Design state:	

Chapter 6

A New Cavity

> “The first step of any project is to grossly underestimate its complexity and difficulty.
>
> Nicoll Hunt

A new optomechanical cavity design for hybrid optomechanics is presented. We introduce several important degrees of freedoms to the cavity, compared to earlier, semi-monolithic designs. We present a set of associated problems, and how we overcame these.

6.1 Motivation & Context

Photo on opposite page: Technical drawing of cavity design.

As described earlier, in Section 2.2, the design choices made for the first optomechanical assemblies in our group was in many ways very good for “pure” optomechanics. I. e., the choices made were conducive to successful quantum optomechanics experiments such as Nielsen et al. (2017), but lacked the the necessary degrees of freedom to easily interface with other quantum systems, e. g., atomic spin systems.

The main design philosophy in the first successful cavity designs implemented in Quantop, was the so-called “monolithic”(1) design. Although the design was not in practice truly monolithic, the design philosophy favored having the smallest amount of parts, to minimize the number of degrees of freedom; all of which could become misaligned upon cryogenic cool down. For a more detailed discussion see Nielsen (2016).

(1) I. e., ideally consisting of a single piece.

The cavity assembly, depicted schematically in Fig. 6.1, consisted in the end of a copper holder, with a spring pushing the (flat) bottom mirror towards a stack of spacers, the membrane, a second copper piece clamping this spacer stack down,

and finally a top copper piece which holds the (curved) top mirror and allows for transverse alignment of the mode. The spring at the bottom allowed for a controllable amount of clamping force, ensuring that the silicon wafers would not shatter while remaining tightly pressed to the plot bottom mirror. In this design, all alignment had to be performed at ambient conditions, and locked down with screws. Once at operating conditions, no mechanical degrees of freedom was accessible to experimenter.

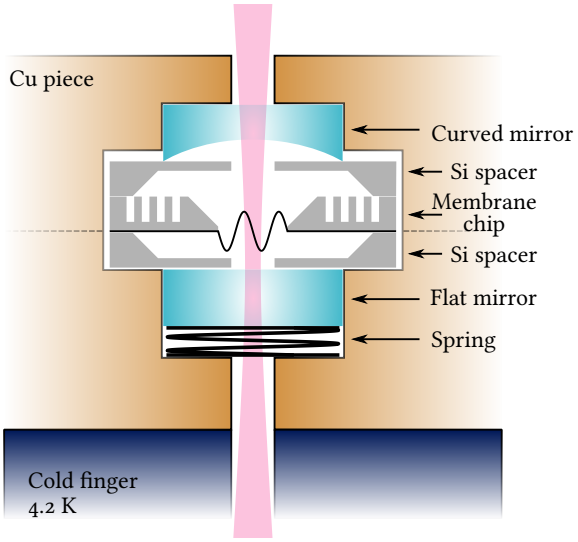

Figure 6.1: The old, monolithic, cavity design concept. In practice, the top (curved) mirror was suspended from a separate copper piece, to allow for transversal alignment of the beam to the defect, and the top spacer was clamped by copper. Adapted from Nielsen 2016, with modifications.

For pure optomechanical experiment this limitation is not a showstopper. Tuning the wavelength through a series of FSRs, thus sampling a variety of different $2kz$-points, allowed for the necessary freedom in being resonant with the cavity and having the membrane at a good coupling point.

In Møller et al. (2017), the membrane system was for the first time coupled to an atomic system. Whereas the optomechanics cares, to good approximation[(2)], only about the membrane position in $2kz$, the cesium atoms care also about the absolute frequency. We typically operate detuned 3 GHz blue detuned of the D_2 line at 852.347 nm plus minus 1 GHz for specific experiments, and with any given experiment needing much smaller changes to the detuning – tens of MHz being a good upper limit of permissible deviations. Since the FSR of optomechanical cavities employed in our lab is much larger[(3)] than the permissible tuning range, having the atoms and cavity be resonant at the same time, with no degrees of freedom in the cavity is simply not feasible.

To overcome this, the top copper part, which had until then only been utilized for transversal alignment of the curved top mirror, was modified by the addition of piezo, in what is internally named the "semi-monolithic" design. The mirror was glued to the piezo, which was itself glued to the top copper part, thus suspending

(2) As long as membrane and mirror reflectivities are constant.

(3) typically 20 GHz to 50 GHz.

the mirror on the piezo alone. This allowed for tuning of the overall cavity length, and thus the cavity could be brought into resonance with the light tuned to the atomic transition.

The main disadvantage of this semi-monolithic cavity was the lack of $2kz$-tuning. Having used the one degree of freedom to put the cavity into resonance with the light, one is simply left with whatever coupling one has. In practice, thermally cycling the entire cavity setup from 4 K to ~ 100 K and back allowed for some change in $2kz$ at the cesium wavelength, but the tuning direction or size was not predictable, and once a good coupling point had been reached, all further experiments had to be performed with the remaining LHe in the dewar, as the thermal shift associated with a dewar change would lead to an undesirable change.

At the end of 2017 we concluded that the (semi-)monolithic design had to be abandoned in favor of a new cavity design, allowing for full electronic $2kz$ control. However, simply repeating the "suspend a mirror from a piezo" would not suffice a second time: the monolithic design assumed the clamping of the membrane chip to the surface of a flat mirror. Being at once suspended and tightly clamped are incommensurate requirements. A new strategy was needed.

6.2 Requirements and Design Constraints

I will now try to describe a set of criteria that sums up the condensed knowledge and experience that crystallized from our iterative development. These requirements and the consequences we draw from them are thus not a list of criteria we consciously set down during the design process, but a *post facto* summary of our final design goals.

The main goal of a new cavity design is thus most easily summed up as:

Requirement 1. *We require full $2kz$ tuning and cavity locking at cryogenic conditions.*

Given the constraints lined out in Section 6.1 this quickly leads to the following

Consequence 1.1. *Either both mirrors must be suspended* or *a compressible element must be placed between one mirror and the membrane.*

The second option, i. e., the mechanically pliable element between one mirror and the membrane was the "simplest" solution, since it involved in principle only changes to one element of the previous design: Replacing a single silicon spacer with one that had been partially edged over a large area to a thickness significantly thinner than the usual 500 µm, whereas the former possibility meant a total redesign. Since a full $2kz$ equals $\lambda/2 \sim 425$ nm, the deformation of the silicon "spring" is by itself not problematic.

The former option, suspending both mirrors, on the other hand required a dramatically different cavity design, with the parallelity of the membrane with the optical mode no longer ensured by the clamping.

Requirement 2. *There must be good thermal contact between the membrane and the cold finger of the cryostat.*

Consequence 2.1. *The membrane must be clamped directly by a copper piece.*

Requirement 3. *It must be possible to change the overall cavity length by several millimeters.*

Since the overall cavity length is directly responsible for parameters such as light-membrane coupling, g_0, and cavity linewidth, κ, we need to be able to adjust the length in a flexible way, e. g., to get more or less sideband resolution. Having the cavity length fixed by the design is undesirable.

Requirement 4. *The cavity must be low loss.*

As discussed in more depth in Chapter 7, this requirement not only means having low loss mirrors and a membrane with good optical qualities, but also imposes strict requirements on the membrane/optical mode alignment.

Consequence 4.1. *Adjusting the effective membrane tilt must be possible.*

Consequence 4.2. *We need to place the mode on the membrane defect, to minimize scattering on the edges.*

Consequence 4.3. *We need the ability to place the membrane at the cavity waist.*

Further, it would be preferable if the degrees of freedom controlling the tilt and transverse position of the cavity mode on the membrane was somehow controlled by a gear or lever, trading actuation range for precision and repeatability. Positioning a mirror to a few tens of µm with your fingers only is not the easiest of tasks, and the alignment procedure in the old design could be excessively frustrating. Even worse, locking the parts in place would often ruin the alignment, such that the procedure in practice involved aligning the mirror to a certain degree of misalignment, which would then be corrected by tightening down the relevant fasteners.

6.3 The Solution

The chosen cavity design, internally called the *high degree of freedom* design, is shown in Fig. 6.2. It consist of a central piece, which holds the membrane, and two xy-translation stages, which support the mirrors. The central piece holds the membrane in a recess, and a lid clamps the membrane in place through an o-ring.

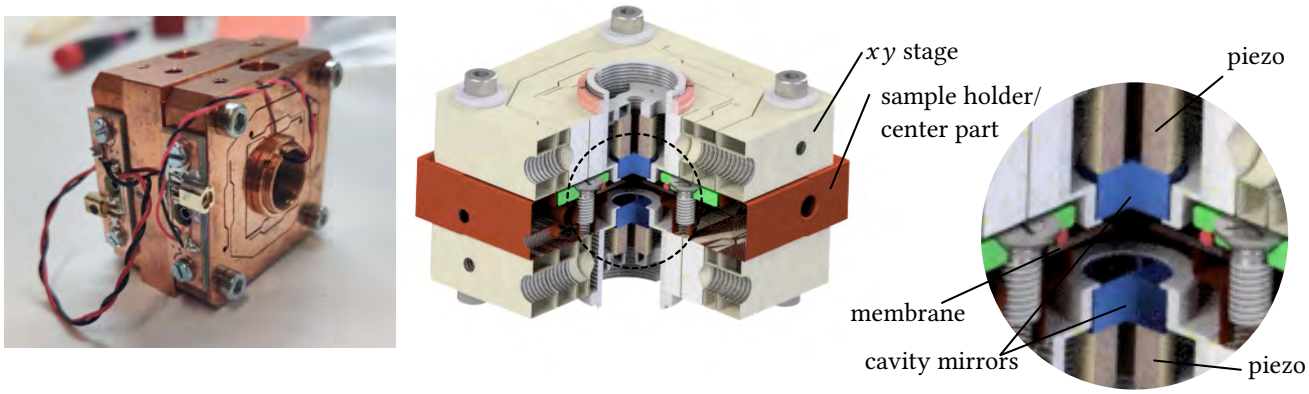

Figure 6.2: New cavity design. Left, picture of fully assembled assembled cavity. Center, CAD drawing with cut-away. Right, zoom in on the actual optical cavity, formed by the two mirrors (blue). The membrane is black with a brow hue on the cut-away sides, and sits below an o-ring (red), clamped by the lid (green).

The central piece is clamped directly to our cold finger. The xy-stages support one "barrel" each, in wihch a mirror–piezo stack is hosted, forming the optical cavity.

Instead of a plano-concave cavity design, with the membrane placed close to the flat mirror, we use a symmetric concave-concave cavity, with the membrane placed close to the center of the cavity.

The entirety of the cavity is machined from Elmedur copper by the institute in-house mechanical workshop; the only exceptions being the fine adjuster bushing, which we purchase from Thorlabs, and the flexture part of the xy stages, which was machined by an external company, plus trivial accessories, such a fasteners and o-rings.

The mirrors are mounted in a "barrel", see Fig. 6.4, which threads into the xy-translation stages with an external SM05 thread[4], and an internal M10 thread. The mirror sits at the front of the barrel, pressed against a thin lip of copper, alternatively a PTFE spacer, as depicted in Fig. 6.3. Behind the mirror sits a piezo, and the stack is clamped by a copper piece which threads into the internal thread of the barrel, internally called the *batman*, because of its vague similarity to that logo. The cutaways in the batman screw allows the piezo leads to exit the rear end of the can. A special tool ("trident") is used to tighten the batman part using the two small holes, while a central pin centers the piezo.

The piezos used are either PIEZOMECHANIK HPCH 150/6-2/x (where x denotes the piezo thickness, usually 6 mm) or THORLABS PK44RB5P2 piezo stacks. Both of these can be driven safely with voltages up to 150 V, and as low as −30 V[5] The Piezomechanik piezos have a listed free stroke[6] of around 3 µm for a 2 mm piezo stack. This value is then reduced first by external forces (the thing that the piezo is moving pushes back) and secondly by a factor of 4-5 by cooling to cryogenic temperatures. This means that in practice we have found the need for *at least* 4 mm piezo stacks, and ideally 6 mm.

The front face of the barrel is machined to a thinness (200 µm) where deformation by the piezo easily pushes the mirror forward, thus tuning the cavity.

(4) SM alludes to the original use in sewing machines, and 05 indicates a half inch diameter. The thread is currently used extensively by Thorlabs, and apparently virtually nowhere else.

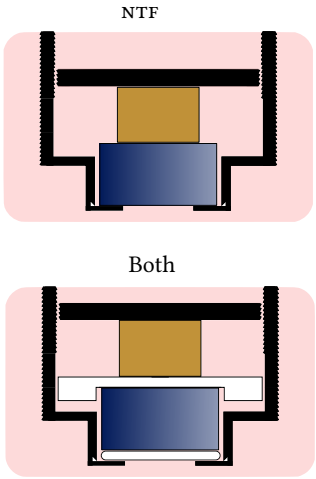

Figure 6.3: Different combinations of PTFE spacers. Also tested, but now shown: only PTFE at the front or back of the mirror. White: PTFE, blue: mirror, black: copper barrel, brown: piezo.

(5) Thorlabs lists the minimum permissible voltage as 0 V, and Piezomechanik as −30 V. In practice we have found no problem with using negative voltages with either.

(6) I. e., expansion of the piezo from one voltage extreme to the other with no force applied to the end faces.

The overall cavity length is controllable by screwing the entire barrel in or out of the *xy*-stage. A lock-ring fixes the barrel once the desired cavity length has been found.

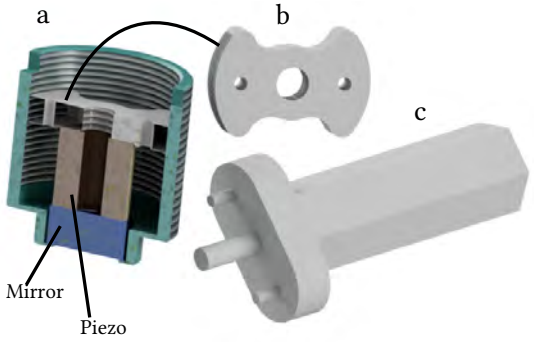

Figure 6.4: The mirror barrel (a) and batman (b), plus assembly tool (c) (sometimes called a "trident"). The barrel is shown with a mirror-piezo-batman stack, but no teflon spacers. All metal parts are machined from copper, except for the assembly tool, which is steel.

The translation states, shown in Fig. 6.5 bottom left, are essentially copper versions of the Thorlabs CP1XY *xy*-translation stage. The original steel version is designed for mounting in Thorlabs' 30 mm cage system, and features a SM05 thread in the center, for mounting optics in half in size or smaller. Two fine adjusters push the central part of the stage in either direction, and a spring mounted diametrically provides a force in the opposite direction, giving approximately ±250 µm travel range in both directions. In our design, the four holes in the corners are used to mount the translation stages to the central part.

The steel version is mechanically superior to our copper version, and was used for initial tests of the design. However, steel has the unlovable characteristic that it effectively stops conducting heat around 20 K, which makes cryogenic operation virtually impossible. One could consider using steel translation stages, with the membrane in a copper holder, but differential thermal expansion makes this a bad choice; maintaining a good alignment from room temperature to 4 K requires that all major elements are made from the same materials.

Unfortunately the flexible part of the *xy*-stage supports two mechanical modes at around 2 kHz, of which one is shown in the bottom left panel of Fig. 6.5. Because the mirrors are directly suspended from the threaded hole in the center, the cavity length is heavily perturbed, and locking becomes impossible if nothing is done to alleviate these oscillations. We dampen these vibrations by placing two rubber o-rings between the *xy*-stages and the center part/lid.

Fig. 6.5 also depicts the central copper part, clamping the membrane (top two panels). The membrane sits in a square recess, and is pressed to the copper by a rubber o-ring, which is clamped by a lid. The lid clamps tightly to the copper piece, ensuring thermalization, but also the the clamping force on the membrane is not sensitive to how tight the screws holding the lid are. Instead, the force is determined solely by the geometry of the recess, a similar recess in the lid, and the membrane and o-ring thicknesses.

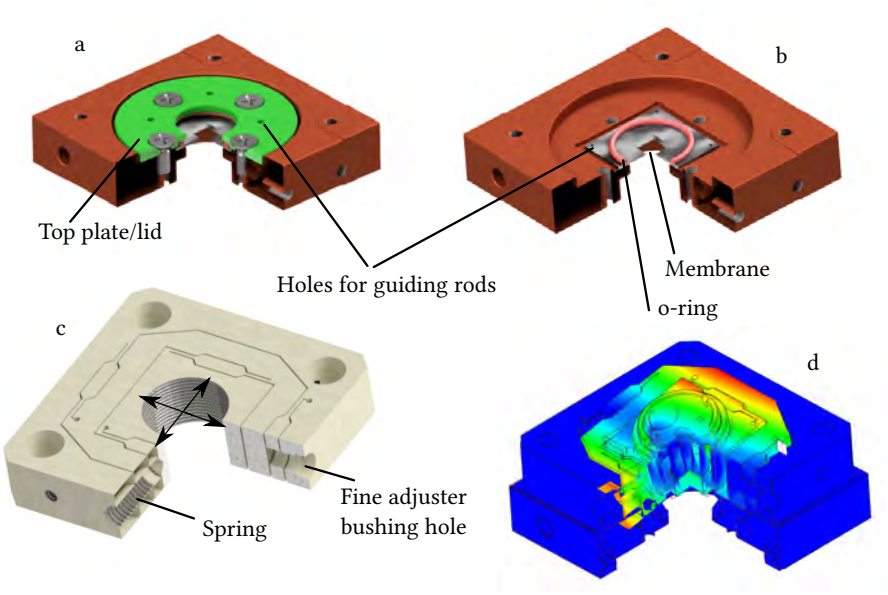

Figure 6.5: The cavity design exploded. The top two panels (a and b) depict the center part (dark orange), with and without the top plate/lid (green). The center part hosts the membrane (grey), which is clamped down by an o-ring (red). The bottom left panel depicts the xy stage; the thread in the center hosts the barrels, and can move in two directions, controllable by fine adjusters, which sit in bushings pushed into a set of holes. Opposite of each fine adjuster is a coarse thread, where a spring can be inserted and held in place by a set screw. Panel d depicts a mechanical mode of the xy stage with a frequency of ~ 2 kHz, which we dampen by placing o-rings between the center piece/lid and the xy-stages. All panels feature a cut-away for one quadrant, allow us to see the inside of the parts.

The lid and center part both have 4 small holes, which correspond to similar holes in the silicon frame of the membranes. By inserting thin rods into these holes, the transverse alignment of the membrane can be improved. After tightening the four screw securing the lid, the rods are removed from the assembly.

Finally, the center part contains two holes orthogonal to the cavity axis. These are used for clamping the center part to the cold finger (see Section 4.3.1), with a set of long bolts.

6.3.1 Aligning the Cavity

In terms of alignment the available degrees of freedom is displayed in Fig. 6.6. The length of the cavity can be changed large scale by the threading on the outside of the barrels, and fine-tuned by using the two piezos (brown). Further, the mirrors can be moved orthogonally to the cavity axis by the xy-stages.

The movement of the membrane in $2kz$ is displayed in Fig. 6.7. The common-mode ("center of mass") movement of the two mirrors keeps the cavity length unchanged, but moves the membrane in $2kz$. Conversely, the differential movement changes the resonance condition, but (for z_m close to $L/2$) keeps $2kz$ unchanged.

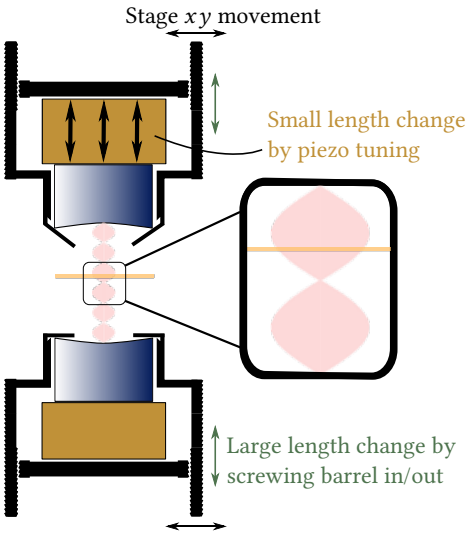

Figure 6.6: High degree of freedom cavity design concept. Each mirror can be moved laterally (in x and y) by the xy stages in which the barrels are mounted. Furhter, large scale length changes can be performed by screwing the barrels in and out. Fine control of the cavity length is achived by the piezos (brown) mounted behind each mirror.

Alternatively, one can think of one mirror as controlling $2kz$ and the other ensuring that the resonance condition is fulfilled for a given optical wavelength; this is how the hybrid experiment is typically operated, but similar designs used for optomechanics-only experiments in our group have used the former picture with success, partly due to their higher wavelength indifference.

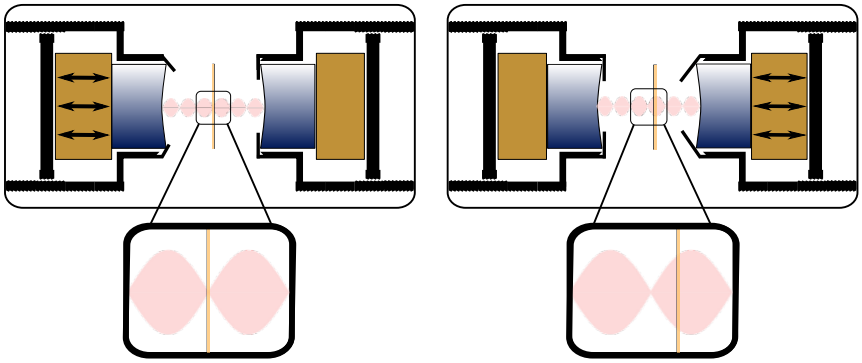

Figure 6.7: Moving the membrane in $2kz$. In the left picture, the membrane is sitting in a node of the cavity field (pink). By moving both mirrors to the left, by contracting the left piezo and extending the right, the standing wave moves left, so the membrane moves from the node to the high coupling point.

In the same vein, the common transverse movement of the mirrors displaces

the entire optical mode. The differential movement is used to control the effective membrane tilt, as displayed in Fig. 6.8. This ability to remove the effective tilt of the membrane is absolutely critical, and relies on the concave-concave geometry. At the same time it removes the necessity of clamping the membrane to one mirror, which in the old assembly was the method of minimizing tilt.

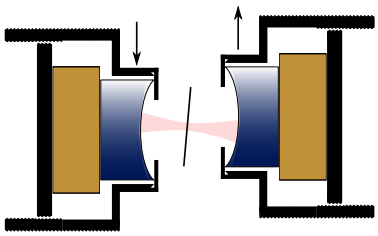

Figure 6.8: Aligning the membrane tilt in the new cavity design. Transverse movement of the mirrors tilts the cavity, such that a tilted membrane can be made perpendicular to the cavity mode.

6.3.1.1 *Practical Alignment Procedure*

A new cavity assembly is most easily aligned in a series of steps. First, the cavity is assembled without a membrane, the input optical mode is coupled into the cavity, and the cavity length is measured, for example by a measurement of the FSR. If needed, the cavity length is adjusted by screwing in or out one or both of the mirror barrels. Since the thread pitch is known (40 TPI, giving 635 µm translation per full revolution), changing the cavity length in relatively well known steps is rather straight forward.

Once the desired length has been established, a membrane is added to the assembly[(7)], and a rough alignment is performed; for this step minimizing losses is not crucial, as the goal is primarily measuring z_{m}, which is most easily done through a $2kz$ measurement (or two, as measuring both sub-cavity lengths gives a sanity check, because the total length is known). In the same manner as before, the subcavity lengths can be adjusted by turning the mirror barrels. Once the (sub-)cavity length(s) has been set, the membrane can be changed, and the cavity re-aligned without needing to change the barrel positions again.

(7) Taking care to always position the membrane in a consistent way, i. e., with the membrane face up or face down in the recess of the sample holder part.

In rough steps, the alignment procedure then goes as:

- Overlap mode with defect
- Remove visual movement of the cavity mode when $2kz$ is scanned
- Remove splitting of higher-order cavity modes

The overlap of the mode with the defect is most easily done by simply imaging the membrane with a camera while scanning one piezo by a full FSR, and overlapping the laser spot with the defect pad. This may require some work to couple into the effective cavity mode, which can be located somewhat far off the defect, and then iteratively moving the cavity mirrors and the mode, while keeping the input mode somewhat well-aligned. Alternatively, removing one mirror allows one to

place the laser spot on the defect freely; once the laser is positioned at the right spot, the mirror is put in place, and both mirrors are moved until the cavity mode overlaps with the well-aligned input mode.

Once the mode is overlapped with the defect has been achieved, removing the tilt of the membrane is the next task. This is achieved in two steps, with the first using visual information. As detailed in Chapter 7, if the membrane is tilted with respect to the cavity mode, the *cavity mode position becomes $2kz$ dependent*. If one changes $2kz$ while keeping the cavity resonant, one can see, often quite clearly, the cavity mode move. Such a situation is seen in Fig. 6.9. In practice, it is easier to use one piezo to scan one FSR slowly (~0.1 Hz) while the other piezo scans one FSR fast (~20 Hz). The fast scan ensures that each camera picture sees the fundamental mode, while the slow scan leads to a time-dependent mode position on the camera image. The movement of the mode can now be suppressed by small alignment changes of the mirrors, while keeping the mode centered on the membrane defect.

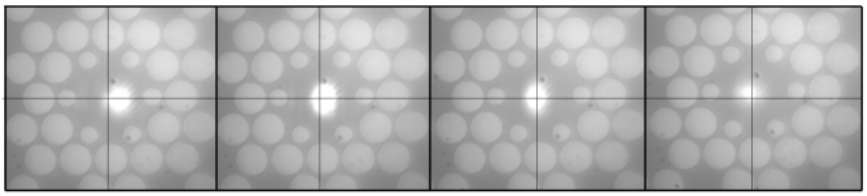

Figure 6.9: The optical mode moves as the cavity is scanned through $2kz$. For this assembly, the tilt is most prominent in the x direction, so the movement is largest in that direction.

On the large tilt has been removed, the last step in our alignment procedure is to remove the last amount of tilt, by minimizing the $2kz$-dependent splitting of higher-order cavity modes. The tilt breaks the degeneracy of the different TEM_{nm} families (for which $n + m$ is constant). For example, the TEM_{01} and TEM_{10} modes are split by a tilted membrane, but the splitting depends on the $2kz$ position. Therefore, we minimize this splitting by monitoring the splitting of these modes, while scanning one piezo over a full FSR. It is often not possible to completely remove the splitting, but it can be dramatically reduced from the initial value.

In this chapter, I introduced our new cavity design, which deviates strongly from the previous design philosophy of "monolithic" cavities, as well as our reasons for this deviation from previous efforts.

The addition of full electronic $2kz$ and resonance tuning, through the addition of a second piezo, is a major stepping stone, however trivial it seems at first glance, to implementing membrane-in-the-middle optomechanical systems in hybrid setps.

Chapter 7

Higher Order Optical Modes in an Optomechanical Cavity

> "It wasn't a dark and stormy night.
>
> It should have been, but that's the weather for you. For every mad scientist who's had a convenient thunderstorm just on the night his Great Work is finished and lying on the slab, there have been dozens who've sat around aimlessly under the peaceful stars while Igor clocks up the overtime.
>
> Terry Pratchett & Neil Gaiman, *Good Omens*

A numerical model for evaluating hybridization and splitting of higher order optical modes in optomechanical cavities. The model gives valuable insight into the detrimental effects of membrane tilt, wavefront curvature and clipping losses. The model is compared to experimental data.

In this chapter, I will present a numerical model for the higher order modes of a plano-concave optical cavity with a tilted, possibly scattering/clipping membrane somewhere in the mode of the bare cavity. The code is available online at https://erda.ku.dk/archives/5526970a884fbef314e5fc9753fcbec3/published-archive.html.

We will see how the model predicts that tilt, scattering and wavefront curvature each lead to detrimental effects for low loss optomechanical cavities; these points were used in the design of our new cavity in Chapter 6. To validate the model, we compare its predictions to experimental data.

7.1 Context & Motivation

When we transitioned away from using rectangular membranes with phononic shields in the silicon frame, and to the soft clamped membranes described in Section 4.1, several detrimental features of our optomechanical assemblies became apparent. This was in a way compounded by the fact that we were at this point gaining electronic $2kz$-tuning, and therefore could much easier investigate these kinds of features. In a monolithic cavity, only discrete points in $2kz$ may be probed, and with a single piezo, probing the whole $2kz$ required tuning the laser. In this way, one would sometimes just get a "bad $2kz$ point", but since this was used for pure optomechanics, jumping to another point was really no problem.

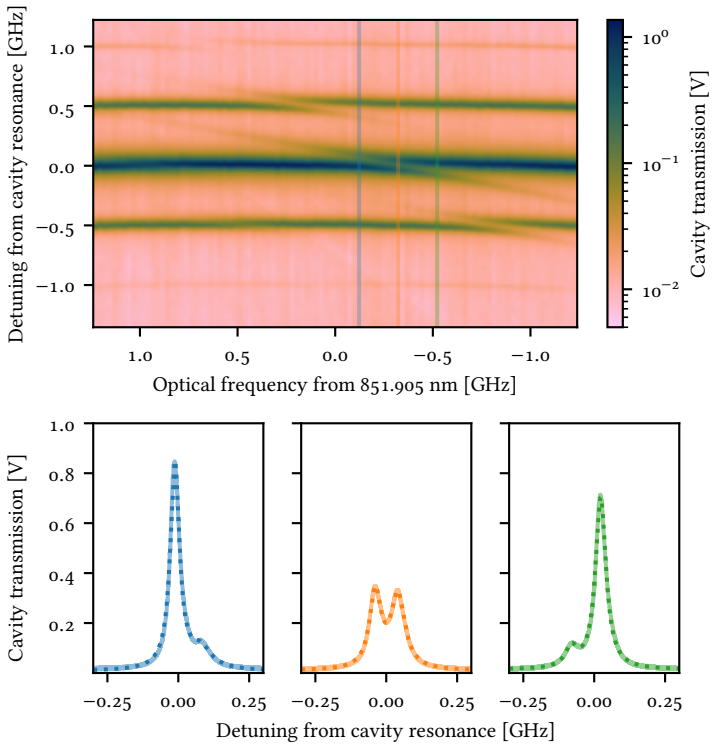

Figure 7.1: Avoided mode crossing of TEM_{00} mode with a higher order mode from a lower longitudinal mode family. The optical field is driven with 500 MHz phase modulation sidebands. Top: Cavity transmission as a function of optical wavelength (horizontal axis) and detuning from the primary cavity resonance. Note that the x-axis goes from high to low frequency, corresponding to low to high wavelength. Bottom: Cavity transmission as a function of detuning from cavity resonance, for a selection of optical frequencies around the avoided crossing. Vertical lines in top figure marks the corresponding figures in the bottom panels. Solid line: data, dashed line: fits to a double-Lorentzian model.

The most prominent sign of something breaking our nice single mode description is depicted in Fig. 7.1: avoided crossings of optical modes, when scanning $2kz$. Landing right on top of such a mode crossing severely broadens the mode, because higher order modes generally scatter more than the fundamental, by virtue

of simply being spatially larger. Any hybridization of the fundamental with higher order modes is thus an undesirable thing for us, leading to deformation of the optical mode (with concomitant decrease of coupling efficiency and homodyning visibility), worse overcoupling, larger cavity linewidth, reduced lock stability, etc. Understanding which factors contribute to splitting of higher order modes and to coupling of the fundamental mode to higher order modes is therefore important.

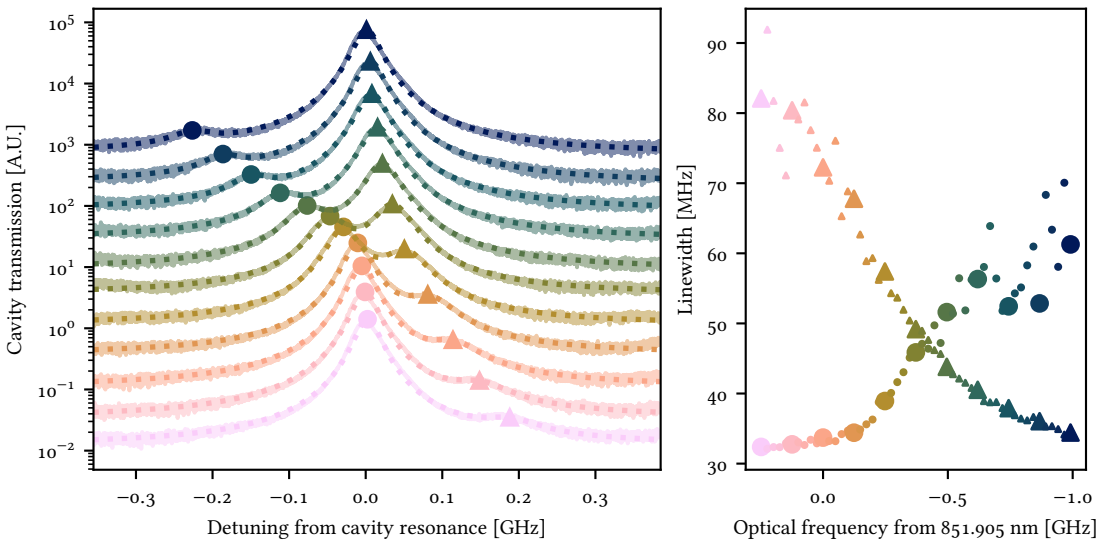

Figure 7.2: Cavity linewidth of two modes in an avoided mode crossing. Left: Fits to two Lorentzian lineshapes plus an offset. Round and triangular markers denote the maxima. Lines are offset vertically for clarity. Right: Linewidths of the two Lorentzians as a function of optical wavelength. We clearly observe the narrow and wide mode switch. Note that the x-axis goes from high to low frequency, corresponding to low to high wavelength. The large markers in the right figure correspond to the traces in the figure on the left, while the small markers correspond to traces not shown.

This hybridization, and broadening of the narrowest mode, can be seen in Fig. 7.2. In the left panel, I fit cuts of the data from Fig. 7.1 to a simple sum of two Lorentzians plus an offset. The round and triangular markers mark the maxima. In the right panel, I plot the fitted cavity linewidths as a function of the optical frequency.

7.2 A Numerical Model

To understand the observed mode crossings, and their causes, we developed a numerical model. The majority of the programming and derivations were done by Jürgen Appel. I present the model here, because the the understanding it brought to our cavity design was important, and comparison of our experimetnal data to a model without any explanation is unsatisfactory. The mathematical derivations of

a number of the expressions in the model will be simply postulated; the presentation here is based on an internal note prepared by J. Appel.

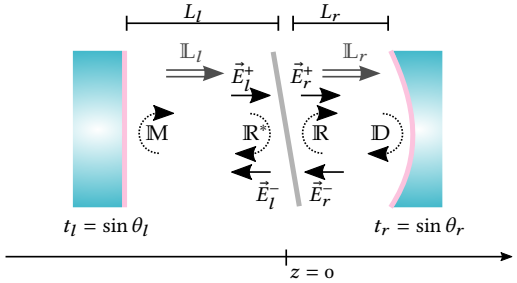

Figure 7.3: Mode model concept.

The basic building blocks of the model are depicted in Fig. 7.3. The cavity consist of one flat mirror at $z = -L_l$, with transmission t_l, a curved mirror at $z = L_r$ (transmission t_r) and a membrane at $z = 0$[(1)]. The transmissions and reflections are parametrized by the angles θ_l, θ_r, implying that no losses is assumed. A number of matrices are defined, which describe the spatial part[(2)] of reflection of the field at various places: $\mathbb{M}, \mathbb{R}, \mathbb{D}$ – we will return to these later. Propagation in a given subcavity is described by a matrix $\mathbb{L}_{l/r}^{(\dagger)}$, with the dagger denoting propagation to the left and no dagger to the right.

The fields are denoted by the subcavity they belong to, l for left and r for right subcavity, as well as the direction they are traveling, + for right and − for left:

$$\vec{E}_{l/r}^{+/-}, \tag{7.1}$$

and where the components of this vector are complex field amplitudes.

We now consider how the field impinging on the membrane relates to those leaving it, and by parametrising the membrane transmission by $t_\mathrm{m} = \sin\theta_\mathrm{m}$[(3)], we get the following expression

$$\underbrace{\begin{pmatrix}\vec{E}_r^+\\ \vec{E}_l^-\end{pmatrix}}_{\text{outgoing fields}} = \underbrace{\begin{pmatrix}\cos\theta_\mathrm{m}\mathbb{1} & -\sin\theta_\mathrm{m}\mathbb{R}\\ \sin\theta_\mathrm{m}\mathbb{R}^\dagger & \cos\theta_\mathrm{m}\mathbb{1}\end{pmatrix}}_{\text{unitary operation, to preserve energy}} \underbrace{\begin{pmatrix}\vec{E}_l^+\\ \vec{E}_r^-\end{pmatrix}}_{\text{incoming fields}}. \tag{7.2}$$

We now consider the fields in the left side of the cavity. The right-propagating field, just before the membrane, $\vec{E}_r^+$ can be expressed purely in terms of the left-propagating $\vec{E}_l^-$ and the matrices $\mathbb{L}$ and $\mathbb{M}$, giving

$$\vec{E}_l^+ = \mathbb{L}_l\mathbb{M}\mathbb{L}_l^\dagger\vec{E}_l^-. \tag{7.3}$$

Similarly, the left-propagating field just left of the membrane can be expressed in terms of reflected part of the right propagating field $\vec{E}_l^+$ and the transmitted part of the left-propagating field in the right sub-cavity

$$\vec{E}_l^- = \sin\theta_\mathrm{m}\mathbb{R}^\dagger\vec{E}_l^+ + \cos\theta_\mathrm{m}\mathbb{1}\vec{E}_r^-. \tag{7.4}$$

(1) The old cavity used this cavity geometry with one flat and one curved mirror, while the new cavity uses two curved mirrors. The numerical model is based around the old geometry, and is not trivially modifiable to a curved–curved geometry, for reasons discussed below.

(2) I. e., describing the change of propagation direction upon reflection off a tilted surface, or the focusing of the beam by reflection on a curved surface.

(3) There is a sneaky assumption here, that the membrane reflection is independent of the angle, which is strictly not true, but since we are always dealing with very small tilts we ignore this and press on.

Combining these two expressions we get

$$\vec{E}_l^+ = \mathbb{L}_l \mathbb{M} \mathbb{L}_l^\dagger \sin\theta_\mathrm{m} \mathbb{R}^\dagger \vec{E}_l^+ + \cos\theta_\mathrm{m} \mathbb{L}_l \mathbb{M} \mathbb{L}_l^\dagger \vec{E}_r^-, \tag{7.5}$$

which, upon collecting terms of the respective fields, becomes

$$\left(\mathbb{1} - \sin\theta_\mathrm{m} \mathbb{L}_l \mathbb{M} \mathbb{L}_l^\dagger \mathbb{R}^\dagger\right) \vec{E}_l^+ = \cos\theta_\mathrm{m} \mathbb{L}_l \mathbb{M} \mathbb{L}_l^\dagger \vec{E}_r^-. \tag{7.6}$$

For future use, we now multiply both sides of the equation by $\cos\theta_\mathrm{m}$, and divide by the prefactor on the left hand side, to obtain

$$\cos\theta_\mathrm{m} \vec{E}_l^+ = \cos^2\theta_\mathrm{m} \left(\mathbb{1} - \sin\theta_\mathrm{m} \mathbb{L}_l \mathbb{M} \mathbb{L}_l^\dagger \mathbb{R}^\dagger\right)^{-1} \mathbb{L}_l \mathbb{M} \mathbb{L}_l^\dagger \vec{E}_r^-. \tag{7.7}$$

Turning to the right hand side of the cavity, we perform a similar procedure, starting with the left-propagating field

$$\vec{E}_r^- = \mathbb{L}_r^\dagger \mathbb{D} \mathbb{L}_r \vec{E}_r^+, \tag{7.8}$$

which is simply expressed in terms of the right-propagating field. This field is in turn expressed as the reflected field in the right side of the cavity, and the transmitted beam from the left hand side, giving us

$$\vec{E}_r^+ = \cos\theta_\mathrm{m} \vec{E}_l^+ - \sin\theta_\mathrm{m} \mathbb{R} \vec{E}_r^-. \tag{7.9}$$

We now insert first the expression for $\cos\theta_\mathrm{m}\vec{E}_l^+$ from (7.7) as well as the expression for $\vec{E}_r^-$, and obtain

$$\vec{E}_r^+ = \left[\cos^2\theta_\mathrm{m} \left(\mathbb{1} - \sin\theta_\mathrm{m} \mathbb{L}_l \mathbb{M} \mathbb{L}_l^\dagger \mathbb{R}^\dagger\right)^{-1} \mathbb{L}_l \mathbb{M} \mathbb{L}_l^\dagger - \sin\theta_\mathrm{m} \mathbb{R}\right] \vec{E}_r^- \tag{7.10}$$

$$= \left[\cos^2\theta_\mathrm{m} \left(\mathbb{1} - \sin\theta_\mathrm{m} \mathbb{L}_l \mathbb{M} \mathbb{L}_l^\dagger \mathbb{R}^\dagger\right)^{-1} \mathbb{L}_l \mathbb{M} \mathbb{L}_l^\dagger - \sin\theta_\mathrm{m} \mathbb{R}\right] \mathbb{L}_r^\dagger \mathbb{D} \mathbb{L}_r \vec{E}_r^+. \tag{7.11}$$

This equation is, despite of the somewhat bulky appearance, essentially just an equation describing a field roundtrip, and can be expressed in the (deceptively) simple form

$$\vec{E}_r^+ = \mathbb{A} \vec{E}_r^+, \tag{7.12}$$

where the problem has now been reduced to finding the eigenvectors and -values of $\mathbb{A}$.

We can further expand this equation a bit, using the expressions

$$\mathbb{D} = \widetilde{\mathbb{D}} \sin\theta_r e^{-\mathrm{i}\varphi} \qquad \mathbb{M} = \widetilde{\mathbb{M}} \sin\theta_l e^{\mathrm{i}\varphi}, \tag{7.13}$$

where we have broken out the geometric effects of the mirrors into the matrices $\widetilde{\mathbb{D}}, \widetilde{\mathbb{M}}$, the transmission by the prefactors $\sin\theta_{l/r}$, and the phase factor $e^{(-)\mathrm{i}\varphi}$ denotes the extra phase accumulated in each subcavity by moving the membrane a tiny amount, i. e., the $2kz$ position[4].

(4) The $2kz$ phase could have been implemented into a small change in the lengths L_r, L_l, but this approach is perfectly sufficient, as long as the change of position needed to scan the entire $2kz$ is much smaller than the lengths of the subcavities, i. e., $z_{2\pi} = 2\pi/2k \ll L_r, L_l$.

Combining all of this, we get

$$\vec{E}_r^+ = \underbrace{\left[\cos^2\theta_\mathrm{m}\sin\theta_l e^{i\varphi}\underbrace{\left(\mathbb{1}-\sin\theta_\mathrm{m}\sin\theta_l e^{i\varphi}\mathbb{L}_l\widetilde{\mathbb{M}}\mathbb{L}_l^\dagger\mathbb{R}^\dagger\right)^{-1}\mathbb{L}_l\widetilde{\mathbb{M}}\mathbb{L}_l^\dagger}_{\equiv\mathbb{Q}}-\sin\theta_\mathrm{m}\mathbb{R}\right]e^{-i\varphi}\sin\theta_r\mathbb{L}_r^\dagger\widetilde{\mathbb{D}}\mathbb{L}_r}_{\equiv\mathbb{A}}\vec{E}_r^+, \tag{7.14}$$

where we have defined the total matrix $\mathbb{A}$ and a sub-matrix $\mathbb{Q}$.

It is now time to turn our attention to the most obvious question left untouched so far: how do we obtain a suitable expression for the propagation matrices $\mathbb{M}, \mathbb{D}, \mathbb{L}_{(l,r)}$?

Our solution will be to expand the field on a (truncated) basis of Laguerre-Gaussian modes, and express the coupling in terms of sums of couplings between these modes. In this way, we avoid having to evaluate the field at a very large number of points in space, but only need to compute $\mathcal{O}(N^2)$ couplings, where N is the total number of modes included in the truncation. We can then evaluate any particular solution as a weighted sum of Laguerre-Gaussians at the locations in the cavity we are interested in.

Some freedom is left w.r.t. the choice of basis. One obvious choice would be to pick the eigenbasis of the entire cavity, without the membrane. Instead, we will pick the eigenbasis of the subcavity with the curved mirror. This choice will make the matrices describing propagation in this subcavity much simpler.

We start with the general expression for the field strength of a Laguerre-Gaussian mode of index p, l, expressed in cylindrical coordinates (W. Bowen and Milburn 2015, chapter 7)

$$\mathrm{LG}_{p,l}(\rho,\varphi,z) = e^{il\varphi}\underbrace{\frac{e^{-\left(\frac{\rho}{w(z)}\right)^2}}{\sqrt{\pi w(z)}}}_{\text{Gaussian}}\underbrace{e^{ik\left(z+\frac{\rho^2}{2R(z)}\right)}}_{\text{Curved phase fronts}}\underbrace{e^{i(|l|+2p+1)\tan^{-1}\left(\frac{z}{z_R}\right)}}_{\text{Gouy phase}}\sqrt{\frac{2p!}{(p+|l|)!}}\left(\frac{\sqrt{2}\rho}{w(z)}\right)^{|l|}\underbrace{\mathcal{L}_p^{|l|}\left(\left(\frac{\sqrt{2}\rho}{w(z)}\right)^2\right)}_{\substack{\text{Generalized}\\ \text{Laguerre polynomial}}}. \tag{7.15}$$

Next, we'd better explain what all the different elements to this equation are. Firstly, the Rayleigh range z_R describes how fast a beam grows transversally as it propagates, and is given by

$$z_R = \frac{w_0^2\pi}{\lambda}, \tag{7.16}$$

where w_0 is the smallest transversal size, the *waist size*. As the beam propagates, the beam size changes as

$$w(z) = w_0\sqrt{1+\left(\frac{z}{z_R}\right)^2}. \tag{7.17}$$

This is depicted in Fig. 7.4. Also pictured is $\theta = \lambda/(\pi w_0)$, the far field opening angle of the beam.

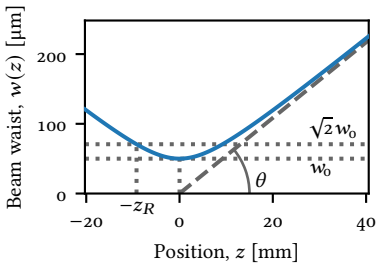

Figure 7.4: Beam size, $w(z)$, of a Laguerre-Gaussian beam with waist size $w_0 = 50\,\mu\mathrm{m}$, which corresponds to a Rayleigh range, z_R, of 9.2 mm. $\lambda = 852\,\mathrm{nm}$.

At the waist, the phase front is flat, and the curvature of the beam is therefore 0. Away from the waist, the radius of curvature $R(z)$ is given by

$$\frac{1}{R(z)} = \frac{z}{z^2 + z_R^2}. \tag{7.18}$$

The curvature of the phase fronts are depicted in Fig. 7.5, where a very tightly focused beam is seen to diverge and develop curved phase fronts as it propagates.

The first few *generalized Laguerre polynomials* $\mathcal{L}_p^{|l|}(x)$ are depicted in Fig. 7.6. The total Laguerre–Gaussian modes (real and imaginary field components plus intensity) at the waist ($z = z_0$) are depicted in Appendix C.

The following two pages of math is mostly relevant for those who want to understand the code in detail. For others, those interested mainly in the physics, understanding this should not be critical.

For compactness we now make the following two substitutions:

$$\xi = \frac{z}{z_R} \qquad \rho_z = \frac{\rho}{w_0\sqrt{\frac{1+\xi^2}{2}}}, \tag{7.19}$$

which leads to

$$\mathrm{LG}_{p,l}(\rho,\varphi,z) = \frac{1}{\sqrt{\pi}}\frac{\rho_z}{z} e^{\mathrm{i}k\xi z_R} e^{\mathrm{i}(|l|+2p+1)\tan^{-1}\xi} e^{-\frac{1}{2}(1+\mathrm{i}\xi)\rho_z^2} e^{\mathrm{i}l\varphi} \rho_z^{|l|} \sqrt{\frac{p!}{(p+|l|)!}} \mathcal{L}_p^{|l|}\left(\rho_z^2\right) \tag{7.20}$$

The "variance" of such a mode, i. e., a measure of the size is given by[5]

$$\int_0^\infty \int_0^{2\pi} \left|\mathrm{LG}_{p,l}(\rho,\varphi,0)\right|^2 \rho^3 \,\mathrm{d}\rho\mathrm{d}\varphi = \frac{w_0^2}{2}(2p+|l|+1). \tag{7.21}$$

Further, all modes are normalized

$$\int_0^\infty \int_0^{2\pi} \left|\mathrm{LG}_{p,l}(\rho,\varphi,z)\right|^2 \rho \,\mathrm{d}\rho\mathrm{d}\varphi = 1, \tag{7.22}$$

and have field amplitude at the transverse center at the beam position of

$$\mathrm{LG}_{p,l}(0,0,0) = \begin{cases} 0 & \text{if } l \neq 0 \\ \sqrt{\frac{2}{\pi w_0^2}} & \text{otherwise.} \end{cases} \tag{7.23}$$

With these identities and a somewhat bolstered understanding of what these modes are all about, we press on and define a number of couplings between different modes. First, we define the overlap of two modes translated by ξz_R

$$\mathrm{OVL}_{p_1,l_1}^{p_2,l_2}(\xi z_R) = e^{\mathrm{i}k\Delta z} \int_0^\infty \int_0^{2\pi} \mathrm{LG}_{p_1,l_1}(\rho,\varphi,0)^* \mathrm{LG}_{p_2,l_2}(\rho,\varphi,\xi z_R)\rho \,\mathrm{d}\rho\mathrm{d}\varphi, \tag{7.24}$$

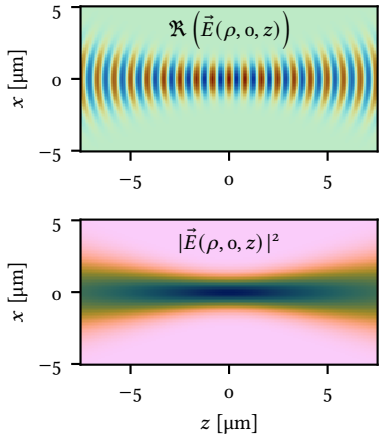

Figure 7.5: Curvature of the phase front. The beam is a very tightly focused beam, $w_0 = 1$ µm. Top: Real part of the electric field. Bottom: Intensity.

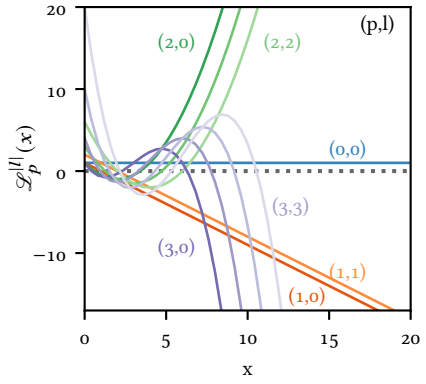

Figure 7.6: Generalized Laguerre polynomials, for $p \in [0..4]$ and $l \in [0..p]$. The extreme curves for each order of p are labeled.

(5) Picking up a factor ρ from the Jacobian, $\rho\,\mathrm{d}\rho\mathrm{d}\varphi$ and ρ^2 from the variance, and using already that we know that the intensity ($\propto |\mathrm{LG}_{p,l}(\rho,\varphi,z)|^2$) of all beams are cylindrically symmetric, so the mean value is 0.

where $ik\Delta z$ represents the trivial propagation phase. This equation may after a lengthy derivation, which I will not discuss or show here, be shown to equal

$$\mathrm{OVL}^{p_2,l_2}_{p_1,l_1}(\xi z_R) = \delta^{l_2}_{l_1} e^{i(1+2p_2+|l|)\tan^{-1}\xi}\left(\frac{-1}{\sqrt{1+\xi^2}}\right)^{1+|l|}\sqrt{\frac{p_1!}{(|l|+p_1)!}\frac{p_2!}{(|l|+p_2)!}}$$
$$\sum_{k_1=0}^{p_1}\sum_{k_2=0}^{p_2}\frac{(|l|+k_1+k_2)!}{k_1!k_2!}\binom{p_1+|l|}{p_1-k_1}\binom{p_2+|l|}{p_2-k_2}\left(-\frac{i+\xi}{i+\xi/2}\right)^{1+|l|+k_1+k_2}\left(\frac{1}{1+\xi^2}\right)^{k_2}. \tag{7.25}$$

Because of the Kronecker delta[6], $\delta^{l_2}_{l_1}$, only a single value of l is relevant, and the subscripts are dropped from all other occurrences in the equation.

In a similar fashion we define the overlap of two modes tilted with respect to one another

$$\mathrm{Tilt}^{p_2,l_2}_{p_1,l_1}(\alpha) = \int_0^\infty\int_0^{2\pi} e^{ik\alpha\rho\sin\varphi}\mathrm{LG}_{p_1,l_1}(\rho,\varphi,0)^*\mathrm{LG}_{p_2,l_2}(\rho,\varphi,0)\rho\,\mathrm{d}\rho\mathrm{d}\varphi, \tag{7.26}$$

which can also be written in a longer, but more numerically approachable fashion, as

$$\mathrm{Tilt}^{p_2,l_2}_{p_1,l_1}(\alpha) = \sqrt{\frac{p_1!}{(|l|+p_1)!}\frac{p_2!}{(|l|+p_2)!}}\begin{cases}(-1)^{|l_1-l_2|} & l_2 > l_1\\ 1 & \text{otherwise}\end{cases}\times$$
$$\sum_{k_1=0}^{p_1}\sum_{k_2=0}^{p_2}\frac{\left(\frac{|l_1|+l_1}{2}+\frac{|l_2|+l_2}{2}+k_1+k_2\right)!}{|l_1-l_2|!k_1!k_2!}\binom{p_1+|l_1|}{p_1-k_1}\binom{p_2+|l_2|}{p_2-k_2}(-1)^{k_1+k_2}\times$$
$${}_1F_1\left(1+\tfrac{|l_1|+l_1}{2}+\tfrac{|l_2|+l_2}{2}+k_1+k_2, 1+|l_1-l_2|; -\left(w_0k\tfrac{\alpha}{2\sqrt{2}}\right)^2\right)\left(w_0k\tfrac{\alpha}{2\sqrt{2}}\right)^{|l_1-l_2|} \tag{7.27}$$

${}_1F_1(a,b;x)$ is the *generalized hypergeometric function*,[7] and $\binom{n}{k}$ are normal binomial coefficients[8].

Finally, a Hole-function is defined, which describes the coupling of modes before and after a circular hole as

$$\mathrm{Hole}^{p_2,l_2}_{p_1,l_1}(r_{\mathrm{hole}},c_{\mathrm{hole}}) = \int_0^\infty\int_0^{2\pi}\mathrm{LG}_{p_1,l_1}(\rho,\varphi,0)^*\mathrm{LG}_{p_2,l_2}(\rho,\varphi,0)\times\Theta(r_{\mathrm{hole}},c_{\mathrm{hole}})\rho\,\mathrm{d}\rho\mathrm{d}\varphi, \tag{7.30}$$

where $\Theta(r,c)$ is a step-like function, equal to 1 where the distance from the point (ρ,φ) to c is less than r and 0 elsewhere. There is no nice analytical expression here – the expression is most easily evaluated numerically.

The beauty of these coupling matrices is that they must only be computed *once* for any given geometry (independent of $2kz$), essentially making the entire problem tractable numerically.

With these coupling matrices defined, we can construct a total propagation matrix for the fields, corresponding to $\mathbb{A}$ from 7.14. Propagation in the left cavity

(6) The discrete variable equivalent of the Dirac delta function, defined as

$$\delta^j_k = \begin{cases}1 & \text{if } k = j,\\ 0 & \text{if } k \neq j.\end{cases}$$

(7) Defined as:

$${}_1F_1(a,b;x) = \sum_{k=0}^{\infty}\frac{(a)_k}{(b)_k k!}x^k, \tag{7.28}$$

where $(\cdot)_k$ is the Pochhammer symbol,

$$(z)_m = \frac{\Gamma(z+m)}{\Gamma(z)}. \tag{7.29}$$

(8) $\binom{n}{k} = \frac{n!}{k!(n-k)!}$

(matrices $\mathbb{L}$ and $\mathbb{M}$) are described respectively by (7.24), and reflection on a flat mirror by the identity; collectively, $\mathbb{L}_l\mathbb{M}\mathbb{L}_l^\dagger$ is implemented as a single matrix $\mathbb{M}$ in the code. For the right hand cavity, we use the fact that *the chosen basis is eigenmodes of the bare subcavity*, which effectively means that the product of matrices $\mathbb{L}_r^\dagger\mathbb{D}\mathbb{L}_r$ is a single *diagonal* matrix, and the diagonal entries are simply the Gouy phases. Finally, losses and the tilted membrane are represented by (7.30) and (7.26) respectively.

From these matrices, the roundtrip matrix $\mathbb{A}$ is calculated, and finding the eigenvectors of this matrix is reduced to a standard linear algebra problem, which can be efficiently solved numerically. This concludes the explanation of the numerical model and its implementation.

7.3 Model Results

We now turn to the numerical results of the model. The output of the model, for a given set of input parameters, is two plots, with the structure of optical modes in units of the FSR as a function of $2kz$, as well as the shape, size and position of the fundamental mode, also as a function of $2kz$.

We start by evaluating the mode for an empty cavity, to verify that it produces the expected results for a Fabry–Perot cavity. The parameters for this base case are listed in Table 7.1. The parameters are chosen to align roughly with the plano-concave cavity in use in the hybrid experiment at the time where the model was developed, and for which we have the best data comparing reality to the model.

The empty cavity result is shown in Fig. 7.7. The top panel displays the eigenmodes of the cavity as a function of $2kz$; since the membrane thickness is set to 0, no optomechanical effects should be present, and we should observe the eigenmodes of a normal Fabry–Perot cavity. For these settings, we observe the fundamental mode, marked with a thick line (and overlaid with the plane-mirror, single optical mode model derived earlier in orange dashes), and then a set of equidistantly spaced higher order mode families. The spectrum is folded over, so higher order modes end up crossing the fundamental; the absolute frequency of the fundamental in units of FSRs is arbitrary. For the highest order modes, the sharp families become sperad out in frequency; this is mainly a product of the truncation of the modes used in the simulation. Increasing the number of modes used increases the order at which numerical instabilities make the results less accurate.

The bottom two panels depict the optical mode intensities along x and y as a function of $2kz$. For x, the red line marks the maximum intensity for a given membrane position, while for y, the green curves mark the e^{-2}-radius, i. e., the waist size. The vertical blue and orange lines mark respectively the $2kz$ positions with the smallest and largest waist sizes; for this (with no optomechanical coupling) plot, the values are nonsensical, but adding optomechanical coupling, we will see that it corresponds roughly to the two high-coupling points.

We now set the membrane thickness to $d = 40\,\mathrm{nm}$[9]. We see in Fig. 7.8 (top panel) that the finite membrane thickness leads to a $2kz$ dependent modulation of the resonance frequencies, i. e., optomechanical coupling, for all modes. The fundamental mode is still very well described by the single mode model. Further, the higher order mode families are now split; we interpret the splitting as arising

(9) This thickness is somewhat arbitrary; for the experiments described later in this chapter we had $d \sim 67\,\mathrm{nm}$, and for the current membranes we typically have $d \sim 14\,\mathrm{nm}$.

from the finite wavefront curvature at the position of the membrane, 500 µm from the flat mirror.

In the bottom panels, we see that the mean x position is unchanged with $2kz$, but the size of the beam *does* depend on the it. Specifically, it grows for one high coupling point (marked by the orange lines), and shrinks at the other (blue lines)[10]. The splitting of the mode families are highest where the individual family has the highest coupling (slope of the resonance frequency with membrane position).

(10) The green lines are only shown in the bottom (y) panel, but the mode exhibits the same behaviour in the x direction.

By varying the length of the subcavities we can assess how wavefront curvature affects the splitting of ideally degenerate modes and the shape of the fundamental. We change the length of both subcavities by 400 µm (in opposite directions, maintaining a fixed total cavity length). In Fig. 7.9 L_l is reduced to 100 µm, while in Fig. 7.10 L_l is increased to 900 µm.

For the case with the membrane closer to the flat mirror (Fig. 7.9), the splitting of the higher order mode families is essentially eliminated, and the mode size modulation is severely reduced. The agreement between the single mode model and the full simulation is also improved.

For the case with the membrane further from the flat mirror (Fig. 7.10) the change is in the other direction: the mode families are split further, and the modulation of the optical mode is stronger. The agreement between the simulation and the single mode model is visibly worse than for either of the other two cases presented so far.

We draw from these observations the conclusion that wavefront curvature is detrimental to the optical qualities of the optomechanical cavity. The hybridization of the fundamental mode of the unperturbed cavity with higher order modes (reflected in the growing mode size) in a realistic cavity will lead to higher susceptibility to clipping losses etc. Further, the splitting of higher order modes leads to more $2kz$ positions where the fundamental mode is degenerate with a higher order mode.

We now introduce membrane tilt to the simulation. The tilt is always introduced around the y axis, such that the change showns up in the x direction. Using the same parameters as Fig. 7.8, we now set $\alpha = 1\,\text{mrad}$, and plot the simulated result in Fig. 7.11. This tilt corresponds roughly to a membrane chip of size 10 mm

Quantity	Symbol	Value
Flat mirror-membrane distance	L_l	0.500 mm
Curved mirror-membrane distance	L_r	0.840 mm
Curved mirror ROC	R	25 mm
Optical wavelength	λ	852 nm
Membrane thickness	d	0 nm
Flat mirror reflectivity	θ_l	$\arccos(\sqrt{20\,\text{ppm}})$
Curved mirror reflectivity	θ_r	$\arccos(\sqrt{1400\,\text{ppm}})$
Membrane tilt	α	0
Membrane diameter	r_{mem}	∞
Membrane center	c_{mem}	(0 mm, 0 mm)

Table 7.1: Parameters for the empty cavity simulation.

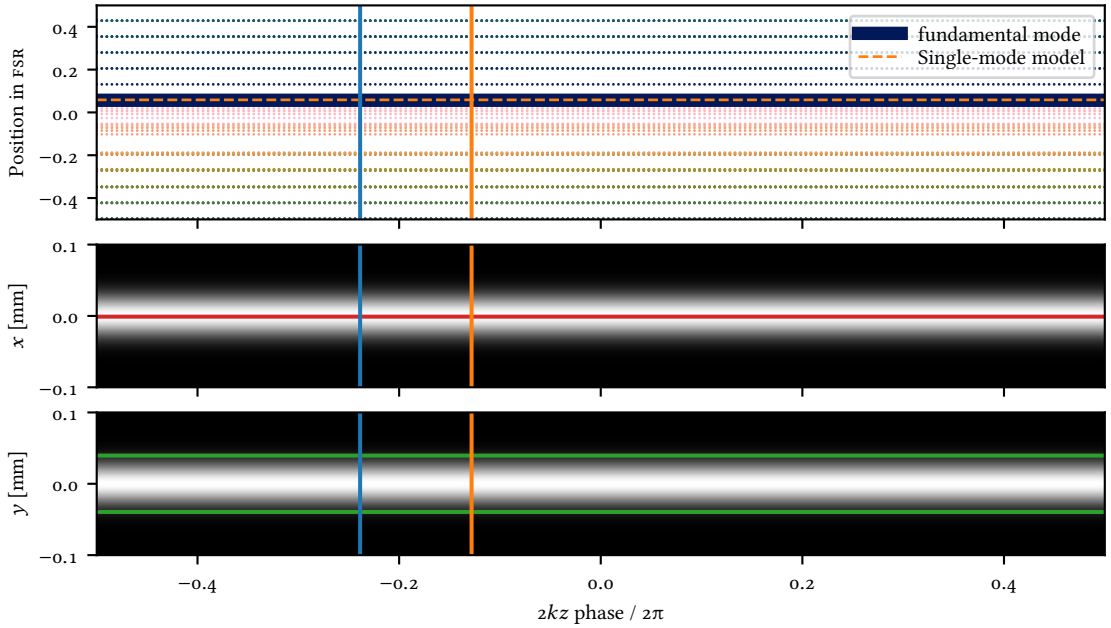

Figure 7.7: Modes and intensity of the fundamental for an empty cavity. Parameters are listed in Table 7.1.

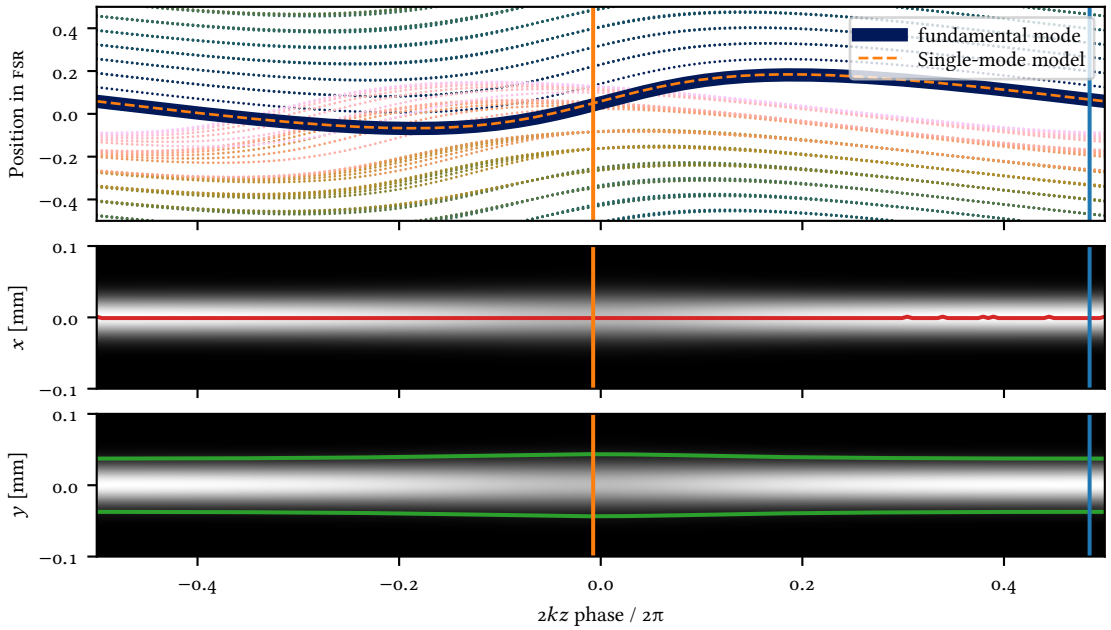

Figure 7.8: Modes and intensity of the fundamental for a cavity with medium wavefront curvature at the membrane. Parameters as in Table 7.1, but with $d = 40\,\mathrm{nm}$.

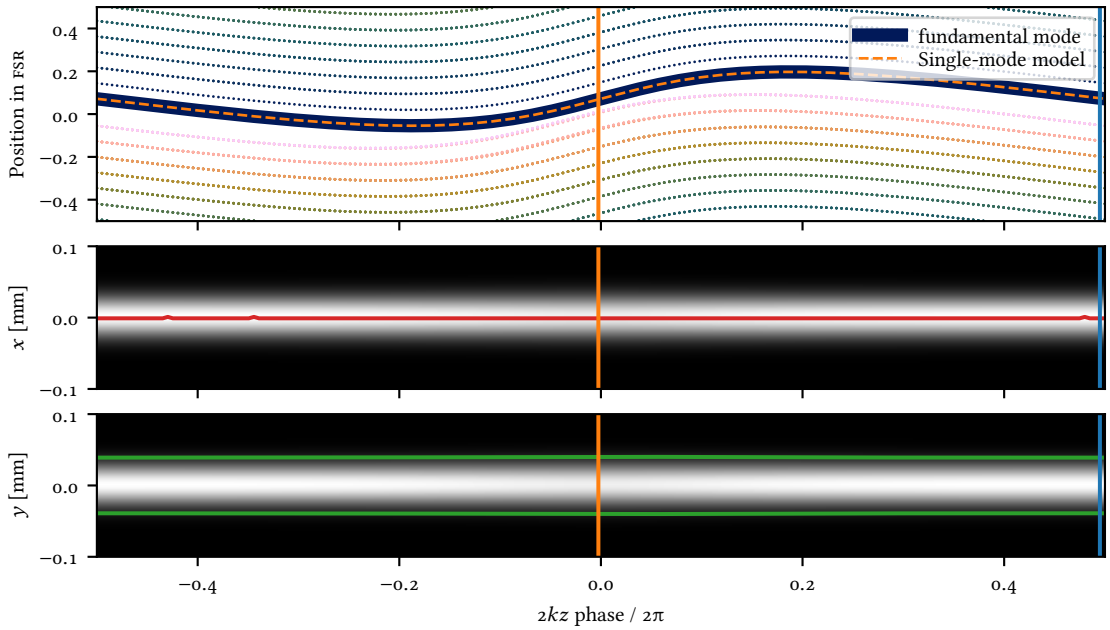

Figure 7.9: Modes and intensity of the fundamental for a cavity with small wavefront curvature at the membrane. Parameters like Fig. 7.8, but $L_l = 100\,\mu\text{m}$ and $L_r = 1240\,\mu\text{m}$.

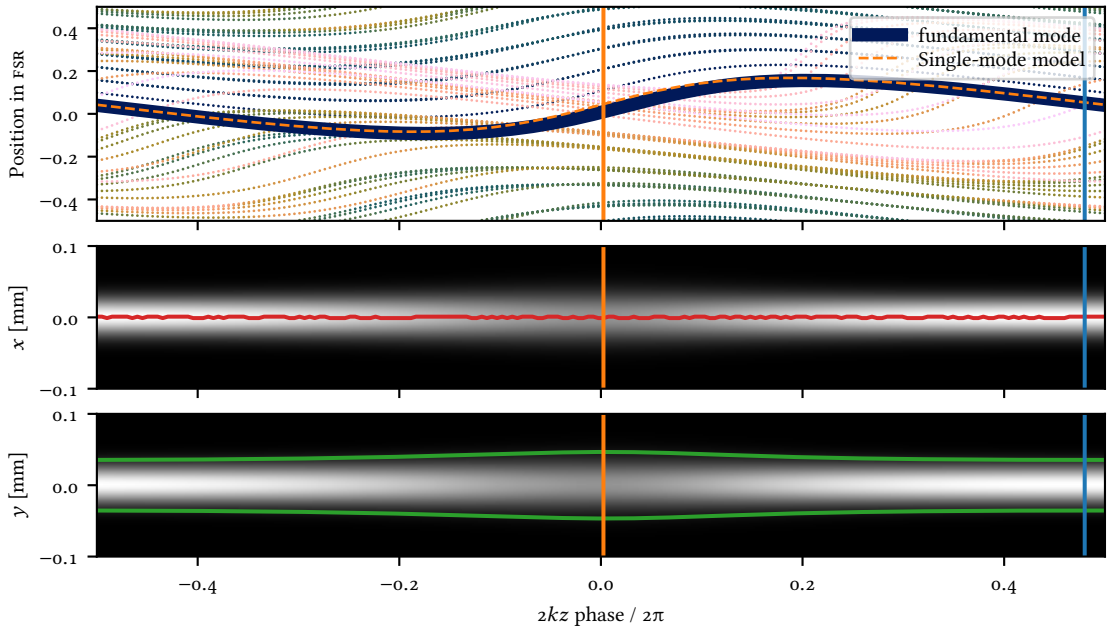

Figure 7.10: Modes and intensity of the fundamental for a cavity with large wavefront curvature at the membrane. Parameters like Fig. 7.8, but $L_l = 900\,\mu\text{m}$ and $L_r = 440\,\mu\text{m}$.

being suspended on a surface that varies by 10 µm from one edge to the other.

The two most prominent features introduced by the tilted membrane is a $2kz$-dependent mode position seen in the x-intensity plot, and the splitting of the higher order modes at different places than those introduced by wavefront curvature. Where the latter effect split the modes at the high coupling points, tilting the membrane split the modes at the extreme absolute frequency shift points, i. e., their zero-coupling points.

The shift of the mode *spatial position* seen in the middle panel of Fig. 7.11 is on the order of a waist radius, which is a large effect, and the maximum displacement coincides with the high-coupling points.

The tilt also introduces a shift of the point where the mode is largest and smallest, as well as increasing the size changes.

In Chapter 6, this lateral change of the mode was introduced as a rough way of estimating the membrane tilt, such that it can be tuned away. We now see roughly how it comes about, and the amount of tilts needed to significantly shift the mode.

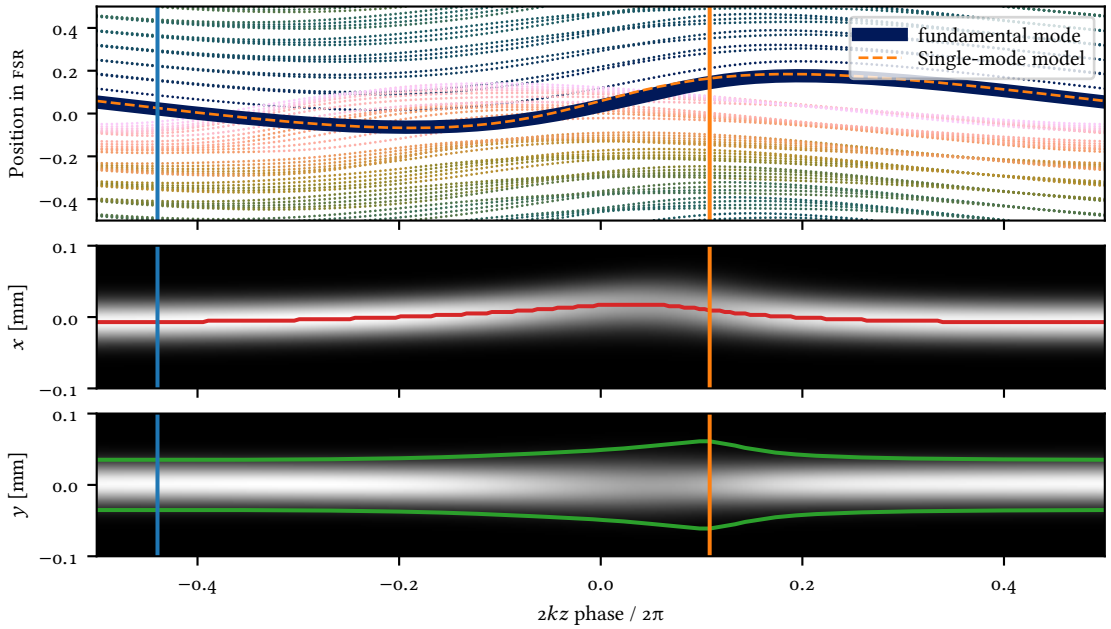

Figure 7.11: Modes and intensity of the fundamental for a cavity with a tilted membrane. Parameters like Fig. 7.8, but $\alpha = 1$ mrad.

Finally, the model is also able to simulate the effects of scattering losses. The implementation is somewhat crude, and the results much harder to interpret. For these reasons I refrain from displaying any plots here. The take-away message from the simulations however, are that one should keep the mode well clear of the edges of the membrane, as even small extra losses can lead to significant hybridization and coupling to higher order modes.

7.4 Experimental Data

To assess the model we compare it to measurements on a realistic cavity assembly. While the model does capture a lot of the physics, particularly the model for losses is quite crude; therefore, it is unrealistic to obtain very good agreement between the data and the model.

We perform the measurement by scanning one piezo over slightly more than one FSR, while we step the wavelength. To optically populate higher order modes, we purposefully mis-align the input mode. For each wavelength we record the spectrum of output light.

The change of wavelength, λ, effectively tunes the $2kz$ position of the membrane, as well as the cavity resonance condition. To compare with the model, we de-trend the change of the resonance condition by rolling and folding the recorded spectra according to the expected sub-cavity length and known change of wavelength. We also use the transversal mode spacing, TMS, to compensate for piezo non-linearities. In this way we obtain the spectrum shown in the left panel of Fig. 7.12. The overall intensity modulation with $2kz$ (or λ) is expected from the transfer matrix model (see Section 3.8.1).

In the right hand panel of that figure we show the model evaluated for the parameters in Table 7.2. The parameters are close to the expected values for our cavity, with the lengths etc. known from separate measurements, and with educated guesses for the membrane tilt (0.4 mrad), effective membrane diameter (300 µm) and cavity spot location (75 µm, −75 µm).

The model shows reasonable agreement with the data for low-order optical modes, and progressively worse agreement for higher order modes, where the loss model implemented disagrees significantly with the real world.

While the agreement between the model and data is not strong enough for a quantitative evaluation of the correctness of the model, the overall behaviour of model corresponds reasonably well to our observations.

Quantity	Symbol	Value
Flat mirror-membrane distance	L_l	0.500 mm
Curved mirror-membrane distance	L_r	0.700 mm
Curved mirror ROC	R	25 mm
Optical wavelength	λ	852 nm
Membrane thickness	d	60 nm
Flat mirror reflectivity	θ_l	$\arccos(\sqrt{20\,\text{ppm}})$
Curved mirror reflectivity	θ_r	$\arccos(\sqrt{1400\,\text{ppm}})$
Membrane tilt	α	0.4 mrad
Membrane diameter	r_{mem}	300 µm
Membrane center	c_{mem}	(75 µm, −75 µm)

Table 7.2: Parameters for the cavity simulation in Fig. 7.12.

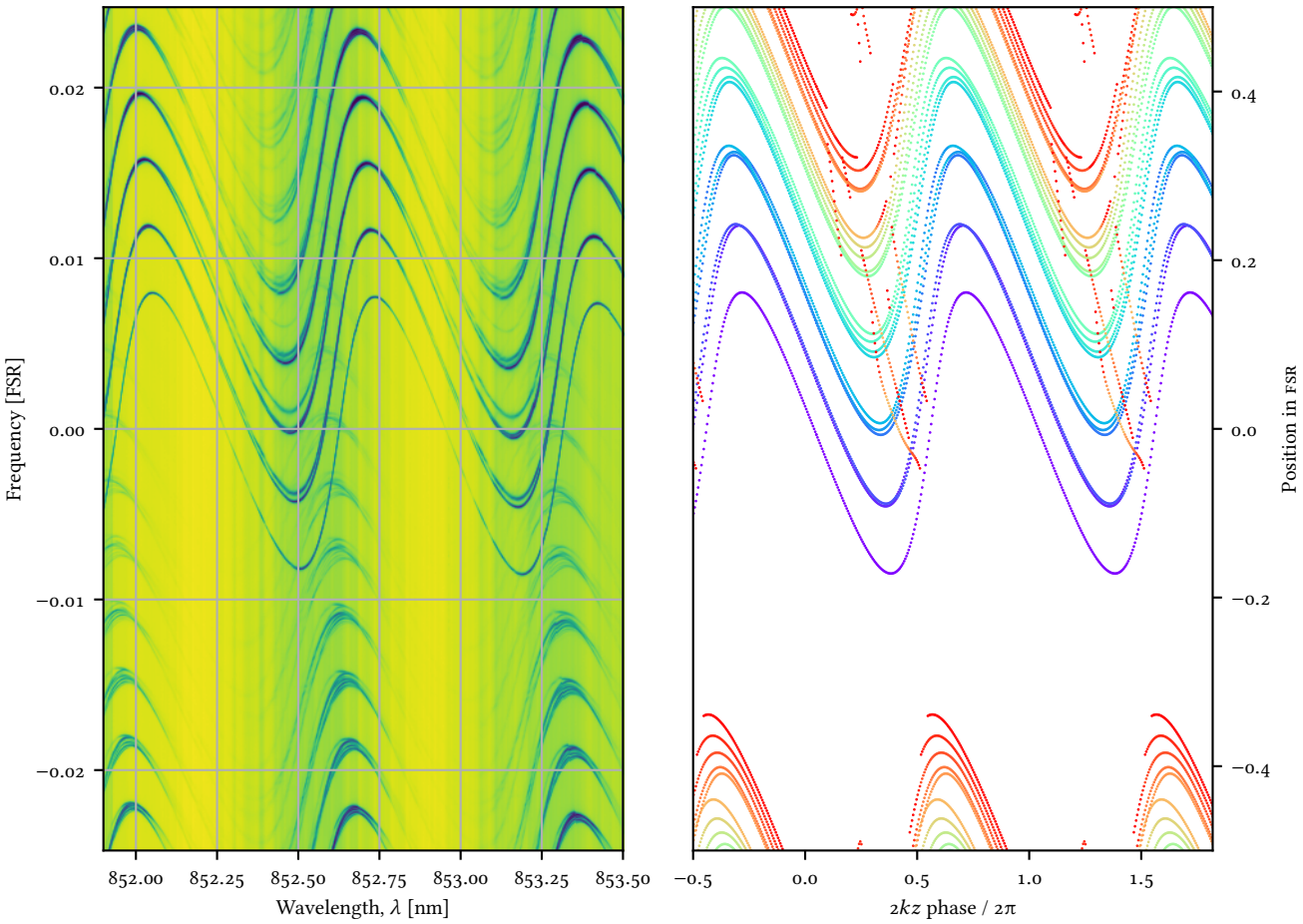

Figure 7.12: $2kz$ all modes. Left panel: experimentally measured optical mode structure as a function of wavelength, wrapped and de-trended as described in the main text. Right: Numerical model evaluated for the parameters described in Table 7.2. Truncation of the basis of modes leads to a finite number of higher order modes in the simulation.

7.5 Design Guidelines Learned

Summarizing the guidelines for optomechanical cavity design learned from this numerical model, we have learned that:

- Wavefront curvature at the membrane position, even for infinitely large, untilted membrane, leads to significant hybridization of the optical modes, manifested as a $2kz$-position dependent size of the fundamental mode. Further, wavefront curvature splits higher order mode families.
- Membrane tilt further hybridizes the optical modes, and splits higher-order mode families, but with a different $2kz$-dependence than wavefront curvature. Tilt induces a $2kz$-dependent *position* shift of the fundamental optical mode, which may be used as a probe of tilt.
- Clipping and scattering losses on the edges of the membrane defect pad is detrimental to the optical quality, but the exact criteria and behaviour is not well described by our crude loss model.

These learning points all played into the design choices described in the previous chapter, as well as our understanding of how to align optomechanical cavities. Particularly the choice of going to a concave-concave cavity design to eliminate the wavefront curvature to a higher degree, as well as the implementation of a repeatable and controllable way of reducing membrane tilt was informed by this model.

Chapter 8

New Mirrors

> “You’d be surprised how many problems are soluble in a solution of Benjamins.
>
> Franklin Veaux

New mirrors for the optomechanical cavity. What we want to achieve, design parameters, FEM-simulations, mirror mode characterization.

In this chapter we discuss the motivation for buying new mirrors for our optomechanical cavity, the investigations into mechanical modes, and briefly comment on choosing coatings. Much of the work described in the chapter was performed by master student Jonas Mathiassen, partly under my supervision, and is also presented in his master’s thesis, Mathiassen (2019)[1], which offers many more details.

(1) Jonas B. Mathiassen (2019). “Characterising and Modelling Thermal Substrate Noise for a Membrane in the Middle Optomechanical Cavity”. M.Sc. thesis. University of Copenhagen.

8.1 Why new Mirrors?

A major source of noise in cavity optomechanics is mechanical modes of the mirrors. Since fluctuations of the end-mirrors turn directly into intra-cavity phase and amplitude fluctuations, having a mechanical mirror mode overlap spectrally with your mechanical degree of interest can be detrimental – like having a big classical noise peak, preventing efficient cooling, efficient state estimation etc.

For the work in Møller et al. (2017) and Rodrigo A. Thomas et al. (2020), the cavity consisted of geometrically disparate mirrors. In Møller et al. (2017), the mirrors were respectively a $\varnothing = 0.25\,\text{in}/6.35\,\text{mm} \times d = 3\,\text{mm}$ curved mirror, and a $\varnothing = 7.5\,\text{mm} \times d = 4\,\text{mm}$ flat mirror. For Rodrigo A. Thomas et al. (2020), we had changed the cavity design from plano-concave to concave-concave, but still used mirrors with different geometries: $\varnothing = 0.25\,\text{in}/6.35\,\text{mm} \times d = 3\,\text{mm}$ and $\varnothing = 7.5\,\text{mm} \times d = 4\,\text{mm}$.

These mirrors, owing to their rather large size, have low fundamental frequencies; since the spectrum is more dense (more modes per frequency span) the higher one goes, having low fundamental frequencies of vibration puts our frequency region of interest into a dense part of the mirror spectrum. Even worse, since the mirrors are different, they will have modes at *different* frequencies, making the spectrum effectively even denser. Møller (2018) shows a frequency window with no detectable mirror modes of only approximately 10 kHz width centered on 1.27 MHz at cryogenic temperatures, $T = 4$ K.

In figure Fig. 8.1 I plot the measured mechanical spectrum of a cavity consisting of two *identical* $\varnothing = 6.35$ mm $\times\, d = 3$ mm mirrors. Even for a cavity like this, with symmetrical mirrors, it is apparently hard to find a frequency region without mechanical peaks.

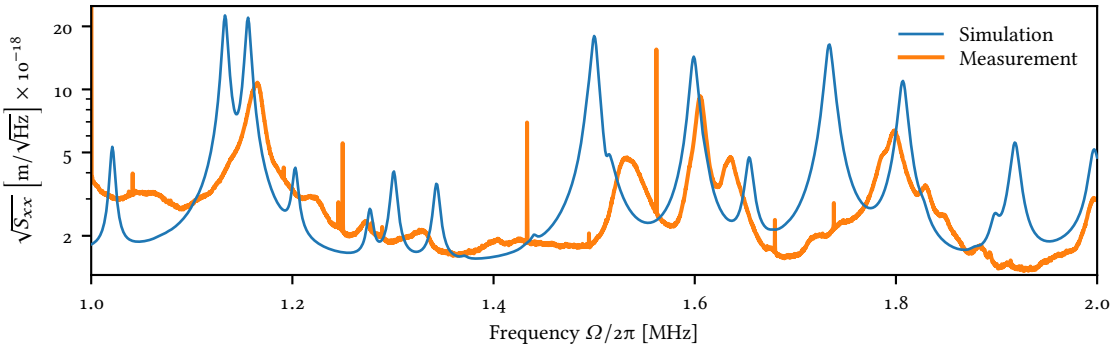

Figure 8.1: Modes of the old mirrors, simulation and measurement. A symmetric cavity . The narrow peaks in the orange spectrum is electronic noise peaks. The peak at 1.6 MHz is used to estimate the loss tangent, with the mode having $Q \sim 200$. The simulated mode has the center of the Gaussian offset by 135 µm; see Fig. 8.3.

8.2 FEM-simulations

8.2.1 Comparing to Old Mirrors

Also shown in Fig. 8.1 is a simulated spectrum for the same mirrors. We are after the thermal fluctuations of the end mirrors[(2)]. In reality the mirrors are clamped to some kind of supporting structure, leading to hybridization of the mechanical mode spectra. Simulating the entire cavity assembly is in principle the right way to go, but accurately quantifying clamping conditions between different elements is hard. Therefore we go a different path: simulate the modes of a free mirror, and (if needed in practice) modify the clamping of the mirrors to minimize mode hybridization.

(2) The masses are way too high for optomechanical effects to play any role here.

The FEM simulation is performed in COMSOL (see Section 4.1.2), and uses the so-called *direct approach* (Levin 1998). The approach turns the problem of finding thermally induced fluctuations of the mirror geometry on its head, and simulates instead the dissipated energy when a harmonic driving force applied to a given area is swept across the frequency region of interest.

With a total force F_0 applied in a Gaussian profile, corresponding to the optical cavity mode,the PSD of fluctuations may be found as

$$S_{xx}(\Omega) = \frac{2k_B T}{\Omega^2} \frac{W_{\text{diss}}}{F_0^2}, \tag{8.1}$$

where W_{diss} is the dissipated power. The dissipated power relies on the mirror material *loss angle* ϕ, which is estimated as $\phi = 1/Q$, from the narrowest peak in the spectrum, which is the peak at 1.6 MHz with $Q \sim 200$. The loss tangent only changes the width of the simulated peaks, not their position or strength.

In Fig. 8.1 such a simulation is plotted together with the measured spectrum. While the match is by no means perfect, it could also be a whole lot worse, given how crudely the calculations simulate reality; expecting the mode spectrum of a free mirror to match that of a clamped mirror, with potentially high mode hybridization is asking a lot.

We also experimentally investigated the clamping conditions of the mirrors, by placing TEFLON™ (Polytetrafluoroethylene, PTFE) spacers around the mirrors. We tested with no spacers ("ntf" for "no teflon"), on both sides of the mirror ("both") as well as on the front and back respectively, with only the former two displayed here. The clamping force was also varied, by torquing down the "batman" screws with a torque wrench. These spectra are shown in Fig. 8.2.

While the torque settings used showed little effect, the addition of spacers around the mirror can be seen to improve the match between experimentally measured displacement and the simulation substantially. We take this a sign that hybridization is playing a significant role, and that simulating a free mass mirror is a reasonable approach *as long as the clamping conditions are suitable.*

As a last point, in Fig. 8.3 we plot the simulated displacement spectrum, as a function of beam position on the mirror. Insets above the spectra show the mode shapes (absolute value of the displacement). This highlights two things: *a)* simulations of the mode spectrum are only reliable, if the rotational symmetry is broken, and *b)* centering the optical mode on the mirror reduces coupling to a lot of the modes. The modes being sampled with the beam centered on the mirror are all those that have rotational symmetry, and a non-zero displacement in the center.

8.2.2 Simulating New Mirrors

Encouraged by the relatively good match of the spectra in Fig. 8.2, the simulation was extended to a search for a new combination of diameter (⌀) and thickness (d).

In general, the approach is to shrink the dimensions of the mirrors, to make the spectrum less dense. The effect of shrinking the dimensions is depicted in Fig. 8.4, where the spectra of two simple drum skins are depicted. The diameters are ⌀ = 7 mm and 4 mm, and the speed of sound $c = 3 \times 10^3$ m/s.

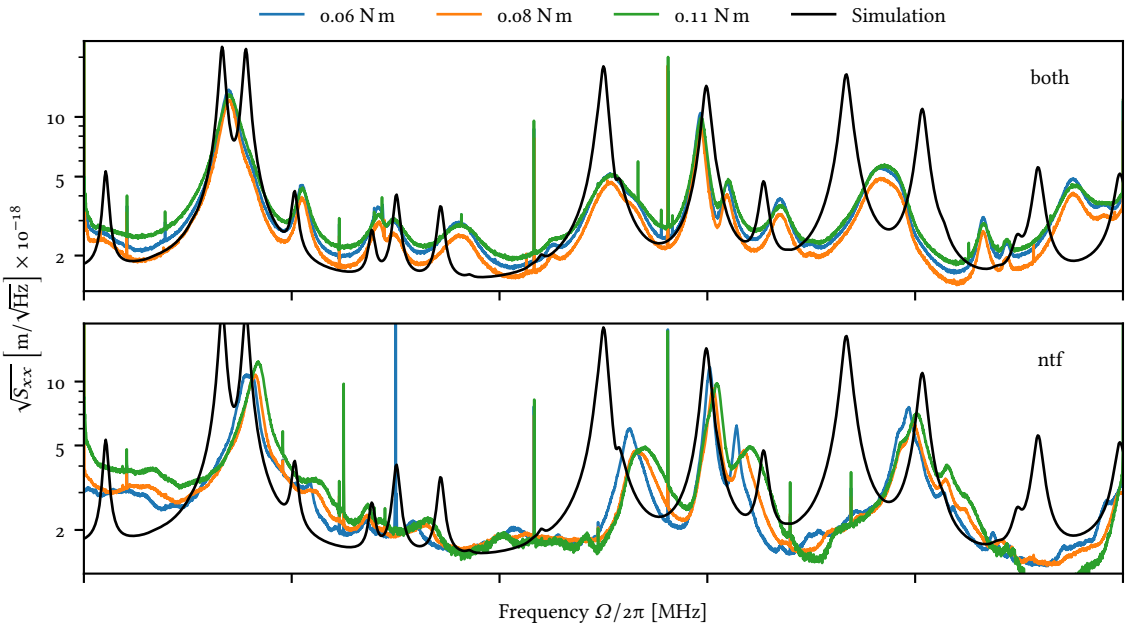

Figure 8.2: Mechanical spectrum of the old mirrors under different clamping conditions. Top: PTFE spacers are placed on both sides of the mirror in the clamping stack. Bottom: spectrum with the mirrors clamped by copper on both ends. The PTFE spacers clearly improve the agreement between measurement and simulation, although significant discrepancy is still present.

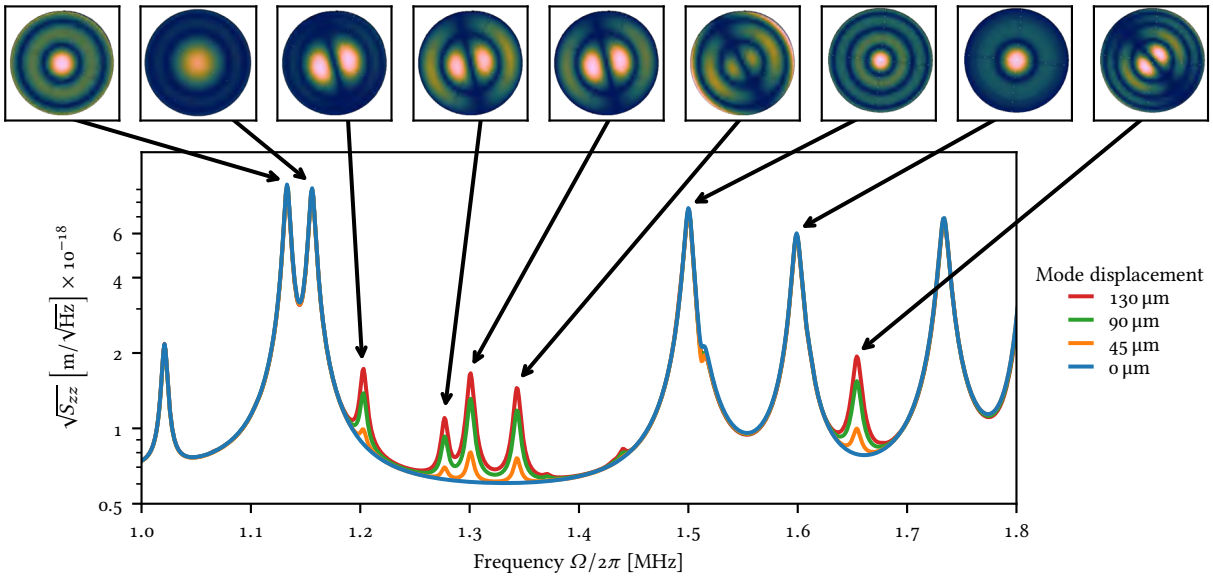

Figure 8.3: Simulated displacement PSD of the old mirrors. The insets display the absolute value of the out-of-plane displacement of the modes. The modes without rotational symmetry are all degenerate with a mode rotated 90°. $T = 10\,\text{K}$.

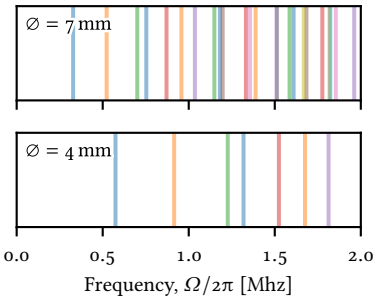

Figure 8.4: Spectra of two simple, circular drum heads with ∅ = 7 mm and 4 mm, $c = 3 \times 10^3$ m/s, with each line representing a mode. The colors indicate the radial mode number m, and are identical for the two plots for comparison. As the size is reduced, the whole spectrum is stretched, making it spectrally less dense.

For practical reasons, one must consider what minimum sizes can be fabricated and used. Since we want to have mirrors with relatively small radii of curvature (ROC), the mirrors can not be so thin that the geometry does not support the ROC. After communication with the company responsible for grinding the mirrors, a minimum thickness of around 1 mm was decided, for a ROC of 25 mm. The diameter of the mirror should be kept above approximately 4 mm, if possible, to allow for easier handling, mounting etc.

We now scan the parameters, ∅ and d, over the relevant ranges, and plot the simulated spectra. For d = 1 mm and 2 mm, measured at the edge of the mirror, the 2D spectra are plotted in Fig. 8.5.

For the thinner of the two, clean regions more than 200 kHz appear. For the higher thickness, some of the modes remain almost unchanged, while a set of other modes appears. While not entirely true, it can therefore be useful to think of the two (those that move with d and those that do not) as being controlled by a single parameter, ∅ or d.

Restricting ourselves to a thickness of $d \sim$ 1 mm, we see that we can effectively move the clean frequency window up and down. Further, there are two almost equally good windows on either side of either side of the mode that runs almost diagonally in Fig. 8.5. Since we know that lower frequency puts us closer to classical laser noise (see Section 9.1.1), we choose to optimize for the higher of the frequency windows, and, somewhat arbitrarily, pick a target frequency of 1.4 MHz.

In Fig. 8.6, the simulated spectrum of the designed new mirror geometry is displayed. It has ∅ = 5.2 mm and d = 1.14 mm for a *center thickness* of 1 mm. This slight increase in thickness over that displayed in Fig. 8.5 moves the window slightly up in frequency, but the effect in simulations is modest.

In a faint grey line, the simulated spectrum of one of the old mirrors is also shown; comparing these two lines, it should be readily apparent what a much wider gap with no significant mechanical mirror modes is a feasible thing to hope

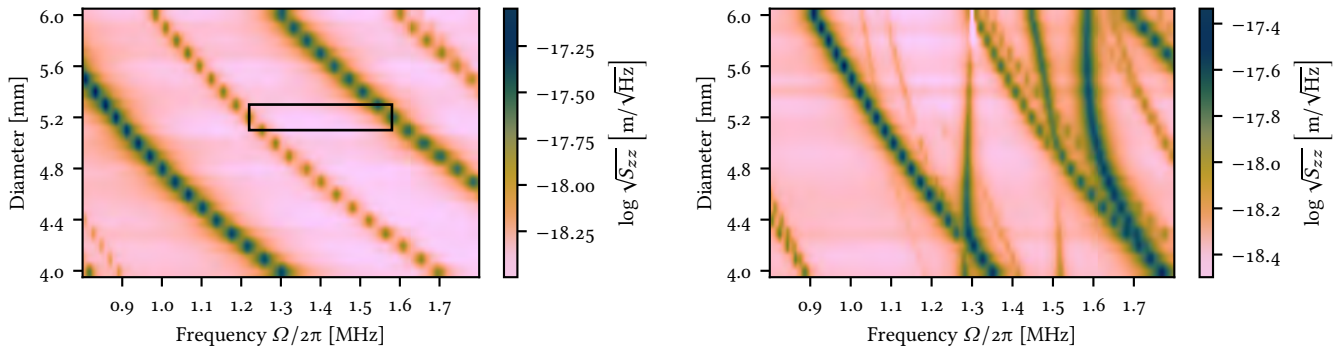

Figure 8.5: The simulated mechanical mode spectrum for varied ∅ and d = 1 mm (left) and d = 2 mm (right). For the thinner of the two, a set of modes all increasing in frequency for smaller diameter. For the thicker these modes appear alongside a number of modes independent of ∅, which significantly deteriorate the spectrum. In the left hand figure, a clean spectral area is marked for ∅ = 5.2 mm, which will be our target geometry.

for.

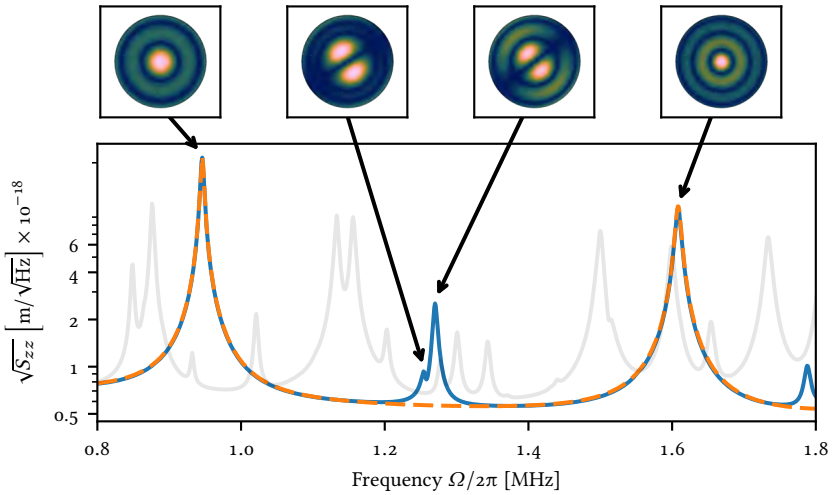

Figure 8.6: Mechanical modes of new and old mirrors. Blue and orange: simulated spectrum of a mirror with ∅ = 5.2 mm, d = 1.14 mm. Orange line: beam centered on the mirror, blue line: beam displaced 130 µm. Grey line: simulated spectrum of a mirror with ∅ = 7.5 mm, d = 4 mm, and the beam displaced 130 µm. The insets depict the mode shapes of the modes indicated. Non-axis-symmetric modes are degenerate with a mode rotated 90°.

8.3 Choosing the Mirror Coatings

Along with a new set of mirror substrates, comes the choice of which coating to apply to them. Here we must balance a set of wishes together with the anticipated substrate and coating losses.

The mirror substrates were polished by Perkins Precision Developments (PPD). According to the manufacturer, they routinely achieve flatness of *flat* mirror blanks of < 1 Å RMS. For mirrors with short ROC, such as the ones we are interested in, fewer guarantees as to the quality can be made.

For a beam sampling a large flat area with RMS surface roughness δ, the fraction of light scattered, S, is given by (Møller 2018, p. 26)

$$S = 1 - \exp\left[-\left(\frac{4\pi\delta}{\lambda}\right)^2\right] \approx \left(\frac{4\pi\delta}{\lambda}\right)^2, \tag{8.2}$$

which for λ = 852 nm and δ = 1 Å gives $S \approx 2$ ppm.

The other main contributor to mirror losses is the coating losses. A reasonable estimate for high quality coatings, such as those provided by Five Nine Optics (FNO), is a couple of ppm, bringing the total loss per mirror to around 4 ppm. This sets a hard upper limit on the achievable finesse of $\mathcal{F} \sim 8 \times 10^5$.

For our experiments, we are very interested in having a high outcoupling efficiency, $\eta_{\text{out}} = \kappa_{\text{out}}/\kappa$. In other words, the outcoupling transmission must be much higher than all other losses in the cavity, $\kappa_{\text{out}} \gg \kappa_{\text{loss}}, \kappa_{\text{HR}}$[3].

(3) For us, the input mirror is also the output mirror in most situations, and the second mirror must be high reflection (HR).

This can of course be achieved by simply choosing a mirror with a high transmissivity; however, we also seek to have a reasonably short cavity and high finesse to boost the optomechanical interaction, as well as a total cavity linewidth that makes the system somewhat resolved, allowing for efficient sideband cooling. The simultaneous requirement of a short cavity with low linewidth, limits the total permissible round trip loss, and thus effectively the the transmissivity of the outcoupling mirror.

In the end, mirror coatings were ordered with one set of mirror having $T = 10\,\text{ppm}$ and another having $T = 500\,\text{ppm}$. After some initial confusion[4] the delivered mirrors were found to be reasonably close to the desired values; the numbers reported by the company was checked by us, and found to be accurate. In Fig. 8.7 I plot the Transfer Matrix Model from Section 3.8.1 evaluated for the ordered and delivered mirror coatings, as tabulated in Table 8.1.

(4) The coating company coated the mirrors with 5 ppm and 1000 ppm instead of 10 ppm and 500 ppm. The error was fixed by addition of a single layer of coating to each set of substrates.

The plots in Fig. 8.7 should be contrasted with Fig. 3.23, the TMM evaluated for the experimental parameters relevant to the results in Rodrigo A. Thomas et al. (2020) and Chapter 10. In general, we will always choose to work at the $2kz$-point which has high κ and high overcoupling in reflection, η. With the expected mirror losses and other parameter choices listed in the caption of Fig. 8.7, we expect to reach an overcoupling of around 98 %, with $\kappa = 4.5\,\text{MHz}$. This represents an increase in overcoupling of ~7 %.

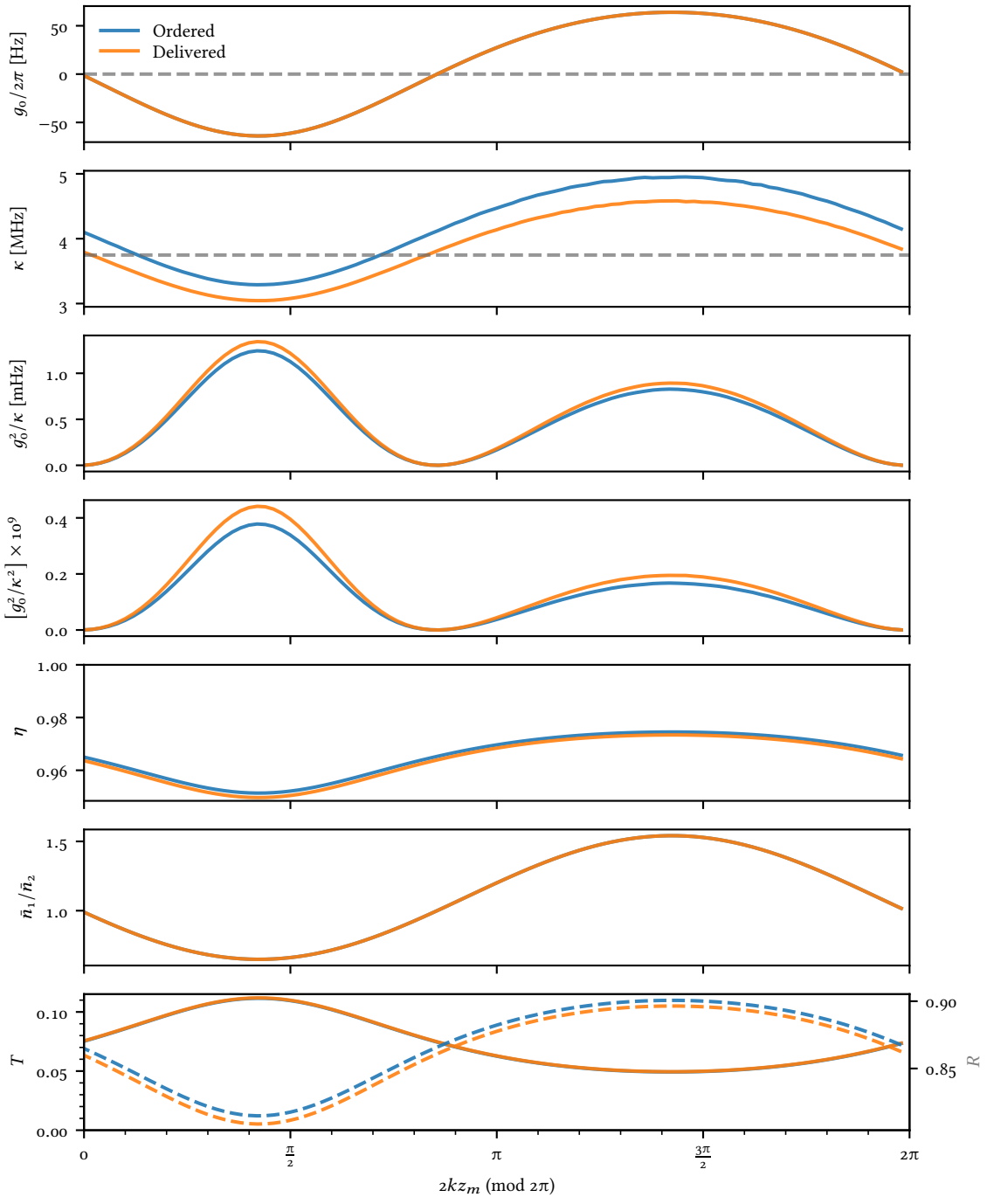

Figure 8.7: TMM evaluted for the optical coatings ordered (blue) and delivered (orange). $L = 3\,\text{mm}$, $z_\text{m} = 1.5\,\text{mm}$, $d_\text{mem} = 20\,\text{nm}$.

	T_1	T_2	δ
Ordered	10 ppm	500 ppm	4 ppm
Delivered	9.3 ppm	462 ppm	
Old	20 ppm	362 ppm	4/20 ppm

Table 8.1: Mirror coatings ordered and delivered. Delivered transmissivities as reported by the manufacturer, FNO. Also listed, transmissivities and losses for our old mirror.

(5) Measurement and data analysis was performed by Sergey Fedorov.

8.4 Delivered Mirrors – Mechanical Mode Characterization

After receiving the mirrors, the mechanical properties of the actually produced mirrors could be measured[5]. The results are shown in Fig. 8.8. The black line shows the simulated mirror spectrum with a loss tangent corresponding to a mirror mode Q of 100. The blue, orange and green shows the experimentally measured cavity length fluctuations (left axis), and the corresponding frequency fluctuations (right axis).

The blue curve corresponds to clamping conditions similar to the one used for the old mirrors, with teflon spacers on both ends, and a reasonably tight batman screw, clamping the spacer-mirror-spacer-piezo stack. This spectrum reveals significantly broadened modes. with mirror mode Qs of 10–30, leading also to a general elevation of the mechanical noise floor.

Significantly reducing the clamping force (the torque used to tighten the batman screw was $<$ 0.03 Nm; an educated guess around 0.01 Nm) leads to the orange and green traces. Here, the mirror modes linewidths are significantly reduced, and matches the simulated spectrum much better. The noise floor level at 1.4 MHz is reduced by a factor $\sim$3, compared to the tighter clamping, and agrees much better with the simulation.

From these findings, we conclude that the smaller mirrors are significantly more sensitive to clamping conditions, and must be clamped with less force to maintain good agreement between between simulation and reality. Further, the non-axis-symmetric mode at 1.3 MHz is split into two large modes by the clamping, effectively reducing the width of the mirror mode free region.

8.5 Delivered Mirrors – Optical Properties Characterization

The mirrors were ordered with respectively 10 ppm and 500 ppm transmissivity at 852 nm. The transmissivities as a function of wavelength, as per the manufacturer datasheet can be seen in Fig. 8.9. Note that the trace for the 10 ppm coating is scaled by a factor 100, to better show both traces on one plot. The two traces are both nicely centered on the design wavelength of 852 nm. The reflection bandwidth is slightly narrower for the high reflection coating, meaning that tuning to higher or lower wavelength *slight* increases the ratio $T_{10\text{ppm}}/T_{500\text{ppm}}$ from 0.02 at 852 nm to 0.026 at at 810 nm. This essentially means that the cavity overcoupling is roughly constant as the wavelength is changed to lower values. Going to higher wavelengths changes the ratio a bit more; at 900 nm the ratio is 0.05.

To assess the specified reflectivities, we assembled a cavity with one of each mirror. The cavity length was measured by finding the FSR, which was found to be 0.1376 nm, or 28.4 GHz, corresponding to a cavity length of 5.27 mm. The cavity linewidth was then measured for the entire tuning range of our Ti:Sapph laser, as depicted in Fig. 8.10. The measured values were then compared to the expected linewidth, assuming 8 ppm of residual scattering and coating losses, independent of wavelength (orange line). We see overall very good agreement between the measured and expected linewidths, for the range where the transmissivities were specified in the datasheet, with some disagreement the further from 852 nm we tune (e. g., κ_{meas} slightly below κ_{calc} for $\lambda \sim 810$ nm).

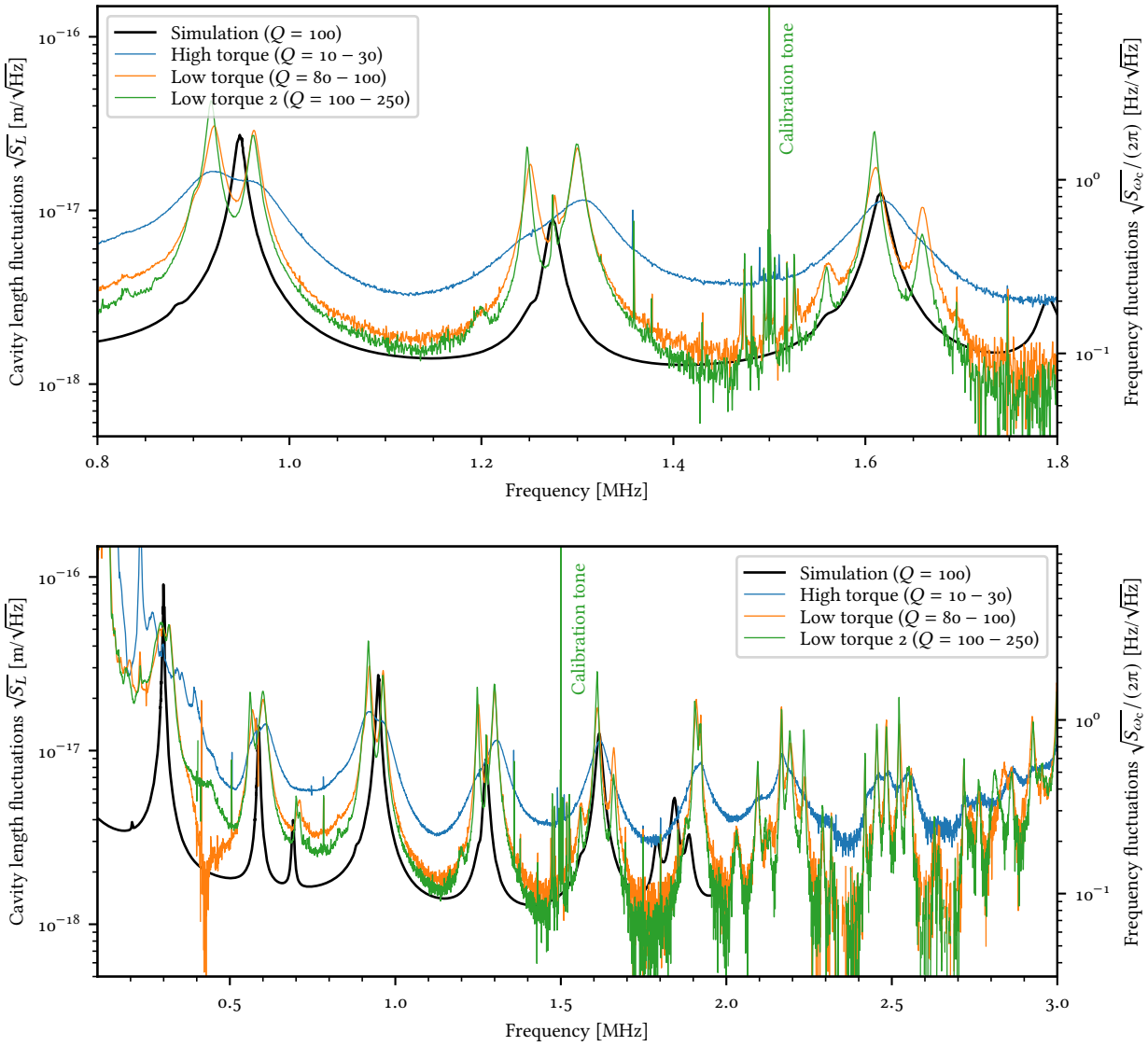

Figure 8.8: Measured mirror modes of new mirrors. Simulated spectrum with Q = 100 (black line), and measured spectra with high clamping torque (low Q, blue line) and low clamping torque (high Q, orange and green lines). Top: zoom on the relevant region 0.8 MHz to 1.8 MHz, bottom: full spectrum. Spectra are calibrated by the use of a phase modulation calibration tone at 1.5 MHz.

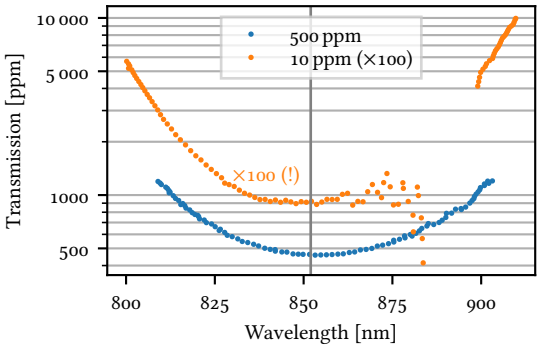

Figure 8.9: Mirror transmissivities from the coating company datasheet. The 10 ppm coating values have been scaled by a factor 100. The gap in values around 875 nm in the 10 ppm trace is due to poor sensitivity of the measuremenat apparatus in this region (also seen in the considerable scatter around 875 nm).

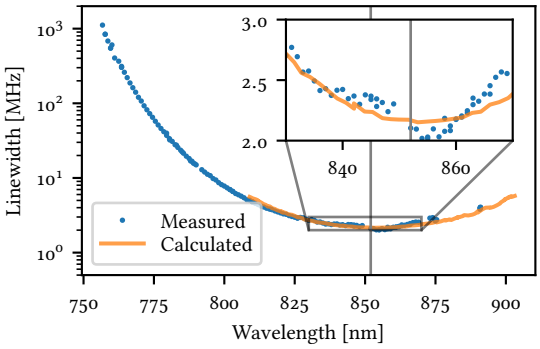

Figure 8.10: Cavity linewidth with the new mirrors. A cavity of length $L = 5.3\,\text{mm}$ was assembled, and the cavity linewidth measured for entire tuning range of our Ti:Sapph laser. For the range where datasheet values are available, we calculate the expected linewidth, which matches well with the measured values. By tuning the optical wavelength we are able to change the cavity linewidth from $\sim 2\,\text{MHz}$ to $1\,\text{GHz}$ – almost an order of magnitude.

In this chapter we discussed our efforts in designing and buying new mirrors, in order to improve both the mechanical and optical properties. The majority of the effort was focused on reducing the mirror sizes, to obtain a sparser mechanical mode spectrum, with larger spectral regions with no added mirror noise.

The new mirrors were not yet implemented into the experiment at the time where the entanglement results were obtained, but are currently being investigated and implemented in the next iteration of our experiment. The mirror have also been put to use in the Fock experiment, and in the group of Albert Schließer.

At the same time, this concludes Part II, where we discussed the new cavity design for cavity optomechanics in a hybrid experiment (which was successfully used in the entanglement experiment), including a numerical model for evaluating and the new mirrors.

Part III

MEASURING MOTION IN A NEGATIVE-MASS REFERENCE FRAME

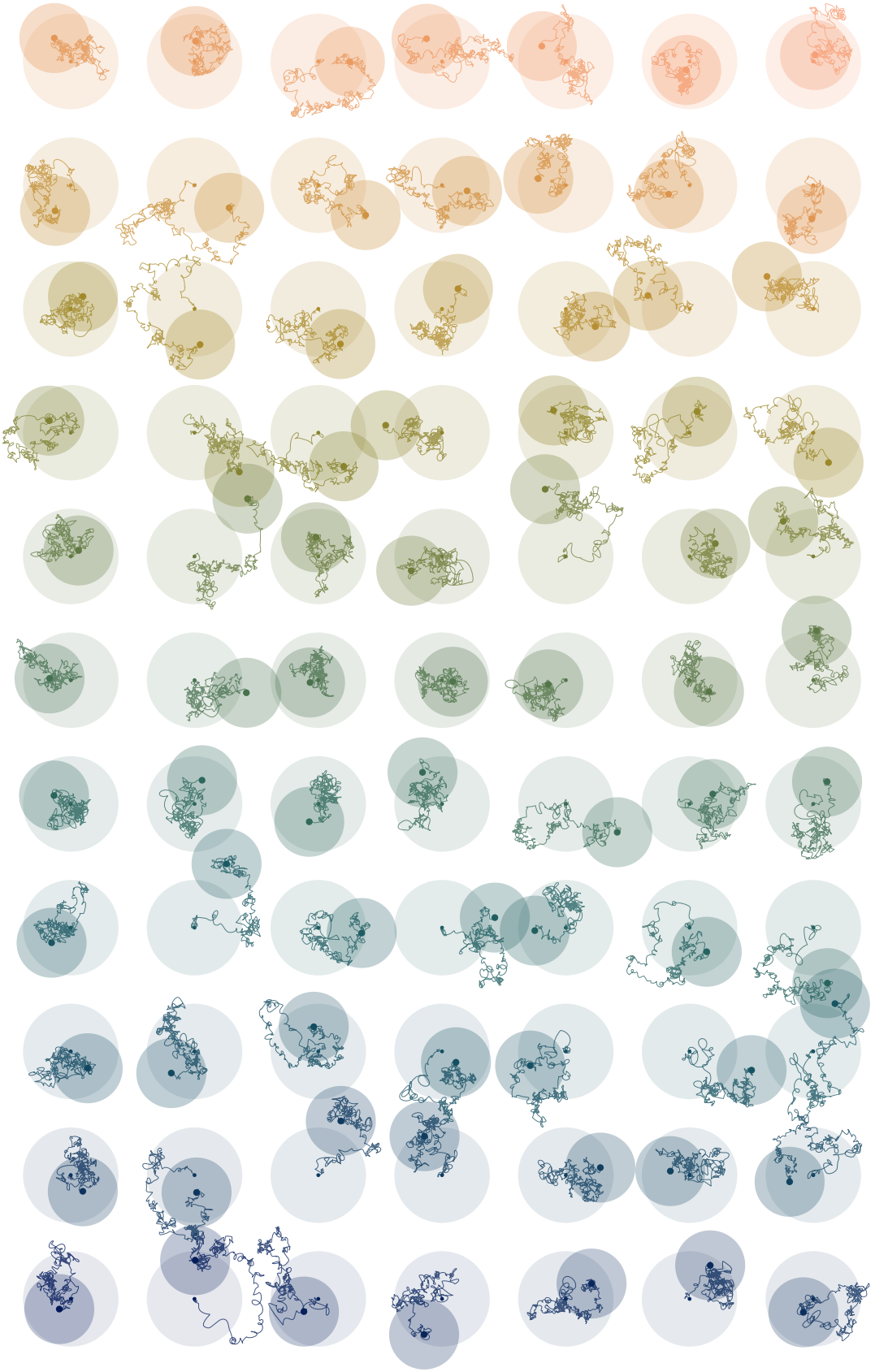

Chapter 9

The Hybrid Setup

> “ Wenn es doch bei dieser verdammten Quantenspringerei bleiben soll, so bedauere ich, mich mit der Quantentheorie überhaupt beschäftigt zu haben.
>
> E. Schrödinger

A brief overview of the technical aspects of the hybrid setup. Lasers, detection and acquisition, basic data analysis.

Having described in detail the design of our optomechanical design in Part II, and the two constituent systems and the theoretical ideas in Part I, we are now ready to tackle the practicalities of a hybrid quantum system.

This chapter will be a small potpourri of technical aspects of our experiment. Lasers, locking, data acquisition, etc.

9.1 Experimental Equipment and Details

9.1.1 Lasers

9.1.1.1 M Squared Ti:Sapph

The main laser of our experiment is a titanium-sapphire (Ti:Sapph[1]) from M Squared. This more or less off-the-shelf laser has been the workhorse for a good handful of years now, and offers many features that benefit an experiment like ours.

The laser is a SolsTiS-7W-SRX-F (M Squared 2013)[2], pumped by a 7 W Sprout diode pump at 532 nm.It features fiber pick-off of light, for absolute wavelength locking by a wavemeter, a reference cavity and an EOM in the laser cavity. At the time of delivery the laser was continually tunable all the way from 720 nm to above

(1) Also Ti:Al_2O_3, from the chemical composition of sapphire.

(2) M Squared (2013). *SolsTiS User Manual.* Version 10.0.

Illustration on opposite page: EPR trajectories. Trajectories start at the small dots, with unconditional uncertainty of the larger circles, and end at the large dots, with conditional uncertainty of the smaller circles. See Chapter 10, particularly Fig. 10.7.

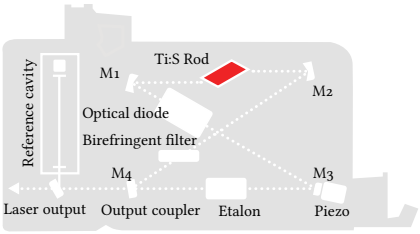

Figure 9.1: Ti:Sapph drawing. The laser cavity, formed by four mirrors, M1-M4, contains a Ti:S rod as a gain medium, an optical diode (isolator), an etalon and a piezo for tuning, and a birefringent filter for broad tuning. The light exits through the flat mirror M4, and a small amount of light is picked off for the reference cavity. Reproduced from M Squared datasheet, text changed.

(3) The strict definition of "shot noise limited" is by some taken to be "less than 3 dB above shot noise", as then shot noise makes up *most* of the noise. In practice, we often use a stronger requirement, which is "adding no detectable amount of noise".

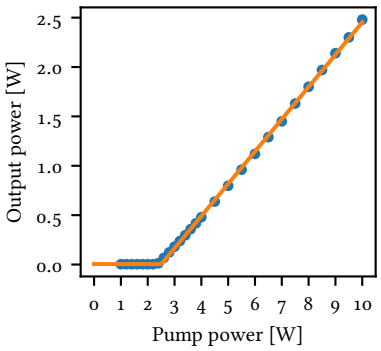

Figure 9.2: Power output of a Ti:Sapph laser similar to ours as a function of the pump power. $\lambda = 852\,\text{nm}$. The laser output power is well approximated by a linear function with a slope of 0.33 W/W above a threshold of 2.51 W (orange curve), with the exact numbers depending on things like the laser output coupler transmission etc.

(4) Michał Parniak et al. (2021). "High-frequency broadband laser phase noise cancellation using a delay line". In: *Opt. Express* 29.5, pp. 6935–6946.

the cesium D_2 line at 895 nm, with an power output of around 1 W with 7 W of input power.

By locking the laser to an High-Finesse WS6-600 we get rather good absolute frequency precision, as well as acceptable short time locking stability. As we will see later, we typically lock the laser ~ 3 GHz detuned from the atomic transition, and the atoms can thus easily accept 100 MHz of frequency drift, which is only a couple of percent change in the detuning. The optomechanical cavity will be locked to the laser, and does not care about frequency drift, as long as the lock can follow.

Another good thing about the Ti:Sapph laser is the generally good noise performance; since we care about the dignified quantum fluctuations of our light, it is paramount that we are shot noise limited. In the amplitude quadrature, the Ti:Sapph suffers from *relaxation oscillations*, which give rise to a distinct hump of excess noise at low frequencies. The peak moves up in frequency as the pump (and thus output) power is increased. In Fig. 9.3 I plot the amplitude quadrature PSD measured in direct detection for a similar laser to the one used in our experiment, for different pump powers. Apart from some sharp electronic noise peaks, all traces are shot noise limited above 1.25 MHz, while for the lowest powers the traces are shot noise limited(3) already well below 1 MHz. Since we care about having the lowest possible noise around 1.35 MHz, it is important for us to use the lowest pump power that we can. In practice we most often use around 2 W of pump power, giving approximately 100 mW of output power at 852 nm.

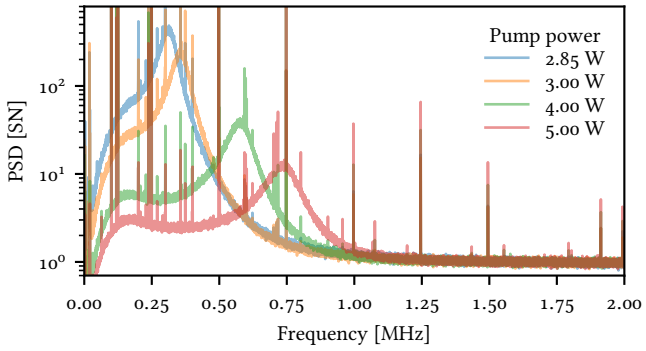

Figure 9.3: Relaxation oscillations in the amplitude quadrature of a Ti:Sapph laser. As the power is increased, the characteristic hump moves to higher frequencies. For lower powers, the spectrum is shot noise limited at the frequencies of interest for us, around 1.35 MHz.

The phase quadrature noise of a laser is harder to measure, requiring either beating it with a another laser with known or much lower phase noise, or beating the laser with itself in a delay line setup, such as that presented in Parniak et al. (2021)(4). Here we note simply that phase noise has not been found to be a major contributor of noise in our experiments. For experiments with stricter phase noise requirements, such as the mechanical Fock state experiment performed here in Quantop, phase noise sets a lower bound to the attainable ground state cooling level; therefore phase noise cancellation such as the scheme reported in Parniak

et al. (2021) can be a necessity. For the hybrid experiment, the atoms are insensitive to the level of phase noise, the interferometers (LO_1/LO_2 and detection) is insensitive as long as the interferometer arms are kept reasonably balanced (i. e., the optical path lengths are close to equal), and the mechanics, while sensitive, is helped by the fact that we are probing the system with very low powers. Measurements performed on the Ti:Sapph for the Fock experiment reveals approximately 1 shot noise unit of phase noise at an optical power of 1 mW at a frequency of 1.37 MHz. This means that for our powers of $P_{m,\mathrm{in}} \sim 10\,\mu\mathrm{W}$, the classical phase noise contribution is much below the shot noise level. Even for significantly higher LO_2 powers, the phase noise contribution is expected to not contribute significant driving of the mechanics.

The SRX laser model has a stated short time RMS linewidth of < 50 kHz when locked to the reference cavity. However, we often want to use the fast external input, which is not available when the reference cavity is utilized. When the reference cavity is disabled, the short time RMS linewidth is < 10 MHz in free running operation. The fast and slow piezo inputs are connected to two different parts of a dual stack piezo actuating the same mirror. The fast input has a scan range of 80 MHz with a sensitivity of 3.4 MHz/V and a flat frequency response up to 30 kHz. From there, the response drops gradually to about 1 MHz/V at 100 kHz. If the laser is locked to the reference cavity, the laser servo will attempt to cancel out all inputs to the fast input; M Squared recommends that only AC signals above ~25 kHz be applied in this case. The slow input is connected to a the long-throw part of the dual piezo stack, and offers a much wider scan range of approximately 25 GHz, but with a bandwidth of only 50 Hz at a sensitivity of 2.5 GHz/V. The same considerations about simultaneous locking to the reference cavity applies, but the much slower bandwidth essentially means that any slow piezo input while locking to the reference cavity leads to no tuning, while putting strain on the locking servo.

A nice feature of the bandwidth of the fast piezo input is that the response at the frequency of our membranes is so low that we do not have to worry about directly inducing fluctuations at 1.3 MHz.

The 7 W pump is shared with a similar Ti:Sapph laser from M Squared, which is primarily used in the Fock experiment. Pump power is split by a simple $\lambda/2$-waveplate and PBS setup, which is usually set to split the light 50:50. The lasers are located on a 2 m by 1 m honeycomb breadboard, placed on top of our larger optical table and suspended on passive isolation mounts (i. e., rubber feet with air cushioning). This setup provides excellent mechanical isolation of the laser from the rest of the optical table, and minimizes laser frequency fluctuations from disturbances when working on the optical setup.

9.1.1.2 Lasers for Atomic Pumping and Repumping

While the Ti:Sapph provides the probe light for the system, pump and repump light for the atoms are provided by a set of lasers from Toptica.

The pump laser is DL PRO, delivering ~30 mW (nominal output 55 mW) at 895 nm, and the repump laser is a DL-100 delivering ~60 mW at 852 nm.

The lasers are locked to their own polarization rotation spectroscopy setup (Wieman and Hänsch 1976)[5]. This modulation-free locking technique relies on on one beam spin-polarizing the atoms and a counter-propagating beam sampling the

(5) C. Wieman and T. W. Hänsch (1976). "Doppler-Free Laser Polarization Spectroscopy". In: *Phys. Rev. Lett.* 36 (20), pp. 1170–1173.

resulting rotation of the light polarization. The technique allows for Doppler-free spectroscopy, and offers convenient zero-crossings for all resonances.

After locking, the two lasers are combined into a single fiber, which is sent to the atomic part of the setup.

9.1.2 Acquisition System and Detectors

9.1.2.1 DAQ card

Digitization of the photodetector signal is performed with a M2i.4931[6] digital acquisition (DAQ) card from SPECTRUM INSTRUMENTATION GMBH. The card has four channels, which can be linked into two pairs for differential detection. The input range is from ±200 mV to ±10 V in six discrete steps and has 16 bit of resolution. It can sample up to 30 MS/s on all four channels simultaneously, with 512 MB (256 MS) of memory, or around 2 s of full speed acquisition on all four channels, or 8 s full speed acquisition on a single channel. All inputs can be either 50 Ω or 1 MΩ terminated.

(6) Spectrum Instrumentation GmbH (2020). *M2i.49xx Datasheet.* Version 7.5.2020.

The card is controlled by a homebuilt piece of software, built using LABVIEW, which exposes the relevant parameters to the experimenter, handles transformation into the Fourier domain etc., as well as saved the averaged spectra as binary files for data storage efficiency.

9.1.2.2 High Quantum Efficiency Balanced Detectors

For quantum (shot noise) limited detection in the frequency region of interests we rely almost solely on homebuilt balanced photodetectors. The detectors use the HAMMAMATSTU S5971[7] diodes, which offer rather good quantum efficiency (QE), good frequency response up to 100 MHz and suitable power handling at a very modest price of less than 30 € per diode.

(7) Hamamatsu Photonics K.K. (2019). *S5971, S5972, S5973 series datasheet.*

The typical response for the diodes are displayed in figure Fig. 9.4, according to the datasheet, which gives the response in A/W. By calculating the number of photons in 1 W at a given wavelength and comparing the current (A = C/s), one may calculate the quantum efficiency. At 852 nm it is typically around 89 %, although some variation exists between different fabrication runs, and our experience is that the values are more often higher than lower. More importantly, the response is measured with a protective glass lid on top of the diode, which leads to around 8 % optical loss (~4 % at each surface due to simple reflection, c.f. Fresnel's equations).

Correcting the response and quantum efficiency by a factor $1/(1-0.04)^2$ as a crude estimate of the losses, leads to the dashed lines in Fig. 9.4, bringing the estimated quantum efficiency of the diodes to around 96 %.

The home-built detectors ("BAC"-detectors) (see schematic in Appendix D) is a balanced detector using two S5971 diodes. It can be built in several different configurations, using different OPAMPS. If used for heterodyne measurements, the electronic noise close to the beat frequency can be suppressed by a notch filter. After the diodes, follows first a transimpedance amplifier (converting the photocurrent into a voltage), a filter and a second (inverting) amplification stage. The output is split into a "DC" part and an "AC" part (with the low frequencies suppressed by a simple capacitor in series). The AC signal is used for data acquisition, while the DC part is suitably lowpassed and used for locking the detection LO phase. Removal of

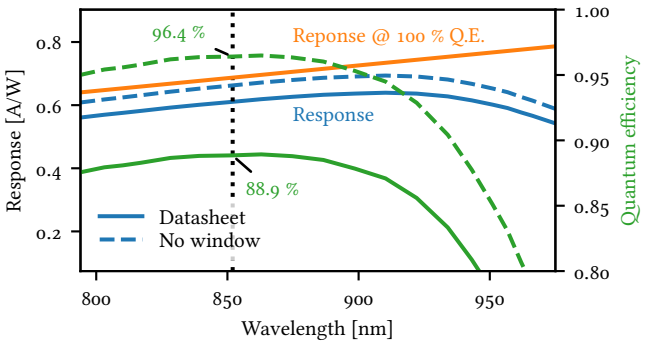

Figure 9.4: Response of a typical S5971 diode. Solid lines are values from the datasheet, as well as the response with a quantum efficiency of 100 % (orange). Correcting the response and quantum efficiency by a factor $1/(1-0.04)^2$ estimates the attainable response achievable by removing the uncoated window, which brings the quantum efficiency to around 96 %.

the DC part from the signal used for data acquisition allows for higher resolution in the digitization, which would be otherwise have to be significantly coarser to avoid saturation of the input DACs in the DAQ card. This is especially true if the light is not balanced, either because the detector is being used in this way on purpose, or because we are measuring an optical quadrature different from the phase quadrature (which is generally measured when the DC signal equals 0).

To increase the permissible amount of light on the detector before saturating the second amplification stage, the gain of the detector is non-trivial, as depicted in Fig. 9.5. Frequencies below ~ 1 kHz has a significantly lower gain than frequencies in the range 0.1 MHz to 10 MHz. As long as the frequencies we care about are safely in a region with flat gain, we are safe. However, for applications where the detector is used in a non-balanced fashion, and the DC value must be compared to the fluctuations, the gain curve poses very real problems[8].

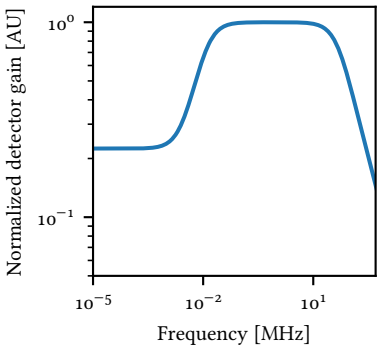

Figure 9.5: Calculated BAC detector frequency dependent gain, for the BAC3 detector. See schematic and component choice in Appendix D.

9.1.3 Cavity Locking

The practical tasks of locking cavities and interferometers requires some kind of PID[9] circuitry.

In the hybrid experiment, the absolute laser frequency is locked with a slow time constant, approximately 3 GHz blue-detuned from the cesium D_2 line. In many other optomechanical experiments, the cavity resonances are fixed, and the laser tuned to these, but the atoms prevents us from doing that. We therefore lock the cavity to the laser instead. In the simplest case, we use the transmission from the cavity, detected by an APD, and simply "slope-lock", i. e., (attempt to) maintain a constant power level transmitted through the cavity.Slope locking has the distinct advantage of being very good at approaching a resonance from far away – a very useful feature when sideband cooling is necessity for locking. However, the slope lock is not ideal, for a number of reasons, including the non-zero error signal at the lock point.

To get a better signal-to-noise ratio for the locking circuitry we most often

(8) This includes, but is not limited to, using the detector to measure the visibility between two beams. Since the gain for fluctuating parts is significantly higher, a beat signal between two beams can be significantly larger than the average signal, thus giving (naïve) visibilities well over 100 %.

(9) Proportional–Integral–Differential, referring to three distinct types of feedback, with adjustable gain for each.

transition from the simple slope lock to dither locking, once an initial cavity lock has been obtained. We dither one cavity piezo at ~60 kHz, which happens to be a quiet window in our spectrum. This small modulation can be extracted by suitable IQ demodulation, and used as an error signal for locking.

Where earlier iterations of the experiment used analog lock boxes (the New Focus LB1005-S PI lock box from Newport was used for a long time), we now rely almost exclusive on FPGA-based locks. To run the experiment, we employ a handful or more of Red Pitaya STEMlab 125-14 boards, with the excellent PyRPL (Neuhaus et al. 2017)[10] software. These cheap (~ 400 €) boards offer excellent programmable feedback electronics, while also functioning, with PyRPL, as oscilloscopes, VNWA, ASGS, IQ demodulators etc.

After generation of a feedback signal by the Red Pitaya, we split the signal into a fast and slow part. The slow part is amplified, and fed to one cavity piezo. The fast signal is sent to the fast input of the Ti:Sapph laser, which helps minimize fast, but small excursions of the cavity, without negatively affecting the atoms.

For previous experiments, e. g., Møller et al. (2017), a much more elaborate lock scheme was used. Here, a two tones were created with separate AOM, one of which was then modulated for PDH locking (Black 2001)[11] on resonance. By changing the relative AOM RF drive frequencies, the probe detuning could then be tuned freely. However, we found that for CW experiments, the needed flexibility was unnecessary, provided little practical benefit, but at the price of added amplitude and phase noise from the modulation. For pulsed experiments, the picture is changed; here, maintaining a weak lock beam on at all times is a practical necessity, and PDH locking is a strong candidate.

(10) L. Neuhaus et al. (2017). "PyRPL (Python Red Pitaya Lockbox) — An open-source software package for FPGA-controlled quantum optics experiments". In: *2017 Conference on Lasers and Electro-Optics Europe & European Quantum Electronics Conference (CLEO/Europe-EQEC)*, pp. 1–1. DOI: 10.1109/CLEOE-EQEC.2017.8087380.

(11) Eric D. Black (2001). "An introduction to Pound–Drever–Hall laser frequency stabilization". In: *American Journal of Physics* 69 (1), pp. 79–87.

9.2 Experiment Layout

Having now covered the individual components of our setup, we move on the setup itself. In Fig. 9.6, a simplified conceptual drawing of the setup is displayed.

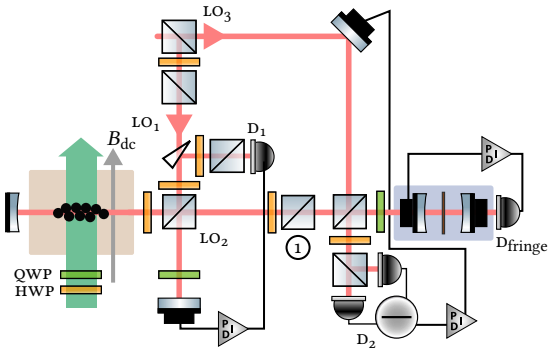

Figure 9.6: The outline of the hybrid experimental setup. See main text for details. Figure reproduced from Rodrigo A. Thomas (2020).

The two systems, the atoms (black dots in a red box) and the membrane (grey

line in the cavity marked by a blue box), are probed sequentially. The 852 nm Ti:Sapph laser enters at the top, where it is split by a polarizing beam splitter (PBS). The transmitted beam, LO_3, will become the LO for the homodyne setup, while the reflected beam becomes LO_1 and LO_2, the beam for atomic read out and membrane read out respectively.

LO_1 and LO_2 are split by another PBS; LO_1 is double passed through the atomic setup, and upon returning to the PBS the linear input polarization has been rotated into orthogonal polarization, or in the Stokes parameter language, the atomic response has been written into S_y and S_z. When impinging on the PBS, these polarizations will be transmitted, and the big classical field LO_1 will be reflected.

LO_2 is retroreflected onto the PBS, where most of it is reflected into the same direction as the atomic sidebands, while a small part is transmitted, allowing us to lock the relative phase of LO_1 and LO_2 using detector D_1, feeding back on a piezo mounted mirror in the LO_2 path. After transmission and reflection on the PBS the quantum signal from the atoms and LO_2 are co-propagating, but in different polarizations. On the PBS marked ①, most of LO_2 is dumped, together with a small fraction of the quantum signal; after transmission most of the signal is retained, but a new, strong co-polarized LO has been effectively added. This removal of LO_1 and addition of a new LO_2 is necessitated in part by the different power requirements of the two systems, in part by the requirement of having the LO respectively cross- and co-polarized, and in part by the necessity to of introducing a phase delay, φ, between the atomic response and the LO driving the mechanics, as described in Chapter 10.

The new LO plus atomic signal is then transmitted through a PBS and coupled into the cavity. After interaction the light leaks primarily ($\eta \sim 92\,\%$) into the same direction from where it came; a quarter wave plate acts, together with the PBS, as a poor man's isolator, sending the light towards the final balanced detection setup with detector D_2, where we perform homodyne detection of the phase quadrature of LO_2 with LO_3. The optical quadrature to be detected is controlled via a piezo in the LO_3 path.

The description above is, although essentially correct, also somewhat simplified. In Fig. 9.7 the full setup is presented. The drawing is a quasi-correct drawing of the setup as it was *actually* built, in the sense that all optical components used are represented in the drawing, and their location is *approximately* correct. The drawing represent roughly 2×1 m of optical table.

While discussing the rationale behind every single change from the idealized setup above would be unhelpful, a couple of points are worth highlighting.

Starting from the atoms, the presence of a polarization rotation detecting setup in single pass is very helpful when aligning the cell, as well as for calibrating some quantities, such as discerning single pass from double pass effects.

A fourth LO (in purple) is derived from the LO_1/LO_2 beam before the "atoms PBS". This beam is split into two beams, the first being the "atoms LO", used for performing phase quadrature homodyning of the atomic signal without the optomechanical part, using the "atom BAC" detector. The second part of the beam is sent through a fiber coupled EOM, allowing us to inject (white) noise into the atoms, or for performing CIFAR, introduced in Section 5.10. For performing CIFAR, we need to lock the phase between the modulated light and LO_1; this is facilitated by the

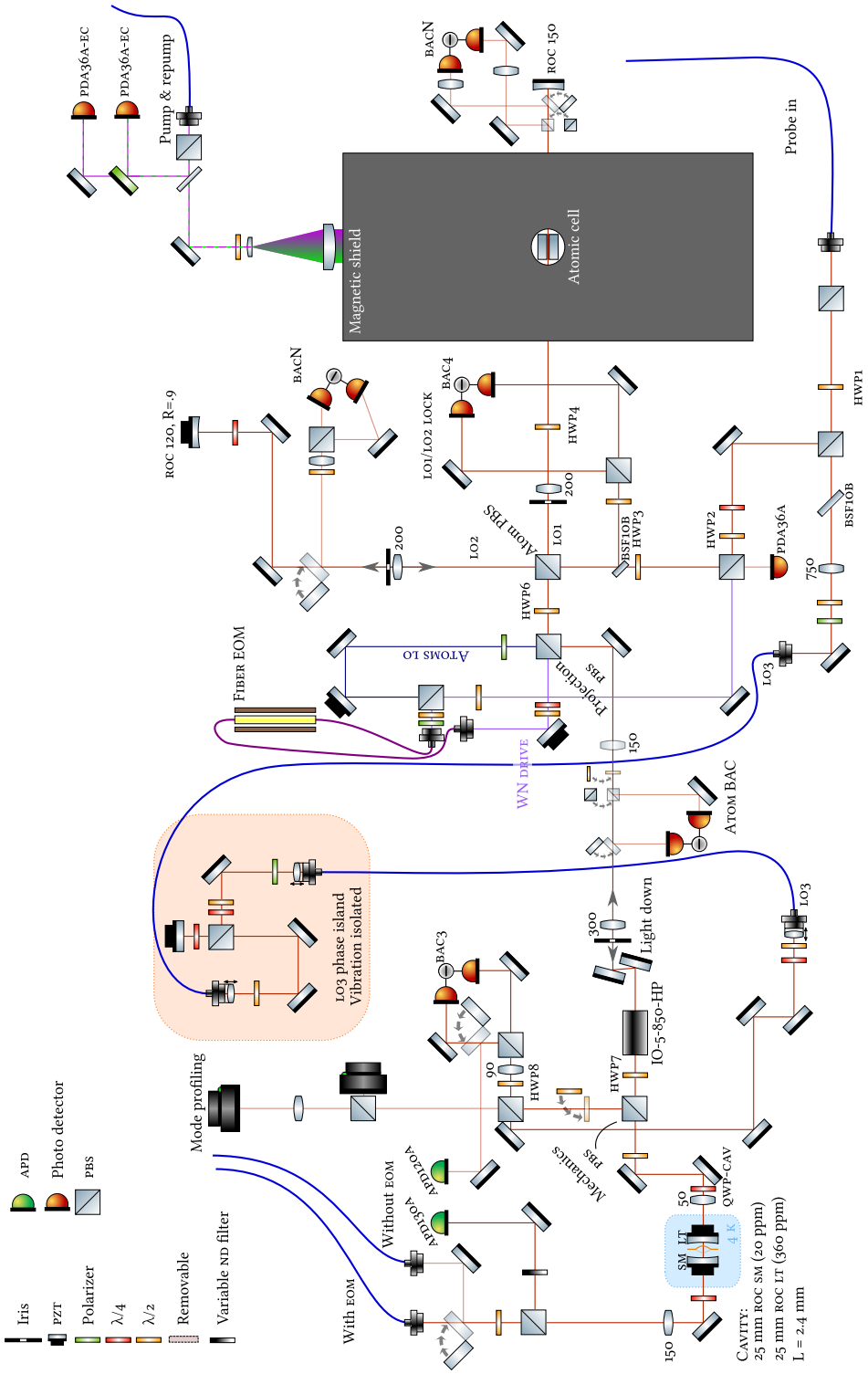

Figure 9.7: Detailed drawing of the experimental setup. See main text for details.

BACN detector.

After the "projection PBS", a Faraday rotator (THORLABS IO-5-850-HP) is placed, i. e., a Faraday isolator with it's polarizing elements removed to minimize optical losses. The isolator prevents light from leaking backwards from the optomechanical cavity to the atoms. The isolator is effectively completed by the the PBS'es on either side, and effectively complements the poor mans isolator compromised of the "mechanics PBS" and the quarter wave plate before the cavity (QWP-CAV).

After leaving the cavity, the light is reflected on the "mechanics PBS". In the simplified setup it is overlapped with LO_3 on this PBS as well. In reality, this leads to a significant amount of LO_3 being reflected off the PBS, towards the atoms. This is solved by overlapping them on a subsequent PBS, at the price of adding an extra waveplate and PBS into the quantum light's path.

To minimize mechanical cross-coupling from the piezo controlling the phase of LO_3 with, e. g., the optomechanical cavity, LO_3 is fiber coupled and sent to a small breadboard, which is vibration isolated from the rest of the table. This does come at the price of increased polarization/amplitude fluctuations of LO_3, however.

Finally, we have several different supplementary beams of light and detectors for the optomechanical part of the setup. From the back, we can send light from the Ti:Sapph, with or without an EOM in the path. The EOM is used for things like OMIT, but sets a rather low limit on optical power due to limitations on the fiber EOM used. For high power beams from the back side (to compensate for the low cavity transmission through the $T = 20\,\text{ppm}$ high reflector mirror) the beam without an EOM may be used. On either side we have an APD for high gain detection of weak beams.

9.3 The Periodogram Estimator - Finite Time PSD

When the light has been detected by our photo detectors, and converted into a voltage and finally digitized by our computer, we are left with a (discrete) time-domain signal. Since we almost always want information in the frequency domain, where we are also doing most of our theoretical modeling, we must somehow transform the data. In the same way that one can in principle choose different estimators for an *average* value, e. g., the aritmetic mean, the median, the harmonic mean, the *weighted* mean etc., several different recipes for obtaining frequency domain information from time domain data exist, each with their own statiscial biases and efficiency. Our choice of estimator is the *periodogram*. As we will see in the following section, the estimator is extremely handy given our way of expressing spectral densities and susceptibilities, introduced already in Section 3.0.2, but it also comes with a couple of features or caveats, of which a diligent experimentalist should be aware.

9.3.1 Discrete Time

The previous discussions have assumed continuous functions $f(t)$ – alas, no data we as physicists acquire is continuous, and we must adapt our descriptions to this unfortunate reality. In reality, we always deal with a finite number of samples acquired in a finite time, In this case, we can approximate, following Nielsen (2016), the continuous Fourier transform with the *discrete Fourier transform* (DFT). With

the N data points f_n, sampled at the frequency F_S, the DFT is given by:

$$\text{DFT}[f](m) \equiv \sum_{n=o}^{N-1} f_n e^{-2\pi i m n/N}, \tag{9.1}$$

where the m index runs from o to $N-1$ and maps to real frequencies as

$$m \longrightarrow m \times F_S/N. \tag{9.2}$$

The ratio F_S/N is known as the *resolution bandwidth* (RBW), i. e., the frequency difference between two different m's, and equals the inverse of the acquisition time, $T = \text{RBW}^{-1} = N/F_S$. Where the continuous time Fourier transform was defined for positive as well as negative frequencies, the DFT is defined, at first glance, for positive frequencies only; however since the function is periodic, indices $\left[-\frac{N}{2}, \frac{N}{2} - 1\right]$ (for even N) could have been used as well, bringing back the negative frequency components.

The (finite) continuous time Fourier transform can now be approximated from the DFT[12] as

$$f_T(\Omega) = \int_{-T/2}^{T/2} f(t) e^{-i\Omega t}\, dt \approx \sum_{n=0}^{N} f_n e^{-2\pi i m n/N}\, \Delta t = \text{DFT}[f](m)\, \Delta t, \tag{9.3}$$

where $\Delta t = 1/F_S$. Comparing to the definition of the of the PSD in (3.13), defining the periodogram, P_f as

$$P_f(m) = \frac{1}{T} \left|\text{DFT}[f](m)\Delta t\right|^2 = \frac{1}{NF_S} \left|\text{DFT}[f](m)\right|^2, \tag{9.4}$$

which converges to the PSD as $T \to \infty$, and will be our estimator of choice for spectral densities. After a lot of mathematical gymnastics, we thus arrive at a rather straightforward recipe: acquire the data, f_n, take the DFT, take the absolute square and divide by NF_S. P_f now estimates S_{ff}.

Since the input signals, f_n, will always be real, it can be shown that only the positive frequency, or similarly the first half of the indices, $m < N/2$, is of importance. The rest of the trace contains the same information. From this, it should also be immediately apparent that the highest frequency one can discern is $F_S/2$, the so-called *Nyquist frequency*.

As noted by Nielsen (2016), the periodogram is a rather inefficient estimator for the spectral density at a given frequency. Where the *mean*, e. g., estimates one number from N values, the periodogram estimates $N/2$[13] numbers from N data points. Intuitively, this leads to the statistical power of the estimator being smaller than one might have hoped for, and a fact we shall discuss next.

(12) The DFT is in principle distinct from the *fast Fourier transform*, FFT, that one often encounters, and which is a numerical method for computing the DFT.

(13) Or N, depending on how one looks at it, but since $N/2$ of those are redundant, only $N/2$ of those are independent estimates.

9.3.2 Variance of the Periodogram Estimator

Perhaps the most striking feature of the periodogram is the variance of the spectral density, which for Gaussian noise approximately can be stated as:

The standard deviation of the periodogram estimator is equal to the expectation value.

Or in other words: the variance is the mean value squared. Given that the periodogram can assume only strictly positive values, this naturally means that the disitribution cannot be Gaussian, as just one standard deviation below the mean is, by definition, not an allowed value.

That this is the truth can be verfied by suitable derivations, by looking up the answer (see Broersen (2006, p. 52)) or by a simple example, the latter of which will follow here.

To demonstrate this property I take a long quasi-continuous time-domain datafile for our hybrid sytem. In total, 300 traces of each 250 000 samples, sampled at 14 MHz, is concatenated into a single stream of data. This stream is then chopped into a varying amount (n) of sub-samples, ranging from 30 to 3000[14]. These samples are then individually transformed by the periodogram estimator, and for each frequency we can then compute the mean value and the standard deviation[15].

For $n = 300$, 50 of such transforms are plotted together in Fig. 9.8. Taking the mean and standard deviations across all traces, for varying values of n, one obtains the traces of Fig. 9.9. The traces are offset vertically by a factor 3 between each trace for better visual separation.

It is clear from these plots that the statistical standard deviation of our chosen estimator has the curious property that the uncertainty is directly proportional to the observed value. Averaging traces of course reduces the uncertainty of the mean value by $1/\sqrt{n}$, so for example for $n = 300$, the uncertainty of a given mean value is equal to 5.8 % of the value.

(14) This effectively changes the resolution bandwidth of each trace, with higher n giving lower spectral resolution, and is sometimes known as *Bartlett's method*. A similar method, *Welch's method* uses overlapping segments, and thus introduces correlation between these.

(15) And higher moments, should we so desire; after all we know that the distribution is non-Gaussian. But we will refrain from digging deeper than needed.

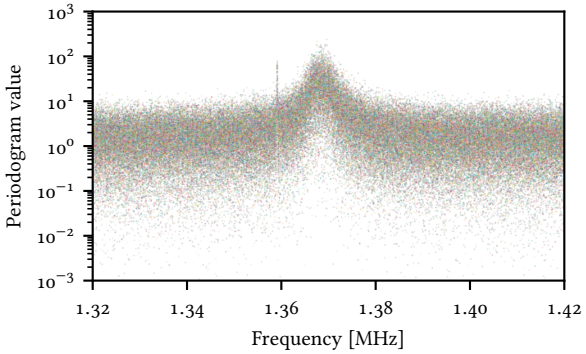

Figure 9.8: 50 periodograms plotted together.

This concludes this somewhat technical exposition of the experimental setup, data acquisition and some technical aspects of data analysis. Armed with this knowledge, we are now ready to finally tackle the hybrid experiment in all its glory.

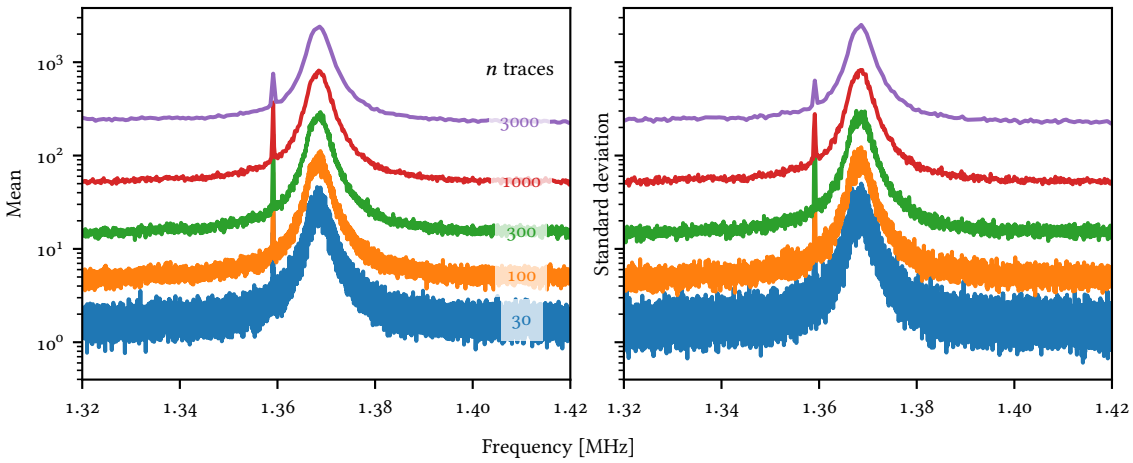

Figure 9.9: Periodogram mean values (left) and standard deviation (right) for varying number of samples. The traces are offset vertically by a factor 3 between each trace for better visual separation.

Chapter 10

Entanglement Between Distant Oscillators

> “Once you’ve ruled out the impossible then whatever is left, however improbable, must be the truth. The problem lay in working out what was impossible, of course. That was the trick, all right.
>
> There was also the curious incident of the orangutan in the night-time…
>
> Terry Pratchett, *Guards! Guards!*

We report the creation and experimental verification of entanglement between the spin and mechanical subsystems of the hybrid setup. This section contains the main scientific result of the thesis.

Finally, we are ready for the big finale. In this chapter, I will present the results of our paper (Rodrigo A. Thomas et al. 2020), showing the creation of an entangled EPR state between our membrane and our spin system.

10.1 EPR States

Until now, we have been dealing with conjugate variables $\hat{X}, \hat{P}$ of single systems, with the commutators $[\hat{X}(t), \hat{P}(t)] = \mathrm{i}$. This non-vanishing commutator limits the product of variances, and thus also their sum, as derived in Chapter 3. In particular,

$$\mathrm{Var}\left(\hat{X}\right) + \mathrm{Var}\left(\hat{P}\right) \geq 1. \qquad \text{(3.64 revisited)}$$

Such a fundamental limit does not exist for a pair of commuting variables. One

such pair of variables can be constructed as

$$\begin{aligned}\hat{X}_{\text{EPR}} &= \frac{1}{\sqrt{2}}\left(\hat{X}_{\text{m}} - \hat{X}_{\text{s}}\right)\\ \hat{P}_{\text{EPR}} &= \frac{1}{\sqrt{2}}\left(\hat{P}_{\text{m}} + \hat{P}_{\text{s}}\right).\end{aligned} \tag{10.1}$$

Such a class of collective variables is named after the authors, Einstein, Podolsky & Rosen, of a seminal 1935 paper[1], and related to the concept of what Einstein called "spooky action at a distance"[2], i. e., the non-local correlations, that allows precise determination of one quantum system by measurement of another. Preparing two systems in an EPR state, which is non-local by virtue of the constituent systems being spatially separated, allows for a non-local collapse of the wavefunction of one system, by measuring the other.

At the same time, EPR states is an important building block, or *resource*, for more general quantum networks – for a good review on entanglement as a resource for quantum technologies see Horodecki et al. (2009)[3]. Simultaneously, there is a recognition that the successful implementation of a large scale quantum network may benefit from harnessing the advantages of different constituent systems, for the creation of hybrid quantum networks. For example, one quantum system may have an advantage that makes it suitable as a quantum memory, but not as a transducer of quantum signals (or vice versa). Therefore, demonstrating the creation of such entangled states between different types of quantum systems is of wide interest.

For the variables defined above, we have

$$\begin{aligned}[\hat{X}_{\text{EPR}}, \hat{P}_{\text{EPR}}] &= \frac{1}{2}\left(\left[\hat{X}_{\text{m}} - \hat{X}_{\text{s}}\right]\left[\hat{P}_{\text{m}} + \hat{P}_{\text{s}}\right] - \left[\hat{P}_{\text{m}} + \hat{P}_{\text{s}}\right]\left[\hat{X}_{\text{m}} - \hat{X}_{\text{s}}\right]\right) &(10.2)\\ &= \frac{1}{2}\left(\hat{X}_{\text{m}}\hat{P}_{\text{m}} + \hat{X}_{\text{m}}\hat{P}_{\text{s}} - \hat{X}_{\text{s}}\hat{P}_{\text{m}} - \hat{X}_{\text{s}}\hat{P}_{\text{s}} - \hat{P}_{\text{m}}\hat{X}_{\text{m}} + \hat{P}_{\text{m}}\hat{X}_{\text{s}} - \hat{P}_{\text{s}}\hat{X}_{\text{m}} + \hat{P}_{\text{s}}\hat{X}_{\text{s}}\right). &(10.3)\end{aligned}$$

Using the fact that operators of different system commute, the terms involving operators of both systems drop out, and we are left with

$$\begin{aligned}&= \frac{1}{2}\left([\hat{X}_{\text{m}}, \hat{P}_{\text{m}}] - [\hat{X}_{\text{s}}, \hat{P}_{\text{s}}]\right). &(10.4)\\ [\hat{X}_{\text{EPR}}, \hat{P}_{\text{EPR}}] &= \frac{1}{2}(\text{i} - \text{i}) = 0. &(10.5)\end{aligned}$$

Since these EPR variables commute, there is no fundamental lower bound to their sum of variances. In fact, Duan et al. (2000)[4] shows that if the sum of variances goes below the single system limit of 1, the two constituent system are *inseparable*, i. e., entangled.

The EPR pair above consists of the difference of positions and the sum of momenta. The other combination, the sum of positions and difference of momenta, is also an EPR pair, and also has a vanishing commutator. In fact, transforming one into the other is simply related to rotating the coordinate system for one system by π, sending, e. g., $\hat{X}_{\text{s}} \to -\hat{X}_{\text{s}}$, which also flips the sign of the momentum, while the physics must stay the same since our choice of coordinate system should not influence anything.

(1) A. Einstein, B. Podolsky, and N. Rosen (1935). "Can Quantum-Mechanical Description of Physical Reality Be Considered Complete?" In: *Phys. Rev.* 47 (10), pp. 777–780.

(2) Or, in the original German, "spukhafte Fernwirkung".

(3) Ryszard Horodecki et al. (2009). "Quantum entanglement". In: *Rev. Mod. Phys.* 81 (2), pp. 865–942.

(4) Lu-Ming Duan et al. (2000). "Inseparability Criterion for Continuous Variable Systems". In: *Phys. Rev. Lett.* 84 (12), pp. 2722–2725.

Taking the generalization of EPR states a final step further, we allow for two more degrees of freedom in the definition of an EPR pair: we allow for different weights of the two systems, and we allow an arbitrary rotation of the spin degrees of freedom into one another. This is akin to defining $\hat{X}_s$ and $\hat{P}_s$ in a coordinate system rotated around the mean spin direction F_x. In total

$$\begin{aligned}\hat{X}^{a,\beta}_{\text{EPR}} &= \frac{1}{\sqrt{1+a^2}}\left(\hat{X}_m - a\hat{X}^{\beta}_s\right)\\ \hat{P}^{a,\beta}_{\text{EPR}} &= \frac{1}{\sqrt{1+a^2}}\left(\hat{P}_m + a\hat{P}^{\beta}_s\right),\end{aligned} \tag{10.6}$$

where a is the weight and

$$\begin{aligned}\hat{X}^{\beta}_s &= \hat{X}_s\cos\beta + \hat{P}_s\sin\beta\\ \hat{P}^{\beta}_s &= \hat{P}_s\cos\beta - \hat{X}_s\sin\beta,\end{aligned} \tag{10.7}$$

are the rotated spin variables. Verifying that these also have a vanishing commutator, $[\hat{X}^{a,\beta}_{\text{EPR}}, \hat{P}^{a,\beta}_{\text{EPR}}] = 0$, is straightforward. For notational brevity, the superscript $(\cdot)^{a,\beta}$ will be suppressed from now on, with the understanding that we are discussing the generalized form.

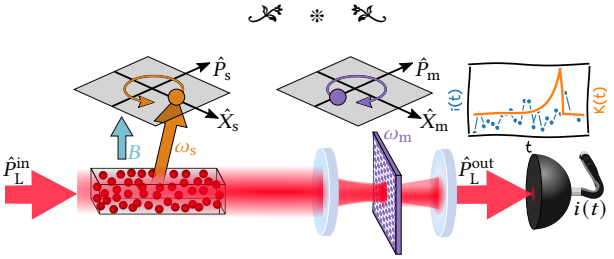

Figure 1.2: (revisited) Cartoon model of the hybrid experiment. A single beam of light, $\hat{P}^{in}_L$ probes the two systems in a cascaded fashion. The first system is the collective spin (subscript s) of a cesium ensemble precessing in a magnetic field, and the second is the motion of a membrane (subscript m) embedded in an optical cavity. After interaction, the output light $\hat{P}^{out}_L$ is detected, and the photocurrent $i(t)$ digitized. The photocurrent is analyzed with a filter $K(t)$ to estimate the EPR variables, Eq. (1.1). By aligning the magnetic field along the direction of the collective spin, the spin oscillator realizes an effective negative mass, and precesses the opposite way of the positive mass membrane. Figure also appears in Rodrigo A. Thomas et al. (2020).

Now that we have defined what kind of quantum states we are after, we briefly revisit the cartoon picture from Chapter 1, repeated here as Fig. 1.2. While simplified, the cartoon accurately captures the essential features in our system. A single beam of light, $\hat{P}^{in}_L$, probes the spins first, then the mechanics and the output light, $\hat{P}^{out}_L$, is detected as a photocurrent $i(t)$. The spins are aligned with the mean spin along an external magnetic field, and thus realize an effective negative mass oscillator – and thus precesses the opposite way in phase space than the (positive mass) mechanical oscillator. By electronically filtering the photocurrent $i(t)$ with the filter $K(t)$, we seek to estimate the EPR variables.

The slightly more realistic, but still simplified setup is depicted in Fig. 10.1. Here we have added the complexities involved in the double pass readout of the

spin system, the stripping of LO_1 and addition of LO_2, detection of the mechanical system in reflection instead of transmission, as well as the homodyne detection with LO_3, instead of the simplified direct detection, allowing us to measure the phase quadrature of light, $\hat{P}_{\text{L}}^{\text{out}}$. This picture is enough for understanding the physics of what is going on – for more technical details, Chapter 9 contains more detailed (and correct) setup drawings.

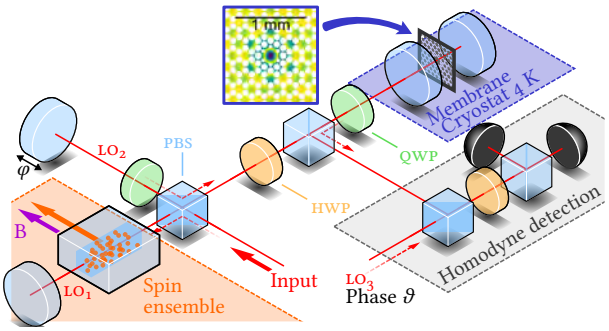

Figure 10.1: Simplified experimental setup for entanglement generation. The local oscillator LO_1 reads out the spin system precessing in the magnetic field B, with the quantum sideband fields written into the orthogonal light polarization. After splitting off LO_1, LO_2, phase shifted by φ relative to LO_1, is mixed with the sidebands. After projection into a common polarization, this light is sent to the mechanical system, which is probed in reflection. Final homodyne measurement of the cascaded hybrid system is performed with LO_3, with phase ϑ. See main text for details. Inset: Mode shape of the mechanical mode under investigation (absolute displacement, linear scale). The figure and caption also appears in Rodrigo A. Thomas et al. (2020).

The rest of the chapter will continue as follows: first we will glue together the input-output relations for the two systems into a complete hybrid model, allowing us to discuss the important concept of quantum back-action evasion in an experimental context, before discussing how to go from input-output relations to an expression for the spectral densities observed. We turn then to quantum back-action in practice, and discuss the achieved QBAE. After that we discuss our filtering procedure, used to extract information about the EPR variables most efficiently, including the important point of *deterministic conditional variance*. Armed with the filtering theory, we analyze our experimental data, and obtain the final result: the time dependent conditional EPR variance, presented in Section 10.5.

10.2 Hybrid Input-Output Relations

From Chapter 5 and Chapter 3 we have the input-output relations for the spin and mechanical system respectively. Now we glue those expressions together, for a complete model of our hybrid spin-mechanical system.

The schematic representation of our entire system is seen in Fig. 10.2. The orange box represent the spin system, with input field $\hat{\boldsymbol{X}}_{\text{L,s}}^{\text{in}}$, spin variables $\hat{X}_{\text{s}}$ and $\hat{P}_{\text{s}}$, thermal noise forces $\hat{f}_{\text{s}}^{X}$, $\hat{f}_{\text{s}}^{P}$, and output field $\hat{\boldsymbol{X}}_{\text{L,s}}^{\text{out}}$.

After leaving the spin system, the light field encounters various propagation losses, which we lump together and model as a beam-splitter loss. For power trans-

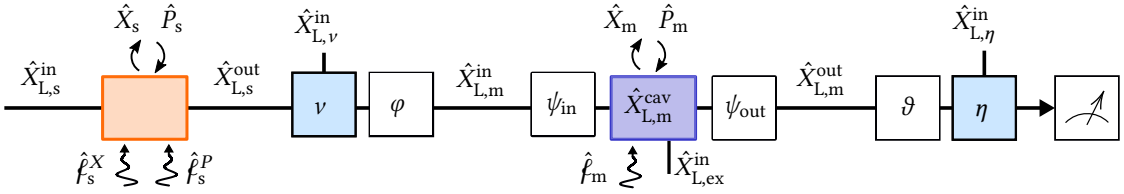

Figure 10.2: Schematic representation of the hybrid system. The light $\hat{X}^\mathrm{in}_{\mathrm{L,s}}$ encounters the spin system (orange box) followed by propagation loss (blue boxes) and phase rotations (white boxes), before interacting with the mechanical system (blue box). Upon leaving the optomechanical cavity the fields are rotated again, before encountering more propagation and detection losses. In the end, the fields are detected with homodyne phase ϑ. This figure is a modified version of the figure in Rodrigo A. Thomas et al. (2020, Supplementary Information).

mission efficiency ν (loss $1-\nu$), the field undergoes the transformation

$$\hat{X}^\mathrm{out}_\mathrm{L} = \sqrt{\nu}\hat{X}^\mathrm{in}_\mathrm{L} + \sqrt{1-\nu}\hat{X}_{\mathrm{L},\nu}, \tag{10.8}$$

where $\hat{X}_{\mathrm{L},\nu}$ represents the (vacuum) field leaking in through the lossy port.

Apart from simple propagation losses, we may also encounter losses related to mismatched visibilities, i. e., mismatching beam profiles, reducing the fringe visibility in an interferometric measurement of two beams. With the usual definition of visibility, two beams of equal intensity and polarization, the visibility may be extracted experimentally as

$$V = \frac{I_\mathrm{max} - I_\mathrm{min}}{I_\mathrm{max} + I_\mathrm{min} - 2I_\mathrm{bg}}, \tag{10.9}$$

where $I_{\{\,\mathrm{max,min,bg}\,\}}$ represent respectively the maximum, minimum and background intensities recorded with a photodetector, when scanning the relative phase of the two optical beams. For a visibility V, we model these losses as $\nu = V^2$, i. e.,

$$\hat{X}^\mathrm{out}_\mathrm{L} = V\hat{X}^\mathrm{in}_\mathrm{L} + \sqrt{1-V^2}\hat{X}_{\mathrm{L},V}. \tag{10.10}$$

When the sidebands of LO_1 is combined with the new LO_2 at the output of the Michelson-type interferometer, the angle φ, proportional to the path length difference between the LOs, determines a rotation of the quantum fluctuations, as

$$\boldsymbol{X}^\mathrm{out}_\mathrm{L} = \boldsymbol{O}_\varphi \boldsymbol{X}^\mathrm{in}_\mathrm{L}. \tag{10.11}$$

One should keep in mind that we are dealing with quantum fluctuations only, and that the big classical fields are only carried implicitly. The same kind of rotation applies when the output of the hybrid system is finally homodyned with LO_3. In this sense, the interferometer described by this equation has only one input and output mode, because we neglect noise in the second port and classical fields are omitted.

We recall the input-output relations of the spin systems, which we found as

$$\hat{\boldsymbol{X}}_\mathrm{s} = 2\sqrt{\Gamma_\mathrm{s}}\boldsymbol{L}\boldsymbol{Z}\hat{\boldsymbol{X}}^\mathrm{in}_\mathrm{L,s} + \boldsymbol{L}\hat{\boldsymbol{f}}_\mathrm{s} \qquad \text{(5.43 revisited)}$$

$$\hat{\boldsymbol{X}}^\mathrm{out}_\mathrm{L,s} = \hat{\boldsymbol{X}}^\mathrm{in}_\mathrm{L,s} + \sqrt{\Gamma_\mathrm{s}}\boldsymbol{Z}\hat{\boldsymbol{X}}_\mathrm{s} = (\mathbb{1}_2 + 2\Gamma_\mathrm{s}\boldsymbol{Z}\boldsymbol{L}\boldsymbol{Z})\hat{\boldsymbol{X}}^\mathrm{in}_\mathrm{L,s} + \sqrt{\Gamma_\mathrm{s}}\boldsymbol{Z}\boldsymbol{L}\hat{\boldsymbol{f}}_\mathrm{s}. \qquad \text{(5.44 revisited)}$$

As depicted in Fig. 10.2, this output is subjected to a loss and rotated, before becoming the mechanical input field,

$$\hat{\boldsymbol{X}}_{\mathrm{L,m}}^{\mathrm{in}} = \boldsymbol{O}_{\varphi}\left(\sqrt{\nu}\hat{\boldsymbol{X}}_{\mathrm{L,s}}^{\mathrm{out}} + \sqrt{1-\nu}\hat{\boldsymbol{X}}_{\mathrm{L},\nu}\right). \tag{10.12}$$

The rotation $\boldsymbol{O}_{\varphi}$ is determined by us, and physically represents the phase offset of LO_2 from LO_1. Since the last term, representing uncorrelated shot noise, is indeed *uncorrelated*, any rotations on this term can be neglected; there is shot noise in both quadratures. In general, the rotation matrix mixes the spin response phase and amplitude quadratures, such that the input to the optomechanical cavity contains the spin response in both quadratures, even for spin QND ($\zeta_{\mathrm{s}} = 0$) readout. As noted in Chapter 3, the input light undergoes further cavity induced rotations of the quadratures whenever $\Delta \neq 0$.

From Section 3.7.3 we recall the solution for the mechanical output optical field

$$\begin{aligned}\hat{\boldsymbol{X}}_{\mathrm{L,m}}^{\mathrm{out}} = {} & \boldsymbol{O}_{\psi_{\mathrm{out}}}^{\mathsf{T}}(\kappa_{\mathrm{in}}\boldsymbol{Y}^{-1} - \mathbb{1}_2)\boldsymbol{O}_{\psi_{\mathrm{in}}}^{\mathsf{T}}\hat{\boldsymbol{X}}_{\mathrm{L,m}}^{\mathrm{in}} + \sqrt{\kappa_{\mathrm{in}}\kappa_{\mathrm{ex}}}\boldsymbol{O}_{\psi_{\mathrm{out}}}^{\mathsf{T}}\boldsymbol{Y}^{-1}\boldsymbol{O}_{\psi_{\mathrm{in}}}^{\mathsf{T}}\hat{\boldsymbol{X}}_{\mathrm{L,m}}^{\mathrm{ex}} \\ & - \sqrt{\kappa_{\mathrm{in}}}\boldsymbol{O}_{\psi_{\mathrm{out}}}^{\mathsf{T}}\boldsymbol{Y}^{-1}\boldsymbol{B}\chi_{\mathrm{moo}}\hat{\boldsymbol{f}}_{\mathrm{m}},\end{aligned} \tag{3.140 revisited}$$

as well as the mechanical response in Eq. (3.138), which by insertion of the rotated, lossy spin signal becomes

$$\begin{aligned}\hat{X}_{\mathrm{m}} = {} & -\chi_{\mathrm{moo}}\boldsymbol{C}\boldsymbol{Y}^{-1}\boldsymbol{O}_{\psi_{\mathrm{in}}}^{\mathsf{T}}\Big(\sqrt{\nu\kappa_{\mathrm{in}}}\boldsymbol{O}_{\varphi}[(\mathbb{1}_2 + 2\Gamma_{\mathrm{s}}\boldsymbol{Z}\boldsymbol{L}\boldsymbol{Z})\hat{\boldsymbol{X}}_{\mathrm{L,s}}^{\mathrm{in}} + \sqrt{\Gamma_{\mathrm{s}}}\boldsymbol{Z}\boldsymbol{L}\hat{\boldsymbol{f}}_{\mathrm{s}}] \\ & + \sqrt{(1-\nu)\kappa_{\mathrm{in}}}\boldsymbol{O}_{\varphi}\hat{\boldsymbol{X}}_{\mathrm{L},\nu} + \sqrt{\kappa_{\mathrm{ex}}}\hat{\boldsymbol{X}}_{\mathrm{L,m}}^{\mathrm{ex}}\Big) + (\chi_{\mathrm{moo}}^{-1} - \boldsymbol{C}\boldsymbol{A}^{-1}\boldsymbol{B})^{-1}\hat{f}_{\mathrm{m}}.\end{aligned} \tag{10.13}$$

We here note, that the mechanical system is not driven solely by its own thermal noise and the light shot noise, but also driven by the *spin* thermal noise as well as the spin optical response written into the optical quadratures leaving the spin.

Finally, the light undergoes another amount of loss, parametrized by η[5], as well as a homodyne detection with the angle ϑ,

$$\hat{\boldsymbol{X}}_{\mathrm{L}}^{\mathrm{meas}} = \sqrt{\eta}\boldsymbol{O}_{\vartheta}\hat{\boldsymbol{X}}_{\mathrm{L,m}}^{\mathrm{out}} + \sqrt{1-\eta}\hat{\boldsymbol{X}}_{\mathrm{L},\eta}. \tag{10.14}$$

(5) Not to be confused with the cavity overcoupling parameter. I retain this notation for consistency with Rodrigo A. Thomas et al. (2020).

The homodyne detection picks out only a single quadrature of $\hat{\boldsymbol{X}}_{\mathrm{L}}^{\mathrm{meas}}$, in particular $\hat{P}_{\mathrm{L}}^{\mathrm{meas}}$. Again, the uncorrelated noise originating from the losses is independent of rotations.

Plugging the (lossy, rorated) solution for $\hat{\boldsymbol{X}}_{\mathrm{L,s}}^{\mathrm{out}}$ into the solution for $\hat{\boldsymbol{X}}_{\mathrm{L,m}}^{\mathrm{out}}$ led to Eq. (10.13); plugging this into expression for $\hat{\boldsymbol{X}}_{\mathrm{L}}^{\mathrm{meas}}$ leads to the full model

$$\begin{aligned}\hat{\boldsymbol{X}}_{\mathrm{L}}^{\mathrm{meas}} = {} & \sqrt{\eta}\boldsymbol{O}_{\vartheta}\boldsymbol{O}_{\psi_{\mathrm{out}}}^{\mathsf{T}}(\kappa_{\mathrm{in}}\boldsymbol{Y}^{-1} - \mathbb{1}_2)\boldsymbol{O}_{\psi_{\mathrm{in}}}^{\mathsf{T}}\times \\ & \left(\sqrt{\nu}\boldsymbol{O}_{\varphi}\left[(\mathbb{1}_2 + 2\Gamma_{\mathrm{s}}\boldsymbol{Z}\boldsymbol{L}\boldsymbol{Z})\hat{\boldsymbol{X}}_{\mathrm{L,s}}^{\mathrm{in}} + \sqrt{\Gamma_{\mathrm{s}}}\boldsymbol{Z}\boldsymbol{L}\hat{\boldsymbol{f}}_{\mathrm{s}}\right] + \sqrt{1-\nu}\boldsymbol{O}_{\varphi}\hat{\boldsymbol{X}}_{\mathrm{L},\nu}\right) \\ & + \sqrt{\eta\kappa_{\mathrm{in}}\kappa_{\mathrm{ex}}}\boldsymbol{O}_{\vartheta}\boldsymbol{O}_{\psi_{\mathrm{out}}}^{\mathsf{T}}\boldsymbol{Y}^{-1}\boldsymbol{O}_{\psi_{\mathrm{in}}}^{\mathsf{T}}\hat{\boldsymbol{X}}_{\mathrm{L,m}}^{\mathrm{ex}} \\ & - \sqrt{\eta\kappa_{\mathrm{in}}}\boldsymbol{O}_{\vartheta}\boldsymbol{O}_{\psi_{\mathrm{out}}}^{\mathsf{T}}\boldsymbol{Y}^{-1}\boldsymbol{B}\chi_{\mathrm{moo}}\hat{f}_{\mathrm{m}} + \sqrt{1-\eta}\hat{\boldsymbol{X}}_{\mathrm{L},\eta}.\end{aligned} \tag{10.15}$$

Going from the last term and working our way towards the beginning, the terms represent: uncorrelated noise associated with the detection losses; thermal noise on

the mechanics, transduced by the optomechanics and the cavity; light shot noise leaking in through the high reflector mirror and other losses in the cavity, again transduced by the cavity; the last term in the parenthesis represents light noise associated with intersystem losses; the term before that thermal spin noise; and lastly, the first term, proportional to $\hat{X}^{\mathrm{in}}_{\mathrm{L,s}}$ represents the QBA of the two systems and their interference.

This equation describes the entirety of the physics of our system, and allows us to fit the model to experimentally measured values and thereby established relevant correlations. However, what it has in terms of correctness it absolutely lacks in terms of clarity. We therefore also seek an approximate solution, inspired by the simplifying assumptions made individually for the

10.2.1 Simplified Input-Output Relations

To begin, we recall the simplified input-output relations for the individual systems

$$\boldsymbol{X}^{\mathrm{out}\prime}_{\mathrm{L,m}} = \boldsymbol{X}^{\mathrm{in}\prime}_{\mathrm{L,m}} + \sqrt{\Gamma_{\mathrm{m}}} \begin{pmatrix} \mathrm{i}\zeta_{\mathrm{m}} \\ 1 \end{pmatrix} \hat{X}_{\mathrm{m}}, \tag{3.150 revisited}$$

$$\boldsymbol{X}^{\mathrm{out}}_{\mathrm{L,s}} = \boldsymbol{X}^{\mathrm{in}}_{\mathrm{L,s}} + \sqrt{\Gamma_{\mathrm{s}}} \begin{pmatrix} -\mathrm{i}\zeta_{\mathrm{s}} \\ 1 \end{pmatrix} \hat{X}_{\mathrm{s}}, \tag{5.50 revisited}$$

as well as the simplified expressions for the system responses

$$\hat{X}_{\mathrm{m}} = \chi_{\mathrm{m}}[2\sqrt{\Gamma_{\mathrm{m}}}(\hat{X}^{\mathrm{in}}_{\mathrm{L,m}} + \mathrm{i}\zeta_{\mathrm{m}}\hat{P}^{\mathrm{in}}_{\mathrm{L,m}}) + \hat{f}_{\mathrm{m}}], \tag{3.147 revisited}$$

$$\hat{X}_{\mathrm{s}} = \chi_{\mathrm{s}} \left[2\sqrt{\Gamma_{\mathrm{s}}} \begin{pmatrix} 1 \\ -\mathrm{i}\zeta_{\mathrm{s}} \end{pmatrix}^{\mathsf{T}} \hat{\boldsymbol{X}}^{\mathrm{in}}_{\mathrm{L,s}} + \hat{f}_{\mathrm{s}} \right] = \chi_{\mathrm{s}} \left[2\sqrt{\Gamma_{\mathrm{s}}}(\hat{X}^{\mathrm{in}}_{\mathrm{L,s}} - \mathrm{i}\zeta_{\mathrm{s}}\hat{P}^{\mathrm{in}}_{\mathrm{L,s}}) + \hat{f}_{\mathrm{s}} \right], \tag{5.49 revisited}$$

and where the system susceptibilities are

$$\chi_{\mathrm{m}}(\Omega) = \frac{\omega_{\mathrm{mo}}}{(\omega^2_{\mathrm{m}} - \Omega^2 - \mathrm{i}\Omega\gamma_{\mathrm{m}})} \tag{3.148 revisited}$$

$$\chi_{\mathrm{s}}(\Omega) = \frac{\omega_{\mathrm{so}}}{(\omega^2_{\mathrm{s}} - \Omega^2 - \mathrm{i}\Omega\gamma_{\mathrm{s}})}, \tag{10.16}$$

where $\gamma_j = \gamma_{j\mathrm{o}} + \delta\gamma_j = \gamma_{j\mathrm{o}} + 2\zeta_j\Gamma_j$, and Γ_j is the readout rate, with j labeling the two systems ($j \in \mathrm{m,s}$). One should also recall that for our experiments $\omega_{\mathrm{so}} < 0$, so the susceptibilities differ by a sign.

Combining these simplified input-output relations, and adjusting the phase φ to π, so that $\hat{X}^{\mathrm{in}}_{\mathrm{L,m}} = -\sqrt{\nu}\hat{X}^{\mathrm{out}}_{\mathrm{L,s}} + \sqrt{1-\nu}\hat{X}_{\mathrm{L},\nu}$, we obtain a simplified expression for the phase quadrature of the output light

$$\hat{P}^{\mathrm{out}}_{\mathrm{L}} = \hat{P}^{\mathrm{in}\prime}_{\mathrm{L}} + \sqrt{\eta}\left(\sqrt{\Gamma_{\mathrm{m}}}\hat{X}_{\mathrm{m}} - \sqrt{\nu\Gamma_{\mathrm{s}}}\hat{X}_{\mathrm{s}}\right) \tag{10.17a}$$

$$\begin{aligned} &\approx \hat{P}^{\mathrm{in}\prime}_{\mathrm{L}} + \sqrt{\eta}\Bigg(- \sqrt{\nu}\left[\tfrac{\chi_{\mathrm{s}}}{\chi_{\mathrm{so}}}\Gamma_{\mathrm{m}}\chi_{\mathrm{m}} + \tfrac{\chi_{\mathrm{m}}}{\chi_{\mathrm{mo}}}\Gamma_{\mathrm{s}}\chi_{\mathrm{s}}\right] 2\hat{X}^{\mathrm{in}}_{\mathrm{L,s}} + \\ &\qquad \sqrt{\Gamma_{\mathrm{m}}}\chi_{\mathrm{m}}[\hat{f}_{\mathrm{m}} + \sqrt{(1-\nu)\Gamma_{\mathrm{m}}}2\hat{X}_{\mathrm{L},\nu}] - \tfrac{\chi_{\mathrm{m}}}{\chi_{\mathrm{ms}}}\sqrt{\nu\Gamma_{\mathrm{s}}}\chi_{\mathrm{s}}\hat{f}_{\mathrm{s}}\Bigg), \end{aligned} \tag{10.17b}$$

In this notation, $\hat{P}_{\mathrm{L}}^{\mathrm{in}\prime}$ includes the input shot noise, the shot noise contributions in the phase quadrature related to losses as well as the broadband spin noise from the spins, effectively treating the broadband noise as simply an elevated noise level.

The second line of Eq. (10.17b) contains the uncorrelated noise sources reaching the detector, respectively the thermal noises and the QBA arising from the shot noise related to intersystem losses. The thermal forces on the two subsystems are suppressed by the presence of dynamical cooling $\delta\gamma_{\mathrm{j}} > 0$, entering through the susceptibilities χ_j. Further, the spin thermal response is filtered by the mechanical response, expressed in the term $\chi_{\mathrm{m}}/\chi_{\mathrm{ms}}$, with the cross-susceptibility

$$\chi_{\mathrm{ms}}^{-1}(\Omega) \equiv \chi_{\mathrm{mo}}^{-1}(\Omega) - 2\mathrm{i}\zeta_{\mathrm{s}}\Gamma_{\mathrm{m}}. \tag{10.18}$$

This non-local suppression of the spin thermal noise dynamically cools the EPR variables, improving the system performance. The effect is related to OMIT, and internally in QUANTOP sometimes referred to as "OMIT cooling".

The first line of Eq. (10.17b) contains the correlated contributions to our signal. This is the quantum back-action contribution, and as we see they can interfere. By rewriting the bracketed term as

$$\frac{\chi_{\mathrm{m}}\chi_{\mathrm{s}}}{\chi_{\mathrm{mo}}\chi_{\mathrm{so}}}\left[\Gamma_{\mathrm{m}}\chi_{\mathrm{mo}} + \Gamma_{\mathrm{s}}\chi_{\mathrm{so}}\right], \tag{10.19}$$

highlighting the requirements for total destructive interference of the QBA: $\Gamma_{\mathrm{m}}\chi_{\mathrm{m}} + \Gamma_{\mathrm{s}}\chi_{\mathrm{so}} = 0$, or, in other words

$$\omega_{\mathrm{m}} \stackrel{!}{=} -\omega_{\mathrm{s}}, \qquad \gamma_{\mathrm{mo}} \stackrel{!}{=} \gamma_{\mathrm{so}} \qquad \text{and} \qquad \Gamma_{\mathrm{m}} \stackrel{!}{=} \Gamma_{\mathrm{s}}. \tag{10.20}$$

Curiously, total backaction evasion of the spin does not require unity transmission between the two system – whatever spin response reaches the mechanics can be cancelled. However, uncorrelated shot noise does leak in, driving the mechanics, leading to uncorrelated mechanical backaction.

Our systems obviously do not meet the criteria in Eq. (10.20). It is, however, still possible to obtain significant quantum backaction evasion; the noise evasion is maximized for $\omega_{\mathrm{m}} = -\omega_{\mathrm{s}}$, even for unmatched intrinsic linewidths, $\gamma_{\mathrm{mo}} \neq \gamma_{\mathrm{so}}$. The form of the QBA interference term, as written in 10.17b may be understood as follows: the spin system produces amplitude squeezed fluctuations $\hat{X}_{\mathrm{L,s}}^{\mathrm{out}} \sim (\chi_{\mathrm{S}}/\chi_{\mathrm{so}})\hat{X}_{\mathrm{L,s}}^{\mathrm{in}}$. These amplitude fluctuations drive the mechanical system, which maps them into the phase quadrature response according to $\Gamma_{\mathrm{m}}\chi_{\mathrm{m}}$, Second, the spin QBA response $\hat{P}_{\mathrm{L,s}}^{\mathrm{out}} \sim \Gamma_{\mathrm{s}}\chi_{\mathrm{s}}\hat{X}_{\mathrm{L,s}}^{\mathrm{in}}$ is subsequently filtered by the mechanical system according to $\chi_{\mathrm{m}}/\chi_{\mathrm{mo}}$.

An important feature of this effects is that the functions χ_j/χ_{j0} suppresses near-resonant spectral components in a bandwidth γ_j with maximal suppression γ_{j0}/γ_j at $\Omega \sim \omega_j$ (for $\delta\gamma_j > 0$). The mechanical noise is reduced by the amplitude squeezing produced by the spins, and the spin response is filtered in an OMIT-like effect. Since $\gamma_{\mathrm{mo}}/\gamma_{\mathrm{m}} \ll 1$, the spin QBA response is very strongly suppressed, whereas the amplitude squeezing by the spin is more moderate $\gamma_{\mathrm{so}}/\gamma_{\mathrm{s}} \approx 0.6$, leading to only a slight reduction of the mechanical noise.

10.2.2 Matrix Formulation

The equations (5.43), (10.13), and (10.15) fully describe the system dynamics, except for one important factor: all the noise operators are, by definition, zero mean stochastic variables. This means that naively propagating these input operators through the equations, one finds (to no big surprise, hopefully) that all output variables also have zero mean. Luckily, we are (mostly) not after trajectories (the first moments of the operators), but after fluctuations (second moments), expressed as power and cross spectral densities. Further, the equations are bulky and somewhat hard to work with. We proceed, in hopes of finding a way of transforming our equations into a form, where we can use them to fit our experimental data, and quantify the correlations among the various constituents .

We note that the equations are all linear in the input noise operators, which means that the entire system may be described by a single rectangular matrix $\boldsymbol{U}$, connecting these input noise operators to the output operators of interest, as

$$\boldsymbol{Q}_{\text{out}} = \boldsymbol{U}\boldsymbol{Q}_{\text{in}}, \tag{10.21}$$

where the inputs are all the relevant noise operators,

$$\boldsymbol{Q}_{\text{in}} \equiv (\hat{f}_{\text{s}}^{X}, \hat{f}_{\text{s}}^{P}, \hat{f}_{\text{m}}, \hat{X}_{\text{L,s}}^{\text{in}}, \hat{P}_{\text{L,s}}^{\text{in}}, \hat{X}_{\text{L},\nu}^{\text{in}}, \hat{P}_{\text{L},\nu}^{\text{in}}, \hat{X}_{\text{L,ex}}^{\text{in}}, \hat{P}_{\text{L,ex}}^{\text{in}}, \hat{X}_{\text{L},\eta}^{\text{in}}, \hat{P}_{\text{L},\eta}^{\text{in}})^{\intercal}, \tag{10.22}$$

and the outputs are the operators of interest to us[6], namely

$$\boldsymbol{Q}_{\text{out}} \equiv (\hat{X}_{\text{m}}, \hat{P}_{\text{m}}, \hat{X}_{\text{s}}, \hat{P}_{\text{s}}, \hat{P}_{\text{L}}^{\text{meas}})^{\intercal}. \tag{10.23}$$

(6) In principle, having access to $\hat{X}_{\text{L}}^{\text{meas}}$ would also be nice, but alas, we can only measure a single quadrature with our homodyne setup.

From the input vector we calculate the symmetrized power (and cross) spectral densities, as

$$\bar{S}_{\text{in}}\delta(\Omega - \Omega') = \frac{1}{2}\left\langle \boldsymbol{Q}_{\text{in}}^{\dagger}(\Omega)[\boldsymbol{Q}_{\text{in}}(\Omega')]^{\intercal} + \boldsymbol{Q}_{\text{in}}(\Omega)[\boldsymbol{Q}_{\text{in}}^{\dagger}(\Omega')]^{\intercal} \right\rangle, \tag{10.24}$$

where $[\cdot]^{\intercal}$ signifies a row-vector, while $\dagger$ indicates Hermitian conjugation of the individual vector elements, not the vector as a whole. For the input noise operators here, $\bar{\text{S}}_{\text{in}}$ is a square matrix with diagonal entries

$$\begin{aligned}\text{diag}(\bar{S}_{\text{in}}) = \Bigg(&\overline{S}_{\hat{f}_{\text{s}}^{X}\hat{f}_{\text{s}}^{X}}, \overline{S}_{\hat{f}_{\text{s}}^{P}\hat{f}_{\text{s}}^{P}}, \overline{S}_{\hat{f}_{\text{m}}\hat{f}_{\text{m}}}, \overline{S}_{X_{\text{L}}X_{\text{L}}}, \overline{S}_{P_{\text{L}}P_{\text{L}}}, \overline{S}_{X_{\text{L}}X_{\text{L}}}, \overline{S}_{P_{\text{L}}P_{\text{L}}} + \frac{\nu}{1-\nu}\overline{S}_{\text{s,bb}}, \\ &\overline{S}_{X_{\text{L}}X_{\text{L}}}, \overline{S}_{P_{\text{L}}P_{\text{L}}}, \overline{S}_{X_{\text{L}}X_{\text{L}}}, \overline{S}_{P_{\text{L}}P_{\text{L}}}\Bigg),\end{aligned} \tag{10.25}$$

and all other elements equal to zero. That is, all off-diagonal elements, the cross spectral densities, are zero, and thus all noise operators are uncorrelated. All light noise operators represent vacuum, and therefore have their indices suppressed for brevity. The first three terms represent the thermal Langevin forces on the spins and mechanics, respectively, and are given by

$$\overline{S}_{\hat{f}_{\text{s}}^{X}\hat{f}_{\text{s}}^{X}}(\Omega)\delta(\Omega - \Omega') \equiv \frac{1}{2}\left\langle \hat{f}_{\text{s}}^{X,\dagger}(\Omega)\hat{f}_{\text{s}}^{X}(\Omega') + \hat{f}_{\text{s}}^{X}(\Omega')\hat{f}_{\text{s}}^{X,\dagger}(\Omega)\right\rangle = \gamma_{\text{so}}(n_{\text{s}} + 1/2)\delta(\Omega - \Omega') \tag{10.26a}$$

$$\overline{S}_{\hat{f}_{\text{s}}^{P}\hat{f}_{\text{s}}^{P}}(\Omega)\delta(\Omega - \Omega') \equiv \frac{1}{2}\left\langle \hat{f}_{\text{s}}^{P,\dagger}(\Omega)\hat{f}_{\text{s}}^{P}(\Omega') + \hat{f}_{\text{s}}^{P}(\Omega')\hat{f}_{\text{s}}^{P,\dagger}(\Omega)\right\rangle = \gamma_{\text{so}}(n_{\text{s}} + 1/2)\delta(\Omega - \Omega') \tag{10.26b}$$

$$\overline{S}_{\hat{f}_{\text{m}}\hat{f}_{\text{m}}}(\Omega)\delta(\Omega - \Omega') \equiv \frac{1}{2}\left\langle \hat{f}_{\text{m}}^{\dagger}(\Omega)\hat{f}_{\text{m}}(\Omega') + \hat{f}_{\text{m}}(\Omega')\hat{f}_{\text{m}}^{\dagger}(\Omega)\right\rangle = 2\gamma_{\text{mo}}(n_{\text{m}} + 1/2)\delta(\Omega - \Omega'), \tag{10.26c}$$

while the rest of the operators represent light shot noise, except for the term involving $\overline{S}_{\text{s,bb}}$, which includes the broadband atomic noise (scaled by the intersystem losses) as an extra noise term. We include the broadband response here mostly out of convenience. At first look the scaling factor $\nu/(1-\nu)$ can look odd, as it divergres for $\nu \to 1$; however, in the model the broadband noise is injected in a port with weight $\sqrt{1-\nu}$ (for the field), while the true weight should have been $\sqrt{\nu}$. We therefore need to multiply the noise PSF by ν and divide by $(1-\nu)$.

Once $\boldsymbol{U}$ has been found and $\overline{\boldsymbol{S}}_{\text{in}}$ specified, we may find the power and cross spectral densities of the output operators as

$$\overline{\boldsymbol{S}}_{\text{out}} = \boldsymbol{U}^{\dagger}\overline{\boldsymbol{S}}_{\text{in}}\boldsymbol{U}, \tag{10.27}$$

where the $(\cdot)^{\dagger}$ now is taken to be the conjugate transposed matrix. $\overline{\boldsymbol{S}}_{\text{out}}$ is a 5×5 matrix, with each entry containing the cross or power spectral density of two given operators, for example the $(1,1)$ element contains the power spectral density of the mechanical oscillator position, $\overline{S}_{X_{\text{m}}X_{\text{m}}}$, and the $(2,5)$ element contains the cross spectral density between the mechanical oscillator momentum and the phase quadrature of the measurement light, $\overline{S}_{P_{\text{m}}P_{\text{L}}^{\text{meas}}}$.

Defining the sub-matrix $\overline{\boldsymbol{S}}_{\text{ms}}$ as the first four rows and columns of $\overline{\boldsymbol{S}}_{\text{out}}$, allows us to define the steady state *unconditional covariance matrix*

$$\boldsymbol{V}_{\text{u}} = \int_{-\infty}^{\infty} \overline{\boldsymbol{S}}_{\text{ms}}(\Omega)\,\frac{\mathrm{d}\Omega}{2\pi}, \tag{10.28}$$

where the elements are the (co)variances of the operators in the order defined in $\boldsymbol{Q}_{\text{out}}$. For example, element $(2,4)$ is the covariance between the mechanical momentum and the spin momentum in the steady state, and the $(3,3)$ element is the variance of the spin position $\hat{X}_{\text{s}}$.

With these variances, one can compute the EPR variance – as it turns out, the unconditional variance of the EPR variables is significantly above the entanglement bound, and we must employ filtering of the collected data to get the variance of the state below the entanglement bound.

While filtering is absolutely a necessity for our setup, there is in principle nothing preventing another physical system from displaying unconditional EPR variance below the entanglement bound. In a sense, with such a system, the experimenter turns on the experiment, and is guaranteed to have an entangled state. We need to work a little harder, by actually using the measurement data to know the state well enough. This will be the subject of Section 10.4.

This was a rather long section, so perhaps a short summary is in order. In this section we derived the full input-output relations for the hybrid system, using the results from Chapter 3 and Chapter 5. Cascading these expressions, together with intersystem losses and rotations, led to a model with all relevant physics included. This model was simplified, and a number of important effects of the hybrid system were discussed, including QBA evasion and the coherent suppression of thermal noise in the two systems. Finally, we expressed the entire dynamics in a matrix formulation, which allowed us to compactly describe power spectral densities of the system operators, given a set of input noise operators, and define the unconditional covariance matrix.

10.3 Quantum Backaction Evasion

With the full model of our system in place, we are armed to tackle the experimental data. We turn first to the *quantum back-action (evasion)* (QBA(E)) effects observed in our system.

In Fig. 10.3a we plot the PSD of the mechanics and spins for a situation where the spin frequency has been increased to $|\omega_s| \sim 1.48\,\mathrm{MHz}$, and the two systems thus spectrally separated, apart from the broadband atomic noise, $\bar{S}_{bb}$, which shows up as an elevated noise floor for both systems, included in the measurement noise. We note that the spin response is for practical purposes unchanged for this $\sim 10\,\%$ change of the resonance frequency except for the trivial shift. The data (orange) has been fit to the full hybrid model (blue), which is then used to decompose the measured spectra into the different components contributing to the total signal, the two thermal noises, the broadband noise, QBA and measurement noise, which includes shot noise and the broadband atomic noise.

Each system is effectively a Lorentzian response, $\propto |\chi_j|^2$, dynamically broadened by the light. For each system, the ratio of QBA to thermal noise TH can be evaluated. For the spin system the ratio $(\mathrm{QBA}/\mathrm{TH})_s = 4.9$, and for the mechanical system $(\mathrm{QBA}/\mathrm{TH})_m = 19$.

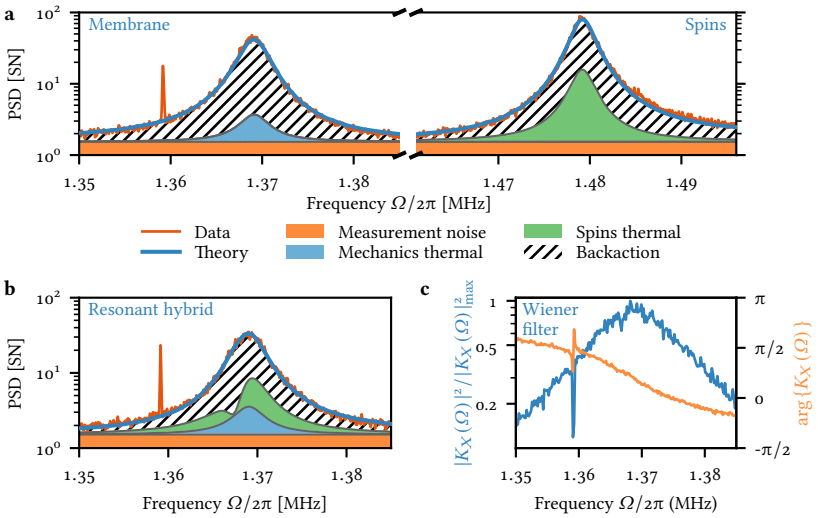

Figure 10.3: Optical phase quadrature power spectral densities for measurement of mechanics and detuned spins (panel **a** left and right) and hybrid (**b**), in units of shot noise (SN). The individual system responses can be seen in panel **a**, with the QBA (hatched area) and thermal contributions (solid blue and green). For the hybrid EPR system, the QBA is reduced, and the thermal forces filtered by the susceptibilities of the other system, as discussed in Section 10.2. The narrow peak at 1.359 MHz is a laser phase noise peak. Note the logaritmic y-axis. Panel **c** depicts the Wiener filter, discussed in Section 10.4, for the resonant case.

In panel Fig. 10.3b the spins are tuned close to resonance with the mechanics, $-\omega_s \approx \omega_m$, by adjusting the magnetic field. Here we observe several effects described in the previous section. First, the overall noise is reduced significantly, compared to a naïve addition of the noise peaks in Fig. 10.3a; in fact, it is even re-

duced below that of the mechanical system alone. This is due, first of all, to the destructive interference (or evasion) of the QBA, and secondly to the dynamical non-local cooling discussed in the previous section. We see how the spin thermal response is very heavily filtered by the mechanics, whereas the reduction of the mechanical thermal noise is much more modest. The slight asymmetry in the hybrid response is due to the small, but non-zero spin-mechanics detuning and the choice of LO_2 phase φ.

The QBA is reduced by 4.6 dB compared to the sum of QBA of the two detuned systems – this should be compared to the results in Møller et al. (2017), which reported a maximum of 1.8 dB of suppression of the QBA noise *compared to the mechanics alone*; with this metric, we observe a QBA reduction of approximately 45 % or 2.6 dB. The thermal noises in the resonant case is reduced by 2.5 dB compared to the sum of individual noises. These two reductions together lead to a reduction of the unconditional variance, defined in Eq. (10.28), of the EPR system by 5.0 dB from 6.07 to 1.91. This is still well above the entanglement bound of 1.

In Fig. 10.4, the spin system is scanned across the mechanical resonance, and the total noise spectrum is recorded for each spin frequency. For $|\omega_\text{s}| < \omega_\text{m}$ (bottom panels), we observe a decrease in noise, i. e., QBAE, on the mechanical resonance. In the bottom panels we see two distinct peaks, with a distinct peak at the spin resonance and one at the mechanical resonance. As $|\omega_\text{s}|$ is increased, the two modes join together to form a single peak, with total noise below that of the mechanics alone (black lines). As we increase it further, the noise level rises above that of the mechanics alone, while still being much lower than the sum of the two peaks, before finally becoming two separate peaks again for the top panel. Note that the top two panels vertical axes are changed by a factor 2.

10.4 Wiener Filtering

In this section I will discuss the Wiener filtering procedure used to extract a *conditional estimate* of the EPR state, as well as the variance of the said estimate.

10.4.1 Wiener Filtering 101

In our experiments we measure $\hat{P}_\text{L}^\text{meas}(t)$, which is turned into a photocurrent $i(t)$. The basic task is to find a filter $K(\tau)$, which optimally estimates the desired quantity, e. g., $\hat{X}_\text{EPR}$ from the measurement record $i(t)$. Since the estimate depends on the data, it is a *conditional* estimate, and it arises from the convolution of the data and filter as

$$X_\text{EPR}^\text{c}(t) = \int_0^t K_X(t' - t; t) i(t') \, \mathrm{d}t', \tag{10.29}$$

where the second argument of $K_X(\tau; t)$ denotes that the filter is optimized for a finite data record of length t, which is also in this case the time we wish to estimate the position. Determining the filter requires detailed knowledge of the systems equations of motion under probing as well as the noise characteristics. By a stroke of luck, the equations of motion are exactly what we derived in the previous section, and the noise is also a well known property of our system, so we continue.

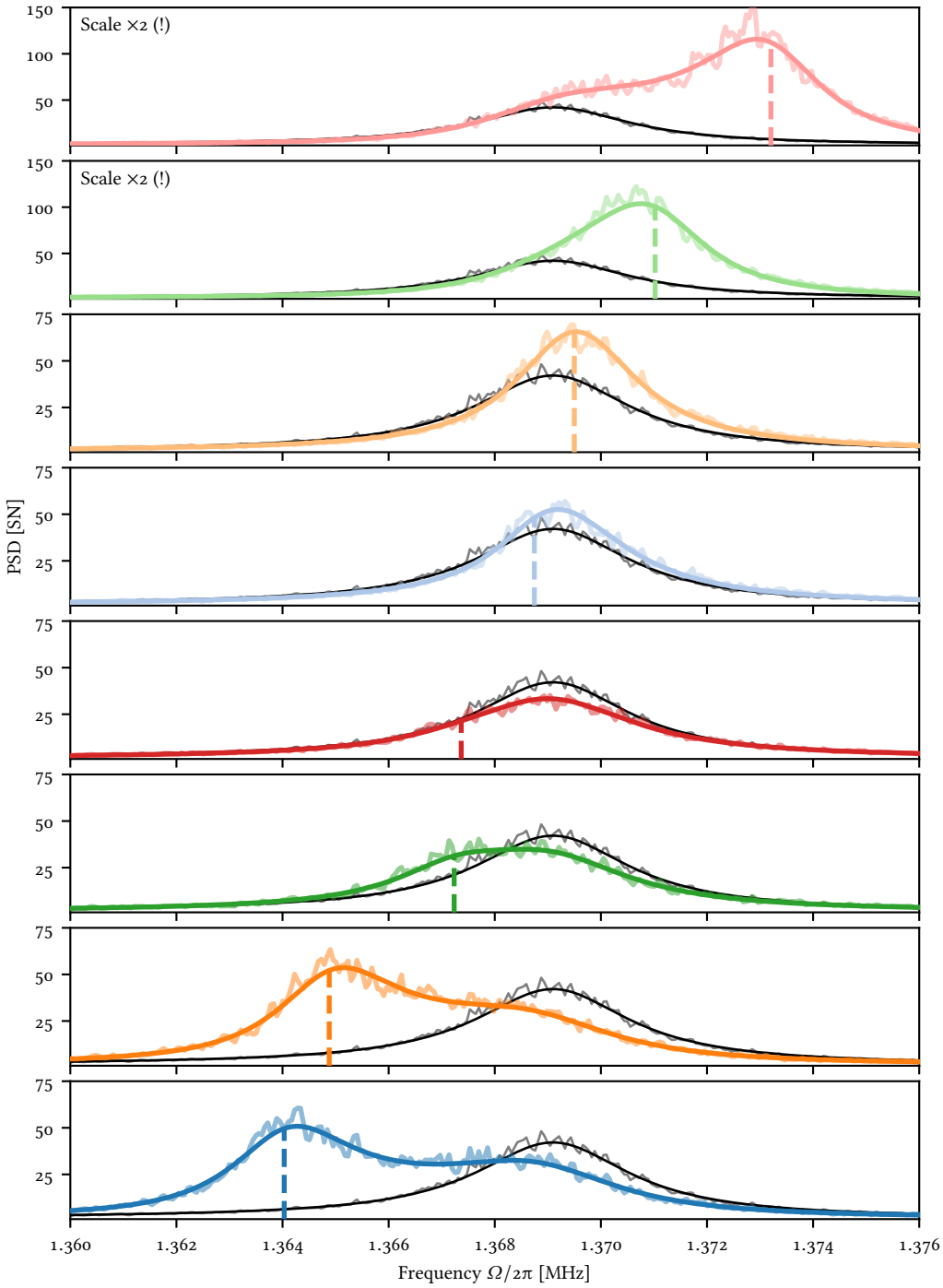

Figure 10.4: QBAE as the Larmor frequency is scanned through the mechanical resonance. Note that the two top panels have a different y-axis scale. Dashed vertical lines indicate the spin Larmor frequency. Black lines show the mechanics-only spectrum. Note: linear scale.

The applicability of such a filtering technique to quantum systems is however not obvious. For Gaussian quantum states, and weak, continuous probing with effective interactions linear in the involved operators, Müller-Ebhardt et al. (2009)[7] and Miao (2010)[8] proved the applicability of classical filtering theory. Our optical probe $\hat{P}_{\mathrm{L}}^{\mathrm{meas}}(t)$ and any given observable of our system $\hat{Y}(t)$, with $\hat{Y}$ denoting for example $\hat{X}_{\mathrm{m}}$ or $\hat{P}_{\mathrm{s}}$, together possess two "classical" properties. As summarised in Müller-Ebhardt et al. (2009)

1. the output optical fields at different times t and t' are individually measurable to arbitrary precision, without inducing any fundamental limits, leading to

$$[\hat{P}_{\mathrm{L}}^{\mathrm{meas}}(t), \hat{P}_{\mathrm{L}}^{\mathrm{meas}}(t')] = 0 \; \forall t \neq t' \tag{10.30}$$

2. the measurement output at the present time does not respond to future changes in system observables, i. e.,

$$[\hat{Y}(t), \hat{P}_{\mathrm{L}}^{\mathrm{meas}}(t')] = 0 \; \forall t > t' \tag{10.31}$$

With the properties, the only manifestation of quantum mechanics in our detection system is that it enforces the presence of amplitude and phase quantum noise in the light. Since the origin of the noise is immaterial to the Wiener filter, the approach is applicable to our Gaussian quantum systems.

As a preparation for the filter itself, we introduce the power spectral density of the measurement current, which with the correct normalization is defined as

$$\overline{S}_{ii} = \overline{S}_{P_{\mathrm{L}}^{\mathrm{meas}} P_{\mathrm{L}}^{\mathrm{meas}}}. \tag{10.32}$$

With this definition, the cross spectral density $\overline{S}_{Q,i}$, describing the correlation between the photocurrent and the system operators, is given by the first four elements in the last row of $\overline{S}_{\mathrm{out}}$. Finally, we note that any given spectral density can be converted into time domain correlation functions $\overline{C}(\tau)$, by virtue of the Wiener-Khinchin theorem (see Eq. (3.16)) and the inverse Fourier transform,

$$\overline{C}_{ab}(\tau) = \mathcal{F}^{-1}\left\{\overline{S}_{ab}(\Omega)\right\}(\tau) = \int_{-\infty}^{\infty} \overline{S}_{ab}(\Omega) \mathrm{e}^{\mathrm{i}\Omega\tau} \, \frac{\mathrm{d}\Omega}{2\pi}, \tag{10.33}$$

with a and b labeling two relevant operators.

Our system is driven solely by optical and thermal forces with wide-sense stationary noise statistics, i. e., both first and second moments of all noises are constant, and all covariances depending only on the time difference, $\tau = t - t'$ (Broersen 2006). Therefore, the appropriate *set* of causal filters $\boldsymbol{K}$ for estimating the systems first and second moments is the so-called *Wiener filter* (Wiener 1964). Convolving the filter with the measurement current yields the best unbiased estimate of the system variables, i. e., the estimate with the minimum mean-square error. In vectorized form, and for data going back infinitely far, this then reads

$$\boldsymbol{Q}_{\infty}^{\mathrm{c}}(t) = \int_{-\infty}^{t} \boldsymbol{K}(t' - t) i(t') \, \mathrm{d}t', \tag{10.34}$$

(7) Helge Müller-Ebhardt et al. (2009). "Quantum-state preparation and macroscopic entanglement in gravitational-wave detectors". In: *Phys. Rev. A* 80 (4), p. 043802.

(8) Haixing Miao (2010). "Exploring Macroscopic Quantum Mechanics in Optomechanical Devices". Ph.D. thesis. University of Western Australia.

where $\boldsymbol{Q}^{\mathrm{c}} = (X_{\mathrm{m}}^{\mathrm{c}}, P_{\mathrm{m}}^{\mathrm{c}}, X_{\mathrm{s}}^{\mathrm{c}}, P_{\mathrm{s}}^{\mathrm{c}})^{\intercal}$ is the conditional trajectory; in other words, it is our best estimate of the positions and momenta *given* (conditioned on) our data $i(t)$ and knowledge of the systems dynamics, which is reflected in the filters.

For a finite length of data, the optimal filter may take a different form than simply truncating the infinite time filter, and (as indicated in Eq. (10.29)) therefore takes the data acquisition time as a meta-parameter,

$$\boldsymbol{Q}^{\mathrm{c}} = \int_{0}^{t} \boldsymbol{K}(t' - t; t) i(t') \, \mathrm{d}t'. \tag{10.35}$$

10.4.2 Finding the Wiener Filter

Having described how filtering works, we turn our attention to actually finding the optimal filter. This is done by solving the Wiener–Hopf equations, which state that the optimal conditional estimates, $\boldsymbol{Q}^{c}(t)$, must obey

$$\bar{C}_{\boldsymbol{Q}^{\mathrm{c}} i}(t') = \bar{C}_{\boldsymbol{Q}i}(t'), \tag{10.36}$$

for all t' within the conditioning window. In words, this equation states that the cross-correlation of the best conditional estimates and the measurement current must equal the cross-correlation between the theoretically calculated quadratures and the measurement current. The right hand term, $\bar{C}_{\boldsymbol{Q}i}(t)$, the inverse Fourier transform of $\overline{S}_{\boldsymbol{Q}i}$, contains the theoretical description of the system, while the left hand term contains the filters, that define $\boldsymbol{Q}^{\mathrm{c}}$, and the cross-correlation with the measurement current.

For infinite conditioning time, the Wiener–Hopf equation, Eq. (10.36), can be stated as

$$\int_{0}^{\infty} \boldsymbol{K}^{\intercal}(-t'') \bar{C}_{ii}(t' - t'') \, \mathrm{d}t'' = \bar{C}_{\boldsymbol{Q}i}(t') \quad \forall \, t' \geq 0, \tag{10.37}$$

where the vector notation should be understood as a set of equations, one for each variable in $\boldsymbol{Q}$ (for us, 4); the transpose on the left hand side is arbitrary – one might just as well have transposed the entire right hand side. Note that the time integral goes to positive infinite time from 0, which is compensated for by the minus sign in the filter argument. In words, this states the the cross-correlation of $\boldsymbol{Q}^{\mathrm{c}}$ and $i(t)$ may be found by convolving the filter $\boldsymbol{K}$ with the autocorrelation of i, $\bar{C}_{ii}$, and that the optimal filter fulfills the Wiener–Hopf equation, Eq. (10.36)

For a finite amount of data, with length t, the integral is limited to the interval $t'' \in [0, t]$, and the filter shape now depends explicitly on t,

$$\int_{0}^{t} \boldsymbol{K}^{\intercal}(-t''; t) \bar{C}_{ii}(t' - t'') \, \mathrm{d}t'' = \bar{C}_{\boldsymbol{Q}i}(t') \quad \forall \, t' \in [0, t]. \tag{10.38}$$

In this form and for finite time, the Wiener–Hopf equation can also be easily discretised and cast in a matrix equation form. The optimal filter is then found via the Levinson–Durbin recursion algorithm. Note that in the finite-time limit, the

Wiener filter $\boldsymbol{K}(t';t)$ is only defined for $-t < t' < 0$, in accordance with the integration domain in Eq. (10.35).

Discretizing the Wiener–Hopf equation is discussed in more detail in Rodrigo A. Thomas (2020, chapter 11.5.3). The short version is that, knowing that the autocorrelations are symmetric around 0, $C(\tau) = C(-\tau)$, we can discretize the acquisition time t into N equally sized time steps Δt, and express a single equation from Eq. (10.38) for the variable Q as

$$\sum_{i=0}^{N-1} C_{ii}(t_n - t_i) K_Q(-t_i; t)\Delta t = C_{Qi}(t_n). \tag{10.39}$$

where t_n takes the role of t' and t_i the role of t''. This can be written for all t_n (but still for a single variable Q) as a matrix product

$$\bar{C}_{ii} K_Q \Delta t = \bar{C}_{Qi}, \tag{10.40}$$

or less compactly

$$\begin{pmatrix} C_{ii}(t_0) & C_{ii}(t_1) & C_{ii}(t_2) & \cdots & C_{ii}(t_{N-1}) \\ C_{ii}(t_1) & C_{ii}(t_0) & C_{ii}(t_1) & \cdots & C_{ii}(t_{N-2}) \\ C_{ii}(t_2) & C_{ii}(t_1) & C_{ii}(t_0) & \cdots & C_{ii}(t_{N-3}) \\ \vdots & \vdots & \vdots & \ddots & \vdots \\ C_{ii}(t_{N-1}) & C_{ii}(t_{N-2}) & C_{ii}(t_{N-3}) & \cdots & C_{ii}(t_0) \end{pmatrix} \begin{pmatrix} K_Q(t_0) \\ K_Q(t_1) \\ K_Q(t_2) \\ \vdots \\ K_Q(t_{N-1}) \end{pmatrix} \Delta t = \begin{pmatrix} C_{Qi}(t_0) \\ C_{Qi}(t_1) \\ C_{Qi}(t_2) \\ \vdots \\ C_{Qi}(t_{N-1}) \end{pmatrix}. \tag{10.41}$$

The Δt can then finally be absorbed into the definition of the discretized filter. As noted in Rodrigo A. Thomas (2020), the matrix $\bar{C}_{ii}$ is a Toeplitz matrix, which means the equation for K can be solved effectively by the Levinson–Durbin algorithm (Durbin 1960)[9].

(9) J. Durbin (1960). "The Fitting of Time-Series Models". In: *Revue de l'Institut International de Statistique / Review of the International Statistical Institute* 28.3, pp. 233–244.

The notation we use here warrants a slight warning. While C_{ii} is a purely *measured* quantity—it is after all just the autocorrelation of the measurement current—C_{Qi} is a purely *calculated* quantity, despite the appearance of the i subscript. It is the predicted autocorrelation of the system variables Q with an ideal, noiseless measurement current i.

10.4.3 Stochastic Trajectories with Deterministic Variance

The trajectories of our systems, and thus our best estimate of said trajectories, $\boldsymbol{Q}^{\mathrm{c}}$, are stochastic. This is however *not* the case for the second moment, the variance, of our estimate. This evolves *deterministically* with the conditioning time, and is given by

$$\boldsymbol{V}_{\mathrm{c}}(t) = \boldsymbol{V}_{\mathrm{u}} - \boldsymbol{V}_{\mathrm{be}}(t), \tag{10.42}$$

with the ensemble covariance matrix of the best estimate given by

$$\boldsymbol{V}_{\mathrm{be}}(t) = \int_0^t \boldsymbol{K}(-t';t)\bar{\boldsymbol{C}}_{Qi}(t')\,\mathrm{d}t' = \mathrm{Cov}\left(\boldsymbol{Q}, \boldsymbol{Q}^{\mathrm{c}}(t)\right), \tag{10.43}$$

which is a 4×4 covariance matrix. In the infinite conditioning time limit, this reduces to the special case

$$\boldsymbol{V}_{\mathrm{be}} = \int_0^\infty \boldsymbol{K}(-t)\bar{\boldsymbol{C}}_{\boldsymbol{Q}i}(t)\,\mathrm{d}t = \mathrm{Cov}\left(\boldsymbol{Q}, \boldsymbol{Q}^{\mathrm{c}}_{\infty}\right). \tag{10.44}$$

$\boldsymbol{V}_{\mathrm{be}}$, for zero conditioning time, $t = 0$, has zeros in all entries, and the conditional variance equals the unconditional. As the conditioning time increases, the ensemble variance of the best estimate increases, thus reducing the conditional variance. To convince oneself of this fact, consider what is the *best*, but not necessarily *good*, estimate for $\boldsymbol{Q}$ with zero conditioning time? Since no data has been obtained, the best estimate must be that of a thermal state, which has zero mean position and momentum. As the conditioning time increases, the different best estimate trajectories spread out in phase space, increasing $\boldsymbol{V}_{\mathrm{be}}$.

It also follows from the relation in Eq. (10.42) that only for *zero* conditional variance does the variance of the best estimate ever reach unconditional variance. This can be understood as the filter being somehow "conservative" in estimating the excursions away from zero; the estimation strategy that minimizes the mean squared error has an ensemble variance that is smaller than the unconditional variance, i. e., the size of the thermal state.

The relation $\boldsymbol{V}_{\mathrm{be}}(t) = \mathrm{Cov}(\boldsymbol{Q}, \boldsymbol{Q}^{\mathrm{c}}(t))$ in Eq. (10.43) follows directly from the Wiener–Hopf equation, Eq. (10.36), by convolving it with $\boldsymbol{K}$.

10.4.4 Optimum EPR Variables

As noted in Eq. (10.6), generalized EPR variables can be constructed to optimize the entanglement. We now explain how we find the optimum combination. The parameter β describes the rotation of the spin variables, cf. Eq. (10.7), while a describes the relative weight of the spin and mechanics.

We write the generalized EPR variables as a vector product of some matrix, $\boldsymbol{u}$, and the vector $\boldsymbol{Q}$. The columns of $\boldsymbol{u}$ are unit-length vectors, and describe the relative weights of the different variables as

$$\hat{X}_{\mathrm{EPR}} = \frac{\hat{X}_{\mathrm{m}} - a\hat{X}'_{\mathrm{m}}}{\sqrt{1+a^2}} = \boldsymbol{u}_X^{\mathsf{T}}\boldsymbol{Q} \tag{10.45}$$

$$\hat{P}_{\mathrm{EPR}} = \frac{\hat{P}_{\mathrm{m}} + a\hat{P}'_{\mathrm{m}}}{\sqrt{1+a^2}} = \boldsymbol{u}_P^{\mathsf{T}}\boldsymbol{Q} \tag{10.46}$$

$$\hat{\boldsymbol{X}}_{\mathrm{EPR}} = \boldsymbol{u}^{\mathsf{T}}\boldsymbol{Q} \tag{10.47}$$

We can now compute an EPR variance (conditional or unconditional) $V = \mathrm{Var}\left[\hat{X}_{\mathrm{EPR}}, \hat{P}_{\mathrm{EPR}}\right]$, with the covariance matrix $\boldsymbol{V}$

$$V_{a,\beta} = \boldsymbol{u}_X^{\mathsf{T}}\boldsymbol{V}\boldsymbol{u}_X + \boldsymbol{u}_P^{\mathsf{T}}\boldsymbol{V}\boldsymbol{u}_P, \tag{10.48}$$

which can be numerically minimized for each spin-mechanics detuning, to obtain the optimal entanglement

$$V_{\mathrm{opt}} = \min_{a,\beta} V_{a,\beta}. \tag{10.49}$$

10.5 Putting the Theory to Work

In Section 10.3 we discussed the QBAE realized experimentally, and showed that the model could successfully be fitted to experimental spectra. Specifically in Fig. 10.3, the detuned spectra of mechanics and spin, as well as their resonant spectrum plus the corresponding Wiener filter was displayed. We now discuss in more detail how these fits were performed, and what we believe we can learn from them.

As noted above, we record spectra of the two systems detuned, and for varying amounts of spin-mechanics detuning (see Fig. 10.4). We fit our complete hybrid model to these spectra *collectively*. Some of the parameters are shared between all traces, while the parameters allowed to change are atomic frequency, LO_1–LO_2 phase, φ, cavity detuning Δ and mechanical coupling rate g. The variation in ω_s should be self-explanatory, while the last three deserve an explanation.

In an ideal setup, LO_1 is stripped completely from the quantum sidebands after interaction with the spin system; in reality a small part of the 350 µW in LO_1 leaks towards the mechanics on the PBS. Fluctuations in the phase φ, which we estimate to be around 3°, thus turn into a fluctuation of the power in LO_2, due to interference of LO_1 and LO_2. Since we lock our cavity in transmission using a simple dither lock, changes in power lead directly to changes in detuning, Δ, and coupling rate, g.

The fit result (discussed in more detail below), thus returns a full set of parameters describing the complete hybrid system. For the near-resonant case, the model is displayed in Fig. 10.5 – this is the same spectra as Fig. 10.3b, but over a wider range. The wider range also displays the colored (non-flat) spectral features in and outside of our mechanical bandgap. These noise peaks are what we seek to reject with our filters.

With the model, the photocurrent and optimized parameters from the fits, we compute the photocurrent autocorrelation $\bar{C}_{ii}$ and the system-photocurrent crosscorrelation C_{Qi}, which allows us to compute the Wiener filters K_Q. The (frequency space) Wiener filter for the resonant case is displayed in the bottom panel of Fig. 10.5. We here see how the filter rejects colored noise peaks in the measured spectrum. Noticeably, the filter bandwidth is much wider than the system linewidths, scaling with the readout rates, Γ_j.

In the spectrum we see a host of things that we exclude from our state estimation. Most prominent are the membrane modes outside of the bandgap, i. e., below ~1.3 MHz and above ~1.53 MHz. In the bandgap we observe a wide peak, related to the mechanical mode of one of the end mirrors, as well as the four mechanical peaks corresponding to the four other modes introduced in Chapter 4. Two of these are virtually uncoupled, and are treated simply as noise, while the two modes with highest frequencies are included in the full model, because of their considerable optomechanical coupling. For the case where the spins are detuned far from the mechanical mode, the separation between these modes and the spin mode is only around 2 kHz, so some interference is possible. While they are included in the full model, they are excluded from the filter, leading to the dip in the filter at around 1.51 MHz.

The full model fit also allows us to calculate the unconditional variance $\boldsymbol{V}_\text{u}$, cf. Eq. (10.28). This variance is displayed for the near-resonant case in Fig. 10.6**a** and for the detuned systems in Fig. 10.6**e**. Panel **c** displays $\boldsymbol{V}_\text{u}$ for the optimized

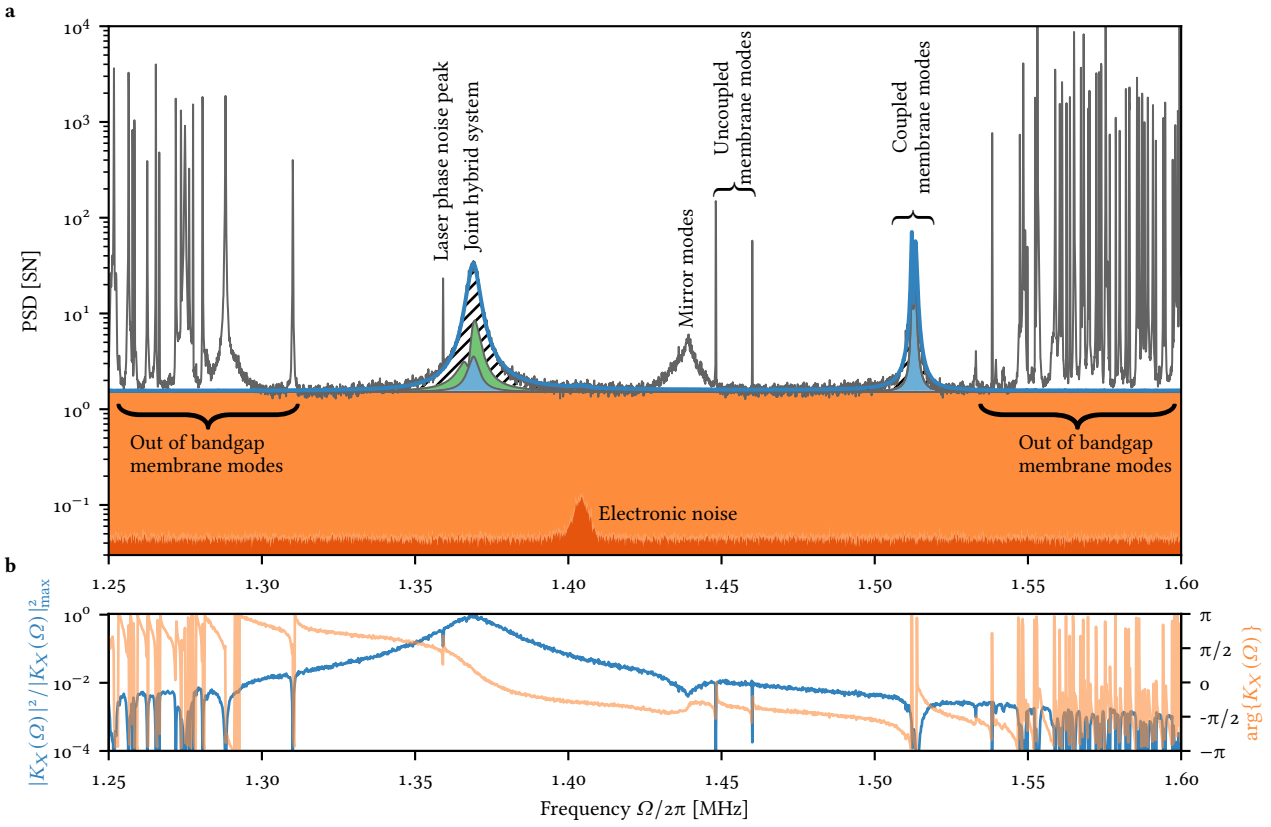

Figure 10.5: Wide range resonant hybrid spectrum and Wiener filter. Top panel (**a**) shows the near-resonant hybrid spectrum from Fig. 10.3(**b**). The spectrum is broken into electronic noise (dark orange), measurement noise (shot noise and broadband atomic noise), hybrid model (blue line) with contributions from quantum back-action (hatched area) and spin and mechanical thermal noise (green and blue areas). The mechanical modes at $\omega_m/2\pi \sim 1.52\,\text{MHz}$ are included into the model, due to an appreciable optomechanical coupling and back-action for these modes. The grey line shows the measured phase quadrature power spectral density in units of shot noise (SN). Bottom panel (**b**) shows the normalized Wiener filter amplitude (blue) and phase (orange), which most successfully rejects the noise peaks not accounted for in the model, i. e., out of bandgap modes, mirror modes, laser phase noise, and the other mechanical modes in the bandgap (including the coupled modes included in the model fit). Note that the Wiener filter bandwidth is significantly higher than the hybrid system linewidth.

choice of EPR basis for the near-resonant case.

For the separate systems-basis ($\{ X_\mathrm{m}, P_\mathrm{m}, X_\mathrm{s}', P_\mathrm{s}' \}$), the near-resonant case shows unconditional variances of around 4.3 for the two system, with strong correlations between the position and momentum variables of the two systems, e. g., $\mathrm{Cov}(X_\mathrm{m}, X_\mathrm{s}') = 3.40$. Importantly, the positions are positively correlated, while the momenta are *anti-correlated*, as we expect for the simultaneous measurement of a positive and negative mass system.

With the Wiener filter, we can also calculate the variance of the best estimates, $\boldsymbol{V}_\mathrm{be}$, cf. Eq. (10.44), and from there the final conditional variance, using Eq. (10.42). We display $\boldsymbol{V}_\mathrm{c}$ for the near-resonant case in Fig. 10.6**b**. Comparing to the unconditional case, we see that the mechanical variance is reduced slightly, while the atomic variances and the covariances remain mostly unchanged. The anti-diagonal, however, is zero—this is ensured by our choice of β, which for the non-EPR basis is arbitrary. The unchanged covariances and spin variance tell us that the filter is not able to separate the two systems effectively, when they are resonant.

Comparing to the far detuned case in panels **e** and **f**, we observe first that the initial variances are lower, with almost no covariances between the two systems. However, now the filter can efficiently reduce the variance of both subsystems. $V_\mathrm{c,m} = \mathrm{Var_c}[X_\mathrm{m}] + \mathrm{Var_c}[P_\mathrm{m}] = 1.6$, significantly lower than the unconditional variance of 4.12, but not below the entanglement bound. A similar reduction is seen for the spins.

With the full conditional variance matrix $\boldsymbol{V}_\mathrm{c}$ for the near-resonant case, such as displayed in Fig. 10.6**b**, we can also use the procedure described in Section 10.4.4 to find the choice of EPR variables the minimizes the final conditional variance. For the near-resonant case, the result is shown in Fig. 10.6**c** and **d**. The fitting routine returns the optimum combinations of $\{ a, \beta \}$, which for this detuning is $a \approx 0.85, \beta \approx 20^\circ$. Panel **c** shows an unconditional variance for the EPR variables of 1.92, while the conjugate variables have $V_\mathrm{u} = 15.33$. This shows that the back-action evasion for the EPR variables comes with the expected pile-up of back-action noise in the other combination of variables. While for example the difference of positions can now be known well, much less is known about the sum of positions.

Applying the filter to the EPR basis leads to the covariance matrix in Fig. 10.6**d**. We see here the main result of this thesis: the reduction of the conditional variance of the EPR variables of the hybrid system below the separability criterion,

$$V = 0.83 < 1. \tag{10.50}$$

The obtained filters discussed so far were the (approximately) infinite-time filters. Turning now to the time evolution of the conditional variance as a function of conditioning time, we plot in the right hand panel Fig. 10.7 the evolution of the conditional variance for the EPR variables in the resonant and far-detuned cases respectively. Both start out significantly above 1, but with the resonant case much lower, due to QBAE and non-local cooling. As conditioning time increases, the variances are reduced; detuned case to around 2, and for the resonant case to around $V_\mathrm{c} = 0.83$ for a conditioning time of 110 µs.

In the left hand panel, we plot the slowly varying EPR variables

$$\tilde{\boldsymbol{X}}^\mathrm{c}_\mathrm{EPR} = \boldsymbol{O}_{\omega_\mathrm{sv} t} \boldsymbol{X}^\mathrm{c}_\mathrm{EPR}, \tag{10.51}$$

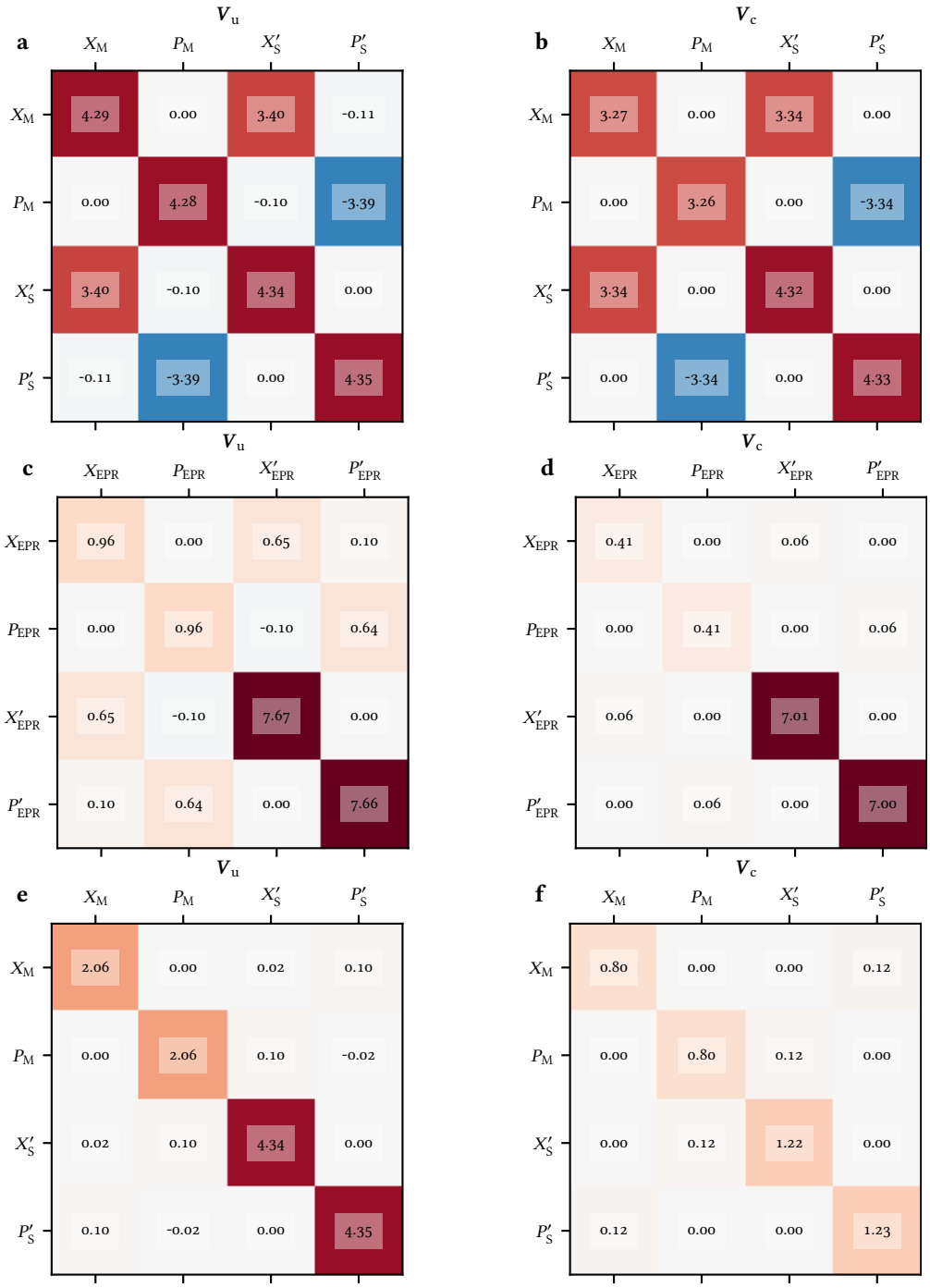

Figure 10.6: Covariance matrices. The left hand column displays unconditional (co)variances, and the right hand column conditional variances. The rows, from top to bottom are for the near-resonant case in the separate-systems basis, the near-resonant case in the EPR basis and finally the original basis for the far-detuned systems.

where we remove the majority of the time evolution, by going to a frame rotating at approximately the system resonances. The choice of the frequency $\omega_{sv}/2\pi = 1.37\,\text{MHz}$ is somewhat arbitrary; for anything but the strictly resonant case, $\omega_m = |\omega_s|$, there is not a single well-defined slowly varying frequency. The example trajectory shown starts out with $\tilde{X}^c_{EPR} = (0,0)^\intercal$, as expected. As time progresses, the system diffuses through phase space. Also shown is the uncertainty of the initial state, $\sqrt{V_u}$ and the conditional uncertainty, $\sqrt{V_c}$ for a conditioning time of $t = 110\,\mu\text{s}$. Also see the stylistic rendering of a larger set of trajectories on 162.

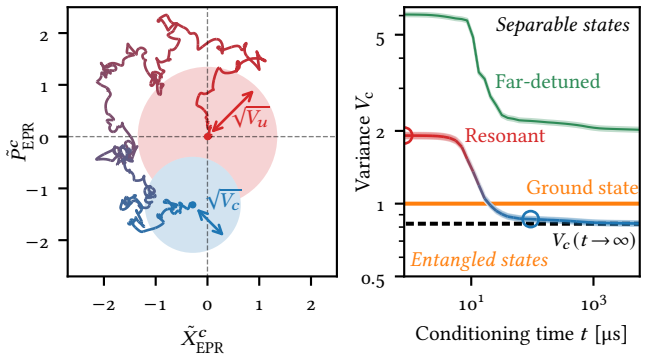

Figure 10.7: EPR trajectory and variance. Left hand panel slows the time evolution of one conditioning run from $t = 0\,\mu\text{s}$ to $t = 110\,\mu\text{s}$, along with the unconditional and conditional uncertainties, $\sqrt{V_{u/c}}$. The right hand panel shows the deterministic time evolution of the conditional variances for the resonant and far detuned cases. As the conditioning time increases, we see a reduction of the conditional variance towards their final values of 0.82 and ~2. The circles show the initial and final variances for the trajectory in the left hand panel. The shaded areas mark the 1σ uncertainty of the conditional variances, discussed below.

10.5.1 Variying the Larmor Frequency

We now turn to an investigation of the entanglement as a function of the spin-mechanics detuning. As explained above, we fit the full hybrid model to a detuning series of spectra simultaneously; while the previous section focused solely on the two cases with near-resonant and far-detuned systems, the full analysis procedure for any other Larmor frequency is virtually identical.

In Fig. 10.8 we plot a subset of these spectra (top panels), as well as the final conditional variances in the bottom panel. The spectra are identical to those shown in Fig. 10.4, but repeated here for a clearer connection between the spectra and final variances. For each detuning, the combination of a and β that minimizes the final V is found; we find that a is approximately constant, while β is approximately 20° for the orange trace, and varies by tens of degrees as ω_s is changed.

We observe robust entanglement over a window more than 10 kHz wide – significantly more than the linewidths of the two systems. This shows, that even though there is a modest overlap of the bare responses, the non-local cooling and QBAE still manages to correlate the systems sufficiently for our detection to mea-

sure the EPR variable with enough precision to prepare the systems in an conditionally entangled state.

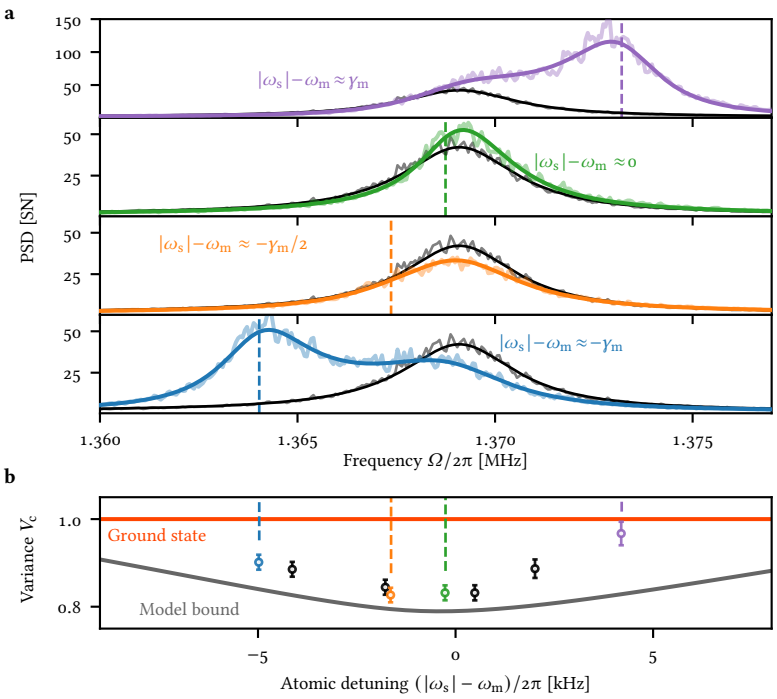

Figure 10.8: Hybrid PSDs and EPR variances for different spin-mechanics detunings. Finite spin-mechanics detuning tunes the distinguishability of the two oscillators, thus reducing the achievable conditional EPR variance. Top panels: hybrid spectra (light colored lines) plus full model fit (dark lines), as well as mechanics-only PSD and fit (grey and black lines respectively). Vertical dashed lines show the spin resonance frequency. Note the different y-axes. Bottom panel: EPR variance with 1σ statistical uncertainties a a function of of spin detuning, $|\omega_s| - \omega_m$. Orange line denotes the ground state variance of a single oscillator system, i. e., the entanglement bound. The dark grey line shows the model bound, i. e., the ideal EPR variance in the absence of experimental noise sources, deduced from the full model with parameters from the orange point. Black points correspond to traces not shown; see Fig. 10.9.

10.5.2 Uncertainties

The claims we have made so far are strong claims, and dependent on an advanced analysis of systems subjected to a set of very strong simplifications. We should therefore also spend some time discussing how certain we are about our conclusions.

To produce the statistical error bars shown in, e. g., Fig. 10.8, we perform Markov Chain Monte Carlo (MCMC) simulations (Foreman-Mackey et al. 2013)[10]. MCMC is a numerical tool for Bayesian inference, evaluating posterior distributions for parameters, given a model and data with uncertainties. More importantly, by

(10) Daniel Foreman-Mackey et al. (2013). "emcee: The MCMC Hammer". In: *Publications of the Astronomical Society of the Pacific* 125.925, pp. 306–312.

evaluating any other function, for example calculating the conditional variance, on the same posterior distribution of the variables, the correct posterior distribution of the variances is also available.

The full model has a large number of parameters; as discussed above many of those are shared across all traces, except for Larmor frequency, the phase φ, cavity detuning Δ and optomechanical coupling g, with the latter three varying due to fluctuations in the LO_1-LO_2 phase, φ. We establish prior estimates for all these parameters, by using the characterization techniques explained in Chapter 3, Chapter 4 and Chapter 5, as well as by other more mundane techniques, such as simply measuring power losses etc.

The majority of the statistical error bars come directly from the variance of the periodogram estimator, discussed in Section 9.3.2. For each detuning we have 200 traces, leading to a relative error bar of $1/\sqrt{200} = 7\,\%$. Further, small uncertainty in the shot-noise (SN) level leads to another percent relative uncertainty. To compensate for the presence of small mirror modes, buried in the shot-noise, we add another 0.1 units of SN, which significantly improves the fits.

We run the MCMC algorithm with 150 walkers for 4000 burn in steps, and 6000 subsequent sampling steps. From these $150 \times 6000 = 900\,000$ points in our N-dimensional parameter space, which together sample the posterior distribution, we randomly select 1000 parameter combinations, for which we compute the entanglement. The choice of the number of samples for entanglement calculation is set by the computational cost of evaluating the conditional variance. Sampling the 1000 points from a larger set of MCMC points reduces the co-variance of the points sampling the posterior log-likelihood landscape.

In general the MCMC results, which are listed in Appendix A, agree well with the priors. The most noteworthy exception is the inter-system quantum efficiency, ν. The posterior value, estimated by measuring trivial power losses, and estimation of the cavity mode matching gave a prior of $\nu_{\text{prior}} = 0.65 \pm 0.03$, while the MCMC returned $\nu = 0.53$ as the optimal value. This excess inter-system loss is unaccounted for, but will only reduce our entanglement. Possible explanations for the discrepancy include an overestimation of the mode matching or polarization-dependent losses for the quantum signal.

Further, we obtain slightly lower posterior detection efficiency $\eta = 0.77$ than the prior, $\eta_{\text{prior}} = 0.80 \pm 0.03$ and higher overcoupling $\kappa_{\text{in}}/\kappa = 0.925 \pm 0.005$ than $\kappa_{\text{in}}/\kappa_{\text{prior}} = 0.91 \pm 0.01$ The atomic parameters are kept reasonably within the prior bounds with $\Gamma_{\text{s,prior}}/2\pi = (18 \pm 1)\,\text{kHz}$ and posterior $\Gamma_{\text{s}}/2\pi = (20.3 \pm 0.4)\,\text{kHz}$ as well as $n_{\text{s,prior}} = 0.72 \pm 0.05$ and posterior $n_{\text{s}} = 0.81 \pm 0.05$.

As stated, we calculate the conditional variance for the different Larmor frequencies 1000 times. The traces and the distribution of calculated V_{c} is shown in Fig. 10.9. All the distributions are reasonably Gaussian, and we therefore feel confident in calculating for each of them a simple mean and standard deviation, which we take as the final uncertainty on the conditional variances. Most notably, the near-resonant trace discussed extensively above, has the final conditional variance of

$$V_{\text{c}} = 0.83 \pm 0.02 < 1, \tag{10.52}$$

which places it squarely below the entanglement limit.

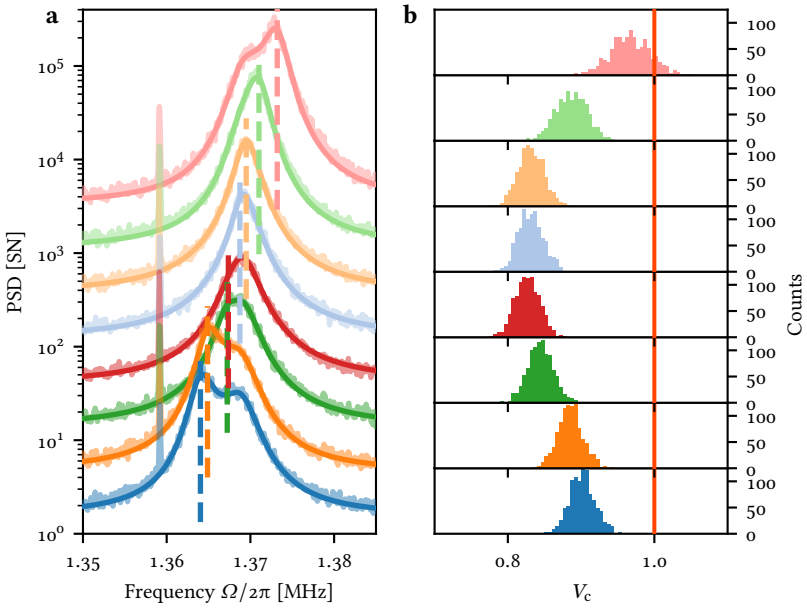

Figure 10.9: Histograms of variances from Monte Carlo simulations. On the left, the traces for different Larmor frequencies, vertically offset for clarity; dashed lined mark the Larmor frequency for each trace. Panel **b**, 1000 conditional variances calculated by sampling the posterior distribution of parameters after MCMC simulation. The distributions are all reasonably Gaussian, allowing us to extract a mean and statistical uncertainty for each V_c, plotted in the bottom panel of Fig. 10.8.

CHAPTER 11

Conclusion & What's Next

> "Harry thought over his collected experimental data. It was only the most crude and preliminary sort of effort, but it was enough to support at least one conclusion: "Aaaaaaargh this doesn't make any sense!"
>
> Harry Potter
>
> - *Harry Potter and the Methods of Rationality,* Eliezer Yudkowsky

A brief summary of the thesis and the results. We put this work and our progress into a wider context, and try to give some idea about where the hybrid experiment in particular is moving.

11.1 Conclusion

In this thesis I have presented our experimental implementation of a hybrid spin–mechanics quantum interface, which allowed us to demonstrate the experimental creation of an entangled Eistein–Podolsky–Rosen state. The work was previously reported in Rodrigo A. Thomas et al. (2020), as well as in the Ph.D. thesis by Rodrigo A. Thomas (2020); whereas the latter focused mostly on the spin system, this thesis has been focused primarily on the optomechanical part of the hybrid system.

In Chapter 1 and Chapter 2, we set the stage for hybrid quantum spin–mechanics experiments, by discussing the motivations and the scientific endeavors in the field, before and concurrently with the Ph.D. project. In Chapter 3 and Chapter 4, the optomechanical subsystem was introduced. In Chapter 5 the atomic spin ensemble was introduced. The needed formalism and theory were detailed, and some practical aspects of implementing good light–matter quantum interfaces were discussed.

Part II concerned the design of a new optomechanical cavity, which allowed us to more easily operate the mechanical system in a hybrid setting; specifically,

by adding electronic tuning of both resonance and $2kz$ position of the membrane, while also facilitating easier alignment. Chapter 6 explained the chosen design for our cavity assembly, Chapter 7 detailed a numerical model informing the design choices, and finally Chapter 8 described the related task of designing new mirrors, for improved optical and mechanical properties.

In the final Part, Part III, the two subsystems were brought together into one hybrid setup, in Chapter 9. With the formalism established for the individual systems in Part I, tying the two together into a full model for the system was presented in Chapter 10. We then experimentally demonstrated first improved QBAE of up to 4.6 dB compared to the QBA for two detuned systems, or 2.6 dB compared to the mechanical system alone – a significant improvement over the 1.8 dB reported in Møller et al. (2017).

After demonstrating improved quantum back-action evasion, we moved on to the main result of the thesis: the successful demonstration of entanglement between the motion of our mechanical resonator and the collective spin of the spin system. Finding an optimal Wiener filter, allowed us to demonstrate the *deterministic* evolution of the conditional variance; demonstrating that this (conditional) variance went below that of a single system ($V < 1$) directly corresponding to demonstrating entanglement. Optimal estimation of the EPR state returned

$$V_c = 0.83 \pm 0.02 < 1. \qquad \text{(10.52 revisited)}$$

This entanglement result reaffirms the roles of room temperature spin ensembles, cavity optomechanics and particularly their combination into a hybrid spin–mechanics system, as viable candidates for implementing practical quantum resources, for example in teleportation based quantum protocols, or for improving measurement sensitivities beyond the standard quantum limits for continuous measurement of motion.

A key aspect of our achievement, is the disparate nature of our two entangled systems; this makes them useful as sensors for different things; the spin senses magnetic field, while the mechanics does not, and the mechanics responds to "classical"[1] forces in a very different manner than the spin.

(1) Meaning here, that it is a solid object which can physically collide with objects; a feature the spin system does not have.

Whereas entanglement has been previously created and shown in a number of different systems, our work marks the first creation of entanglement between separated, disparate material quantum systems, extending the range of systems in the hybrid quantum toolbox.

11.2 The Next Step: Teleportation

(2) I. e., after the publication of the entanglement results.

The current endeavours[2] in the hybrid experiment is aimed towards using the established EPR link to perform teleportation from one system to the other. To motivate why this particular avenue was chosen, we must first discuss a number of shortcomings of the experiment described in this thesis, and possible avenues for remedying these. This section is not exhaustive, and the level of detail will be quite superficial.

11.2.1 Experimental Shortcomings in the Hybrid Setup

The current hybrid experiment, described in (e. g.) Chapter 9 and shown in Fig. 9.7, has several shortcomings, including, but not limited to:

1. Optical losses between the two systems , for which some possible sources are
   a) Suspected bad/distorted optical mode leaving the cell, the severity of which is likely increased by the double pass nature of setup. Mode distortion reduces mode matching to the optomechanical cavity and the homodyning LO
   b) The optical isolator in the beam path, which removes back-reflections from mechanics to spins
   c) Bad polarisation rejection of LO_1 and LO_2
2. Broadband atomic noise, leading to an elevated effective detection noise level
3. Higher than ideal intrinsic decay rate of atoms; Γ_s/γ_{so} is too low, and Γ_s is effectively set by the requirement of matching the membrane Γ_s
4. Bad overcoupling of optomechanical cavity
5. Weird phase rotation effects due to bad LO_1/LO_2 locking

Item 1 is a rather large problem. We currently have intersystem power transmission efficiency of $\nu \sim 55\,\%$ and detection efficiency of $\eta \sim 77\,\%$. In the simple QND model presented in our Rodrigo A. Thomas et al. (2020), detection losses limits the conditional variance V_c (entanglement) to

$$V_c = \frac{1}{\sqrt{\eta}}\sqrt{\frac{1}{2C_q}}. \tag{11.1}$$

This should be compared to the back action-full (single system) conditional variance

$$V_c = \frac{1}{\sqrt{\eta}}\sqrt{1+\frac{1}{2C_q}}. \tag{11.2}$$

The ideal back action evasion thus removes the constant factor under the square root; if we have inter system losses, back-action of the second system cannot be cancelled, as it is driven by a new vacuum. This obviously detrimental effect is something we must try to reduce. As outlined below, this is hard in the setup presented.

Item 2, similarly limiting entanglement, can essentially be only solved by increasing the filling factor of the cell, i.e. how large a fraction of the cell is covered by the interrogating light. Without adding extra losses, this means that there is a finite upper limit to what can be achieved with Gaussian modes of light interrogating the atoms. This thus leads us to pursue probing the atoms with a square top-hat beam[3].

However, because transforming a top hat mode back into a Gaussian, which can coupled efficiently to a cavity mode is, for practical considerations, not possible with an efficiency close to what we need. Therefore the order with which the

(3) Or, alternatively, a round top-hat beam probing a circular cell. We have a square top-hat beam shaper and cells with square channels, so this is the obvious choice for us. Cylindrical cells are simpler in other ways, e.g. analytical treatments.

itinerant light interacts with the systems must be flipped. The self-homodyne detection suggested below (allowed by the strong LO interrogating the spin system) also mitigates the problems related to item 1a, as LO and signal will experience the same distortions.

Item 3 pertains mainly to the choice of the cell and the choice of implementing a double pass or not. The double pass boosts the read out rate Γ_s, but is incompatible with the top hat beam. It also, in the current setup, leads to extra need for isolation and thus losses, cf. 1b, as well as potentially the spurious phase fluctuations, cf. 5.

Item 4 is essentially "just" a matter of new mirrors, discussed in Chapter 8. A further benefit is the anticipated absence of mirror modes in the spectrum, allowing for a wider selection of membranes which can be used. Calculated optical characteristics of the new cavity are shown in Fig. 8.7. The measured mechanical modes of the new mirrors is shown in Fig. 8.8

Item 5 arises from spurious reflections in the atomic double pass arm (we think), and leads to spurious fluctuations of the LO_1-LO_2 phase, ϑ. These fluctuations are rather large, and lead to mixing of squeezed and anti-squeezed quadratures. It is perhaps related to item 1c on the PBS where we split/combine LO_1 and LO_2.

Combining these shortcomings and possible solutions, we decided on the following avenue:

- Flip the order, so the light probes mechanics first and spin last
- Implement a top hat beam for the spin probe, and perform self-homodyning of the light
- Probe the optomechanics in transmission, in a new cavity with mirrors with improved optical and mechanical properties
- Use a larger cell, which reduces γ_{s0}, but boosts the number of atoms (by simply increasing the volume of atomic vapor in the channel), and thereby also Γ_s. The new cell has dimensions of $1\,\text{mm} \times 1\,\text{mm} \times 40\,\text{mm}$, or roughly 44 times larger volume than the old cell, thus more than compensating for the departure from the increase in readout rate offered by a double pass setup. The larger cross section also makes creation of a high quality top hat beam easier

Because the next logical step for our setup in the implementation of a teleportation protocol, we also need to consider changes needed to change from CW to pulsed operation. This, among other things means the inclusion of a lock beam, shifted from the interrogating LO by a modulator.

Further, if we want to implement a teleportation protocol, we must be able to measure the two systems in a collective measurement, and subsequently measure one system by itself for verification. This can be done by changing the magnetic field to move the atoms out of resonance with the mechanics, but the needed electronics to reliably switch magnetic fields fast is not easily implemented. Thus, we opt for using a Pockels cell to send the light from the optomechanics to a separate verification setup.

In total, a quite realistic proposal for a new setup is shown in Fig. 11.1. The setup is being implemented at the time of writing, with the overall ideas presented here.

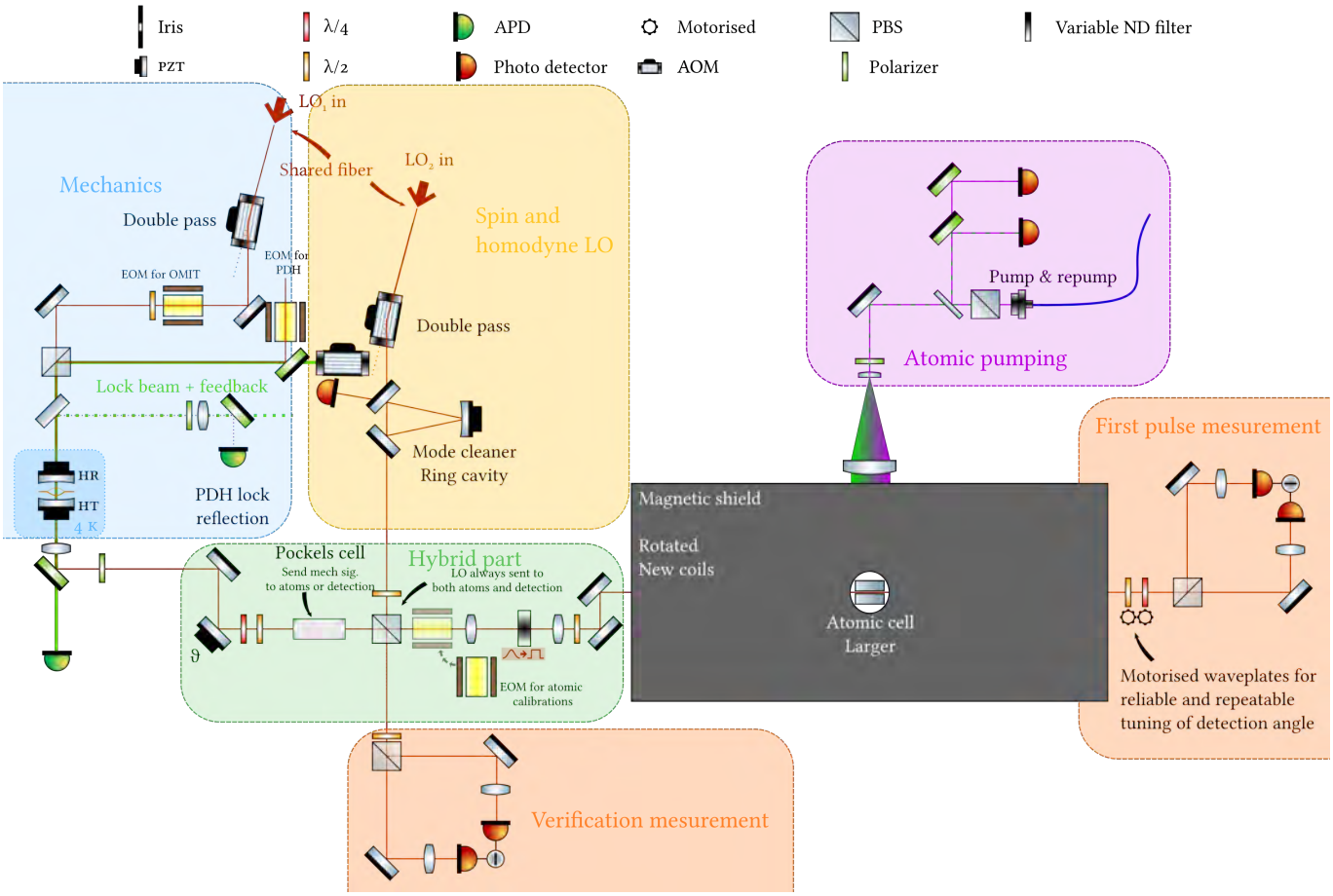

Figure 11.1: Flipped experiment drawing. In this setup, the optomechanics is probed first, and the spin last. The introduction of a top hat beam shaper should reduce the effect of the broadband atomic noise. The introduction of modulators for pulsed operation is an important step towards implementing a teleportation protocol in a hybrid spin–mechanics system. See main text for more details and discussion.

The experiment, hindered by a global pandemic, significant change in the experiment staff, and sickness, is now well underway to the new configuration. As with all major rebuilds, hitches arise, goals shift and new opportunities opens up along the way.

At the time of finishing this thesis, the atomic part of the setup is close to optimized; here, we have recently observed more than 7 dB of ponderomotive squeezing from the atoms, a significant improvement over previously reported squeezing results from warm atomic ensembles. Where other experiments, such as Boyer et al. (2008)[4], have showed 4 dB of two-mode squeezing, we perform single mode squeezing. Also note, that while our observed squeezing is high for

(4) Vincent Boyer et al. (2008). "Entangled Images from Four-Wave Mixing". In: *Science* 321.5888, pp. 544–547.

$\chi^{(3)}$ type systems, it is nowhere close to what has been observed for $\chi^{(2)}$ type squeezing from OPOs, such as the 15 dB reported in Vahlbruch et al. (2016). We have a manuscript in preparation detailing these developments.

The mechanical and hybrid parts of the setup are also coming along, with a significant learning curve for our team in terms of running the optomechanical experiment pulsed, and in a significantly different regime in almost every regard.

Having now established our chosen avenue of research with the hybrid experiment, towards pulsed operation in a flipped configuration, we end the thesis with a short discussion of what teleportation is, and why it is interesting. Indeed, what does "teleporation" mean?

First proposed in Bennett et al. (1993)[5] and expanded on soon after by Vaidman (1994)[6], I here define teleportation as

the disembodied transfer of a quantum state between two quantum systems.

In the words of Bennett et al. (1993), it is possible to perform

> "teleportation" of an intact quantum state from one place to another, by a sender who knows neither the state to be teleported nor the location of the intended receiver.

The protocol necessitates the use of two channels: one classical channel, sharing the classical measurement result of a measurement on the joint quantum system, and one quantum, or EPR, channel.

What this means is that there are also a couple of things that quantum teleportation are *not*:

- faster than light; the classical channel very effectively puts a stop to this
- involving the transfer of anything material; the protocol takes the quantum state of one object and *transfers* that state to the other (material) system
- classical; well, it says in the name, and the necessary EPR state should also make it obvious. But what it does mean is that there should be a *classical limit* to beat, if one wishes to demonstrate successful quantum teleportation

A very similar experiment, involving two atomic samples instead, was reported from out group in (Krauter et al. 2013). In a sense, we seek to replicate that experiment, but with one atomic sample replaced by an optomechanical system.

The chosen configuration means that we will be attempting to teleport the state of the spin system onto the mechanics. For example, a spin squeezed state (Vasilakis, Shen, et al. 2015) may be prepared in the spin, and teleported onto the mechanics. If successful, this would open up an avenue towards squeezing of the mechanical state in a cavity optomechanical system, something which so far has been a hard experimental task. Squeezing the mechanical state would allow for improved force sensitivity, when using mechanical oscillators as force sensors. One could also envision using the mechanical resonator as quantum memory, where the spin would effectively act as a transducer from magnetic or optical signals, to a stationary quantum state, which can be teleported onto the mechanics.

(5) Charles H. Bennett et al. (1993). "Teleporting an unknown quantum state via dual classical and Einstein-Podolsky-Rosen channels". In: *Physical Review Letters* 70 (13), p. 1895.

(6) Lev Vaidman (1994). "Teleportation of quantum states". In: *Phys. Rev. A* 49 (2), pp. 1473–1476.

Part IV

APPENDICES etc.

Experimental Parameters

This appendix contains experimental parameters for the entanglement experiment, reported in Chapter 10. Most parameters are *posterior estimates*, as evaluated by the Bayesian estimation MCMC routine. A few of them are directly measured (e. g., optical powers) See main text in Chapter 10, in particular Section 10.5.2, for details.

Parameter	Symbol	Value
	Atomic spin oscillator	
Decoherence rate in the dark	$\gamma_{\mathrm{so,dark}}/2\pi$	450 Hz
Intrinsic linewidth	$\gamma_{\mathrm{so}}/2\pi$	1.7 kHz
Effective linewidth (incl. dynamical damping)	$\gamma_{\mathrm{s}}/2\pi$	2.9 kHz
Tensor contribution	ζ_{s}	0.028
LO_1 driving power		350 µW
Readout rate	$\Gamma_{\mathrm{s}}/2\pi$	20 kHz
Spin Polarisation	p	0.82
Spin thermal occupancy	n_{s}	0.8
Microcell single pass optical losses	$\eta_{\mathrm{microcell}}$	4 %
Microcell temperature		50°C
Quantum cooperativity	$C_{\mathrm{q}}^{\mathrm{s}}$	~ 5
	Mechanical oscillator and cavity	
Intrinsic mechanical frequency	$\omega_{\mathrm{mo}}/2\pi$	1.370 MHz
Intrinsic damping rate	$\gamma_{\mathrm{mo}}/2\pi$	2.1 mHz
Optical damping rate	$\gamma_{\mathrm{m}}/2\pi$	3.9 kHz
Cavity detuning	$\Delta/2\pi$	−0.7 MHz
Total cavity linewidth	$\kappa/2\pi$	4.2 MHz
LO_2 drive power		~8 µW
Intracavity photons	N	1.6×10^6
Single photon coupling rate	$g_{\mathrm{o}}/2\pi$	6×10^1 Hz
Readout rate	$\Gamma_{\mathrm{m}}/2\pi$	15 kHz
Cavity overcoupling	$\kappa_{\mathrm{in}}/\kappa$	0.93
Thermal bath temperature	T	11 K
Bath occupancy	n_{mo}	173×10^3
Mean occupancy	n_{m}	~ 2
Quantum cooperativity	$C_{\mathrm{q}}^{\mathrm{m}}$	~ 15
	Hybrid & detection	
Quantum efficiency between systems	ν	0.53
Cavity mode-matching (amplitude)		0.9
Power transmission between systems		0.8
Detection efficiency	η	0.77
Homodyning visibility		0.96
Power transmission and detector QE		0.87
LO_1–LO_2 phase	φ	~180°
Detection phase	ϑ	2°

Table A.1: Summary of notation and experimental parameters. When applicable, we quote the posterior mean values from the MCMC simulation. See Section 10.5.2 for details and discussion.

APPENDIX B

Si_3N_4 Material Constants

Material constants for stochiometric silicon nitride LPCVD deposited thin film, Si_3N_4.

Quantity	Symbol	Value	Reference
Tensile stress	$\mathcal{T}$	1.0 GPa	Tabata et al. (1989)
		(1.27 ± 0.02) GPa	Yeghishe Tsaturyan (2019)
Poisson's ratio	ν	0.23 ± 0.02	Edwards, Coles, and Sharpe (2004)
Young's modulus	E	(325 ± 30) GPa	Kaushik, Kahn, and Heuer (2005)
		270 GPa	Yeghishe Tsaturyan (2019)
Density	ρ	3.19 g/cm^3	Pierson (1999)

Table B.1: Material constants for Si_3N_4.

Appendix C

Laguerre-Gaussian Modes

This Appendix is simply a set of illustrations of Laguerre-Gaussian modes, as used in the numerical model introduced in Chapter 7.

I plot the real and imaginary parts in Fig. C.1 and Fig. C.2 respectively, as well as the intensity distributions in Fig. C.3. The parameters are listed in Table C.1.

Radial index, p	$[0..4]$
Angular index, l	$[-3..3]$
Waist size, w_0	50 µm
Waist position, z_0	0 nm
Optical wavelength, λ	852 nm

Table C.1: Parameters for the figures in this appendix.

Note that the real parts are identical for modes with angular index $\pm l$, the imaginary part antisymmetric for $l = \pm l$ and vanishes for $l = 0$.

The intensities are all rotationally symmetric, with increasing p leading to more radial oscillations, and increasing l leading to a larger radial size for identical p's. Only the modes with $l = 0$ have a non-zero intensity at the origin.

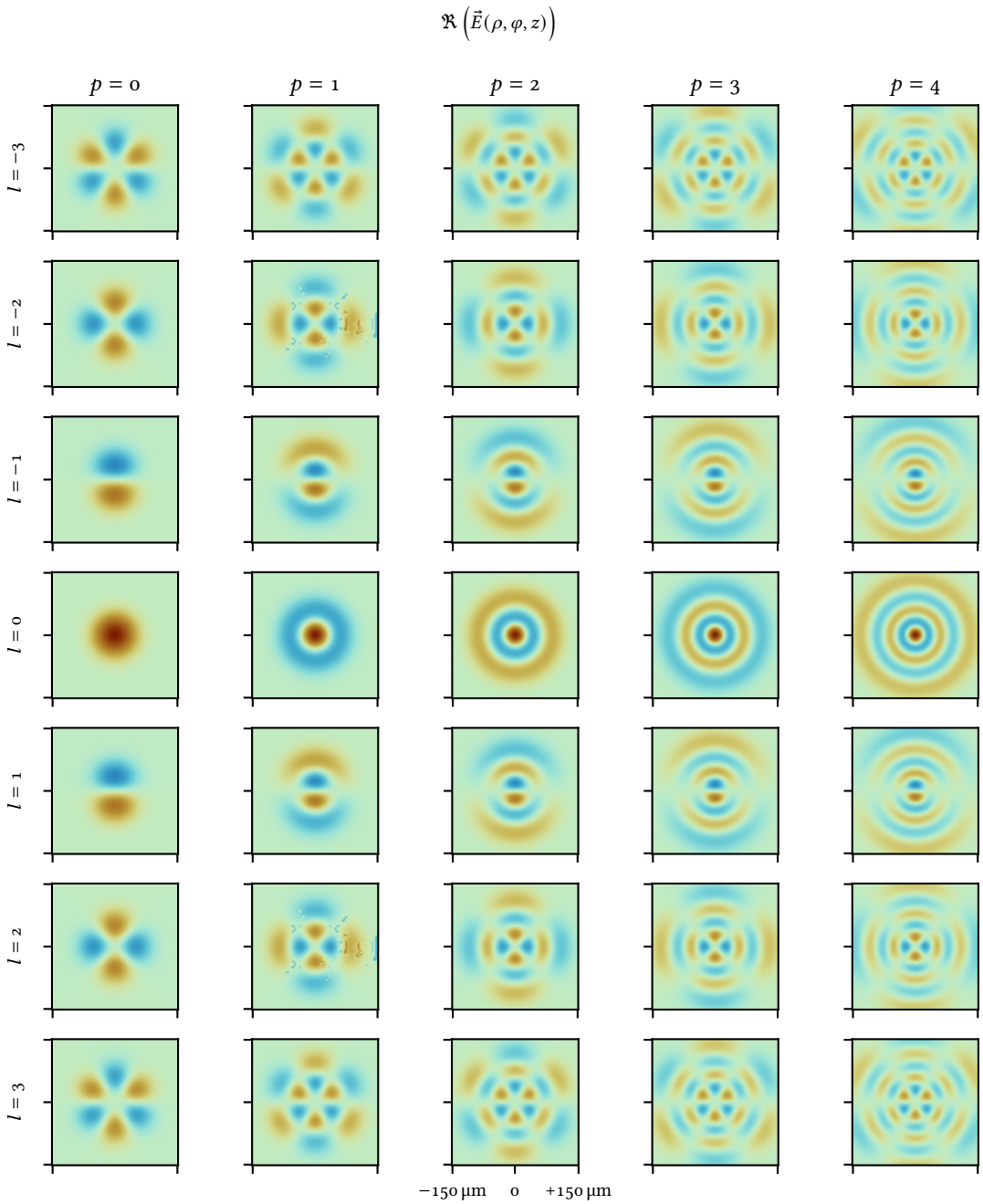

Figure C.1: Real part of $\mathrm{LG}_p^l(\rho, \varphi, z = 0)$.

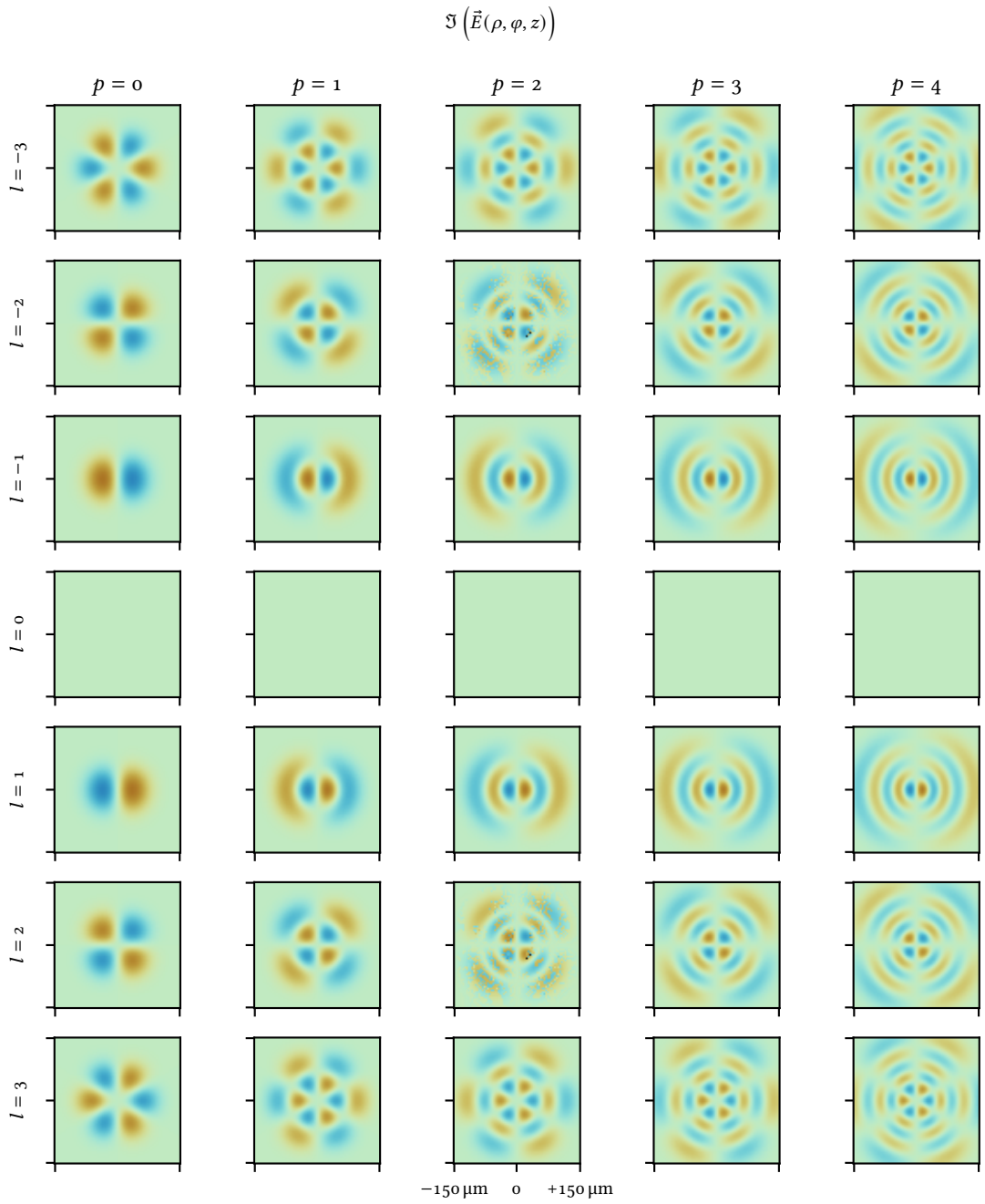

Figure C.2: Imaginary part of $\mathrm{LG}_p^l(\rho, \varphi, z = 0)$.

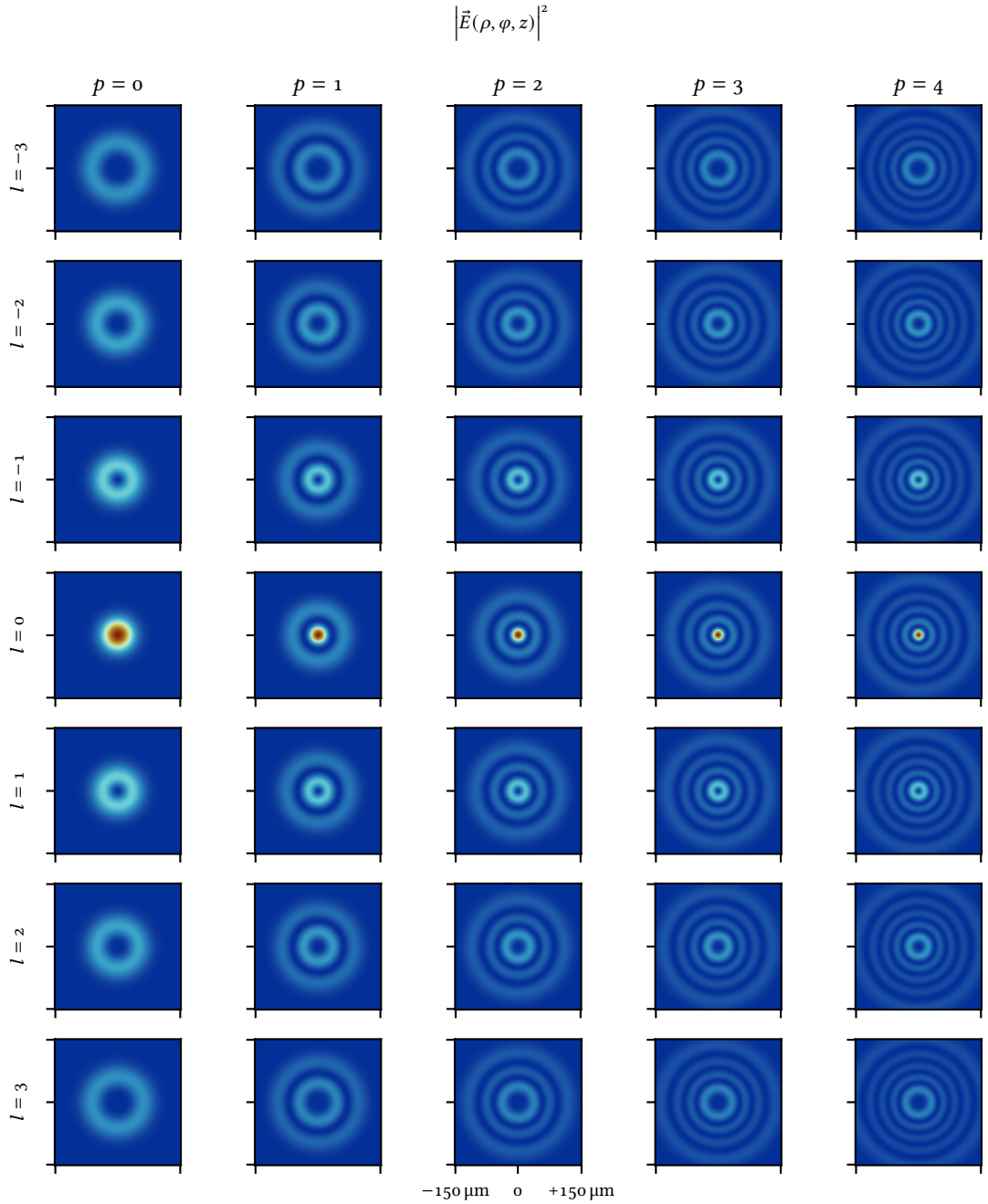

Figure C.3: Squared absolute amplitude of $\mathrm{LG}_p^l(\rho, \varphi, z = 0)$.

Appendix D

BAC Detectors

The electronic diagram for the BAC3 detector described in Section 9.1.2.2 is presented in the next figure.

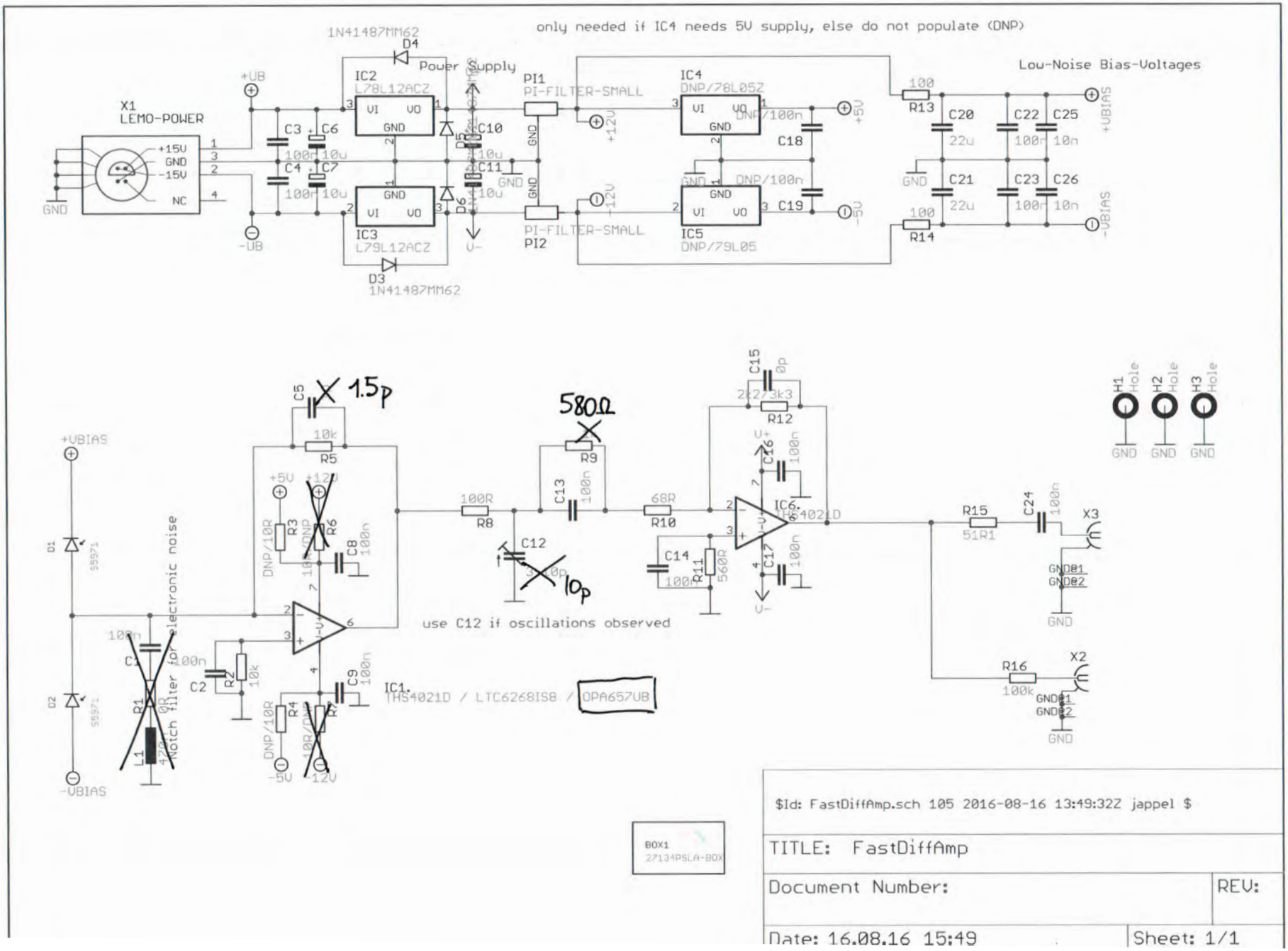
only needed if IC4 needs 5V supply, else do not populate (DNP)
1N41487MM62
D4
Power Supply
IC2
L78L12ACZ
PI1
PI-FILTER-SMALL
IC4
DNP/78L05Z
Low-Noise Bias-Voltages
X1
LEMO-POWER
+15V
GND
-15V
NC
+UB
-UB
C3
C6
C4
C7
C10
C11
C18
C19
R13
R14
C20
C21
C22
C23
C25
C26
+VBIAS
-VBIAS
IC3
L79L12ACZ
D3
1N41487MM62
PI2
IC5
DNP/79L05
C5
1.5p
580Ω
R9
R5
10k
R12
2k2/3k3
C15
0p
R8
100R
C13
100n
R10
68R
C12
10p
use C12 if oscillations observed
IC6.
THS4021D
C16
C17
C14
R11
560R
R15
51R1
C24
X3
R16
100k
X2
H1
H2
H3
Hole
Notch filter for electronic noise
R1
L1
C1
C2
R2
10k
C8
C9
R3
R6
R4
R7
DNP/10R
IC1.
THS4021D / LTC6268IS8 / OPA657UB
BOX1
27134PSLA-BOX
$Id: FastDiffAmp.sch 105 2016-08-16 13:49:32Z jappel $
TITLE: FastDiffAmp
Document Number:
REV:
Date: 16.08.16 15:49
Sheet: 1/1

APPENDIX E

The Schur Complement

For q and p real non-negative integers, and the complex-valued matrices $\boldsymbol{A}, \boldsymbol{B}, \boldsymbol{C}, \boldsymbol{D}$ of size $p \times p$, $p \times q$, $q \times p$ and $q \times q$ with, let

$$\boldsymbol{M} = \begin{pmatrix} \boldsymbol{A} & \boldsymbol{B} \\ \boldsymbol{C} & \boldsymbol{D} \end{pmatrix}, \tag{E.1}$$

a matrix of size $(p+q) \times (p+q)$.

If $\boldsymbol{D}$ is invertible, the *Schur complement* of the block $\boldsymbol{D}$ of $\boldsymbol{M}$ is a $p \times p$ matrix defined as

$$(\boldsymbol{M}/\boldsymbol{D}) \equiv \boldsymbol{A} - \boldsymbol{B}\boldsymbol{D}^{-1}\boldsymbol{C}. \tag{E.2}$$

Similarly, if $\boldsymbol{A}$ is invertible, the Schur complement of the block $\boldsymbol{A}$ of $\boldsymbol{M}$ is a $q \times q$ matrix defined as

$$(\boldsymbol{M}/\boldsymbol{A}) \equiv \boldsymbol{D} - \boldsymbol{C}\boldsymbol{A}^{-1}\boldsymbol{B}. \tag{E.3}$$

The Schur complements are related to the Guass–Jordan elimination of $\boldsymbol{M}$. For us, the most useful property is that the inverse of $\boldsymbol{M}$ may be found easily, as

$$\boldsymbol{M}^{-1} = \begin{pmatrix} \boldsymbol{A} & \boldsymbol{B} \\ \boldsymbol{C} & \boldsymbol{D} \end{pmatrix}^{-1} = \begin{pmatrix} (\boldsymbol{M}/\boldsymbol{D})^{-1} & -(\boldsymbol{M}/\boldsymbol{D})^{-1}\boldsymbol{B}\boldsymbol{D}^{-1} \\ -\boldsymbol{D}^{-1}\boldsymbol{C}(\boldsymbol{M}/\boldsymbol{D})^{-1} & \boldsymbol{D}^{-1} + \boldsymbol{D}^{-1}\boldsymbol{C}(\boldsymbol{M}/\boldsymbol{D})^{-1}\boldsymbol{B}\boldsymbol{D}^{-1} \end{pmatrix} \tag{E.4}$$

$$= \begin{pmatrix} \boldsymbol{A}^{-1} + \boldsymbol{A}^{-1}\boldsymbol{B}(\boldsymbol{M}/\boldsymbol{A})^{-1}\boldsymbol{C}\boldsymbol{A}^{-1} & -\boldsymbol{A}^{-1}\boldsymbol{B}(\boldsymbol{M}/\boldsymbol{A})^{-1} \\ -(\boldsymbol{M}/\boldsymbol{A})^{-1}\boldsymbol{C}\boldsymbol{A}^{-1} & (\boldsymbol{M}/\boldsymbol{A})^{-1} \end{pmatrix}, \tag{E.5}$$

as long as the relevant matrices are invertible.

Apart from finding the inverse of $\boldsymbol{M}$, one can also relate the sub-matrices to one another, for example

$$(\boldsymbol{M}/\boldsymbol{D})^{-1} = [\boldsymbol{A} - \boldsymbol{B}\boldsymbol{D}^{-1}\boldsymbol{C}]^{-1} = \boldsymbol{A}^{-1} + \boldsymbol{A}^{-1}\boldsymbol{B}(\boldsymbol{M}/\boldsymbol{A})^{-1}\boldsymbol{C}\boldsymbol{A}^{-1}. \tag{E.6}$$

List of Figures

Fig. 1.1 The comets tail pointing away from the sun. 3

Fig. 1.2 Cartoon model of the hybrid experiment. 7

Fig. 2.1 The zoo of quantum platforms. 10
Fig. 2.2 Atomic cell and level scheme. 11
Fig. 2.3 Different mechanical oscillators. 13
Fig. 6.1 The old, monolithic, cavity design concept. 17
Fig. 2.4 QBAE in a hybrid experiment, as reported in Møller et al. (2017). 18
Fig. 2.5 The SQL for continuous measurement of a mechanical oscillator. 19

Fig. 3.1 The idealized 1D harmonic oscillator. 25
Fig. 3.2 Mechanical susceptibilities. 26
Fig. 3.3 A rectangular membrane. 27
Fig. 3.4 Mode shapes, $M_{nm}(x, y)$ of four combinations of (n, m) for a square membrane. 27
Fig. 3.5 Full susceptibility and Lorentzian approximation. 30
Fig. 3.6 Thermal response of harmonic oscillators to a Gaussian/thermal driving force. 32
Fig. 3.7 A coherent state phase space representation 35
Fig. 3.8 Radiation pressure force on a harmonically suspended mirror. 36
Fig. 3.9 A simple optical cavity. 37
Fig. 3.10 Cavity resonances for different values of the finesse. 38
Fig. 3.11 Reflection and transmission through a lossless cavity. 39
Fig. 3.12 Cavity finesse, $\mathcal{F}$, for a symmetric cavity. 40
Fig. 3.13 Relative power transmission as a function of the cavity coupling parameter, η. 40
Fig. 3.14 Canonical optomechanical system. 41
Fig. 3.15 Cavity rotations. 46
Fig. 3.16 Optical spring and damping. 49
Fig. 3.17 Sideband resolution. 49
Fig. 3.18 Optical readout rate and sideband asymmetry. 51
Fig. 3.19 Canonical and MIM optomechanical systems. 52
Fig. 3.20 TMM concept 53
Fig. 3.21 Membrane position in the cavity field, $2kz$. 54
Fig. 3.22 Frequency shift as a function of $2kz$. 55
Fig. 3.23 Transfer matrix model. 57
Fig. 3.24 OMIT level scheme. 59

Fig. 3.25 OMIT signal. 61
Fig. 3.26 Ponderomotive squeezing in reflection for varied g. 63
Fig. 3.27 Ponderomotive squeezing in reflection for varied T. 63
Fig. 3.28 Ponderomotive squeezing in reflection for varied T. 64
Fig. 3.29 Ponderomotive squeezing in reflection. 65
Fig. 3.30 Ponderomotive squeezing in transmission. 65
Fig. 3.31 Static bistability. 66

Fig. 4.1 Membrane generations. 70
Fig. 4.2 Out of plane displacement for the five different modes in the bandgap. 73
Fig. 4.3 Cuts of membrane displacement. 74
Fig. 4.4 Membrane reflection and g_0 as a function of thickness. 74
Fig. 4.5 Resonator stability diagram. 75
Fig. 4.6 Cavity waist size as a function of cavity length, L, for a symmetric cavity. 77
Fig. 4.7 Free Spectral Range, FSR, and Transverse Mode Spacing, TMS. 77
Fig. 4.8 Free spectral range and Transversal mode spacing, and their ratio, for a symmetric cavity. 78
Fig. 4.9 The optical mode on the membrane. 79
Fig. 4.10 The ST-100 cryostat. 79
Fig. 4.11 Approximate geometry of the cold finger. 80
Fig. 4.12 Q_{gas} as a function of pressure p, for $T = 300\,\text{K}$ and $10\,\text{K}$. $d = 20\,\text{nm}$, $\omega/2\pi = 1.3\,\text{MHz}$, $\rho = 3.17\,\text{g/cm}^3$, $m_{\text{molar}} = 29\,\text{g/mol}$. 82
Fig. 4.13 Michelson type interferometer for membrane Q measurements. 83
Fig. 4.14 Ringdown measurement example. 84

Fig. 5.2 Cesium D_2 levels in both the upper and lower manifolds. 88
Fig. 5.1 Level scheme of cesium, with our optical probing, pumping and repumping scheme. 88
Fig. 5.3 Cesium D_2 level structure. 90
Fig. 5.4 Positive and negative mass configurations of the spin. 93
Fig. 5.5 Driven response of the spin oscillator with positive and negative mass. 93
Fig. 5.6 Poincare sphere. Modified figure, original by Geek3, published under CC BY 3.0. 94
Fig. 5.7 Stokes parameter measurements. 95
Fig. 5.8 MORS. 102
Fig. 5.9 Cell chip photograph. 102
Fig. 5.10 Microcell photograph and end view drawing. 102
Fig. 5.11 Spin noise a function of beam size. 104
Fig. 5.12 Spin system experimental setup concept. 105
Fig. 5.13 Repumping on $F' = 2$ or $F' = 4$. 106
Fig. 5.14 Power broadening of the γ_{43} linewidth. 107
Fig. 5.15 Spin transverse variance and thermal occupations as a function of spin polarization, $|p|$. 108
Fig. 5.16 Theoretical spin noise curves. 109
Fig. 5.17 Peak height and linewidths from Fig. 5.16. 110
Fig. 5.18 Spin LW and peak signal size as a function of probe power. 110
Fig. 5.19 Spin signal vs. probe power. 110

Fig. 5.20 CIFAR setup. 111
Fig. 5.21 CIFAR simple theory. 114
Fig. 5.22 CIFAR as a function of modulation amplitude. 115
Fig. 5.23 CIFAR residuals from Fig. 5.22. 116
Fig. 5.24 CIFAR as a function of cell temperature, effectively changing Γ_s/γ_s. 117
Fig. 5.25 CIFAR signal for different tensor coupling parameters ζ_s. 118
Fig. 5.26 Coherent interference between the responses of the narrow and broadband spin modes. 119

Fig. 6.1 The old, monolithic, cavity design concept. 124
Fig. 6.2 New cavity design. 127
Fig. 6.3 Different combinations of PTFE spacers. Also tested, but now shown: only PTFE at the front or back of the mirror. White: PTFE, blue: mirror, black: copper barrel, brown: piezo. 127
Fig. 6.4 The mirror barrel and batman screw, plus assembly tool. 128
Fig. 6.5 The cavity design exploded. 129
Fig. 6.6 High degree of freedom cavity design concept. 130
Fig. 6.7 Moving the membrane in $2kz$. 130
Fig. 6.8 Aligning the membrane tilt in the new cavity design. 131
Fig. 6.9 The optical mode moves as the cavity is scanned through $2kz$. 132

Fig. 7.1 Avoided mode crossing of TEM_{00} mode with a higher order mode from a lower longitudinal mode family. 134
Fig. 7.2 Cavity linewidth of two modes in an avoided mode crossing. 135
Fig. 7.3 Mode model concept. 136
Fig. 7.4 Beam size, $w(z)$, of a Laguerre-Gaussian beam 138
Fig. 7.5 Curvature of the phase front. 139
Fig. 7.6 Generalized Laguerre polynomials. 139
Fig. 7.7 Modes and intensity of the fundamental for an empty cavity. Parameters are listed in Table 7.1. 143
Fig. 7.8 Modes and intensity of the fundamental for a cavity with medium wavefront curvature at the membrane. Parameters as in Table 7.1, but with $d = 40\,\text{nm}$. 143
Fig. 7.9 Modes and intensity of the fundamental for a cavity with small wavefront curvature at the membrane. 144
Fig. 7.10 Modes and intensity of the fundamental for a cavity with large wavefront curvature at the membrane. 144
Fig. 7.11 Modes and intensity of the fundamental for a cavity with a tilted membrane. 145
Fig. 7.12 $2kz$ all modes. 147

Fig. 8.1 Modes of the old mirrors, simulation and measurement. 150
Fig. 8.2 Mechanical spectrum of the old mirrors under different clamping conditions. 152
Fig. 8.3 Simulated modes of the old mirrors. 153
Fig. 8.4 Spectra of two simple. circular drum heads. As the size is reduced, the whole spectrum is stretched, making it spectrally less dense. 154
Fig. 8.5 The simulated mechanical mode spectrum for varied $\varnothing$ and d. 154

Fig. 8.6 Mechanical modes of new and old mirrors. 155
Fig. 8.7 TMM evaluted for the optical coatings ordered and delivered. 157
Fig. 8.8 Measured mirror modes of new mirrors. 159
Fig. 8.9 Mirror transmissivities from the coating company datasheet. 160
Fig. 8.10 Cavity linewidth with the new mirrors. 160

Fig. 9.1 Ti:Sapph drawing. 164
Fig. 9.2 Power output of a Ti:Sapph laser as a function of the pump power. 164
Fig. 9.3 Relaxation oscillations. 164
Fig. 9.4 Response of a typical S5971 diode. 167
Fig. 9.5 BAC detector frequency dependent gain. 167
Fig. 9.6 The outline of the hybrid experimental setup. 168
Fig. 9.7 Detailed drawing of the experimental setup. 170
Fig. 9.8 50 periodograms plotted together. 173
Fig. 9.9 Periodogram mean and standard deviation. 174

Fig. 1.2 Cartoon model of the hybrid experiment, revisited. 177
Fig. 10.1 Simplified experimental setup for entanglement generation. 178
Fig. 10.2 Schematic representation of the hybrid system. 179
Fig. 10.3 Spectra of mechanics, spins and hybrid, plus Wiener filter for resonant case. 185
Fig. 10.4 QBAE as the Larmor frequency is scanned through the mechanical resonance. 187
Fig. 10.5 Wide range resonant hybrid spectrum and Wiener filter. 193
Fig. 10.6 Covariance matrices. 195
Fig. 10.7 EPR trajectory and variance. 196
Fig. 10.8 Hybrid PSDS and EPR variances for different spin-mechanics detunings. 197
Fig. 10.9 Histograms of variances from Monte Carlo simulations. 199

Fig. 11.1 Flipped experiment drawing. 205

Fig. C.1 Real part of $\mathrm{LG}_p^l(\rho, \varphi, z = 0)$. 214
Fig. C.2 Imaginary part of $\mathrm{LG}_p^l(\rho, \varphi, z = 0)$. 215
Fig. C.3 Squared absolute amplitude of $\mathrm{LG}_p^l(\rho, \varphi, z = 0)$. 216

List of Tables

3.1 Parameters for the TMM. 58

7.1 Parameters for the empty cavity simulation. 142
7.2 Parameters for the cavity simulation in Fig. 7.12. 146

8.1 Mirror coatings ordered and delivered. 158

A.1 Summary of notation and experimental parameters. 210

B.1 Material constants for Si_3N_4. 211

C.1 Parameters for the figures in this appendix. 213

Nomenclature

The Nomenclature contains a list of abbreviations and important symbols used throughout this thesis.

AC	Alternating Current. Time-varying signals.
AOM	Acousto-Optic Modulator. A device that transforms an electrical signal into a modulation on a light-beam through photon-phonon coupling in a crystal. The electrical signal induces vibrations in a crystal, which in effect create a moving diffraction grating in the crystal. The device thus changes the frequency of the photons, as well as allowing for very fast switching of optical signals.
APD	Avalanche Photo Diode. A very sensitive photo diode. High sensitiviy and high electronic noise. Saturate with optical powers needed for homoyne detection.
AR	Anti-Reflection. AR coatings are applied to optical surfaces to reduce optical losses.
CAD	Computer-Aided Design.
CIFAR	Coherently Induced FAraday Rotation. A novel method for measuring spin readout rates. See Section 5.10.
CSD	Cross Spectral Density. See Eq. (3.9), page 21.
DAQ	Digital AcQuisition.
DC	Direct Current. Time-constant signals.
DDS	Direct Digital Synthesizer. A device capable of generating arbitrary waveforms from a fixed frequency reference.
DFT	Discrete Fourier Transform. See Eq. (9.1), page 168.
EOM	Electro Optical Modulator. A device that imprints an electric modulation to, e. g., the phase or polarization of a light-field.
EPR	Einstein–Podolsky–Rosen. Usually used to refer to a certain type of entangled quantum states (EPR states), such as the one repored in Chapter 10.
FEM	Finite Element Method. A numerical method for solving coupled differential equations in complex geometries.

FFT	Fast Fourier Transform. An algorithm for computing the DFT.
$\mathscr{F}$	Finesse. A measure of cavity resonance linewidths, or, equivalently, the round trip losses. See Eq. (3.80), page 36.
FPGA	Field-Programmable Gate Array. User-programmable integrated circuits, i. e., programmable *hardware*. By programming custom algorithms an modules in hardware instead of software, significant speed up of many tasks can be achieved.
FSR	Free Spectral Range. The spectral separation between consecutive resonances of (the transverse fundamental mode of) a cavity. See Eq. (3.79), page 35.
FWHM	Full Width at Half Max. A measure of widths of distributions and lineshapes, particularly Lorentzians, for which the standard deviations (and mean) is undefined. Defined as the distance between the two values where the lineshape goes below half the maximum value.
GWD	Gravitational Wave Detecion. The art of measuring gravitational waves. Performed by detectors such as LIGO and VIRGO.
HR	High Reflection. HR coatings are applied to glass substrates to make mirrors. Very good coatings have a transmission of $T = 10\,\text{ppm}$.
HWHM	Half Width at Half Max. Half the FWHM.
HWP	Half Wave Plate. An optical element, where light polarized along one axis is retarded by half a wavelength, relative to the other axis. Also: $\lambda/2$. Rotates the polarization direction of linearly polarized light.
LHE	Liquied Helium. Used to cool our membrane to cryogenic temperatures. LHE has a boiling point of 4.2 K at atmospheric pressure.
LO	Local Oscillator. A strong electromagnetic field in a hetero- or homodyning measurement, where two or more fields are overlapped on a photo-detector.
MCMC	Markov Chain Monte Carlo. See Section 10.5.2.
MIM	Membrane-In-the-Middle. A type optomechanical systems, where a resonator (typically a membrane) is placed in the middle of a Fabry–Perot resonator.
MORS	Magneto-Optical Resonance Spectroscopy. See Section 5.6.
NBI	The Niels Bohr Institute.
OMIT	Optomechanically Induced Transparency. See Section 3.9.1.
PBS	Polarizing Beam-Splitter. An optical device that transmits one and reflects the other linear polarization.
PD	Photo Detector. A device that converts light into currents and/or voltages.
PDF	Probability Distribution Function.

PDH Pound–Drever–Hall. A modulation based method of locking cavities.

PID Proportional-Integral-Differential. A feedback system which reacts to the instantaneous error signal (proportional), the accumulated error signal (integral) and the change in error signal (differential). The differential feedback is often omitted.

PLL Phase-Locked Loop. A feedback mechanism where two oscillators are locked such that their beatnote is phase-stable relative to a third frequency. Example: One laser is locked to another such that their beatnote matches a normal RF signal.

PSD Power Spectral Density. See Eq. (3.8), page 21.

PTFE PolyTetraFluoroEthylene. A white synthethic flouropolymer material. Also known as Teflon™.

QBA Quantum Back Action. The probe-induced noise imprinted onto a quantum system, and read out by said probe.

QBAE Quantum Back Action Evasion. The process of cancelling or evading QBA in a measurement.

QE Quantum Efficiency. The probability of a given photo detector generating a photo-electron upon absorption of one photon. Depends on the wavelength, λ.

QND Quantum Non-Demolition.

QUANTOP The Danish Center for Quantum Optics, QUANTOP. My research group, led by proff. Eugene S. Polzik.

QWP Quarter Wave Plate. An optical element, where light polarized along one axis is retarded by a quater of a wavelength, relative to the other axis. Also: $\lambda/4$. Turns linearly polarized light into elliptically (circularly) polarized light, and vice versa.

RBW Resolution BandWidth. The spectral resolution of a DFT or spectrogram. See Eq. (9.2), page 168.

RF Radio Frequency. Signals or drives in the frequency range from $\sim$ 20 kHz to $\sim$ 1 GHz, depending on definition. Higher frequencies than RF are usually called microwave (μ-wave).

RMS Root Mean Square. What is says on the tin: the square root of the mean value of the squares of a bunch of numbers, $\sqrt{\sum x_i^2/N}$.

ROC Radius Of Curvature. Descibes the curvature of mirrors.

SLAB Schließer LAB, the research group of proff. Albert Schließer at NBI.

SN Shot Noise. The inherent quantum fluctuations of light.

SQL Standard Quantum Limit. A lower bound on the uncertainty achievable in measurements on "standard" quantum systems. The limit may be circumvented through, e. g., squeezing of another quadrature.

TEM	Transverse Electromagnetic Mode. The field distribution transverse to the propagation of a given mode. In free space and cavites, Laguerre–Gaussian modes (TEM_{pl}) and Hermite–Gaussian modes (TEM_{mn}) modes can serve as a basis for an arbitrary field. See Appendix C.
TLS	Two Level System. Often used in the context of the bath of effective two level defects, which increase the decoherence rates of many mechanical oscillators.
TMM	Transfer Matrix Model. See Section 3.8.1.
TMS	Transversal Mode Spacing. See Eq. (4.13), page 73.
TPI	Threads Per Inch. A measure of thread pitch on imperial screws and bolts.

Bibliography

Abbott, B. P. et al. (2016). "Observation of Gravitational Waves from a Binary Black Hole Merger". In: *Phys. Rev. Lett.* 116 (6), p. 061102 (cit. on pp. 4, 12).

Agarwal, G. S. and S. Chaturvedi (2003). "Scheme to measure quantum stokes parameters and their fluctuations and correlations". In: *Journal of Modern Optics* 50.5, pp. 711–716 (cit. on p. 95).

Agarwal, G. S. and Sumei Huang (2010). "Electromagnetically induced transparency in mechanical effects of light". In: *Phys. Rev. A* 81 (4), p. 041803 (cit. on p. 58).

Anderson, Dana Z. (1984). "Alignment of resonant optical cavities". In: *Appl. Opt.* 23.17, pp. 2944–2949 (cit. on p. 78).

Appel, J., P. J. Windpassinger, D. Oblak, U. B. Hoff, N. Kjærgaard, and E. S. Polzik (2009). "Mesoscopic atomic entanglement for precision measurements beyond the standard quantum limit". In: *Proceedings of the National Academy of Sciences* 106.27, pp. 10960–10965 (cit. on p. 16).

Arrangoiz-Arriola, Patricio, E. Alex Wollack, Zhaoyou Wang, Marek Pechal, Wentao Jiang, Timothy P. McKenna, Jeremy D. Witmer, Raphaël Van Laer, and Amir H. Safavi-Naeini (2019). "Resolving the energy levels of a nanomechanical oscillator". In: *Nature* 571 (7766), pp. 537–540 (cit. on pp. 15, 16).

Arute, Frank et al. (2019). "Quantum supremacy using a programmable superconducting processor". In: *Nature* 574 (7779), pp. 505–510 (cit. on p. 11).

Aspelmeyer, Markus, Tobias J. Kippenberg, and Florian Marquardt (2014). "Cavity optomechanics". In: *Rev. Mod. Phys.* 86 (4), pp. 1391–1452 (cit. on pp. 12–14, 19, 64, 81, 82).

Balabas, M. V., K. Jensen, W. Wasilewski, H. Krauter, L. S. Madsen, J. H. Müller, T. Fernholz, and E. S. Polzik (2010). "High quality anti-relaxation coating material for alkali atom vapor cells". In: *Opt. Express* 18.6, pp. 5825–5830 (cit. on p. 102).

Balabas, M. V., T. Karaulanov, M. P. Ledbetter, and D. Budker (2010). "Polarized Alkali-Metal Vapor with Minute-Long Transverse Spin-Relaxation Time". In: *Phys. Rev. Lett.* 105 (7), p. 070801 (cit. on pp. 102, 103).

Bao, Minhang, Heng Yang, Hao Yin, and Yuancheng Sun (2002). "Energy transfer model for squeeze-film air damping in low vacuum". In: *Journal of Micromechanics and Microengineering* 12.3, pp. 341–346 (cit. on p. 82).

Barg, Andreas (2014). "Optical Characterization of Micromechanical Membranes". M.Sc. thesis. University of Copenhagen & University of Hamburg (cit. on p. 82).

Barzanjeh, S, E S Redchenko, M Peruzzo, M Wulf, D P Lewis, G Arnold, and J M Fink (2019). "Stationary entangled radiation from micromechanical motion". In: *Nature* 570 (7762), pp. 480–483 (cit. on pp. 14, 15).

Bennett, Charles H., Gilles Brassard, Claude Crépeau, Richard Jozsa, Asher Peres, and William K. Wootters (1993). "Teleporting an unknown quantum state via dual classical and Einstein-Podolsky-Rosen channels". In: *Physical Review Letters* 70 (13), p. 1895 (cit. on p. 206).

Black, Eric D. (2001). "An introduction to Pound–Drever–Hall laser frequency stabilization". In: *American Journal of Physics* 69 (1), pp. 79–87 (cit. on p. 168).

Borregaard, J., M. Zugenmaier, J. M. Petersen, H. Shen, G. Vasilakis, K. Jensen, E. S. Polzik, and A. S. Sørensen (2016). "Scalable photonic network architecture based on motional averaging in room temperature gas". In: *Nature Communications* 7.1, p. 11356 (cit. on p. 103).

Bowen, W.P. and G.J. Milburn (2015). *Quantum Optomechanics*. Taylor & Francis (cit. on pp. 3, 5, 6, 31, 33, 35, 44, 138).

Bowen, Warwick P., Roman Schnabel, Hans-A. Bachor, and Ping Koy Lam (2002). "Polarization Squeezing of Continuous Variable Stokes Parameters". In: *Phys. Rev. Lett.* 88 (9), p. 093601 (cit. on p. 95).

Boyer, Vincent, Alberto M. Marino, Raphael C. Pooser, and Paul D. Lett (2008). "Entangled Images from Four-Wave Mixing". In: *Science* 321.5888, pp. 544–547 (cit. on p. 205).

Braginsky, V. B. and A. B. Manukin (1967). "Ponderomotive Effects of Electromagnetic Radiation". In: *Soviet Physics JETP* (cit. on p. 4).

Braginsky, V. B., A. B. Manukin, and M. Yu Tikhonov (1970). "Investigation of dissipative ponderomotive effects of electromagnetic radiation". In: *Soviet Physics JETP* (cit. on p. 4).

Braginsky, Vladimir B., Yuri I. Vorontsov, and Kip S. Thorne (1980). "Quantum Nondemolition Measurements". In: *Science* 209.4456, pp. 547–557 (cit. on p. 4).

Broersen, Piet M. T (2006). *Automatic Autocorrelation and Spectral Analysis*. Berlin, Heidelberg: Springer-Verlag, p. 298 (cit. on pp. 173, 188).

Brooks, Daniel W.C., Thierry Botter, Sydney Schreppler, Thomas P. Purdy, Nathan Brahms, and Dan M. Stamper-Kurn (2012). "Non-classical light generated by quantum-noise-driven cavity optomechanics". In: *Nature* 488 (7412), pp. 476–480 (cit. on p. 62).

Brown, Kenneth R., Jungsang Kim, and Christopher Monroe (2016). "Co-designing a scalable quantum computer with trapped atomic ions". In: *npj Quantum Information* 2.1, p. 16034 (cit. on p. 15).

Capelle, Thibault et al. (2020). "Probing a Two-Level System Bath via the Frequency Shift of an Off-Resonantly Driven Cavity". In: *Phys. Rev. Applied* 13 (3), p. 034022 (cit. on p. 14).

Carroll, Bradley W. and Dale A. Ostlie (2007). *An Introduction to Modern Astrophysics*. Ed. by San Francisco: Pearson Addison-Wesley. 2nd (International) (cit. on p. 3).

Caves, Carlton M. (1980). "Quantum-Mechanical Radiation-Pressure Fluctuations in an Interferometer". In: *Phys. Rev. Lett.* 45 (2), pp. 75–79 (cit. on p. 4).

— (1981). "Quantum-mechanical noise in an interferometer". In: *Phys. Rev. D* 23 (8), pp. 1693–1708 (cit. on p. 4).

Chen, Yanbei (2013). "Macroscopic quantum mechanics: theory and experimental concepts of optomechanics". In: *Journal of Physics B: Atomic, Molecular and Optical Physics* 46.10, p. 104001 (cit. on p. 14).

Christoph, Philipp, Tobias Wagner, Hai Zhong, Roland Wiesendanger, Klaus Sengstock, Alexander Schwarz, and Christoph Becker (2018). "Combined feedback and sympathetic cooling of a mechanical oscillator coupled to ultracold atoms". In: *New Journal of Physics* 20.9, p. 093020 (cit. on pp. 15, 16).

Chu, Yiwen, Prashanta Kharel, Taekwan Yoon, Luigi Frunzio, Peter T. Rakich, and Robert J. Schoelkopf (2018). "Creation and control of multi-phonon Fock states in a bulk acoustic-wave resonator". In: *Nature* 563 (7733), pp. 666–670 (cit. on pp. 14, 15).

Cirac, J. I. and P. Zoller (1995). "Quantum Computations with Cold Trapped Ions". In: *Phys. Rev. Lett.* 74 (20), pp. 4091–4094 (cit. on p. 15).

Colangelo, Giorgio, Ferran Martin Ciurana, Lorena C Bianchet, Robert J Sewell, and Morgan W Mitchell (2017). "Simultaneous tracking of spin angle and amplitude beyond classical limits". In: *Nature* 543 (7646), pp. 525–528 (cit. on p. 12).

Crameri, Fabio, Grace E. Shephard, and Philip J. Heron (2020). "The misuse of colour in science communication". In: *Nature Communications* 11 (1), pp. 1–10 (cit. on p. x).

Das Sarma, Sankar, Michael Freedman, and Chetan Nayak (2006). "Topological quantum computation". In: *Physics Today* 59.7, pp. 32–38 (cit. on p. 11).

de Lépinay, Laure Mercier, Caspar F. Ockeloen-Korppi, Matthew J. Woolley, and Mika A. Sillanpää (2021). "Quantum mechanics–free subsystem with mechanical oscillators". In: *Science* 372.6542, pp. 625–629 (cit. on p. 20).

Degen, C. L., F. Reinhard, and P. Cappellaro (2017). "Quantum sensing". In: *Rev. Mod. Phys.* 89 (3), p. 035002 (cit. on p. 10).

Delaney, R. D., A. P. Reed, R. W. Andrews, and K. W. Lehnert (2019). "Measurement of Motion beyond the Quantum Limit by Transient Amplification". In: *Phys. Rev. Lett.* 123 (18), p. 183603 (cit. on p. 20).

Delić, Uroš, Manuel Reisenbauer, Kahan Dare, David Grass, Vladan Vuletić, Nikolai Kiesel, and Markus Aspelmeyer (2020). "Cooling of a levitated nanoparticle to the motional quantum ground state". In: *Science* 367.6480, pp. 892–895 (cit. on pp. 14, 15).

Deutsch, Ivan H. and Poul S. Jessen (2010). "Quantum control and measurement of atomic spins in polarization spectroscopy". In: *Optics Communications* 283.5. Quo vadis Quantum Optics?, pp. 681–694 (cit. on p. 97).

Dideriksen, Karsten B, Rebecca Schmieg, Michael Zugenmaier, and E. S. Polzik (2021). "Room-temperature single-photon source with near-millisecond built-in memory". In: *Nature Communications* 12 (1), p. 3699 (cit. on p. 12).

Duan, Lu-Ming, G. Giedke, J. I. Cirac, and P. Zoller (2000). "Inseparability Criterion for Continuous Variable Systems". In: *Phys. Rev. Lett.* 84 (12), pp. 2722–2725 (cit. on p. 176).

Dumont, Vincent, Simon Bernard, Christoph Reinhardt, Alex Kato, Maximilian Ruf, and Jack C. Sankey (2019). "Flexure-tuned membrane-at-the-edge optomechanical system". In: *Opt. Express* 27.18, pp. 25731–25748 (cit. on pp. 42, 55).

Durbin, J. (1960). "The Fitting of Time-Series Models". In: *Revue de l'Institut International de Statistique / Review of the International Statistical Institute* 28.3, pp. 233–244 (cit. on p. 190).

Edwards, R L, G Coles, and W N Sharpe (2004). "Comparison of tensile and bulge tests for thin-film silicon nitride". In: *Experimental Mechanics* 44, pp. 49–54 (cit. on p. 211).

Einstein, A., B. Podolsky, and N. Rosen (1935). "Can Quantum-Mechanical Description of Physical Reality Be Considered Complete?" In: *Phys. Rev.* 47 (10), pp. 777–780 (cit. on p. 176).

Erhart, Jacqueline, Stephan Sponar, Georg Sulyok, Gerald Badurek, Masanao Ozawa, and Yuji Hasegawa (2012). "Experimental demonstration of a universally valid error–disturbance uncertainty relation in spin measurements". In: *Nature Physics*, p. 15 (cit. on p. 6).

Fedorov, S. A., A. Beccari, N. J. Engelsen, and T. J. Kippenberg (2020). "Fractal-like Mechanical Resonators with a Soft-Clamped Fundamental Mode". In: *Phys. Rev. Lett.* 124 (2), p. 025502 (cit. on pp. 12, 14).

Foreman-Mackey, Daniel, David W. Hogg, Dustin Lang, and Jonathan Goodman (2013). "emcee: The MCMC Hammer". In: *Publications of the Astronomical Society of the Pacific* 125.925, pp. 306–312 (cit. on p. 197).

Gardiner, C. W. and P. Zoller (2000). *Quantum Noise*. 2nd edition. Springer-Verlag (cit. on p. 44).

Geremia, J. M., John K. Stockton, and Hideo Mabuchi (2006). "Tensor polarizability and dispersive quantum measurement of multilevel atoms". In: *Phys. Rev. A* 73 (4), p. 042112 (cit. on p. 96).

Gerry, C.C. and P.L. Knight (2005). *Introductory Quantum Optics*. Cambridge University Press (cit. on pp. 33, 35).

Ghadimi, A. H., S. A. Fedorov, N. J. Engelsen, M. J. Bereyhi, R. Schilling, D. J. Wilson, and T. J. Kippenberg (2018). "Elastic strain engineering for ultralow mechanical dissipation". In: *Science* 360.6390, pp. 764–768 (cit. on pp. 12, 14).

Giacomini, Flaminia, Esteban Castro-Ruiz, and Časlav Brukner (2019). "Quantum mechanics and the covariance of physical laws in quantum reference frames". In: *Nature Communications* 10, p. 494 (cit. on p. 92).

Gordon, J. P., H. J. Zeiger, and C. H. Townes (1955). "The Maser—New Type of Microwave Amplifier, Frequency Standard, and Spectrometer". In: *Phys. Rev.* 99 (4), pp. 1264–1274 (cit. on p. 4).

Gorodetsky, M. L., A. Schliesser, G. Anetsberger, S. Deleglise, and T. J. Kippenberg (2010). "Determination of the vacuum optomechanical coupling rate using frequency noise calibration". In: *Opt. Express* 18.22, pp. 23236–23246 (cit. on p. 84).

Griffiths, David J. (2005). *Introduction to quantum mechanics*. Pearson Prentice Hall, p. 468 (cit. on p. 33).

Gross, Christian and Immanuel Bloch (2017). "Quantum simulations with ultracold atoms in optical lattices". In: *Science* 357.6355, pp. 995–1001 (cit. on p. 15).

Hacker, Bastian, Stephan Welte, Severin Daiss, Armin Shaukat, Stephan Ritter, Lin Li, and Gerhard Rempe (2019). "Deterministic creation of entangled atom–light Schrödinger-cat states". In: *Nature Photonics* 13 (2), pp. 110–115 (cit. on p. 12).

Hales, Andrew H., Kipling D. Williams, and Joel Rector (2017). "Alienating the Audience: How Abbreviations Hamper Scientific Communication". In: *APS observer* 30 (cit. on p. x).

Hammerer, K., M. Aspelmeyer, E. S. Polzik, and P. Zoller (2009). "Establishing Einstein-Poldosky-Rosen Channels between Nanomechanics and Atomic Ensembles". In: *Phys. Rev. Lett.* 102 (2), p. 020501 (cit. on p. 18).

Hammerer, Klemens (2006). "Quantum Information Processing with Atomic Ensembles and Light". Ph.D. thesis. Technische Universität München (cit. on p. 91).

Hammerer, Klemens, Anders S. Sørensen, and E. S. Polzik (2010). "Quantum interface between light and atomic ensembles". In: *Rev. Mod. Phys.* 82 (2), pp. 1041–1093 (cit. on p. 11).

Hecht, Eugene (2002). *Optics*. 4th International Edition. Addison Wesley (cit. on p. 37).

Higginbotham, A. P., P. S. Burns, M. D. Urmey, R. W. Peterson, N. S. Kampel, B. M. Brubaker, G. Smith, K. W. Lehnert, and C. A. Regal (2018). "Harnessing electro-optic correlations in an efficient mechanical converter". In: *Nature Physics* 14.10, pp. 1038–1042 (cit. on pp. 15, 16).

Holstein, T. and H. Primakoff (1940). "Field Dependence of the Intrinsic Domain Magnetization of a Ferromagnet". In: *Phys. Rev.* 58 (12), pp. 1098–1113 (cit. on p. 91).

Horodecki, Ryszard, Paweł Horodecki, Michał Horodecki, and Karol Horodecki (2009). "Quantum entanglement". In: *Rev. Mod. Phys.* 81 (2), pp. 865–942 (cit. on p. 176).

Huang, Xinyao, Emil Zeuthen, Denis V. Vasilyev, Qiongyi He, Klemens Hammerer, and E. S. Polzik (2018). "Unconditional Steady-State Entanglement in Macroscopic Hybrid Systems by Coherent Noise Cancellation". In: *Phys. Rev. Lett.* 121 (10), p. 103602 (cit. on p. 20).

Jayich, A M, J C Sankey, B M Zwickl, C Yang, J D Thompson, S M Girvin, A A Clerk, F Marquardt, and J G E Harris (2008). "Dispersive optomechanics: a membrane inside a cavity". In: *New Journal of Physics* 10.9, p. 095008 (cit. on pp. 52, 53, 69).

Jöckel, Andreas, Aline Faber, Tobias Kampschulte, Maria Korppi, Matthew T Rakher, and Philipp Treutlein (2015). "Sympathetic cooling of a membrane oscillator in a hybrid mechanical–atomic system". In: *Nature Nanotechnology* 10.1, pp. 55–59 (cit. on pp. 15, 16).

Julsgaard, B., A. Kozhekin, and E. S. Polzik (2001). "Experimental long-lived entanglement of two macroscopic objects". In: *Nature* 413 (6854), pp. 400–403 (cit. on pp. 11, 19).

Julsgaard, B., J. Sherson, J. L. Sørensen, and E. S. Polzik (2004). "Characterizing the spin state of an atomic ensemble using the magneto-optical resonance method". In: *Journal of Optics B: Quantum and Semiclassical Optics* 6.1, pp. 5–14 (cit. on p. 100).

Julsgaard, Brian (2003). "Entanglement and Quantum Interactions with Macroscopic Gas Samples". Ph.D. thesis. University of Aarhus (cit. on pp. 87, 90, 91, 95, 96, 100).

Karg, Thomas M., Baptiste Gouraud, Chun Tat Ngai, Gian-Luca Schmid, Klemens Hammerer, and Philipp Treutlein (2020). "Light-mediated strong coupling between a mechanical oscillator and atomic spins 1 meter apart". In: *Science* (cit. on pp. 15, 16).

Kaushik, A., H. Kahn, and A.H. Heuer (2005). "Wafer-level mechanical characterization of silicon nitride MEMS". In: *Journal of Microelectromechanical Systems* 14.2, pp. 359–367 (cit. on p. 211).

Keplero, Iohanne (1619). *De Cometis libelli tres.* Typis Andreae Apergeri, p. 168 (cit. on p. 3).

Khalili, F. Ya. and E. S. Polzik (2018). "Overcoming the Standard Quantum Limit in Gravitational Wave Detectors Using Spin Systems with a Negative Effective Mass". In: *Phys. Rev. Lett.* 121 (3), p. 031101 (cit. on pp. 5, 20).

Kimble, H. J. (2008). "The quantum internet". In: *Nature* 453.7198, pp. 1023–1030 (cit. on p. 10).

Kjaergaard, Morten, Mollie E. Schwartz, Jochen Braumüller, Philip Krantz, Joel I.-J. Wang, Simon Gustavsson, and William D. Oliver (2020). "Superconducting Qubits: Current State of Play". In: *Annual Review of Condensed Matter Physics* 11.1, pp. 369–395 (cit. on p. 11).

Kleckner, Dustin, Brian Pepper, Evan Jeffrey, Petro Sonin, Susanna M. Thon, and Dirk Bouwmeester (2011). "Optomechanical trampoline resonators". In: *Opt. Express* 19.20, pp. 19708–19716 (cit. on pp. 12, 14).

Kogelnik, H. and T. Li (1966). "Laser Beams and Resonators". In: *Appl. Opt.* 5.10, pp. 1550–1567 (cit. on p. 75).

Kohler, Jonathan, Justin A. Gerber, Emma Dowd, and Dan M. Stamper-Kurn (2018). "Negative-Mass Instability of the Spin and Motion of an Atomic Gas Driven by Optical Cavity Backaction". In: *Phys. Rev. Lett.* 120 (1), p. 013601 (cit. on p. 15).

Koschorreck, M., M. Napolitano, B. Dubost, and M. W. Mitchell (2010). "Sub-Projection-Noise Sensitivity in Broadband Atomic Magnetometry". In: *Phys. Rev. Lett.* 104 (9), p. 093602 (cit. on p. 12).

Krauter, H, D Salart, C A Muschik, J M Petersen, Heng Shen, T Fernholz, and E. S. Polzik (2013). "Deterministic quantum teleportation between distant atomic objects". In: *Nature Physics* 9 (7), pp. 400–404 (cit. on pp. 12, 206).

Krauter, Hanna, Christine A. Muschik, Kasper Jensen, Wojciech Wasilewski, Jonas M. Petersen, J. Ignacio Cirac, and E. S. Polzik (2011). "Entanglement Generated by Dissipation and Steady State Entanglement of Two Macroscopic Objects". In: *Phys. Rev. Lett.* 107 (8), p. 080503 (cit. on p. 11).

Kurizki, Gershon, Patrice Bertet, Yuimaru Kubo, Klaus Mølmer, David Petrosyan, Peter Rabl, and Jörg Schmiedmayer (2015). "Quantum technologies with hybrid systems". In: *Proceedings of the National Academy of Sciences* 112.13, pp. 3866–3873 (cit. on p. 10).

Lebedew, Peter (1901). "Untersuchungen über die Druckkräfte des Lichtes". In: *Annalen der Physik* 311.11, pp. 433–458 (cit. on p. 3).

Lee, K. C. et al. (2011). "Entangling Macroscopic Diamonds at Room Temperature". In: *Science* 334.6060, pp. 1253–1256 (cit. on pp. 14, 15).

Lee, S.-K. (2008). "Spin noise at an arbitrary spin temperature". In: (cit. on p. 101).

Leroux, Ian D., Monika H. Schleier-Smith, and Vladan Vuletić (2010). "Implementation of Cavity Squeezing of a Collective Atomic Spin". In: *Phys. Rev. Lett.* 104 (7), p. 073602 (cit. on p. 12).

Levin, Yu. (1998). "Internal thermal noise in the LIGO test masses: A direct approach". In: *Phys. Rev. D* 57 (2), pp. 659–663 (cit. on p. 150).

Lodahl, Peter, Sahand Mahmoodian, and Søren Stobbe (2015). "Interfacing single photons and single quantum dots with photonic nanostructures". In: *Rev. Mod. Phys.* 87 (2), pp. 347–400 (cit. on p. 11).

Spectrum Instrumentation GmbH (2020). *M2i.49xx Datasheet.* Version 7.5.2020 (cit. on p. 166).

MacCabe, Gregory S., Hengjiang Ren, Jie Luo, Justin D. Cohen, Hengyun Zhou, Alp Sipahigil, Mohammad Mirhosseini, and Oskar Painter (2020). "Nano-acoustic resonator with ultralong phonon lifetime". In: *Science* 370.6518, pp. 840–843 (cit. on p. 14).

Manukhova, A. D., A. A. Rakhubovsky, and R. Filip (2020). "Pulsed atom-mechanical quantum non-demolition gate". In: *npj Quantum Information* 6.1, p. 4 (cit. on p. 20).

Marinković, Igor, Andreas Wallucks, Ralf Riedinger, Sungkun Hong, Markus Aspelmeyer, and Simon Gröblacher (2018). "Optomechanical Bell Test". In: *Phys. Rev. Lett.* 121 (22), p. 220404 (cit. on pp. 14, 15).

Mason, David, Junxin Chen, Massimiliano Rossi, Yeghishe Tsaturyan, and Albert Schliesser (2019). "Continuous force and displacement measurement below the standard quantum limit". In: *Nature Physics* 15 (8), pp. 745–749 (cit. on p. 14).

Mathiassen, Jonas B. (2019). "Characterising and Modelling Thermal Substrate Noise for a Membrane in the Middle Optomechanical Cavity". M.Sc. thesis. University of Copenhagen (cit. on p. 149).

Maxwell, James Clerk (1873). *A treatise on electricity and magnetism.* Vol. 1. Clarendon press (cit. on p. 3).

McConnell, Robert, Hao Zhang, Jiazhong Hu, Senka Ćuk, and Vladan Vuletić (2015). "Entanglement with negative Wigner function of almost 3,000 atoms heralded by one photon". In: *Nature* 519 (7544), pp. 439–442 (cit. on p. 12).

Mermin, N. David (1989). "What's Wrong with these Equations?" In: *Physics Today* 42.10, pp. 9–11 (cit. on p. xi).

Meystre, P., E. M. Wright, J. D. McCullen, and E. Vignes (1985). "Theory of radiation-pressure-driven interferometers". In: *J. Opt. Soc. Am. B* 2.11, pp. 1830–1840 (cit. on p. 62).

Miao, Haixing (2010). "Exploring Macroscopic Quantum Mechanics in Optomechanical Devices". Ph.D. thesis. University of Western Australia (cit. on p. 188).

Midolo, Leonardo, Albert Schliesser, and Andrea Fiore (2018). "Nano-opto-electro-mechanical systems". In: *Nature Nanotechnology* 13, pp. 11–18 (cit. on pp. 15, 16).

Milonni, Peter W. and Joseph H. Eberly (2010). *Laser physics.* Wiley (cit. on p. 75).

Mirhosseini, Mohammad, Alp Sipahigil, Mahmoud Kalaee, and Oskar Painter (2020). "Superconducting qubit to optical photon transduction". In: *Nature* 588 (7839), pp. 599–603 (cit. on pp. 15, 16).

Møller, Christoffer B. (2018). "Quantum Back-Action Evasion in a Hybrid Spin-Optomechanical System". Ph.D. thesis. University of Copenhagen (cit. on pp. 17, 22, 53, 58, 60, 62, 70, 82, 85, 94, 95, 150, 155).

Møller, Christoffer B., Rodrigo A. Thomas, Georgios Vasilakis, Emil Zeuthen, Yeghishe Tsaturyan, Mikhail Balabas, Kasper Jensen, Albert Schliesser, Klemens Hammerer, and E. S. Polzik (2017). "Quantum back-action-evading mea-

surement of motion in a negative mass reference frame". In: *Nature* 547.7662, pp. 191–195 (cit. on pp. 16–18, 22, 71, 85, 124, 149, 168, 186, 202).

Müller-Ebhardt, Helge, Henning Rehbein, Chao Li, Yasushi Mino, Kentaro Somiya, Roman Schnabel, Karsten Danzmann, and Yanbei Chen (2009). "Quantum-state preparation and macroscopic entanglement in gravitational-wave detectors". In: *Phys. Rev. A* 80 (4), p. 043802 (cit. on p. 188).

Muschik, Christine A., E. S. Polzik, and J. Ignacio Cirac (2011). "Dissipatively driven entanglement of two macroscopic atomic ensembles". In: *Phys. Rev. A* 83 (5), p. 052312 (cit. on pp. 11, 12).

NCEI Geomagnetic Modeling Team and British Geological Survey (2019). *World Magnetic Model 2020*. NOAA National Centers for Environmental Information. DOI: 10.25921/11v3-da71. (Visited on 08/12/2022) (cit. on p. 105).

Neuhaus, L., R. Metzdorff, S. Chua, T. Jacqmin, T. Briant, A. Heidmann, P.-F. Cohadon, and S. Deléglise (2017). "PyRPL (Python Red Pitaya Lockbox) — An open-source software package for FPGA-controlled quantum optics experiments". In: *2017 Conference on Lasers and Electro-Optics Europe & European Quantum Electronics Conference (CLEO/Europe-EQEC)*, pp. 1–1. DOI: 10.1109/CLEOE-EQEC.2017.8087380 (cit. on p. 168).

Newville, Matt et al. (2021). *LMFIT: Non-Linear Least-Square Minimization and Curve-Fitting for Python*. zenodo.org/record/4516651. Version 1.0.2 (cit. on p. 115).

Nielsen, William H. P. (2016). "Quantum Cavity Optomechanics with Phononic Bandgap Shielded Silicon Nitride Membranes". Ph.D. thesis. University of Copenhagen (cit. on pp. 16, 17, 22, 23, 26, 27, 31, 53, 55, 58, 61, 62, 72, 80, 84, 123, 124, 171, 172).

Nielsen, William H. P., Yeghishe Tsaturyan, Christoffer B. Møller, E. S. Polzik, and Albert Schliesser (2017). "Multimode optomechanical system in the quantum regime". In: *Proceedings of the National Academy of Sciences* 114.1, pp. 62–66 (cit. on pp. 16, 62, 71, 72, 123).

Ockeloen-Korppi, C. F., E. Damskägg, J. M. Pirkkalainen, M. Asjad, A. A. Clerk, F. Massel, M. J. Woolley, and M. A. Sillanpää (2018). "Stabilized entanglement of massive mechanical oscillators". In: *Nature* 556 (7702), pp. 478–482 (cit. on p. 20).

Ozawa, Masanao (2003). "Universally valid reformulation of the Heisenberg uncertainty principle on noise and disturbance in measurement". In: *Phys. Rev. A* 67 (4), p. 042105 (cit. on p. 6).

Parniak, Michał, Ivan Galinskiy, Timo Zwettler, and E. S. Polzik (2021). "High-frequency broadband laser phase noise cancellation using a delay line". In: *Opt. Express* 29.5, pp. 6935–6946 (cit. on p. 164).

Pierson, Hugh O. (1999). *Handbook of Chemical Vapor Deposition (CVD)*. Park Ridge, New Jersey, U.S.A.: Noyes Publications (cit. on p. 211).

Polzik, E. S. and Klemens Hammerer (2015). "Trajectories without quantum uncertainties". In: *Annalen der Physik* 527.1-2, A15–A20 (cit. on p. 19).

Purdy, T. P., P.-L. Yu, R. W. Peterson, N. S. Kampel, and C. A. Regal (2013). "Strong Optomechanical Squeezing of Light". In: *Phys. Rev. X* 3 (3), p. 031012 (cit. on p. 62).

Reed, A. P. et al. (2017). "Faithful conversion of propagating quantum information to mechanical motion". In: *Nature Physics* 13 (12), pp. 1163–1167 (cit. on pp. 15, 16).

Riedinger, Ralf, Andreas Wallucks, Igor Marinković, Clemens Löschnauer, Markus Aspelmeyer, Sungkun Hong, and Simon Gröblacher (2018). "Remote quantum entanglement between two micromechanical oscillators". In: *Nature* 556 (7702), pp. 473–477 (cit. on pp. 14, 15).

Rossi, Massimiliano (2020). "Quantum Measurement and Control of a Mechanical Resonator". Ph.D. thesis. University of Copgenhagen (cit. on p. 81).

Rossi, Massimiliano, David Mason, Junxin Chen, and Albert Schliesser (2019). "Observing and Verifying the Quantum Trajectory of a Mechanical Resonator". In: *Phys. Rev. Lett.* 123 (16), p. 163601 (cit. on p. 14).

Rossi, Massimiliano, David Mason, Junxin Chen, Yeghishe Tsaturyan, and Albert Schliesser (2018). "Measurement-based quantum control of mechanical motion". In: *Nature* 563 (7729), pp. 53–58 (cit. on p. 14).

Hamamatsu Photonics K.K. (2019). *S5971, S5972, S5973 series datasheet* (cit. on p. 166).

Safavi-Naeini, Amir H., Simon Gröblacher, Jeff T. Hill, Jasper Chan, Markus Aspelmeyer, and Oskar Painter (2013). "Squeezed light from a silicon micromechanical resonator". In: *Nature* 500 (7461), pp. 185–189 (cit. on p. 62).

Schliesser, Albert (2009). "Cavity Optomechanics and Optical Frequency Comb Generation with Silica Whispering-Gallery-Mode Microresonators". Ph.D. thesis. Ludwig–Maximilians–Universität München (cit. on p. 58).

Seis, Yannick (2021). "Ultra-Coherent Electro-Mechanics in the Quantum Regime". Ph.D. thesis. University of Copenhagen (cit. on p. 81).

Shah, V., G. Vasilakis, and M. V. Romalis (2010). "High Bandwidth Atomic Magnetometery with Continuous Quantum Nondemolition Measurements". In: *Phys. Rev. Lett.* 104 (1), p. 013601 (cit. on p. 12).

Shaham, Roy, Or Katz, and Ofer Firstenberg (2020). "Quantum dynamics of collective spin states in a thermal gas". In: *Phys. Rev. A* 102 (1), p. 012822 (cit. on pp. 12, 104).

Shomroni, Itay, Liu Qiu, Daniel Malz, Andreas Nunnenkamp, and Tobias J. Kippenberg (2019). "Optical backaction-evading measurement of a mechanical oscillator". In: *Nature Communications* 10 (1) (cit. on p. 20).

Siegman, A.E. (1986). *Lasers*. University Science Books (cit. on p. 54).

Slusher, R. E., L. W. Hollberg, B. Yurke, J. C. Mertz, and J. F. Valley (1985). "Observation of Squeezed States Generated by Four-Wave Mixing in an Optical Cavity". In: *Phys. Rev. Lett.* 55 (22), pp. 2409–2412 (cit. on p. 62).

M Squared (2013). *SolsTiS User Manual*. Version 10.0 (cit. on p. 163).

Sørensen, H. L., J.-B. Béguin, K. W. Kluge, I. Iakoupov, A. S. Sørensen, J. H. Müller, E. S. Polzik, and J. Appel (2016). "Coherent Backscattering of Light Off One-Dimensional Atomic Strings". In: *Phys. Rev. Lett.* 117 (13), p. 133604 (cit. on p. 16).

Stannigel, K, P Rabl, and P Zoller (2012). "Driven-dissipative preparation of entangled states in cascaded quantum-optical networks". In: *New Journal of Physics* 14.6, p. 063014 (cit. on p. 20).

Steck, Daniel A. (2019). *Cesium D Line Data.* available online at http://steck.us/alkalidata (revision 2.2.21, 21 November 2019) (cit. on pp. 88–90).

Szorkovszky, A, A A Clerk, A C Doherty, and W P Bowen (2014). "Mechanical entanglement via detuned parametric amplification". In: *New Journal of Physics* 16.6, p. 063043 (cit. on p. 20).

Tabata, Osamu, Ken Kawahata, Susumu Sugiyama, and Isemi Igarashi (1989). "Mechanical property measurements of thin films using load-deflection of composite rectangular membranes". In: *Sensors and Actuators* 20 (1-2). A Special Issue Devoted to Micromechanics, pp. 135–141 (cit. on p. 211).

Tagantsev, A. K. and E. S. Polzik (2021). "Dissipative optomechanical coupling with a membrane outside of an optical cavity". In: *Phys. Rev. A* 103 (6), p. 063503 (cit. on p. 42).

Tan, Huatang, L. F. Buchmann, H. Seok, and Gaoxiang Li (2013). "Achieving steady-state entanglement of remote micromechanical oscillators by cascaded cavity coupling". In: *Phys. Rev. A* 87, p. 022318 (cit. on pp. 14, 15).

Tang, Yuanjiang, Ya Wen, Ling Cai, and Kaifeng Zhao (2020). "Spin-noise spectrum of hot vapor atoms in an anti-relaxation-coated cell". In: *Phys. Rev. A* 101 (1), p. 013821 (cit. on p. 104).

Thomas, Rodrigo A. (2020). "Optical spin-mehcanics quantum interface: entanglement and back-action evasion". Ph.D. thesis. University of Copenhagen (cit. on pp. 17, 18, 22, 46, 87, 90, 91, 93, 96, 99–105, 107, 168, 190, 201).

Thomas, Rodrigo A., Christoffer Østfeldt, Christian Bærentsen, Michał Parniak, and E. S. Polzik (2021). "Calibration of spin-light coupling by coherently induced Faraday rotation". In: *Opt. Express* 29.15, pp. 23637–23653 (cit. on pp. 87, 111).

Thomas, Rodrigo A., Michał Parniak, Christoffer Østfeldt, Christoffer B. Møller, Christian Bærentsen, Yeghishe Tsaturyan, Albert Schliesser, Jürgen Appel, Emil Zeuthen, and E. S. Polzik (2020). "Entanglement between distant macroscopic mechanical and spin systems". In: *Nature Physics* 17, pp. 228–233 (cit. on pp. ix, 7, 22, 47, 90, 98, 111, 149, 156, 175, 177–180, 201, 203).

Thompson, J. D., B. M. Zwickl, A. M. Jayich, Florian Marquardt, S. M. Girvin, and J. G.E. Harris (Mar. 2008). "Strong dispersive coupling of a high-finesse cavity to a micromechanical membrane". In: *Nature* 452 (7183), pp. 72–75 (cit. on p. 12).

Tsang, Mankei and Carlton M. Caves (2010). "Coherent Quantum-Noise Cancellation for Optomechanical Sensors". In: *Phys. Rev. Lett.* 105 (12), p. 123601 (cit. on p. 19).

— (2012). "Evading Quantum Mechanics: Engineering a Classical Subsystem within a Quantum Environment". In: *Phys. Rev. X* 2 (3), p. 031016 (cit. on p. 19).

Tsaturyan, Y., A. Barg, A. Simonsen, L. G. Villanueva, S. Schmid, A. Schliesser, and E. S. Polzik (2014). "Demonstration of suppressed phonon tunneling losses in phononic bandgap shielded membrane resonators for high-Q optomechanics". In: *Opt. Express* 22.6, pp. 6810–6821 (cit. on pp. 16, 70).

Tsaturyan, Yeghishe (2019). "Ultracoherent soft-clamped mechanical resonators for quantum cavity optomechanics". Ph.D. thesis. University of Copenhagen (cit. on pp. 28, 58, 60, 62, 70, 82, 211).

Tsaturyan, Yeghishe, A. Barg, E. S. Polzik, and A. Schliesser (2017). "Ultracoherent nanomechanical resonators via soft clamping and dissipation dilution". In: *Nature Nanotechnology* 12 (8), pp. 776–783 (cit. on pp. 12, 14, 16, 33, 70–72, 74).

Uhlenbeck, G. E. and L. S. Ornstein (1930). "On the Theory of the Brownian Motion". In: *Phys. Rev.* 36 (5), pp. 823–841 (cit. on p. 29).

Vahlbruch, Henning, Moritz Mehmet, Karsten Danzmann, and Roman Schnabel (2016). "Detection of 15 dB Squeezed States of Light and their Application for the Absolute Calibration of Photoelectric Quantum Efficiency". In: *Phys. Rev. Lett.* 117 (11), p. 110801 (cit. on pp. 62, 206).

Vaidman, Lev (1994). "Teleportation of quantum states". In: *Phys. Rev. A* 49 (2), pp. 1473–1476 (cit. on p. 206).

Vasilakis, G., V. Shah, and M. V. Romalis (2011). "Stroboscopic Backaction Evasion in a Dense Alkali-Metal Vapor". In: *Phys. Rev. Lett.* 106 (14), p. 143601 (cit. on pp. 12, 100).

Vasilakis, G., H. Shen, K. Jensen, M. Balabas, D. Salart, B. Chen, and E. S Polzik (2015). "Generation of a squeezed state of an oscillator by stroboscopic back-action-evading measurement". In: *Nature Physics* 11 (5), pp. 389–392 (cit. on pp. 12, 206).

Vasilyev, Denis V., Christine A. Muschik, and Klemens Hammerer (2013). "Dissipative versus conditional generation of Gaussian entanglement and spin squeezing". In: *Phys. Rev. A* 87 (5), p. 053820 (cit. on p. 20).

Wallucks, Andreas, Igor Marinković, Bas Hensen, Robert Stockill, and Simon Gröblacher (2020). "A quantum memory at telecom wavelengths". In: *Nature Physics* 16 (7), pp. 772–777 (cit. on pp. 14, 15).

Wasilewski, W., T. Fernholz, K. Jensen, L. S. Madsen, H. Krauter, C. Muschik, and E. S. Polzik (2009). "Generation of two-mode squeezed and entangled light in a single temporal and spatial mode". In: *Opt. Express* 17.16, pp. 14444–14457 (cit. on p. 11).

Wasilewski, W., K. Jensen, H. Krauter, J. J. Renema, M. V. Balabas, and E. S. Polzik (2010). "Quantum Noise Limited and Entanglement-Assisted Magnetometry". In: *Phys. Rev. Lett.* 104, p. 133601 (cit. on pp. 11, 20).

Weis, Stefan, Rémi Rivière, Samuel Deléglise, Emanuel Gavartin, Olivier Arcizet, Albert Schliesser, and Tobias J. Kippenberg (2010). "Optomechanically Induced Transparency". In: *Science* 330.6010, pp. 1520–1523 (cit. on p. 58).

Wieczorek, Witlef, Sebastian G. Hofer, Jason Hoelscher-Obermaier, Ralf Riedinger, Klemens Hammerer, and Markus Aspelmeyer (2015). "Optimal State Estimation for Cavity Optomechanical Systems". In: *Phys. Rev. Lett.* 114 (22), p. 223601 (cit. on p. 14).

Wieman, C. and T. W. Hänsch (1976). "Doppler-Free Laser Polarization Spectroscopy". In: *Phys. Rev. Lett.* 36 (20), pp. 1170–1173 (cit. on p. 165).

Wiener, N. (1964). *Extrapolation, Interpolation, and Smoothing of Stationary Time Series: With Engineering Applications*. Massachusetts Institute of Technology : Paperback series. M.I.T. Press (cit. on p. 188).

Wilson, D. J., V. Sudhir, N. Piro, R. Schilling, A. Ghadimi, and T. J. Kippenberg (2015). "Measurement-based control of a mechanical oscillator at its thermal decoherence rate". In: *Nature* 524 (7565), pp. 325–329 (cit. on p. 14).

Wilson, Dalziel J. (2012). "Cavity Optomechanics with High-Stress Nitride Films". Ph.D. thesis. California Institute of Technology (cit. on pp. 29, 52, 69).

Wilson, Dalziel J., C. A. Regal, S. B. Papp, and H. J. Kimble (2009). "Cavity Optomechanics with Stoichiometric SiN Films". In: *Phys. Rev. Lett.* 103 (20), p. 207204 (cit. on p. 69).

Woolley, M. J. and A. A. Clerk (2013). "Two-mode back-action-evading measurements in cavity optomechanics". In: *Phys. Rev. A* 87 (6), p. 063846 (cit. on pp. 14, 15).

Yap, Min Jet et al. (2020). "Broadband reduction of quantum radiation pressure noise via squeezed light injection". In: *Nature Photonics* 14, pp. 19–23 (cit. on pp. 14, 15).

Yu, P.-L., K. Cicak, N. S. Kampel, Y. Tsaturyan, T. P. Purdy, R. W. Simmonds, and C. A. Regal (2014). "A phononic bandgap shield for high-Q membrane microresonators". In: *Applied Physics Letters* 104.2, p. 023510 (cit. on pp. 12, 16, 70).

Zeuthen, E., E. S. Polzik, and F. Ya. Khalili (2019). "Gravitational wave detection beyond the standard quantum limit using a negative-mass spin system and virtual rigidity". In: *Phys. Rev. D* 100 (6), p. 062004 (cit. on pp. 5, 20).

Zhang, Keye, Pierre Meystre, and Weiping Zhang (2013). "Back-action-free quantum optomechanics with negative-mass Bose-Einstein condensates". In: *Phys. Rev. A* 88 (4), p. 043632 (cit. on p. 20).

Zugenmaier, Michael (2018). "Towards a Room Temperature Single Photon Source Based on Atomic Vapour". Ph.D. thesis. University of Copenhagen (cit. on p. 101).